Orchestrating nanomechanical motion with light

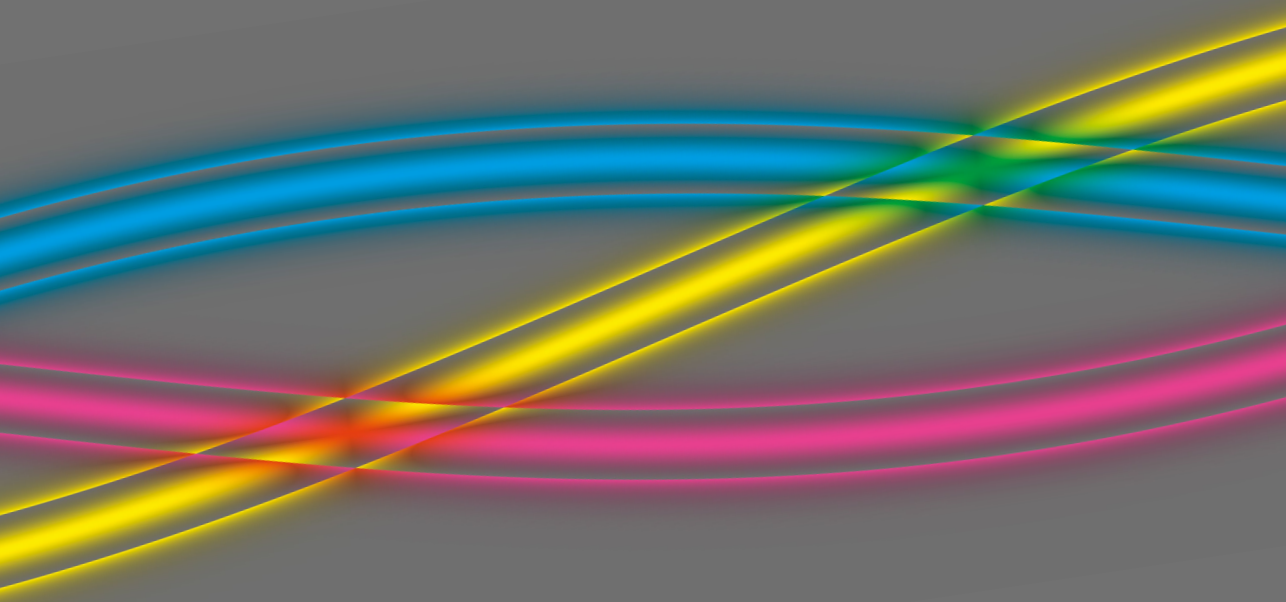

Jesse J. Slim

Orchestrating nanomechanical motion with light

Jesse J. Slim

Cover image: Coloured bands represent phase and amplitude of the complex cross-correlation spectrum of circulating thermal fluctuations (Figure 4.3d).

Ph.D. thesis, Eindhoven University of Technology, March 2023
Orchestrating nanomechanical motion with light
Jesse J. Slim
ISBN: 978-94-92323-65-1

The work described in this thesis was performed at:
AMOLF, Science Park 104, 1098 XG Amsterdam, The Netherlands.

This work is part of the research programme of the Netherlands Organisation for Scientific Research (NWO).

More information about the *Photonic Forces* group at AMOLF can be found at `https://www.optomechanics.nl`.

A digital version of this thesis is freely available at:
`https://ir.amolf.nl/` and `https://research.tue.nl/`.

Orchestrating nanomechanical motion with light

PROEFSCHRIFT

ter verkrijging van de graad van doctor aan de Technische Universiteit Eindhoven, op gezag van de rector magnificus prof.dr.ir. F.P.T. Baaijens, voor een commissie aangewezen door het College voor Promoties, in het openbaar te verdedigen op donderdag 9 maart 2023 om 16:00 uur

door

Jesse Joost Slim

geboren te Groningen

Dit proefschrift is goedgekeurd door de promotoren en de samenstelling van de promotiecommissie is als volgt:

voorzitter:	prof. dr. S. Calero	
promotor:	prof. dr. E. Verhagen	
copromotor:	dr. A. Nunnenkamp	(Universität Wien)
leden:	prof. dr. O. Zilberberg	(Universität Konstanz)
	prof. dr. G.A. Steele	(Technische Universiteit Delft)
	prof. dr. R.A. Duine	
	prof. dr. A. Fiore	

Het onderzoek dat in dit proefschrift wordt beschreven is uitgevoerd in overeenstemming met de TU/e Gedragscode Wetenschapsbeoefening.

Gain lozer goud as mìnsen, je kinnen der oapen mit vangen.

Contents

1

Introduction

Materials are all around us, shaping our everyday, macroscopic world. However, most of their properties derive from the arrangement of the microscopic constituents that make up a material. For example, the interaction between electron waves and atoms neatly ordered into a crystal determines whether a material will conduct electricity (e.g. copper) or be an insulator (e.g. quartz). This is a central result in the field of solid-state physics [1], and hinges on the observation that a periodic crystal potential organizes the energy levels of electron waves into bands, separated by gaps.

The interactions inside a material are usually bound by basic principles of physics. These fundamentally constrain the material's properties: For example, time-reversal symmetry dictates that electricity will flow through a wire from left to right just as well as from right to left — a property known as reciprocity. Likewise, glass is equally transparent for light in both directions[1]. Other fundamental constraints include conservation of energy and the second law of thermodynamics, or derive from spatial symmetries. A way to break these shackles would thus enable unique and potentially useful material responses.

1.1. Metamaterials

Over the last decades, metamaterials have garnered a lot of attention. These 'effective' materials use larger building blocks than the atoms making up regular materials, giving room to engineer their properties and fine-tune their constitutional interactions through careful design and control of the building blocks and their couplings. Photonic crystals [2] can be considered a metamaterial, and form a prime example: By combining real materials with varying refractive indices in a periodic arrangement, a composite effective medium is established with an optical 'crystal potential' that gives rise to a band structure for light. Similar to electron

[1] This even holds true for so-called 'one-way mirrors', for which the perceived difference in transparency actually comes about by illuminating both sides with a different brightness.

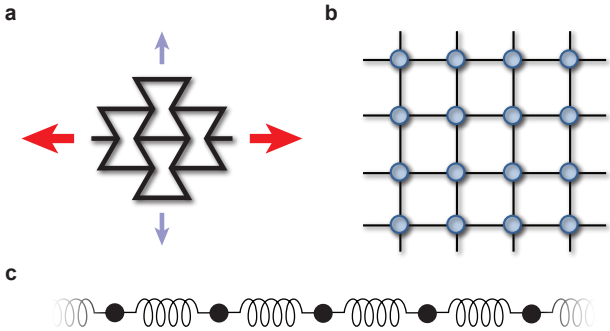

Figure 1.1: **Metamaterials. (a)** Structure of a metamaterial with a negative Poisson's ratio: When stretched in the direction indicated by the red arrows, the material expands laterally (blue arrows). **(b)** Example of a tight-binding model. Each circle indicates a lattice site that is coupled to its neighbours. **(c)** One-dimensional chain of masses coupled by springs. This model can be used to study the vibrations of atoms in a periodic lattice potential.

waves, tuning the corresponding photonic bandgaps then allows blocking or enabling the propagation of light in desired wavelength ranges. By now, this unique ability to manipulate the flow of light has found many applications, e.g. in Bragg reflectors, anti-reflective coatings, and photonic-crystal fibers. This technique naturally carries over to other wave phenomena as well: For example, soundproofing is facilitated by acoustic metamaterials [3].

Metamaterials can be composed of small, subwavelength building blocks, but also of macroscopic units like beams, springs, resonators, or optical cavities. Interesting collective responses can then be induced when multiple of these units are combined to form coupled networks or complete lattices. Importantly, judicious engineering of their structure bestows metamaterials with responses unparalleled in atomic materials. Figure 1.1a shows a material with a negative Poisson's ratio, expanding laterally when stretched [4]. In the microwave and optical domains, metamaterials can be constructed with the ability to cloak a scattering object [5, 6] or with a negative refractive index [7, 8]. Moreover, by exposing the elements to external driving, controllable active metamaterials [9–11] are formed, in which even fundamental symmetries such as time-reversal symmetry or the conservation of energy can be broken.

The dynamics of many materials, real and artificial alike, can be modelled by a lattice of fixed sites coupled by interactions. An example is the tight-binding model (Figure 1.1b), often used in condensed matter physics. With this method, the electronic properties of e.g. graphene can be derived from the interactions between the orbitals of nearby carbon atoms [12], illustrating a fermionic tight-binding model. Another powerful class of tight-binding models arises in the study of bosonic excitations, and deals with networks of coupled harmonic oscillators. As a demonstration, Figure 1.1c shows how such a model can describe atoms vibrating around their equilibrium position in a lattice potential [13].

1.2. Nanomechanical resonators

In this spirit, nanomechanical resonators present an interesting building block to create metamaterials. Nanomechanical resonators [14–16] are conceptually simple, yet surprisingly versatile physical systems. Their ability to interface with many different degrees of freedom puts them forth as sensors [17, 18] and transducers [19] even for quantum signals [20, 21], while their high coherence and tunability find application in signal filtering and processing [22]. Due to their small mass, stochastic forces from the thermal environment play a considerable role in their dynamics, advancing them as an important testbed for stochastic thermodynamics [23, 24]. Finally, nanomechanical resonators are used to create computational elements [25] and perform fundamental tests of quantum mechanics by controlling and measuring their quantum states of motion [26, 27].

Nanomechanical resonators have been studied extensively in isolation. By coupling them, intriguing dynamics are unlocked including chaos [28], synchronization [29], and multimode lasing of mechanical vibrations [30] — all depending on nonlinear processes. In this thesis, we realize small, *linear* nanomechanical metamaterials by constructing tunable nanomechanical networks. Our aim is then to use this experimental platform to study the emergence of, and mechanisms behind, unusual collective responses induced through the controlled breaking of symmetries. In particular, we will orchestrate these networks in a reconfigurable fashion using light. Apart from demonstrating our platform as a proof-of-concept implementing a highly-tunable metamaterial, we believe that the physics we uncover could be useful in the traditional application domains of nanomechanical resonators as well.

The remainder of this chapter provides a basic introduction to the main concepts that are combined in this thesis: breaking time-reversal symmetry by dynamic modulation, the quantum Hall effect and topology, non-Hermitian dynamics, and cavity optomechanics. We conclude with an outline of the contents of the thesis.

1.3. Breaking time-reversal symmetry

In this thesis, we explore the physics of mechanical systems and lattices with broken symmetries. In particular, we study the effect of broken *time-reversal* ($\mathcal{T}$) *symmetry*, where the operator $\mathcal{T} : t \mapsto -t$ reverses time t. A 'trivial' way to break $\mathcal{T}$-symmetry is by adding dissipation to a system. However, richer dynamics are enabled by $\mathcal{T}$-symmetry-breaking *gauge fields*, which allow nonreciprocal functionality (i.e. direction-dependent asymmetry in transmission) [31–35] and underlie topological isolation in extended systems [36–38]. The latter form is what we focus on.

For charged particles such as electrons, magnetic fields break $\mathcal{T}$-symmetry. As shown in Figure 1.2a, free electrons are forced along circular trajectories by the Lorentz force, with a handedness ('chirality') dictated by the sign of the magnetic field. In particular, this means that an electron cannot follow the same orbit in the opposite direction, if the magnetic field remains unchanged. This last condition implies that the time-reversal operation we consider acts only on the electron, and not on the source of the magnetic field. The external magnetic field thus 'biases' the system.

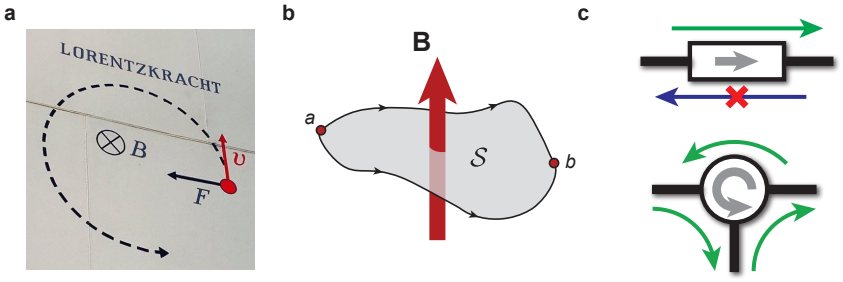

Figure 1.2: **Breaking time-reversal symmetry. (a)** The Lorentz force deflects an electron along a circular trajectory, with handedness dictated by the sign of the magnetic field $\mathbf{B}$ (muurformules.nl). **(b)** Electron wavepackets travelling through a magnetic vector potential $\mathbf{A}$ pick up a nonreciprocal phase. The phase difference $\Delta\varphi$ between two paths is gauge-invariant and proportional to the magnetic flux piercing the enclosed surface $\mathcal{S}$. This leads to a measurable interference phenomenon known as the Aharonov-Bohm effect. **(c)** Nonreciprocal elements. An isolator (top) allows transmission of a signal in one direction while blocking it in the other. A circulator (bottom) routes signals in a chiral fashion.

On the level of electron wavepackets, the hallmark of this interaction is a phase φ picked up by the electron as it travels through a magnetic vector potential $\mathbf{A}$, as shown in Figure 1.2b. Importantly, as the sign of the phase pick-up depends on the direction of propagation, φ is a nonreciprocal phase. While there is gauge freedom in the definition of $\mathbf{A}$, and thus in φ, the phase difference $\Delta\varphi$ between two paths is gauge-invariant and proportional to the enclosed magnetic flux. This phase difference is known as the Aharonov-Bohm phase and leads to measurable interference phenomena in the famous Aharonov-Bohm effect [39].

The Aharonov-Bohm phase is an example of a geometric phase [40], in this case defined in real space. In general, a geometric phase arises when the parameters of a system are slowly cycled along a closed path, and expresses the phase difference that remains between initial and final states of the system after the cycle is completed. This phase difference, known also as the Berry phase, depends only on the geometry of the cycle in the system's abstract parameter space, and manifests in many phenomena across physics, including Foucault's pendulum [41] and the polarization of light [42].

On a tight-binding lattice, the hopping of an electron from site a to b is described by the Hamiltonian

$$\hat{H}_{\text{hop}} = J\left(e^{-\mathrm{i}\varphi_{ab}}\hat{a}^\dagger\hat{b} + e^{\mathrm{i}\varphi_{ab}}\hat{a}\hat{b}^\dagger\right), \tag{1.1}$$

where J is the coupling rate and $\hat{a}$, $\hat{b}$ are the site annihilation operators. In this Hamiltonian, the magnetic vector potential $\mathbf{A}$ is embodied by the nonreciprocal hopping phase

$$\varphi_{ab} = \frac{q}{\hbar}\int_a^b \mathbf{A}\cdot\mathrm{d}\boldsymbol{\ell}, \tag{1.2}$$

known as the Peierls phase, where q is the charge of the electron. When the electron hops in the opposite direction, the limits of the integral are swapped, and the negative Peierls phase $\varphi_{ba} = -\varphi_{ab}$ is acquired. An electron going around a loop enclosing surface $\mathcal{S}$ then acquires the gauge-invariant phase

$$\Phi = \frac{q}{\hbar} \iint_{\mathcal{S}} \mathbf{B} \cdot \mathrm{d}\mathbf{S}. \tag{1.3}$$

We will often refer to this loop phase as the (magnetic) flux.

Neutral excitations, such as optical photons and mechanical phonons, do not interact directly with a magnetic field, as their charge q in (1.2) is zero. Magnetically-active materials then provide a way to break $\mathcal{T}$, enabling for example the construction of bulk optical nonreciprocal elements such as isolators and circulators (Figure 1.2c) based on the Faraday effect. Another, perhaps more explicit way of breaking $\mathcal{T}$ is offered by dynamic modulation of a system's Hamiltonian by an external drive [43, 44]. Harmonic modulation can stimulate the frequency conversion of a signal, imprinting the phase of the modulation on the transfer from one frequency to another analogous to a magnetic vector potential for a traveling electron [45]. Thus, by incorporating multiple up- and down-converting steps with individual control over the respective phases, it is possible to exploit Aharonov-Bohm interference in frequency space to realize nonreciprocal transmission, as proposed and demonstrated in the photonic domain [46–52]. Similar mechanisms allow nonreciprocal phenomena also at microwave frequencies in superconducting systems [31, 53–55] and cold atoms in optical lattices [56–59].

In mechanics and acoustics, various schemes have been explored to create nonreciprocal responses through breaking time-reversal symmetry [11]. Sound isolation was demonstrated through biasing by rotating air flows [60]. In gyroscopic metamaterials, the spinning of coupled mechanical elements formed artificial magnetic fields to induce unidirectional edge states [9]. Moreover, similar to photonic methods, dynamic modulation allows inducing nonreciprocal transmission in systems of coupled resonators [61] and modulated elastic waves [62]. Notably, recent demonstrations in the nanomechanical domain have employed modulated radiation pressure forces [63, 64]. We will discuss this last interaction further in section 1.6.

1.4. Quantum Hall effect and topological insulators

In extended systems, broken $\mathcal{T}$-symmetry leads to intriguing physics. A quintessential example is the integer quantum Hall effect (QHE), discovered in 1980 [65] and celebrated as a milestone in physics [66]. As shown in Figure 1.3a, it occurs in two-dimensional electron gases subject to a perpendicular magnetic field. In the bulk of the material, the magnetic field localizes the electronic states into cyclotron orbits that do not allow conduction. However, along the boundary of the material, electrons can 'skip', giving rise to conduction channels along the edge. Strikingly, these channels are unidirectional ('chiral'), owing to the $\mathcal{T}$-breaking magnetic field. Indeed, Robert Laughlin explained shortly after the first observation that the emergence of chiral edge states can be understood from interferences between

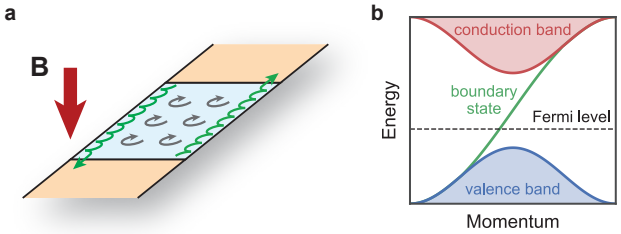

Figure 1.3: **Quantum Hall effect and topology. (a)** The quantum Hall effect arises in a two-dimensional electron gas (blue) subject to a perpendicular magnetic field $\mathbf{B}$. In the bulk, electrons are confined into cyclotron orbits (grey) and do not contribute to conduction. Along the boundaries, unidirectional skipping orbits (green) are formed that allow electron transport between the two conductors (orange) connected to the electron gas. The number of chiral conduction channels is strictly quantized. **(b)** Schematic representation of the band structure of a semi-infinite topological insulator with broken $\mathcal{T}$-symmetry. There are no bulk states available at the Fermi level, while there is a single unidirectional state available at the boundary.

electron wavepackets that pick up a nonreciprocal phase while travelling through the magnetic vector potential [67] — thus linking the quantum Hall effect to the Aharonov-Bohm phase introduced above.

As the quantum Hall conduction is sustained by a discrete number of channels, it is strictly quantized, giving the QHE a central role in the international system of units SI [68]. It is now understood that the QHE derives this robust quantized conductance from the *topology* of its band structure [36].

Topology is the branch of mathematics that studies the properties of geometric objects that are preserved under continuous deformations [69]. These properties are then characterized by numbers called *topological invariants*. The objects under consideration may exist in real space, such as balls, donuts, and pretzels characterized by a different number of holes, or they may exist in an abstract space. The latter applies to quantum Hall systems: Their energy bands in momentum space are characterized by an integer topological invariant called the Chern number [36]. Importantly, because the Chern number is a *global* property of the band structure, it is robust to *local* perturbations and disorder in the underlying lattice, as long as the bandgap separating the band from its neighbours remains open.

When two materials characterized by bands with different Chern number are brought into contact, for example the quantum Hall electron gas and its surroundings, topology dictates that the gap must be closed at the boundary (Figure 1.3b). This is known as the bulk-edge or bulk-boundary correspondence, and the localized edge states it procures in the QHE are precisely the chiral conduction channels. Their existence and direction are thus *topologically protected*. This means that defects along the edge can not cause any back-scattering.

The QHE is a basic example of a *topological phase* of matter. In turn, it spurred the exploration of various other topological phases with unique properties. Notably, the requirement of breaking $\mathcal{T}$-symmetry was lifted with the discovery of the quantum spin-Hall effect (QSHE), and led to the discovery of a new class of materials called topological insulators [70–72]. The QSHE relies on the electron spin: While

the bulk of a quantum spin-Hall material is insulating, spin-orbit coupling mandates that electrons with positive spin propagate along the edge in one direction, whereas electrons with negative spin travel in the opposite direction. This chiral transport is topologically protected from back-scattering, as long as defects do not induce spin-flips.

Both the QHE and QHSE have been emulated in other domains, including bosonic systems [73–76]. Through biasing with an actual magnetic field, robust unidirectional edge transport has been demonstrated for microwave radiation using gyrotropic materials [77, 78] and for exciton-polaritons that exhibit Zeeman splitting [79]. In the photonic domain [38], analogues of the QSHE — featuring preserved $\mathcal{T}$-symmetry — have been observed in photonic crystals, where the spin degree of freedom is associated with the polarization [80, 81] or the band valley [82, 83] of light. A particularly practical way to observe a QHE for light is by mapping the temporal dimension to a spatial dimension, studying the spatial evolution of light along arrays of waveguides whose properties are varying along the propagation dimension to emulate broken time-reversal symmetry [84].

In this context, another concept that has proven useful is to exploit 'synthetic dimensions', formed by coupling the internal degrees of freedom of resonators at different frequencies. For example, multiple optical modes of a ring resonator [85] or the internal states of a cold atom [58] may be coupled via frequency-converting temporal modulations. This allows to create effective topological systems with higher dimensionality than the physical system [86, 87].

In the mechanical domain, topological phases [37] have been implemented in gyroscopic metamaterials, where the spinning of coupled mechanical elements formed an artificial magnetic field to induce unidirectional edge states [9]. In addition, frequency-converting harmonic modulation has been used to show a topological insulator comprising piezoelectrically modulated disks [88]. Finally, mechanical topological insulators without broken $\mathcal{T}$-symmetry have been implemented using macroscopic pendula coupled by springs [89], and in nanomechanical periodic thin-film structures [90–92].

1.5. Non-Hermitian dynamics

In a closed system, energy is necessarily conserved. This cornerstone of physics derives from time-translation symmetry, and requires that closed systems are governed by Hermitian Hamiltonians ($H = H^\dagger$). Hermiticity guarantees a real energy spectrum, and in the quantum domain, a unitary time evolution that preserves probability. However, allowing a system to interact with an environment — turning it into an open system — relaxes this requirement. The interaction with the environment usually removes energy through dissipation. Alternatively, it may also add energy through driving or pumping. In many cases, such systems can be described by a *non-Hermitian* effective Hamiltonian [93], which in general hosts complex eigenfrequencies and can generate unbounded dynamics.

However, in 1998, Bender and Boettcher identified a class of open-system Hamiltonians that still exhibit a real energy spectrum [95]. While non-Hermitian, these Hamiltonians are invariant upon applying both a parity operation $\mathcal{P}$ that reflects

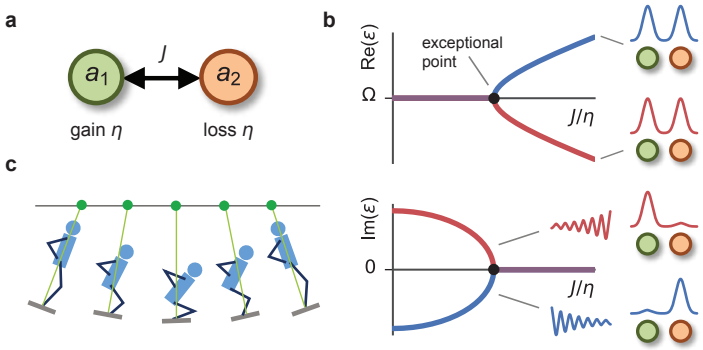

Figure 1.4: **Non-Hermitian dynamics. (a)** The parity-time ($\mathcal{PT}$) dimer comprises two resonators coupled by rate J. One site experiences gain η, while the other site decays with the opposite rate $-\eta$. **(b)** Real (top) and imaginary (bottom) parts of the complex eigenfrequencies $\epsilon_\pm$ of the $\mathcal{PT}$-dimer. For $J > \eta$, the eigenstates respect the $\mathcal{PT}$-symmetry of the dimer and delocalize evenly over both resonators. For $\eta < J$, the eigenstates spontaneously break $\mathcal{PT}$-symmetry and localize in the site with either gain or loss. This transition is marked by an exceptional point at $J = \eta$, where both the complex eigenvalues and the eigenvectors coalesce. **(c)** Parametric amplification in an everyday setting. By moving their center of mass, a person on a swing can modulate the swing's resonance frequency and amplify their motion. *Image reproduced from [94] under a CC-BY 4.0 license (*`http://creativecommons.org/licenses/by/4.0/`*).*

the system in space, and the operation $\mathcal{T}$ that reverses time. Recently, such $\mathcal{PT}$-symmetric systems have been widely studied in optics [96]. A prototypical example of a $\mathcal{PT}$-symmetric system is given by the Hamiltonian

$$H = \begin{pmatrix} \Omega + \mathrm{i}\eta & J \\ J & \Omega - \mathrm{i}\eta \end{pmatrix}, \tag{1.4}$$

where we have set $\hbar = 1$. This Hamiltonian matrix governs the evolution of the $\mathcal{PT}$-dimer [97, 98] shown in Figure 1.4a, formed by the two resonators a_1 and a_2, via the equation of motion $\dot{\mathbf{a}} = -\mathrm{i}H\mathbf{a}$ of the vector $\mathbf{a} = (a_1, a_2)^T$ of complex mode amplitudes.

The resonators oscillate with equal frequency Ω and are coupled with rate J. Through the interaction with the (otherwise unspecified) environment, resonator a_1 experiences gain with rate $+\eta$, while the other resonator decays with the opposite rate $-\eta$. In this system, the parity operation $\mathcal{P}$ exchanges the two sites $a_1 \leftrightarrow a_2$, while the time-reversal operation $\mathcal{T}$ is equivalent to complex conjugation $\mathrm{i} \mapsto -\mathrm{i}$, turning gain into loss and vice versa.

The eigenvalues of the matrix (1.4) are given by

$$\epsilon_\pm = \Omega \pm \sqrt{J^2 - \eta^2}. \tag{1.5}$$

For $\eta = 0$, the Hamiltonian $H = H^\dagger$ is Hermitian and energy is conserved during the evolution. We then find two hybridized eigenmodes with split frequencies $\epsilon_\pm = \Omega \pm J$, formed by the (anti)symmetric superpositions of a_1 and a_2. As shown in Figure 1.4b, for $\eta < J$, the spectrum of H remains real, until the eigenvalues

$\epsilon_+ = \epsilon_- = \Omega$ coalesce at $J = \eta$. Beyond this point, for $\eta > J$, the equality of the eigenmode oscillation frequencies persist ($\mathrm{Re}(\epsilon_\pm) = \Omega$), while their imaginary parts now split.

By analysing the corresponding eigenvectors $\mathbf{a}_\pm$, we find for $\eta < J$ that the eigenmodes are delocalized over both resonators and respect the $\mathcal{PT}$-symmetry of the dimer. However, for $J > \eta$, the eigenmodes spontaneously break $\mathcal{PT}$-symmetry, and localize in the site with either gain or loss. This transition is marked by an *exceptional point* at $J = \eta$, where both the eigenvalues $\epsilon_\pm$ *and* the eigenvectors $\mathbf{a}_\pm$ coalesce. This is a truly non-Hermitian phenomenon: The orthogonality of eigenmodes is guaranteed in Hermitian systems and prevents those from coalescing.

The stable dynamics of the $\mathcal{PT}$-dimer in the $\mathcal{PT}$-symmetric phase ($\eta < J$) derive from the balance between gain η and loss $-\eta$. This is, however, not a strict requirement: For gain and loss $\bar{\eta} \pm \Delta\eta$ centered around an average value of $\bar{\eta}$, 'virtual' $\mathcal{PT}$-symmetry is recovered in the dynamically offset basis $\mathbf{a}'(t) = e^{-\bar{\eta}t}\mathbf{a}(t)$, with an exceptional point at $J = \Delta\eta$ [99]. This even applies to systems that are lossy overall, where the 'gain' $\bar{\eta} + \Delta\eta < 0$ is negative. We refer to this situation as 'passive' $\mathcal{PT}$-symmetry [98].

In principle, the derivative $2|\partial\,\mathrm{Re}(\epsilon_\pm)/\partial J|$ of the frequency splitting diverges at the exceptional point. While this has been proposed as a way to improve sensing of perturbations in J (or η) [100], the benefits of this approach are still under debate [101]. Notwithstanding, devices relying on this sensing mechanism have been constructed [102–105].

There exist also strong ties between topology and non-Hermitian physics. In a sense, objects with interesting geometry are more abundant in non-Hermitian systems, as many of their properties are now described by complex numbers, defined in spaces with higher dimensionality than their Hermitian counterparts [106, 107]. A basic example emerges even by supplementing the $\mathcal{PT}$-dimer with a variable detuning δ between the resonators, and considering the Riemann sheet defined by its complex eigenvalues in the two-dimensional δ – η parameter space. Using the topology of this manifold, topological transfer of energy between two modes has been demonstrated [108]. In a three-mode system, braiding of eigenvalues has been observed [109].

Lattice models with non-Hermitian dynamics and topological features have also been proposed, including the Hatano-Nelson chain [110], featuring asymmetric hopping amplitudes in different directions, and the Lee ladder [111]. Remarkably, the usual bulk-boundary correspondence (BBC) that characterizes Hermitian topological phases does not apply in these models [112]. In Hermitian systems, the BBC relies on the notion that introducing boundaries does not impact states in the bulk significantly, that is to say, going from periodic to open boundary conditions does not induce a phase transition [106]. However, the bulk of a non-Hermitian system can be drastically sensitive to boundaries, with bulk states 'piling up' at an open boundary. This has recently been dubbed the 'non-Hermitian skin effect' [112] and profoundly impacts the behaviour of non-Hermitian lattices.

For bosonic systems, a natural way to induce non-Hermitian dynamics is through parametric amplification. This phenomenon is in fact very common, and

explains how a person on a playground swing can sustain and even amplify their motion. As shown in Figure 1.4c, varying the center of mass modulates an important parameter of the system: the swing's resonance frequency. Hence, this process is called parametric modulation or driving, and when it occurs at twice the natural frequency of the swing, motion is amplified. Notably, the amplification occurs only for a particular phase, or *quadrature*, of motion: The orthogonal quadrature is deamplified. Important for applications, this process underlies e.g. phase-sensitive amplifiers of microwave or optical signals [113]. Applied to thermal or quantum states, both characterized by a spread in phase space rather than a definite state, parametric amplification changes their distribution asymmetrically. Hence, this process is also known as *squeezing* [114]. In quantum-limited optics, squeezing is used to increase the sensitivity of e.g. gravitational wave detectors [115].

1.6. Cavity optomechanics

In this thesis, we will orchestrate nanomechanical interactions using light, as further detailed in chapter 2. The interaction between an optical cavity and a mechanical resonator coupled to it is the subject of the field of *cavity optomechanics*. Cavity optomechanical systems come in many shapes and sizes, from kilometer-scale gravitational wave detectors [116] to clouds of atoms trapped in a Fabry-Pérot cavity [117]. We refer to the review by Aspelmeyer, Kippenberg & Marquardt [118] for an overview.

A cavity serves to confine light in space and store it in time, thereby enhancing the effects of the light-motion interaction. Using lasers as an exceptionally clean light source, the cavity optomechanical interaction allows extremely precise sensing of motion, up to quantum-level precision. Conversely, the radiation pressure force of the cavity field actuates the resonator. Notably, the coupling between the optical field and the resonator motion can be quantum-coherent [26, 119, 120], enabling entanglement between radiation fields and motion [121] and even mediating remote entanglement between micromechanical resonators [27].

As displacement modifies the cavity field, which in turn modulates the radiation-pressure force acting back on the resonator, a feedback mechanism emerges known as optomechanical backaction. The displacement-dependent radiation pressure force acts as an *optical spring*. Importantly, the optical spring can be modulated dynamically by the laser driving the cavity, enabling frequency conversion between multiple resonators coupled to the same cavity [122]. As we will explain in chapter 2, this will be an enabling mechanism throughout this thesis.

Multimode cavity optomechanical systems are thus an interesting platform for breaking time-reversal symmetry, providing effective time-varying potentials for either light or sound [123]. In suitable multi-mode optomechanical cavities, this can lead to nonreciprocal effects such as a proposed phononic circulator [122]. Optical nonreciprocity was predicted in light-driven optomechanical ring resonators [124], which can in fact also be completely understood in terms of a synthetic magnetic field [32]. Nonreciprocal transmission of photons was observed in optomechanical systems both in the optical and microwave domains [32, 33, 125–128]. Suitable combinations of nonreciprocal coupling and dissipation allow in principle ideal

isolation [129, 130], and optomechanical systems were also configured as magnet-free three- or four-port circulators [131–133].

Conversely, optomechanical interactions can induce nonreciprocal coupling between mechanical modes [63, 64]. When extending these mechanisms to many-mode lattices, topological phases for sound and light have been envisioned, including Chern-type topological insulators with broken time-reversal symmetry [64, 134, 135]. In addition, this platform presents various interesting possibilities, including nonlinear behaviour and dynamical gauge fields linked to optomechanical limit-cycle oscillators [136].

If the photon lifetime in the cavity approaches the mechanical period, the optomechanical backaction attains a dynamical character and allows to cool or amplify mechanical motion. This principle, known as optomechanical sideband cooling, allows to cool mechanical motion near the quantum ground state [26, 119, 120]. Alternatively, the required phase offset between position and force to damp or amplify motion can be obtained using measurement-based feedback [137].

1.7. Outline of this thesis

In this thesis, we realize, and explore the dynamics of, networks of nanomechanical resonators connected via time-modulated radiation pressure. Multiple flexural mechanical resonances of a silicon nanostructure couple simultaneously to a photonic crystal nanocavity, allowing sensitive optical readout of mechanical motion with a resolution well below the thermal fluctuation level. In addition, by suitable modulation of a detuned drive laser, light-mediated effective mechanical couplings are established.

This experimental platform is introduced in chapter 2. Departing from a general discussion of the multimode cavity optomechanical interaction, we show that dynamic modulation of the optical spring can establish both nanomechanical hopping and squeezing interactions, by stimulating the appropriate frequency conversions. We implement a phase-coherent driving and detection scheme that enables the controlled breaking of time-reversal symmetry, and allows the construction of arbitrary multi-mode quadratic phononic Hamiltonians in time and (synthetic) space. To analyse the resulting, possibly non-Hermitian dynamics, the Bogoliubov-de Gennes formalism is introduced. We demonstrate control over the mechanical linewidths both through feedback and dynamical opto-thermal backaction.

In chapter 3, we focus on particle-conserving hopping interactions and construct phononic networks that are subject to synthetic magnetic fields. For a three-mode network with a single plaquette, we observe chiral circulation of coherent vibrations. For networks featuring multiple plaquettes, we study the interplay of aligned and opposed synthetic fluxes. Finally, in a five-mode lattice pierced by a homogeneous synthetic flux, we demonstrate the emergence of chiral transport of phonons along the edge.

Chapter 4 explores the interaction between synthetic flux for phonons and thermal fluctuations. The chirality imposed before on coherent excitations is shown to carry over to thermally excited vibrations. Combined with the different Bose occupations of the thermal baths feeding the mechanical resonators, flux-dependent

circulation of energy leads to a redistribution of thermal energy in the loop. We develop a procedure to directly measure the flow of heat along the networks' links, revealing flux-dependent reversal of thermal currents.

We exploit the opportunity to induce non-Hermitian dynamics through squeezing in chapter 5 to reveal a non-Hermitian version of the Aharonov-Bohm effect. First, we focus on the 'squeezing dimer' that combines hopping and single-mode squeezing interactions. We show that this dimer features a geometric phase, revealed diagrammatically after applying the Bogoliubov-de Gennes formalism to separate 'hole'-like and 'particle'-like degrees of freedom. This geometrical phase, acting as a flux through the non-Hermitian particle-hole loop, now tunes both frequency and linewidth of the dimer's normal modes. In addition, the flux tunes squeezing, stability, and the occurrence of exceptional points in the dimer's spectrum. Finally, we construct a three-mode loop closed by a single hopping and two two-mode squeezing interactions. This system features a flux-tunable third-order exceptional point and unidirectional phononic amplification.

Nonreciprocal transport is generally associated with the breaking of time-reversal symmetry. In chapter 6, we introduce an extended notion of unidirectional transmission for quadrature-resolved signals, dubbed 'quadrature nonreciprocity' (qNR), that does not rely on the breaking of $\mathcal{T}$-symmetry. Instead, it relies on the interference of hopping and two-mode squeezing interactions. We develop a theoretical framework to characterize and identify qNR for arbitrary systems, and test it in experiment for a two-mode dimer and a four-mode ring.

In chapter 7, we implement in experiment one of the seminal models put forward earlier in the area of quadrature-dependent transport: the bosonic Kitaev chain (BKC). We show that the transmission through the BKC is chiral, with the direction of propagation depending on the excited quadrature. In addition, the presence of squeezing interactions allows amplification or damping of signals that propagate along the chain. By closing the chain into a ring, a dramatic change in stability is observed as signals are then allowed to amplify indefinitely. The strong dependence of the BKC's dynamics on its boundary conditions is a uniquely non-Hermitian effect that links to the non-Hermitian skin effect. By tuning the phases of the hopping and squeezing interactions, we show a transition from global to local response in the chain.

Finally, we conclude in chapter 8 with a general discussion of the results presented in this thesis, and provide an outlook on further research in this field. To that end, we present experiments demonstrating that the cavity response can induce a highly-tunable effective Duffing nonlinearity in the mechanical resonators, which could be used to study nonlinear topological phenomena. The nonlinearity is shown to carry over to light-mediated effective mechanical interactions, while it can be cancelled on the single-resonator level by a two-laser driving scheme.

2

Effective mechanical interactions mediated by radiation pressure

We introduce the main theoretical and experimental methods used in the thesis. We explain how in cavity optomechanical systems different mechanical modes can be coupled through time-modulated laser drives. This allows the implementation of arbitrary quadratic bosonic Hamiltonians, which we suitably describe in a Bogoliubov-de-Gennes formalism to account for both beamsplitter and squeezing interactions. We introduce the experimental system, the optical set-up, and the experimental techniques for temporal control and measurement of coherent and incoherent mechanical excitations.

2.1. Introduction

In this chapter, we put forward optical driving as a technique to control the dynamics of a multimode nanomechanical system. Through the optomechanical interaction of multiple nanomechanical resonances with a common optical mode, we mediate tunable effective interactions between the resonators. By careful dynamic modulation of optomechanical backaction, we induce both beamsplitter and squeezing interactions and construct arbitrary quadratic multi-mode phononic Hamiltonians. Crucially, we are able to construct Hamiltonians that break *time-reversal symmetry* — a central theme in this research. In addition, measurement-based resonant feedback allows to tune the damping of the nanomechanical modes. These ingredients combined form a versatile toolbox to conduct the experiments demonstrated in the following chapters of this thesis.

We start the chapter with a general overview of radiation pressure and cavity optomechanics. Subsequently, we intuitively explore the effect of dynamically modulated optomechanical backaction, followed by an introduction of optomechanics in a quantum formalism. We then arrive at the heart of this chapter: We study the effect of modulated optical driving in the quantum optomechanical framework, and show how this leads to a reconfigurable quadratic effective mechanical Hamiltonian. We move on to review the Bogoliubov-de Gennes framework to model nanomechanical evolution in the presence of beamsplitter and squeezing interactions. We conclude the chapter by discussing the experimental platform: We review the experimental set-up and procedures, and consider the techniques used to analyse our measurement results.

2.2. Radiation pressure

To manipulate nanomechanical resonators, we exploit the optical force that arises when light interacts with matter. Recognized already by Kepler [138] in the 17th century when he observed that a comet's dust tail always points away from the sun, this mechanism was given a theoretical underpinning by Maxwell. Specifically, Maxwell realized that light carries momentum, and the transfer of this momentum 'kicks' an object when light is reflected or absorbed. This effect is known as *radiation pressure*.

On the macroscopic scale, radiation pressure forces are usually negligible compared to e.g. electrostatic forces, thermal expansion, or friction. To observe them, several strategies exist. The first is to work in vacuum, where friction and heating effects of the surrounding medium (air) are removed: this enabled the first experiments to observe radiation pressure around 1900 [139, 140]. Another approach is to use tightly focused light and transparent objects with a very small mass, which inspired the development of optical tweezers [141] in the 1970s. Finally, one may utilize an optical cavity to recycle light and increase the number of reflections, thereby boosting the interaction between light and matter. This is the idea behind the field of cavity optomechanics [118].

In the single nanoscale device used in every experiment presented in this thesis, shown in Figure 2.1, we exploit all three strategies. While the device will be properly

introduced in section 2.3.3, we note that it is housed in a vacuum chamber, has transparent[1] vibrating elements with a very low mass ($\sim$ pg) and features a photonic crystal cavity [2] that traps light. As such, carefully modulated optical driving offers a great degree of control over the mechanical degrees of freedom in the device.

2.3. Cavity optomechanics

Like many mechanisms in physics, the interaction between light and matter works both ways. Radiation pressure is one side of the coin, while the effect of motion on light allows the optical read-out of mechanical displacement, as used e.g. in gravitational wave detectors [116]. Together they constitute the optomechanical interaction.

More specifically, *cavity optomechanics* [118] is the field that studies this mutual interaction between a mechanical resonator and an optical cavity. Cavity optomechanical systems span a wide range of sizes: from kilometer-scale gravitational wave detectors [116] to clouds of atoms trapped in a Fabry-Pérot cavity [117]. Our interest lies in nanoscale systems, where low mass, tight confinement of both light and motion, and the engineerability of their co-localization transpire to induce large optomechanical interactions.

2.3.1. Toy model: moving-mirror cavity

In the following sections, we explore the theory of the cavity optomechanical interaction. The canonical toy model of the field is shown in Figure 2.1d: a Fabry-Pérot cavity formed by two mirrors, one of which is mounted on a spring. While simple, it illustrates the dynamics of a wide variety of systems and geometries. In this section we highlight some of its properties; further details may be found in the review by Aspelmeyer, Kippenberg & Marquardt [118], or in the textbook by Bowen & Milburn [142]. A useful discussion tailored towards the sliced nanobeam device used here can be found in the thesis of Leijssen [143].

The spring-mounted mirror forms a mechanical resonator that oscillates with mechanical frequency Ω. The mechanical displacement x modifies the length $L+x$ of the cavity and thereby modulates the optical resonance frequency $\omega_c(x)$. For the Fabry-Pérot cavity considered here, $\omega_c(x) = \pi jc/(L+x)$ is a simple function of x, where c is the speed of light. We restrict the discussion to a single optical mode with index j, driven by an external field with frequency $\omega_L \approx \omega_c$.

Systems with a different geometry generally have a less straightforward relation between cavity frequency and displacement. In nanoscale systems, two coupling mechanisms are important: the moving boundary effect (demonstrated in the moving-mirror cavity) and the photo-elastic effect. Regardless of the origin of the optomechanical interaction, for small x, it usually suffices to expand ω_c around the equilibrium value $\omega_0 = \omega_c(0)$,

$$\omega_c(x) = \omega_0 + \frac{\partial \omega_c}{\partial x} x + \frac{1}{2}\frac{\partial^2 \omega_c}{\partial x^2} x + \ldots, \tag{2.1}$$

[1] For infrared (telecom) light.

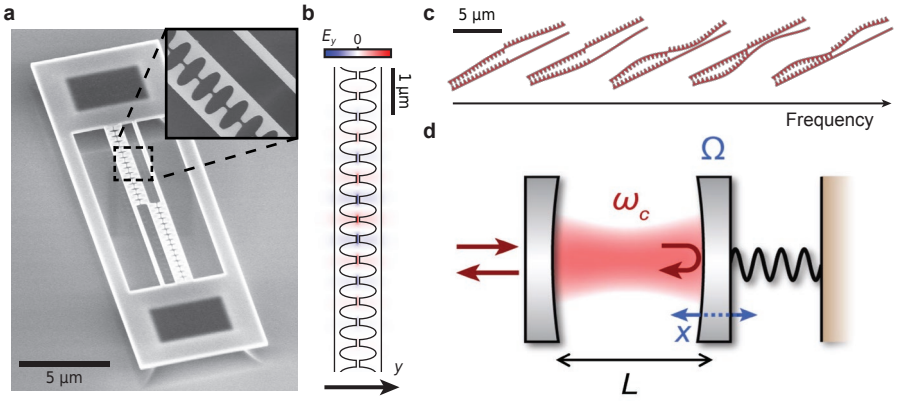

Figure 2.1: **Cavity optomechanics in a nano-optomechanical device. (a)** Scanning electron micrograph (tilt 45°; inset, top view) showing a device as used in our experiments. In the top silicon device layer (thickness 220 nm), supported by silicon oxide pedestals, three suspended beams are defined with teeth separated by a narrow slit ($\sim$ 50 nm). Between each outer beam and the central beam, a photonic crystal cavity is defined. In the experiments presented in this thesis, only one of the two optical cavities is used. **(b)** Simulated electric field y-component E_y of the optical cavity mode. The mode's energy is strongly confined to the narrow slit, inducing a large optomechanical interaction with flexural mechanical resonances of the two adjacent beams. The cavity's off-centre position ensures coupling to both even and odd resonances. Measured resonance frequency of the experimental cavity $\omega_0 = 195.62$ THz (vacuum wavelength $\lambda_0 = 1532.5$ nm), spectral linewidth $\kappa = 320$ GHz (wavelength linewidth $\Delta\lambda = 2.5$ nm). **(c)** Simulated displacement field of the five lowest frequency flexural modes. The displacement is greatly exaggerated for clarity; typical (thermal) displacement amplitudes are on the order of picometers. Measured mechanical frequencies range from 3.7 – 26 MHz. **(d)** Toy model to illustrate the optomechanical interaction. A Fabry-Pérot cavity with equilibrium length L is formed by two highly reflective mirrors. An external optical driving field is coupled into the cavity through the left mirror. The right mirror is mounted on a spring, forming a mechanical resonator. Its displacement x oscillates at the mechanical frequency Ω, changing the cavity length $L + x$ and modulating the optical resonance frequency ω_c.

and assume that only the term linear in displacement contributes significantly. We capture the strength of the (linear) optomechanical interaction in the coupling strength $G = -\partial\omega_c/\partial x$.

2.3.2. Mechanical resonator

Conversely, the light circulating in the cavity pushes on the mirror. Every round trip, taking time $\Delta t = 2(L + x)/c \approx 2L/c$, the light imparts a momentum $\Delta p = 2E_c/c$ on the mirror, with E_c the circulating optical energy. The radiation pressure force exerted is

$$F_{\text{opt}} = \Delta p/\Delta t = E_c/L \approx GE_c/\omega_c = \hbar G n_c, \tag{2.2}$$

where we note that $G = \pi jc/L^2 = \omega_0/L$ for the moving-mirror Fabry-Pérot cavity. In anticipation of a later quantum treatment, we have defined the cavity photon number $n_c = E_c/\hbar\omega_c$. The last expression is the general form of the radiation

pressure force and applies to all cavity optomechanical systems: one just needs to distinguish G.

We review some basic properties of the mechanical resonator. In addition to optical forces, the mechanical resonator is subject to damping with rate γ. Its equation of motion reads

$$\ddot{x} = -\Omega^2 x - \gamma v + F_{\text{opt}}/m + F_{\text{ext}}/m, \tag{2.3}$$

where $v = \dot{x}$ is the velocity, m the mass of the mirror, and F_{ext} any other force that acts on the resonator. In the frequency domain, accessed by applying the Fourier transform $y(\omega) = \int_{-\infty}^{\infty} y(t) e^{+\mathrm{i}\omega t}\,\mathrm{d}t$ to the position $x(t)$ and force $F_{\text{ext}}(t)$, the response of the resonator $x(\omega) = \chi_{\text{m}} F_{\text{ext}}(\omega)$ to an external force is quantified by the mechanical susceptibility

$$\chi_{\text{m}}(\omega) = \frac{1}{m\left(\Omega^2 - \omega^2\right) - \mathrm{i}m\gamma\omega}. \tag{2.4}$$

Instead of measuring $x(t)$ directly, we often measure quantities related to the energy $x(t)^2$. For convenience, we define the transfer function $|\chi_{\text{m}}(\omega)|^2$, given by

$$|\chi_{\text{m}}(\omega)|^2 = \frac{1}{m^2}\frac{1}{\gamma^2\omega^2 + (\Omega^2 - \omega^2)^2} \approx \frac{1}{4m^2\Omega^2}\frac{1}{(\omega - \Omega)^2 + \gamma^2/4}. \tag{2.5}$$

The last approximation is a Lorentzian function and valid for a weakly damped resonator ($\Omega \gg \gamma$) around its resonance frequency.

In the Fabry-Pérot cavity, the displacement coordinate x and the motional mass m are easily recognized. For mechanical resonators with a more complicated motional pattern, the definition of x is ambiguous and essentially arbitrary. However, any choice of coordinate x suffices, as long as the effective motional mass m_{eff} is defined accordingly to satisfy the relation

$$U_{\text{m}} = \frac{1}{2} m_{\text{eff}} \Omega^2 x^2 \tag{2.6}$$

for the mechanical potential energy U_{m}.

For resonators with a high quality factor $Q = \Omega/\gamma \gg 1$, the second-order differential equation (2.3) may be approximated (see the thesis of Mason [144] for details) by a first-order differential equation for the complex amplitude

$$a = \frac{1}{\tilde{x}}\left(x + \frac{\mathrm{i}v}{\Omega}\right), \tag{2.7}$$

such that

$$x = (a + a^*)\,\tilde{x}/2, \qquad v = -\mathrm{i}\,(a - a^*)\,\tilde{x}/2. \tag{2.8}$$

Here, $\tilde{x}$ is a fixed length scale that we will later use to normalize a.

The equation of motion for a reads

$$\dot{a} = -\mathrm{i}\,(\Omega - \mathrm{i}\gamma/2)\,a + f_{\text{opt}} + f_{\text{ext}}, \tag{2.9}$$

which describes a rotation in the complex plane with frequency $+\Omega$. In the so-called rotating wave approximation, we have neglected a contribution $\propto a^*$ that counter-rotates with frequency $-\Omega$, as it represents a highly off-resonant drive for the narrow-band resonator under consideration. The drive terms f_k are given by

$$f_k = \mathrm{i}\frac{F_k}{m\Omega\tilde{x}}. \tag{2.10}$$

In the frequency domain, the response of $a(\omega) = \chi_a(\omega) f_{\mathrm{ext}}(\omega)$ to an external force is quantified by the susceptibility

$$\chi_a(\omega) = \frac{1}{\mathrm{i}(\Omega-\omega)+\gamma/2} \approx (2m\Omega/\mathrm{i})\chi_{\mathrm{m}}(\omega), \tag{2.11}$$

where the last approximation holds in the high-Q regime $\Omega \gg \gamma$. The prefactor arises from (2.8) and (2.10).

Pre-empting a later quantum treatment, a natural choice for $\tilde{x}$ is related to the standard deviation of the mechanical ground state

$$x_{\mathrm{zpf}} = \sqrt{\frac{\hbar}{2m_{\mathrm{eff}}\Omega}}, \tag{2.12}$$

also known as the zero-point fluctuation amplitude. Choosing $\tilde{x} = 2x_{\mathrm{zpf}}$ ensures that $|a|^2$ represents the phonon number of the resonator.

Even though the length scale x_{zpf} has no intrinsic meaning in the classical domain, using it still presents an advantage. As the definition of the coordinate x suffers from ambiguity, so does the optomechanical coupling strength G. However, the *photon-phonon coupling rate* or *vacuum optomechanical coupling rate*

$$g_0 = G x_{\mathrm{zpf}} \tag{2.13}$$

does not depend on the definition of x as a consequence of the relation between x_{zpf} and m_{eff} in (2.12). The rate g_0 is therefore a more fundamental quantity than G.

2.3.3. Sliced nanobeam device

We now introduce the single nano-optomechanical device used in all experiments in this thesis. The device is nano-fabricated in the AMOLF NanoLab Amsterdam cleanroom and shown in Figure 2.1a. Designed with a sliced nanobeam geometry [145], it features a one-dimensional photonic crystal [2] with a single-site defect obtained by locally varying the hole pitch. The defect creates an optical cavity mode, longitudinally confined by the photonic crystal, with resonance frequency $\omega_0 = 195.62$ THz (vacuum wavelength $\lambda_0 = 1532.5$ nm, in the telecom range). Furthermore, the point defect ensures a considerable coupling to focused light normally incident from free space and endows the cavity with a relatively large optical linewidth $\kappa = 320$ GHz (wavelength linewidth $\Delta\lambda = 2.5$ nm). The narrow slit (width ~ 50 nm) between the beam halves introduces a dielectric discontinuity that serves to confine the field of the optical mode (Figure 2.1b) to the deeply subwavelength region between the beam's teeth.

The high concentration of optical energy near the dielectric boundary sensitizes the optical mode to in-plane flexural displacement of the beam halves. As the cavity is defined away from the beam center, this leads to strong optomechanical coupling to mechanical modes with both even and odd symmetries. Each beam half supports a ladder of flexural overtones, all with distinct resonance frequencies due to the mass difference between the beam halves. The first five flexural modes, with frequencies between 3.7 and 26 MHz, are shown in Figure 2.1c and have optomechanical coupling rates g_0 between 2 and 6 MHz. These mechanical modes constitute the 'resonators' that we use in our experiments.

We briefly review the procedure used to nano-fabricate the sliced nanobeam device. We start with a silicon-on-insulator substrate, with a 220 nm device layer and a $3\,\mu\mathrm{m}$ buried oxide layer (BOX). A 50 nm layer of diluted hydrogen silsesquioxane resist (1:2 in methyl isobutyl ketone) is spin-coated, and electron-beam lithography (Raith Voyager) is used to write patterns on the sample. After developing in tetramethylammonium hydroxide, an anisotropic etch of the exposed device layer is done using inductively coupled plasma–reactive ion etching with HBr and O_2 gases. Finally, the nanobeams are suspended in a wet etch of the underlying BOX layer with hydrofluoric acid followed by critical point drying. More details on the relevant fabrication techniques can be found in the thesis of Leijssen [143].

2.3.4. Optical spring shift

In this section, we explore a basic consequence of the optomechanical interaction that is central to our experiments: the optical spring shift. We start with the equation governing the evolution of the field c of a driven cavity,

$$\dot{c} = \mathrm{i}\left(\Delta + \mathrm{i}\kappa/2\right) c + \sqrt{\kappa_{\mathrm{in}}} c_{\mathrm{in}}. \tag{2.14}$$

The cavity is driven by an external laser with optical frequency ω_{L} coupling in through the port field c_{in} with rate κ_{in}. As we discuss in more detail in section 2.8, this port is in our case formed by the free-space radiation of the cavity mode, which we use to couple light both in and out of the cavity from normal incidence. Furthermore, $\Delta = \omega_{\mathrm{L}} - \omega_{\mathrm{c}}$ is the detuning between the driving field and the cavity, κ the total cavity energy decay rate, and $|c|^2 = n_{\mathrm{c}}$ is normalized to express the cavity photon number. We describe $c = \tilde{c}e^{-\mathrm{i}\omega_{\mathrm{L}}t}$ in a frame that rotates along with the drive laser field, where $\tilde{c}$ is the cavity field in the stationary lab frame.

Let us now consider a time-varying displacement $x(t)$ of the mechanical resonator. Through the optomechanical interaction, it shifts the detuning Δ and thus the response of the cavity to the external drive. In turn, this will alter the cavity photon number n_{c} and thereby the optical force acting back on the resonator. This feedback mechanism is known as *optomechanical backaction*.

Two different regimes are distinguished. In the *bad-cavity limit* or *Doppler regime*, the cavity decay rate κ is much larger than the mechanical frequency Ω. This means that the cavity relaxes to a steady-state faster than the motion modulates its frequency. In other words, on the optical timescale, the mechanical displacement appears to be "frozen".

The complementary regime, where $\Omega > \kappa$, is known as the *resolved-sideband regime*. Optical sidebands produced by mechanical oscillations are then resolved by the cavity. In this regime, the dynamics of the cavity need to be accounted for and result in *dynamical backaction* that does not follow the mechanical motion instantaneously.

For our nanodevice, the sideband resolution $\Omega/\kappa < 10^{-4}$ is much smaller than unity. Thus, for simplicity, we restrict the current discussion to the bad-cavity limit. For a frozen Δ, the steady state amplitude $c_{\rm ss}$ of the cavity is given by

$$c_{\rm ss} = \frac{\sqrt{\kappa_{\rm in}} c_{\rm in}}{\kappa/2 - {\rm i}\Delta} = \sqrt{\kappa_{\rm in}} c_{\rm in} \chi_{\rm c}(\Delta), \tag{2.15}$$

where we have defined the cavity susceptibility $\chi_{\rm c}(\Delta) = (\kappa/2 - {\rm i}\Delta)^{-1}$. The instantaneous photon number $n_{\rm c}$ follows a Lorentzian response,

$$n_{\rm c} = |c_{\rm ss}|^2 = \kappa_{\rm in} |c_{\rm in}\chi_{\rm c}(\Delta)|^2 = n_{\rm max} \frac{\kappa^2}{\kappa^2 + 4\Delta^2} = n_{\rm max} \cdot h(u), \tag{2.16}$$

as shown in Figure 2.2. Here, $n_{\rm max}$ is the maximum number of photons that a drive field with power $P = \hbar\omega_{\rm L}|c_{\rm in}|^2$ can excite in the cavity, attained on resonance ($\Delta = 0$) and given by

$$n_{\rm max} = 4|c_{\rm in}|^2 \kappa_{\rm in}/\kappa. \tag{2.17}$$

The ratio $\eta_{\rm in} \equiv \kappa_{\rm in}/\kappa$ is known as the incoupling efficiency. Finally, we define the dimensionless detuning $u \equiv 2\Delta/\kappa$ and the Lorentzian relative cavity population function

$$h(u) = \frac{1}{1+u^2}. \tag{2.18}$$

Next, we express the displacement using a dimensionless coordinate $z = x/x_{\rm zpf}$. Recalling that Δ depends on the displacement through $\Delta = \Delta_0 + Gx = \Delta_0 + g_0 z$ with equilibrium detuning $\Delta_0 = \omega_{\rm L} - \omega_{\rm c}$, the cavity photon number is a function of z and reads

$$n_{\rm c}(z) = n_{\rm max} h(u_0 + 2g_0 z/\kappa). \tag{2.19}$$

Here, $u_0 = 2\Delta_0/\kappa$. The variable cavity field generates a varying optical force, such that the evolution of the displacement z is governed by

$$\ddot{z} = -\Omega^2 z - \gamma\dot{z} + \hbar G n_{\rm c}(z)/(m x_{\rm zpf}) = -\Omega^2 z - \gamma\dot{z} + 2\Omega g_0 n_{\rm c}(z). \tag{2.20}$$

Plugging (2.19) into (2.20) gives a full description of the mechanical evolution in the bad-cavity limit.

For small displacements $Gx = g_0 z \ll \kappa$, we gain additional insight by expanding $n_{\rm c}(z)$ around $z = 0$,

$$n_{\rm c}(z) = n_{\rm max}\left[h(u_0) + \frac{\partial h(u_0)}{\partial u}\frac{\partial u}{\partial z} z + \frac{1}{2}\frac{\partial^2 h(u_0)}{\partial u^2}\left(\frac{\partial u}{\partial z}\right)^2 z^2 + \dots\right]. \tag{2.21}$$

The constant term $n_{\max}h(u_0) = \bar{n}_c$ yields an average cavity photon population $\bar{n}_c$ and generates a static optical force that displaces the resonator to a new equilibrium position $z_{eq} = 2g_0\bar{n}_c/\Omega$. It is generally omitted after shifting the displacement origin by z_{eq}. In addition, modulating $n_{\max}(t)$ in time by varying the drive laser intensity allows to drive the mechanical resonator.

The term linear in z,

$$n_c^{(\mathrm{lin})}(z) = n_{\max}h'(u_0)\frac{2g_0}{\kappa} \times z, \tag{2.22}$$

generates an optical force that is linear with displacement. This is known as the *optical spring effect* and its strength depends on the derivative of $h(u)$,

$$h'(u) = \frac{-2u}{(1+u^2)^2} = \frac{-2u}{1+u^2}h(u). \tag{2.23}$$

The optical spring constant $k_{\mathrm{opt}} = -\partial F_{\mathrm{opt}}(x)/\partial x$ supplements the intrinsic mechanical spring constant $k_{\mathrm{mech}} = m\Omega^2$ and changes the mechanical resonance frequency. We estimate the mechanical frequency shift $\delta\Omega$ from (2.20) by using the approximation $(\Omega+\delta\Omega)^2 \approx \Omega^2 + 2\Omega\delta\Omega$, valid for $\delta\Omega \ll \Omega$, and arrive at

$$\begin{aligned}\delta\Omega &= -2g_0^2 n_{\max}h'(u_0)/\kappa = \frac{g_0^2 n_{\max}}{\kappa}\frac{4u_0}{(1+u_0^2)^2} \\ &= g_0^2 n_{\max}\frac{8\Delta_0\kappa^2}{\left(4\Delta_0^2+\kappa^2\right)^2} = g_0^2\bar{n}_c\frac{2\Delta_0}{\Delta_0+\kappa^2/4},\end{aligned} \tag{2.24}$$

given in several different forms for later reference. In the last expression, we recognize the cavity-enhanced optomechanical coupling rate $g \equiv g_0\sqrt{\bar{n}_c}$.

The sign and magnitude of the spring shift depend on detuning, as illustrated in Figure 2.2. For $\Delta_0 > 0$, the optical contribution stiffens the total restoring force and shifts the mechanical frequency up. Conversely, for $\Delta_0 < 0$, the optical spring counters the intrinsic spring and the mechanical frequency shifts down. For a given drive laser power, the largest spring shift is attained when $|h'(u_0)|$ is maximal. Solving $h''(u_0) = 0$ results in the two detunings $u_\pm = \pm 1/\sqrt{3}$, or equivalently, $\Delta_\pm = \pm\kappa/(2\sqrt{3})$ at which the spring shift is maximally positive and negative, respectively.

Finally, for larger displacements $Gx = g_0 z \gtrsim \kappa$, the effect of higher-order terms in (2.21) becomes important. This will be discussed chapter 8. Until then, we neglect these higher-order contributions.

2.3.5. Optical detection of mechanical motion

We illuminate the cavity using the input channel described by c_{in} and incoupling rate κ_{in}. This builds up a field with amplitude c in the cavity that is subsequently absorbed and radiated out, until steady-state is reached. Detection of the light escaping the cavity thus allows us to estimate the amplitude of the cavity field. Moreover, it allows the optical detection of the resonator position, as we will see in the current section.

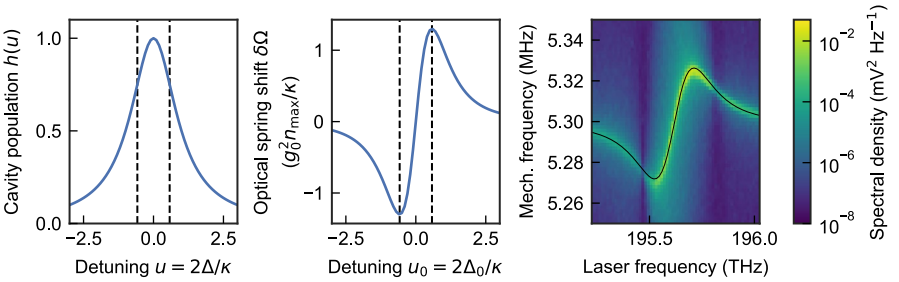

Figure 2.2: **Optical spring shift.** A drive laser with relative detuning $u = 2\Delta/\kappa$ and fixed intensity excites a photon population $n_{\max}h(u_0)$ in the cavity. The relative cavity population $h(u_0)$ (left) is a Lorentzian function of detuning. A mechanical displacement x changes the detuning $u = u_0 + Gx$ and alters the cavity photon population instantaneously in the bad-cavity regime. In turn, this modulates the optical force acting back on the resonator. The optomechanical backaction results in a shift $\delta\Omega$ of the mechanical resonance frequency (center). The magnitude of the optical spring shift $\delta\Omega$ is largest when $|h'(u_0)|$ is maximal, which occurs for $u_\pm = \pm 1/\sqrt{3}$ (dashed lines). The spring shift is observed experimentally in the thermomechanical spectrum (right) of a resonator as the frequency of the laser driving the cavity is swept. A fit of the optical spring shift model is overlaid (thin black line). The detected intensity of the mechanical resonance varies as the linear transduction coefficient $\partial R/\partial x$ dictated by (2.26) changes with laser detuning.

We describe the detected radiation mode as an output channel c_{out} with out-coupling rate κ_{out}. In general, the output mode and input mode may have arbitrary overlap, such that κ_{in} and κ_{out}, while both bounded by the total decay rate κ, are unrelated. In addition to light scattered resonantly by the cavity, light can also be coupled directly from the input to the output channel. For the Fabry-Pérot cavity, this happens through reflection off the highly-reflective front mirror (reflection coefficient ~ 1) and leads to the input-output relation $c_{\text{out}} = c_{\text{in}} - \sqrt{\kappa_{\text{out}}}c$ where energy conservation enforces the phase relation indicated by the minus sign.

In general, the direct reflection coefficient may differ from unity. We represent the amplitude and phase of non-resonant scattering in our nanobeam system by a complex reflection coefficient $re^{i\psi}$ [143]. This leads to the input-output relation

$$c_{\text{out}} = re^{i\psi}c_{\text{in}} - \sqrt{\kappa_{\text{out}}}c = re^{i\psi}c_{\text{in}} - \frac{\sqrt{\kappa_{\text{out}}\kappa_{\text{in}}}c_{\text{in}}}{\kappa/2 - i\Delta} \tag{2.25}$$

after plugging in the steady-state cavity field (2.15). Now, we recall that the cavity detuning $\Delta = \Delta_0 + Gx$ is a function of displacement x. Equation (2.25) thus allows optical detection of the resonator position from the output field.

Depending on the equilibrium detuning Δ_0 and the reflection coefficient $re^{i\psi}$, the displacement x may be encoded the amplitude and/or phase of the output light. The amplitude quadrature can be measured directly with a photodiode, while phase-sensitive detection of the output light requires interferometric techniques. In this thesis, we only measure the intensity $|c_{\text{out}}|^2$ of the output light, related to the

input intensity $|c_{\text{in}}|^2$ by the reflection

$$R(x) = |c_{\text{out}}|^2/|c_{\text{in}}|^2 = \left| re^{\mathrm{i}\psi} - \frac{\sqrt{\kappa_{\text{out}}\kappa_{\text{in}}}}{\kappa/2 - \mathrm{i}\Delta_0 + \mathrm{i}Gx} \right|^2 . \tag{2.26}$$

We do not attempt to determine the coefficients $re^{\mathrm{i}\psi}$, κ_{in}, κ_{out}, and G directly. Instead, we assume small displacements x and characterize the linear transduction $\partial R/\partial x$ experimentally, as detailed in the next section. Finally, we note that measuring the values of the higher-order nonlinear transduction coefficients $\partial^n R/\partial x^n$ allows to determine the optomechanical coupling g_0 [146].

2.3.6. Thermal fluctuations and spectral density

In many experiments, we do not drive the mechanical resonators directly. Instead, we rely on the interaction with their thermal environment to set the resonators into Brownian motion; the detection is sensitive enough to resolve those thermal vibrations. This interaction is extensively discussed in chapter 4. In the current section, we discuss some essential results.

The thermal environment of a resonator is modelled by a fluctuating thermal force $F_{\text{th}}(t)$ with zero average $\langle F_{\text{th}}(t)\rangle = 0$. In response to $F_{\text{th}}(t)$, the displacement $x(t)$ will be a stochastic quantity, whose frequency content can be quantified using the *spectral density*. Let us assume we have measured $x(t)$ during a measurement interval t_{M} and calculate the gated Fourier transform of $x(t)$,

$$X_{t_{\text{M}}}(\omega) = \frac{1}{\sqrt{t_{\text{M}}}} \int_{-t_{\text{M}}/2}^{+t_{\text{M}}/2} x(t) e^{-\mathrm{i}\omega t}\, \mathrm{d}t. \tag{2.27}$$

After collecting many time traces of $x(t)$, the power spectral density is defined as the ensemble average

$$S_{xx}(\omega) = \lim_{t_{\text{M}}\to\infty} \langle |X_{t_{\text{M}}}(\omega)|^2 \rangle, \tag{2.28}$$

and is approximated well from traces of finite duration if the timescale of correlations in $x(t)$ is much shorter than the measurement time t_{M}. We note that the prefactor $1/\sqrt{t_{\text{M}}}$ in (2.27) ensures that $S_{xx}(\omega)$ is independent of the measurement time. For our high-Q mechanical resonators, the spectral density $S_{xx}(\omega)$ will contain frequency contributions in a narrow band of width γ around their resonance frequency Ω. Finally, we note that if two processes x, y are linearly related in the frequency domain through $y(\omega) = h(\omega)x(\omega)$, then their spectral densities are related by $S_{yy}(\omega) = |h(\omega)|^2 S_{xx}(\omega)$. We call $|h(\omega)|^2$ the transfer function.

Another useful concept is the autocorrelation function[2]

$$R_{xx}(\tau) = \langle x(t+\tau)x^*(t)\rangle_t \,, \tag{2.29}$$

defined here for a general, possibly complex process $x(t)$. Here, $\langle\cdot\rangle_t$ represents an average over time t and τ is called the time lag. For our resonators, the typical

[2] Other common definitions use a different sign convention for τ or swap the conjugation.

timescale of correlations is related to their dissipation rate and given by $2/\gamma$. We thus need to make sure that $t_{\mathrm{M}} \gg 2/\gamma$. We usually assume that x is a stationary process, i.e. the statistics of x, including $R_{xx}(\tau)$, do not change over time. In that case, according to the Wiener-Khinchin theorem, the spectral density $S_{xx}(\omega)$ is given by the Fourier transform of the autocorrelation [147],

$$S_{xx}(\omega) = \int_{-\infty}^{\infty} R_{xx}(\tau) e^{+\mathrm{i}\omega\tau}\, \mathrm{d}\tau. \tag{2.30}$$

By inverting the Fourier transform, we derive the useful property that the variance of $x(t)$ is given by the integral of $S_{xx}(\omega)$,

$$\frac{1}{2\pi}\int_{-\infty}^{\infty} S_{xx}(\omega)\, \mathrm{d}\omega = R_{xx}(0) = \langle |x(t)|^2 \rangle. \tag{2.31}$$

Now we are in a position to analyse the stochastic thermal force $F_{\mathrm{th}}(t)$. The fluctuation-dissipation theorem [142] relates the strength of the thermal force to the dissipation rate γ — both arising from interactions with the thermal environment. It states that the thermal force satisfies the correlation function

$$\langle F(t)F(t-t')\rangle = 2\gamma m k_{\mathrm{B}} T \delta(t-t'). \tag{2.32}$$

As this correlator only depends on the time difference $\tau = t - t'$, it represents a stochastic process that is stationary in time. Moreover, the correlation is zero when $t \neq t'$, which means that the thermal environment retains no 'memory' of previous interactions. The spectral density $S_{FF}(\omega)$ of the thermal force is frequency-independent and given by

$$S_{FF}(\omega) = 2\gamma m k_{\mathrm{B}} T. \tag{2.33}$$

This flat frequency spectrum is known as a *white noise spectrum*.

From the mechanical susceptibility $\chi_{\mathrm{m}}(\omega)$ given in (2.4), we expect a high-Q resonator only to pick up thermal fluctuations in a narrow bandwidth around the resonance frequency. This is confirmed by calculating the spectral density, or more specifically the *thermomechanical spectrum*

$$S_{xx}(\omega) = |\chi_{\mathrm{m}}(\omega)|^2 S_{FF}(\omega) \approx \frac{\gamma k_{\mathrm{B}} T}{2m\Omega^2} \frac{1}{(\omega-\Omega)^2 + \gamma^2/4}, \tag{2.34}$$

which indeed describes a peaked, Lorentzian function centered at the resonance frequency Ω. Its full width at half-maximum is given by the dissipation rate γ, hence also known as the spectral linewidth. Note that the mechanical transfer function $|\chi_{\mathrm{m}}(\omega)|^2$ is even: it also contains a peaked contribution at the negative frequency $-\Omega$ that the Lorentzian approximation lacks. The variance $\langle x(t)^2 \rangle$, acquired by integrating (2.34) over the full frequency spectrum, is given by

$$\langle x(t)^2 \rangle = \frac{k_{\mathrm{B}} T}{m\Omega^2} = \frac{k_{\mathrm{B}} T}{k}, \tag{2.35}$$

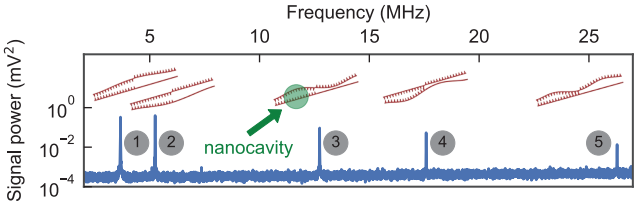

Figure 2.3: **Thermal vibrations in the sliced nanobeam device.** Thermomechanical fluctuation spectrum of the sliced photonic crystal nanobeam, imprinted on the intensity of laser light reflected from the nanocavity. Lorentzian resonances correspond to mechanical flexural modes at frequencies $\Omega_j/(2\pi)$ = {3.7, 5.3, 12.8, 17.6, 26.2} MHz with loss rates $\gamma_j/(2\pi) \approx 1-7$ kHz and estimated vacuum optomechanical coupling rates $g_0^{(j)}/(2\pi) = \{5.3, 5.9, 3.3, 3.1, 1.9\}$ MHz.

in accordance with the equipartition theorem.

Equation (2.35) is an important result. It allows to use the thermal variance of the displacement as a reference length scale, e.g. for calibrating the linear optomechanical transduction coefficient $\partial R/\partial x$. In experiments, we measure the detector voltage $V(t) = \cdots + v_x x(t)$, related to the position via the transduction coefficient $v_x = (\partial V/\partial R)(\partial R/\partial x)$, and evaluate its spectral density $S_{VV}(\omega) = \cdots + v_x^2 S_{xx}(\omega)$. In addition, $S_{VV}(\omega)$ contains other contributions, e.g. from other resonators coupled to the same cavity or electronic noise sources, as illustrated in Figure 2.3. To estimate the portion of the variance of $V(t)$ attributable to $x(t)$, we integrate $S_{VV}(\omega)$ over a small frequency band of width $\Delta\omega > \gamma$ that is larger than the spectral linewidth γ but small enough to not include other frequency contributions:

$$\langle V(t)^2\rangle^{(x)} = 2\int_{\Omega-\Delta\omega/2}^{\Omega+\Delta\omega/2} S_{VV}(\omega)\,\frac{\mathrm{d}\omega}{2\pi} \approx v_x^2\langle x(t)^2\rangle = \underbrace{\frac{v_x^2}{m\Omega^2}}_{A_x} k_\mathrm{B}T. \tag{2.36}$$

Note that we have to double the value of the integral, as we only integrate over the positive frequency contribution.

At this point, we recall that the definition of x is essentially arbitrary and tied to the effective mass m. This ambiguity does not apply to the energy $m\Omega^2\langle x(t)^2\rangle = k_B T$. We therefore measure and use the well-defined energy transduction constant $A_x = v_x^2/(m\Omega^2)$ to normalize our experiments. Alternatively, we may work with the dimensionless displacement $z(t) = x(t)/x_\mathrm{zpf}$ introduced before. Plugging the voltage transduction coefficient $v_z = v_x x_\mathrm{zpf}$ for $z(t)$ into A_x yields

$$\langle V(t)^2\rangle^{(z)} = \frac{v_z^2}{m\Omega^2 x_\mathrm{zpf}^2} k_\mathrm{B}T = 2v_z^2\frac{k_\mathrm{B}T}{\hbar\Omega} = 2v_z^2\bar{n}^\mathrm{th}, \tag{2.37}$$

where we have recognized the phonon occupation $\bar{n}^\mathrm{th} = k_\mathrm{B}T/\hbar\Omega$ of the thermal environment, valid in the high-temperature limit $k_\mathrm{B}T \gg \hbar\Omega$. Again, we measure and use the well-defined transduction constant $2v_z^2$ for normalization.

The required reference measurements to determine the normalization coefficients A_x and $2v_z^2$ are generally taken immediately before every experimental run, to compensate for changes in transduction due to e.g. drifts in optical alignment.

2.4. Dynamic modulation of the optical spring

Next, we consider an optical cavity coupled to multiple mechanical resonators. Each resonator j is associated with a linear optomechanical coupling G_j, phonon-photon coupling rate $g_0^{(j)}$, mechanical frequency Ω_j, damping γ_j and spring shift $\delta\Omega_j$. The cavity frequency $\omega_\mathrm{c}(x_1,\ldots,x_N) \approx \omega_0 - \sum_j G_j x_j$ is then a function of N displacement coordinates x_j.

We start with $N = 2$. Again, we define dimensionless displacement coordinates $z_j = x_j/x_{\mathrm{zpf},j}$. The cavity photon number

$$n_\mathrm{c}(z_1,z_2) = n_\mathrm{max} h\left(u_0 + 2g_0^{(1)} z_1/\kappa + 2g_0^{(2)} z_2/\kappa\right) \tag{2.38}$$

is now a function of two coordinates. Its expansion around $z_{1,2} = 0$ features two linear contributions of the form in (2.22), one for each z_j. Following (2.20), the equation of motion for z_1 reads

$$\ddot{z}_1 = -\Omega_1^2 z_1 - \gamma_1 \dot{z}_1 + n_\mathrm{max}\frac{4\Omega_1 g_0^{(1)} g_0^{(2)} h'(u_0)}{\kappa} z_2, \tag{2.39}$$

where we have absorbed the optical spring shift into the mechanical frequency $\Omega_1 \mapsto \Omega_1 + \delta\Omega_1$ and approximated $\Omega_1 + \delta\Omega_1 \approx \Omega_j$ in the last term. A similar equation is obtained for $\ddot{z}_2$ upon exchanging the indices $1 \leftrightarrow 2$.

The final term in (2.39) represents an optical force $F_{12}(x_2)$ acting on resonator 1 that depends linearly on the displacement of resonator 2. Ostensibly, the cavity field mediates an optical spring that couples the two resonators with a stiffness $k_{12} = -\partial F_{12}/\partial x_2 \propto n_\mathrm{max}$ that scales with the intensity of the optical drive. For resonators with equal frequencies $\Omega_1 \approx \Omega_2$, this immediately leads to hybridized mechanical modes [148].

For detuned resonators, the inter-resonator force is off-resonant and does not induce hybridization. However, as the force $F_{12}(t) = -k_{12}(t)x_2(t)$ mixes the inter-resonator optical spring $k_{12}(t)$ with the displacement $x_2(t)$, we realize that dynamic modulation of $k_{12}(t)$ enables frequency conversion [149].

Modulating the drive laser intensity $|c_\mathrm{in}(t)|^2$ with frequency $\omega_\mathrm{m} \ll \kappa$ and phase offset ϕ_m instantaneously addresses the cavity photon population n_c in the bad-cavity limit and thus modulates the inter-resonator spring $k_{12}(t) \propto \cos(\omega_\mathrm{m} t + \phi_\mathrm{m})$. With the displacement $x_2(t) \propto \cos(\Omega_2 t + \phi_2)$ oscillating harmonically at Ω_2 with phase offset ϕ_2, this creates sidebands in the optical force

$$\begin{aligned} F_{12}(t) &\propto \cos(\omega_\mathrm{m} t + \phi_\mathrm{m}) \cdot \cos(\Omega_2 t + \phi_2) \\ &= \frac{1}{2}\cos\left((\Omega_2 - \omega_\mathrm{m})t + \phi_2 - \phi_\mathrm{m}\right) \qquad (2.40) \\ &\quad + \frac{1}{2}\cos\left((\Omega_2 + \omega_\mathrm{m})t + \phi_2 + \phi_\mathrm{m}\right). \qquad (2.41) \end{aligned}$$

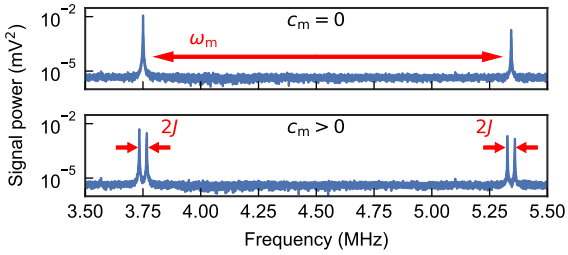

Figure 2.4: **Coupling detuned resonators by a modulated optical spring.** Thermomechanical fluctuation spectra of the sliced nanobeam, imprinted on the intensity of a far-detuned detection laser reflected off the cavity. An additional drive laser is detuned by $\kappa/(2\sqrt{3})$ and induces a positive optical spring shift. With a static drive laser (top), two mechanical modes are revealed with spring-shifted frequencies $\Omega_j = \{3.7, 5.3\}$ MHz. By modulating the drive laser with finite depth $c_\mathrm{m} > 0$ at the frequency difference $\omega_\mathrm{m} = \Omega_2 - \Omega_1$ between the two modes (bottom), a linear interaction is induced between the resonator through frequency conversion. The resonators form hybridised Floquet modes with frequency splitting $2J > \gamma_j$ larger than the mechanical linewidths $\gamma_j \sim$ kHz.

By choosing $\omega_\mathrm{m} = \Omega_2 - \Omega_1$, the down-converted sideband (2.40) becomes resonant with resonator 1. At the same time, the optical inter-resonator force $F_{21}(t)$ acting on the *other* resonator acquires a resonant *up-converted* sideband, given by (2.41) upon exchanging the indices $1 \leftrightarrow 2$. This mutual interaction leads to the formation of hybridised Floquet modes of the two resonators, shown in Figure 2.4, and enables mechanical state transfer [149]. Moreover, we note that the modulation phase ϕ_m appears with a negative sign $-\phi_\mathrm{m}$ in the down-converted sideband, but with a positive sign $+\phi_\mathrm{m}$ in the up-converted one. As was demonstrated in [64], this causes ϕ_m to be imprinted as a nonreciprocal Peierls phase (section 1.3) on transferred vibrations.

Choosing $\omega_\mathrm{m} = \Omega_1 + \Omega_2$ presents another opportunity to create inter-resonant sidebands. However, in that case, it is the down-conversion sideband (2.40) imprinting phase $-\phi_\mathrm{m}$ that is resonant in *both* F_{12} and F_{21}. This leads to a fundamentally different interaction between the two modes: They now experience two-mode parametric amplification. In effect, the modulation couples the negative frequency component $e^{-\mathrm{i}\Omega_1 t}$ of one resonator to the positive frequency component $e^{\mathrm{i}\Omega_2 t}$ of the other, and vice versa (Figure 2.5). Similarly, modulating the drive laser intensity at $\omega_\mathrm{m} = 2\tilde{\Omega}_j$ induces single-mode parametric amplification of resonator j through modulation of the single-mode optical spring constant k_{jj}. In this case, the modulation couples the negative and positive frequency components of the same resonator.

We discuss these interactions and their consequences in more detail in section 2.6 using the quantum framework laid out in the next section.

2.5. Quantum optomechanics

While the experiments in this thesis are distinctly classical, we will adopt a quantum formalism to describe them. This is standard practice in the field of classical cavity optomechanics and illustrates the connection to other (quantum) systems such

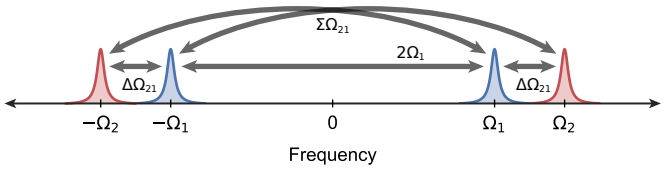

Figure 2.5: **Dynamic modulation in a sideband picture.** Positive and negative frequency sidebands corresponding to two resonances are shown at $\pm\Omega_{1,2}$. Dynamic modulation of the spring shift at the difference frequency $\Delta\Omega_{21} = \Omega_2 - \Omega_1$ inter-couples the positive and negative frequency sidebands of both resonators. Modulating the spring shift at the double frequency $2\Omega_1$ couples the positive frequency sideband to the negative frequency sideband of the same resonator, while modulation at the sum frequency $\Sigma\Omega_{21} = \Omega_2 + \Omega_1$ cross-couples positive and negative frequency sideband between resonators.

as superconducting resonators or photonics. Moreover, it facilitates the potential extension of our findings in the quantum domain. In this section, we introduce a quantum treatment of the optomechanical interaction between a cavity mode and a single resonator, before expanding the system to multiple resonators in the next section.

Both the cavity and the mechanical resonator constitute harmonic oscillators, with their quantized energy packets $\hbar\omega_c$ and $\hbar\Omega$ known as (optical) photons and (mechanical) phonons. We describe the optical and mechanical degrees of freedom by the annihilation operators $\hat{c}$ and $\hat{a}$, respectively. The mechanical displacement operator $\hat{x}$ and momentum operator $\hat{p}$ are given by

$$\hat{x} = x_{\mathrm{zpf}}\left(\hat{a} + \hat{a}^\dagger\right), \qquad \hat{p} = -\mathrm{i}m\Omega x_{\mathrm{zpf}}\left(\hat{a} - \hat{a}^\dagger\right), \tag{2.42}$$

where we recall that x_{zpf} is the zero-point fluctuation amplitude given in (2.12). This choice of normalization ensures that the mechanical number operator $\hat{a}^\dagger\hat{a}$ expresses the phonon number $\hat{n}$. Similarly, $\hat{c}^\dagger\hat{c}$ is normalized to express the number of cavity photons $\hat{n}_{\mathrm{c}}$.

In the rotating frame of the optical control field, the Hamiltonian of the interacting system reads

$$\hat{H} = -\hbar\Delta(\hat{x})\left(\hat{c}^\dagger\hat{c} + \frac{1}{2}\right) + \hbar\Omega\left(\hat{a}^\dagger\hat{a} + \frac{1}{2}\right), \tag{2.43}$$

where the detuning $\Delta(\hat{x}) = \Delta_0 + G\hat{x}$ is defined as before. From now on, we leave out the ground state energy offsets $\propto 1/2$ in the brackets in (2.43), as these do not affect the system's dynamics. We express the cavity detuning in terms of $\hat{x}$ and obtain

$$\hat{H} = \hbar\Omega\hat{a}^\dagger\hat{a} - \hbar\Delta_0\hat{c}^\dagger\hat{c} - \hbar g_0\hat{c}^\dagger\hat{c}\left(\hat{a} + \hat{a}^\dagger\right). \tag{2.44}$$

Here, we recognize the radiation pressure force

$$\hat{F}_{\mathrm{opt}} = -\frac{\partial\hat{H}}{\partial\hat{x}} = \hbar G\hat{n}_c, \tag{2.45}$$

which corresponds to its classical counterpart (2.2).

Equation (2.44) governs the dynamics of a closed system. In reality, both the cavity and the mechanical resonator interact with the environment. To model this, we employ input-output theory [147], which adds terms describing decay, fluctuations and driving to quantum equations of motion in the Heisenberg picture. We have already used this formalism tacitly in sections 2.3.4 and 2.3.5.

We assume that the cavity is coupled to an input port described by the input field operator $\hat{a}_{\text{in}}$ with rate κ_{in}. The cavity experiences loss at a rate κ, both through the input port and other channels. Through these additional ports, vacuum fluctuations described by the operator $\hat{f}_{\text{env}}$ feed back into the cavity with rate $\kappa_0 = \kappa - \kappa_{\text{in}}$. The mechanical resonator dissipates energy into its environment at a rate γ. Conversely, fluctuations described by the operator $\hat{a}_{\text{env}}$ feed into the resonator with the same rate. For the MHz-frequency resonators used in this thesis, the phonon energy $\hbar\Omega \ll k_{\text{B}}T$ is much smaller than the thermal energy for the lab temperature $T \approx 300$ K, such that $\hat{a}_{\text{env}}$ is dominated by thermal fluctuations.

The Heisenberg-Langevin equations of motion then read

$$\dot{\hat{c}} = -\frac{\kappa}{2}\hat{c} + \mathrm{i}\left(\Delta_0 + G\hat{x}\right)\hat{c} + \sqrt{\kappa_{\text{in}}}\hat{c}_{\text{in}} + \sqrt{\kappa_0}\hat{f}_{\text{env}}, \tag{2.46}$$

$$\dot{\hat{a}} = -\frac{\gamma}{2}\hat{a} - \mathrm{i}\Omega\hat{a} + \mathrm{i}g_0\hat{c}^\dagger\hat{c} + \sqrt{\gamma}\hat{a}_{\text{env}}. \tag{2.47}$$

From (2.46) and (2.47), the classical evolution of a coherent state can be obtained by taking the expectation value of the operators $\hat{a} \mapsto \langle\hat{a}\rangle \equiv a$ and $\hat{c} \mapsto \langle\hat{c}\rangle \equiv c$. This yields the classical equations of motion

$$\dot{c} = \mathrm{i}\left(\Delta_0 + Gx + \mathrm{i}\kappa/2\right)c + \sqrt{\kappa_{\text{in}}}c_{\text{in}}, \tag{2.48}$$

$$\dot{a} = -\mathrm{i}\left(\Omega - \mathrm{i}\gamma/2\right)a + \underbrace{\mathrm{i}g_0|c|^2}_{f_{\text{opt}}} + f_{\text{th}}, \tag{2.49}$$

where we have removed the effect of quantum fluctuations, but kept a stochastic drive term f_{th} for the mechanical resonator that represents a fluctuating thermal force.

Quantum fluctuations are not relevant in our experiments as their impact on the mechanical degrees of freedom is always smaller than that of f_{th}. In the remainder of this thesis, we therefore drop the hats for notational compactness and let the meaning of a symbol $\mathcal{O}$ be inferred from context: the operator $\hat{\mathcal{O}}$ is meant whenever Hamiltonians are defined, while equations of motion are written for the expectation value $\langle\hat{\mathcal{O}}\rangle$.

At this point, we recognize the similarity between (2.49) and the classically derived evolution (2.9) for a high-Q resonator. Indeed, our choice $\tilde{x} = 2x_{\text{zpf}}$ for the classical normalization length guarantees that we can translate Heisenberg-Langevin equations directly into classical equations of motion. As an example, we note that the optical drive indicated by f_{opt} in (2.49) is exactly the result of plugging the radiation pressure force $F_{\text{opt}} = \hbar G|c|^2$ into the classical driving term (2.10).

The evolution described in (2.46) and (2.47) is not linear and can in general not be solved exactly. This reflects the fact that the optomechanical interaction

Hamiltonian

$$\hat{H}_{\text{int}} = -\hbar g_0 \hat{c}^\dagger \hat{c} \left(\hat{a} + \hat{a}^\dagger\right) \tag{2.50}$$

involves combinations of three operators and thus describes a nonlinear (three-wave mixing) process. In the following section, we advance by linearising the evolution around a large coherent cavity amplitude, after first expanding our system to include multiple mechanical resonators.

2.6. Optically-mediated mechanical interactions

The aim of the current section is to quantify the effective mechanical interactions introduced in section 2.4, mediated by dynamic modulation of the cavity backaction. To do so, we extend our system to a single optical mode annihilated by c coupled to N mechanical modes annihilated by $\breve{a}_j$ in the laboratory frame, with frequencies Ω_j and vacuum optomechanical coupling rates $g_0^{(j)}$. The Hamiltonian of this system is an extension of (2.44) and reads

$$\breve{H}/\hbar = \sum_{j=1}^{N} \Omega_j \breve{a}_j^\dagger \breve{a}_j - \Delta_0 c^\dagger c - \sum_{j=1}^{N} g_0^{(j)} c^\dagger c \left(\breve{a}_j + \breve{a}_j^\dagger\right). \tag{2.51}$$

We work in the bad-cavity limit $\kappa \gg \Omega_j$. The cavity is driven by a control field with slowly varying amplitude $c_{\text{in}}(t)$ that addresses the cavity photon population instantaneously. Following (2.15), the cavity mode is displaced by a steady-state amplitude approximated by the homogeneous ($g_0^{(j)} = 0$) solution

$$\bar{c}(t) \approx \sqrt{\kappa_{\text{in}}}\chi_c(\Delta_0) c_{\text{in}}(t). \tag{2.52}$$

We linearise the radiation-pressure interaction (2.51) by displacing the cavity amplitude around (2.52), i.e. $c(t) \mapsto \bar{c}(t) + \delta c(t)$ and neglecting terms $\mathcal{O}((\delta c)^2)$, assuming small cavity fluctuations $\delta c(t)$. Ignoring constant offsets, Hamiltonian (2.51) then reads

$$\begin{aligned}\breve{H}/\hbar \approx &- \Delta_0 \delta c^\dagger \delta c + \sum_{j=1}^{N} \left[\Omega_j \breve{a}_j^\dagger \breve{a}_j - |\bar{c}(t)|^2 g_0^{(j)} \left(\breve{a}_j + \breve{a}_j^\dagger\right)\right] \\ &- \left(\bar{c}(t)\delta c^\dagger + \bar{c}(t)^* \delta c\right) \sum_{j=1}^{N} g_0^{(j)} \left(\breve{a}_j + \breve{a}_j^\dagger\right).\end{aligned} \tag{2.53}$$

Subsequently, we apply a unitary transformation $U_F = \exp\left(-\mathrm{i}t \sum_j \Omega_j \breve{a}_j^\dagger \breve{a}\right)$ to describe the mechanical resonators in a rotating frame with operators $a_j = U_F \breve{a}_j U_F^\dagger = e^{\mathrm{i}\Omega_j t}\breve{a}_j$. The lab frame Hamiltonian $\breve{H}$ is transformed to the rotating frame via $H = U_F^\dagger \breve{H} U_F + \mathrm{i}\hbar U_F \partial U_F^\dagger/\partial t$ and results in the rotating

frame Hamiltonian

$$\begin{aligned} H/\hbar = &- \Delta_0 \delta c^\dagger \delta c - \overbrace{\sum_{j=1}^{N} |\bar{c}(t)|^2 g_0^{(j)} \left(a_j e^{\mathrm{i}\Omega_j t} + a_j^\dagger e^{-\mathrm{i}\Omega_j t} \right)}^{\text{static rpf}} \\ &\underbrace{- \left(\bar{c}(t) \delta c^\dagger + \bar{c}(t)^* \delta c \right) \sum_{j=1}^{N} g_0^{(j)} \left(a_j e^{\mathrm{i}\Omega_j t} + a_j^\dagger e^{-\mathrm{i}\Omega_j t} \right)}_{\text{backaction rpf}} . \end{aligned} \tag{2.54}$$

Following the approach in section 2.5, we derive the classical Langevin equations

$$\delta \dot{c} = (\mathrm{i}\Delta_0 + \kappa/2)\delta c \; + \; \mathrm{i}\bar{c}(t) \sum_j g_0^{(j)} \left(a_j e^{\mathrm{i}\Omega_j t} + a_j^* e^{-\mathrm{i}\Omega_j t} \right) \tag{2.55}$$

$$\dot{a}_j = \underbrace{-(\gamma/2)a}_{\text{dissipation}} + \underbrace{\mathrm{i}|\bar{c}(t)|^2 g_0^{(j)} e^{-\mathrm{i}\Omega_j t}}_{\text{static rpf}} + \underbrace{\mathrm{i} g_0^{(j)} \left(\bar{c}(t) \delta c^\dagger + \bar{c}(t)^* \delta c \right) e^{-\mathrm{i}\Omega_j t}}_{\text{backaction rpf}} \tag{2.56}$$

In contrast to the equations of motion (2.48) and (2.49) for the full cavity field, equations (2.55) and (2.56) are linear and can be analysed further for example in the frequency domain [118, 143].

Working in the bad-cavity limit, we separate the optical timescale from the mechanical timescale by setting $\delta \dot{c} \approx 0$. This results in cavity fluctuations that are stationary on the mechanical timescale and given by

$$\delta c \approx \mathrm{i}\chi_\mathrm{c}(\Delta_0) \sum_j g_0^{(j)} \bar{c}(t) \left(a_j e^{\mathrm{i}\Omega_j t} + a_j^\dagger e^{-\mathrm{i}\Omega_j t} \right) . \tag{2.57}$$

Here, we have tacitly assumed that the cavity susceptibility $\chi(\Delta_0 + \omega)$ doesn't change over the frequency components ω of the optomechanical drive term, which are on the order of Ω_j.

After plugging (2.57) into (2.56) and some algebra, we arrive at the system of equations for the resonator amplitudes

$$\begin{aligned} \dot{a}_j = &- (\gamma/2)a + \mathrm{i}|\bar{c}(t)|^2 g_0^{(j)} e^{-\mathrm{i}\Omega_j t} \\ &- 2\mathrm{i}|\bar{c}(t)|^2 \, \mathrm{Im}\left[\chi_\mathrm{c}(\Delta_0)\right] \sum_k g_0^{(j)} g_0^{(k)} \left(a_k^* e^{-\mathrm{i}\Omega_k t} + a_k e^{\mathrm{i}\Omega_k t} \right) e^{-\mathrm{i}\Omega_j t} . \end{aligned} \tag{2.58}$$

We note that the prefactor $\mathrm{Im}\left[\chi_\mathrm{c}(\Delta_0)\right] = \Delta_0 |\chi_\mathrm{c}(\Delta_0)|^2$ is a good approximation of $\mathrm{Im}\left[\chi_\mathrm{c}(\Delta_0 + \omega)\right]$ if $\Delta_0 \gg \omega \sim \Omega_j$.

Finally, we recognize that the equations of motion (2.58) correspond to the Hamiltonian $H_\mathrm{eff} = H_\mathrm{d} + H_\mathrm{eff}^\mathrm{int}$ comprising the displacement contribution

$$H_\mathrm{d}/\hbar = -|\bar{c}(t)|^2 \sum_j g_0^{(j)} \left(a_j e^{-\mathrm{i}\Omega_j t} + \mathrm{H.c.} \right) \tag{2.59}$$

and the interaction Hamiltonian

$$H_{\text{eff}}^{\text{int}}/\hbar = \Delta_0|\chi_{\text{c}}(\Delta_0)|^4\kappa_{\text{in}}|c_{\text{in}}(t)|^2\left(\sum_j g_0^{(j)}\left(a_j e^{-i\Omega_j t}+\text{H.c.}\right)\right)^2. \tag{2.60}$$

Alternatively, the effective interaction Hamiltonian (2.60) can be derived using a proper open-system quantum treatment as well, after adiabatic elimination of the cavity fluctuations [150]. This procedure is detailed in the Supplementary Information of [151].

2.6.1. Control field modulation

We introduce modulation of the control field intensity $|c_{\text{in}}(t)|^2$ using multiple harmonic driving tones l with frequencies $\omega_{\text{m}}^{(l)}$, modulation depths $c_{\text{m}}^{(l)}$, and phases $\phi_{\text{m}}^{(l)}$. The homogeneous cavity intensity $\bar{n}_{\text{c}}(t) = |\bar{c}(t)|^2$ responds linearly to $|c_{\text{in}}(t)|^2$ via (2.52) and reads $\bar{n}_{\text{c}}(t) = \bar{n}_0\left[1+\sum_l c_{\text{m}}^{(l)}\cos\left(\omega_{\text{m}}^{(l)}t+\phi_{\text{m}}^{(l)}\right)\right]$, where $\bar{n}_0 = \kappa_{\text{in}}|\chi_{\text{c}}(\Delta_0)\bar{c}_{\text{in}}|^2$ is the average photon number.

First, we analyse the effect of a varying control field on the displacement term H_{d} given in (2.59). The static component $\bar{n}_0$ of the modulation generates a static force that displaces the resonators. This static displacement δx_j constitutes a new equilibrium position for each resonator and is customarily accounted for by shifting their displacement origin by δx_j. In addition, modulation tones that are resonant with a mechanical frequency $\omega_{\text{m}}^{(l)} = \Omega_j$ allow to drive the corresponding resonator j with drive strength f_j (cf. equations (2.10), (2.49)) proportional to the modulation depth,

$$f_j = \text{i}e^{\text{i}\phi_{\text{m}}^{(l)}}c_{\text{m}}^{(l)}g_0^{(j)}\bar{n}_0/2. \tag{2.61}$$

The large frequency separation between different resonators ensures that the tone l only drives a single mode. In the rotating frame, the effect of l on the other resonators induces quickly rotating terms that are subsequently neglected in a rotating wave approximation.

Next, we consider the effect on the interaction Hamiltonian $H_{\text{eff}}^{\text{int}}$. We plug in the modulated control field and expand the quadratic term in (2.60) into the terms $H_{\text{eff}}^{\text{int}} = \sum_{j,k} H_{\text{eff}}^{(j,k)}$ given by

$$H_{\text{eff}}^{\text{int}}/\hbar = g_{jk}(t)\left(a_j e^{-i\Omega_j t}+\text{H.c.}\right)\left(a_k e^{-i\Omega_k t}+\text{H.c.}\right). \tag{2.62}$$

Here, $g_{jk}(t) = \Delta_0|\chi_{\text{c}}(\Delta_0)|^2 g_0^{(j)}g_0^{(k)}\bar{n}_{\text{c}}(t)$ represents the cavity-mediated modulated interaction between j and k.

2.6.2. Interaction Hamiltonian

To proceed, we apply a rotating wave approximation (RWA) that keeps the *co-rotating* terms with slow evolution in the rotating frame. At this point, the frequency

content of the control field modulation becomes important: it selects which terms are mixed down to zero frequency and thus survive the RWA.

We start with the static component $\bar{n}_0$. This adds a stationary contribution to the self-interaction terms $H_{\text{eff}}^{(j,j)} = \hbar\delta\Omega_j a_j^\dagger a_j + \dots$ that shifts the mechanical resonance frequencies by $\delta\Omega_j = 2(g_0^{(j)})^2\bar{n}_0\Delta_0|\chi_c(\Delta_0)|^2 = 2g_j^2\Delta_0/(\Delta_0^2+\kappa^2/4)$, known as the optical spring shift and derived in section 2.3.4 for the classical system. Here, $g_j^2 = g_0^{(j)}\sqrt{\bar{n}_0}$ denotes the cavity-enhanced optomechanical coupling rate. For convenience, we reabsorb the optical spring shift in the definition of $\Omega_j \mapsto \Omega_j + \delta\Omega_j$.

Other frequency components (modulation tones) that induce RWA-surviving interaction terms have frequencies $\omega_{\text{m}}^{(l)}$ approaching either a mechanical sum frequency $\Sigma\Omega^{(jk)} = \Omega_j + \Omega_k$ or difference frequency $\Delta\Omega^{(jk)} = \Omega_j - \Omega_k$. The full interaction Hamiltonian in the RWA then reads

$$\begin{aligned} H_{\text{eff}}^{\text{int}}/\hbar \approx & \sum_{\omega_{\text{m}}^{(l)}\approx\Delta\Omega^{(jk)}} J_{jk}a_j^\dagger a_k e^{-\text{i}\left[\omega_{\text{m}}^{(l)}-\Delta\Omega^{(jk)}\right]t+\varphi_{jk}} + \text{H.c.} \\ & + \sum_{\omega_{\text{m}}^{(l)}\approx\Delta\Sigma^{(jk)}} \eta_{jk}a_j^\dagger a_k^\dagger e^{-\text{i}\left[\omega_{\text{m}}^{(l)}-\Sigma\Omega^{(jk)}\right]t+\theta_{jk}} + \text{H.c.}, \end{aligned} \tag{2.63}$$

where the sums run over the tones l and indices (j,k) that satisfy the specified resonance conditions. Note that a single pair of indices (j,k) satisfies resonance with a difference frequency $\Delta\Omega^{(jk)}$, whereas resonance with a sum frequency $\Sigma\Omega^{(jk)}$ is satisfied by both (j,k) and (k,j). This Hamiltonian underlies most of the experiments performed in this thesis.

From (2.63), we recognize that difference frequency modulations induce beamsplitter/hopping interactions, while sum frequency modulations induce squeezing interactions/parametric amplification corresponding to pairwise creation or annihilation of phonons in a quantum picture. The hopping and squeezing interaction rates J_{jk} and η_{jk}, respectively, are tuned by the depth $c_{\text{m}}^{(l)}$ of the corresponding modulation tone and given by [64, 152]

$$\{J_{jk},\eta_{jk}\} = c_{\text{m}}^{(l)}\frac{g_j g_k\Delta_0}{(\Delta_0^2+\kappa^2/4)} = c_{\text{m}}^{(l)}\frac{\sqrt{\delta\Omega_j\delta\Omega_k}}{2}. \tag{2.64}$$

Similarly, the hopping (squeezing) phases, denoted φ_{ij} (θ_{ij}), are set by corresponding modulation phase $\phi_{\text{m}}^{(l)}$, and crucially allow to imprint a non-trivial Peierls phase on the interaction [64, 74]. Note that $\delta\Omega_j$, $\delta\Omega_k$ always have the same sign. The scaling of the interaction rates with the geometric mean $\sqrt{\delta\Omega_j\delta\Omega_k}$ of the resonators' optical spring shifts reflects the fact that dynamically modulated optomechanical backaction underlies the effective interaction. Maximal coupling rates are thus attained for the optimal detunings $\Delta\pm = \pm\kappa(2\sqrt{3})$, when $|\delta\Omega_j|$ are maximal.

Finally, we comment on the validity of the RWA. It is valid for moderate effective coupling strengths $J_{jk},\eta_{jk} \ll \Omega_j$, (in the experiment, $J_{jk}/\Omega_j, \eta_{jk}/\Omega_j \sim 10^{-3} - 10^{-2}$), resolved mechanical sidebands (in the experiment $\gamma_j/\Omega_j \sim 10^{-3} - 10^{-2}$) and moderate detuning of the control tones, as well as no commensurable frequency

scales ($\Omega_i \pm \Omega_j \neq \Omega_k$ for all modes i, j, k). Besides moderate effective coupling, the RWA relies on the assumption that the modulated drive is quasi-resonant with each relevant process. In the large detuning and parametric drive limit, significant deviations are expected [153]. Parametric resonators are more naturally treated in this case in terms of the displacement coordinate x [154, 155] or employing quadratures in a generalised rotating frame [156].

2.6.3. Time-independent effective Hamiltonian

For modulation frequencies exactly resonant with $\Delta\Omega^{(jk)}, \Sigma\Omega^{(jk)}$, Hamiltonian (2.63) is time-independent. In this limit, we encode the beamsplitter interactions that conserve the total phonon number $n_{\mathrm{ph}} = \sum_{j=1}^{N} a_j^\dagger a_j$ in the elements $\mathcal{A}_{jk} = J_{jk} e^{-\mathrm{i}\varphi_{jk}}$, $\mathcal{A}_{kj} = \mathcal{A}_{jk}^*$ of the Hermitian *hopping matrix* $\mathcal{A}$. Consequently, we define the symmetric *squeezing matrix* $\mathcal{B}$ that encodes the particle-non-conserving squeezing interactions in its elements $\mathcal{B}_{jk} = \eta_{jk} e^{\mathrm{i}\theta_{jk}}$, $\mathcal{B}_{kj} = \mathcal{B}_{jk}$. Equation (2.63) then writes succinctly as the general quadratic form

$$H_{\mathrm{eff}} \approx \sum_{j,k} a_j^\dagger \mathcal{A}_{jk} a_k + \frac{1}{2}(a_j^\dagger \mathcal{B}_{jk} a_k^\dagger + a_j \mathcal{B}_{jk}^* a_k), \tag{2.65}$$

where we have set $\hbar = 1$ for convenience. We apply this convention in the remainder of this thesis.

2.6.4. Basic consequences of interactions

We conclude this section by briefly discussing the basic consequences of beamsplitter and squeezing interactions. As demonstrated experimentally in Figure 2.6a, a beamsplitter interaction $J > \gamma_j$, i.e. in the strong coupling regime, hybridizes resonators into Floquet modes and induces a frequency splitting $2J$ in their spectra. In addition, we track the evolution of two coupled resonators in time in Figure 2.6b. After a coherent excitation is initialized in resonator 1 by resonant drive laser modulation, the drive is switched off and the interaction modulation is switched on. Subsequently, Rabi-like oscillations are observed [149]: Through the frequency-converting interaction, energy is continuously exchanged back and forth between the resonators until the coherent energy in the resonators is dissipated. The period $4\pi J^{-1}$ of the Rabi oscillations is set by the interaction rate J. A detailed explanation of the experimental control and readout methods will be given in section 2.8.

For a beamsplitter interaction, the evolution of energy initially localized in a single resonator does not depend on the resonator quadrature that is excited. In addition, the beamsplitter interaction preserves the total phonon number in a closed system, such that amplitude in an open system can only decay. This is markedly different for a single-mode squeezing interaction: One resonator quadrature experiences parametric amplification while the orthogonal quadrature experiences damping. As demonstrated experimentally in Figure 2.7a and c, the parametric gain η modulates the spectral linewidth of the resonator, until for $2\eta > \gamma_j$ the parametric amplification overcomes the intrinsic decay rate γ_j and a narrow, high-amplitude parametric resonance is observed. In that case, the resonator is driven into self-

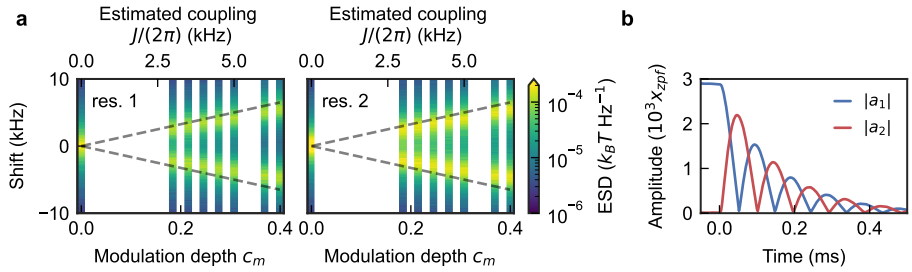

Figure 2.6: **Beamsplitter interaction. (a)** Thermomechanical spectra of resonators 1 and 2 shown in Figure 2.3 coupled by an optically-mediated effective beamsplitter interaction in their rotating frame. The interaction is induced by modulating the intensity of a drive laser, optimally detuned by $\Delta_0 = -\kappa/(2\sqrt{3})$, at the frequency difference $\Delta\Omega_{21} = \Omega_2 - \Omega_1$ between the mechanical resonances. The strength of the interaction $J = c_\mathrm{m}/2\sqrt{\delta\Omega_j \delta\Omega_k}$ is controlled by the depth c_m of the modulation and limited by the resonators' spring shifts $\delta\Omega_j$. The interaction hybridizes the strongly-coupled resonators into Floquet modes and induces a frequency splitting $2J > \gamma_j$ in their spectra that is larger than their dissipation rates γ_j. A slight difference (on the order of 10%) remains between the observed and the expected mode splitting (dashed lines) and is usually corrected for in later experiments. **(b)** Measured time evolution of the coherent amplitude (in units of their zero-point fluctuation amplitude) of a pair of resonators (1, blue and 2, red) subject to a beamsplitter interaction of strength $J/(2\pi) = 5$ kHz. Resonator 1 is initially (time $t < 0$) driven to a high amplitude steady state by a coherent laser intensity modulation. At $t = 0$, the drive modulation is switched off and the interaction modulation is switched on. Rabi-like oscillations induced by the coupling interaction are observed, where energy is transferred back and forth between the resonator until the coherent energy in the resonators is dissipated. The evolution is averaged over 24000 runs of the experiment.

oscillation with a growing amplitude that is ultimately limited by the nonlinearity of the resonator.

The effect of a single-mode squeezing interaction on thermal fluctuations is to break the quadrature-symmetry of the thermal state, as demonstrated earlier in electromechanical [157, 158] and optomechanical [159] systems. After recording a time trace of the thermally fluctuating complex amplitude $a_j(t)$ of resonator j, we construct a histogram of the distribution of the instantaneous quadrature amplitudes $X_j(t) \equiv \mathrm{Re}\, a_j(t)$ and $Y_j(t) \equiv \mathrm{Im}\, a_j(t)$. As detailed in section 2.8.7, the phase of $a_j(t)$ is referenced by independently measuring the propagation delay through the set-up. In Figure 2.7b we show such experimental phase-space distributions for resonators 3 and 4 subject to a single-mode squeezing interaction $\eta/(2\pi) = 1$ kHz smaller than their amplitude decay rates $\gamma_j/2$. For the particular squeezing interaction angle $\theta = \pi/2$ set in the experiment, the average amplitude of the X quadrature expressed in phonon amplitude is reduced ('squeezed') below the thermal quadrature amplitude $\sqrt{\bar{n}_j}/2$ while the average amplitude of Y is increased ('anti-squeezed') above $\sqrt{\bar{n}_j}/2$. In general, the squeezing angle θ rotates the phase-space distribution.

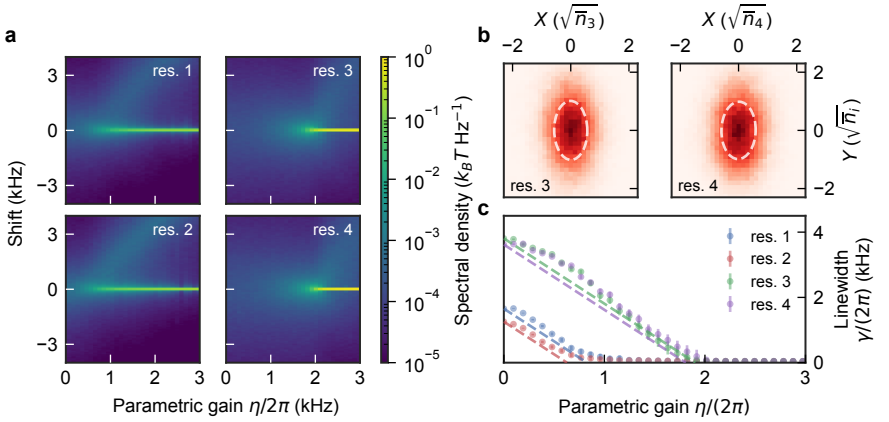

Figure 2.7: **Single-mode squeezing and linewidth modulation by parametric driving. (a)** Parametric gain induced by a single-mode squeezing interaction observed in thermomechanical spectra. Each panel corresponds to a separate experiment where resonator j (1 through 4) is subjected to a single-mode squeezing interaction of strength η. As η is increased, the resonance transitions from the broad intrinsic linewidth to a narrow parametric resonance. **b** The phase-space distribution of the thermal fluctuations of resonator j (left: 3, right: 4) subject to a single-mode squeezing interaction of strength $\eta/(2\pi) = 1$ kHz with squeezing angle $\theta = \pi/2$ reveals a squeezed thermal state. The squeezed (anti-squeezed) quadrature X (Y), measured in units of the thermal equilibrium amplitude $\sqrt{\bar{n}_j}$, are referenced by independently measuring the propagation delay through the set-up (section 2.8.7). **c** Fitted Lorentzian full-width at half-maximum linewidths of the resonances shown in (a). Even though a superposition of two degenerate resonances is expected – a broadened resonance of the anti-squeezed quadrature and a narrowed resonance of the squeezed quadrature – only a single one can be successfully fitted in each spectrum. This reflects the fact that the highly populated narrowed resonance dominates the broadened resonance. As the parametric gain η is increased, each resonator's squeezed quadrature linewidth is expected to decrease by $\Delta\gamma = -2\eta$ (dashed lines), until parametric threshold is reached at $\eta = \gamma_j/2$, where γ_j is the intrinsic linewidth of resonator j. The fitted linewidths follow the expected trend quite closely for intermediate η, while for lower η the narrow resonance is presumably not yet fully dominant and for larger η high-amplitude nonlinear effects are prominent. Error bars correspond to fit uncertainty, and are smaller than symbol size in most points.

2.7. Bogoliubov-de Gennes (BdG) formalism

To analyse the quadratic Hamiltonian (2.65), we use the Bogoliubov-de Gennes (BdG) framework [160–162] commonly used to model the dynamics of quasiparticle excitations in many-body systems. In this section, we briefly review this formalism and apply it to calculate the time evolution of interacting resonators.

In the absence of squeezing interactions, a quadratic Hamiltonian can be diagonalized by a unitary transformation that does not mix the system's annihilation operators a_j and creation operators $a_j^\dagger$. That is no longer the case if squeezing is involved: The Hamiltonian can then only be diagonalized by a *Bogoliubov transformation* that mixes the a_j's and $a_j^\dagger$'s into *quasiparticles*. The quasiparticle annihilation and creation operators still satisfy the appropriate (bosonic or fermionic) commutation relations. For bosons, the quasiparticle excitations are known as *normal modes*.

Finally, in terminology borrowed from partially-filled electronic systems, a_j's are often indicated as particle (annihilation) operators, while the creation operators $a_j^\dagger$ are referred to as hole (annihilation) operators.

2.7.1. BdG dynamical matrix and symmetries

In the BdG formalism, we therefore treat the operators a_j and $a_j^\dagger$ of the N interacting modes on equal footing, in effect doubling the apparent degrees of freedom of the system. We extend the vector $\mathbf{a} = (a_1, \cdots, a_N)^T$ of annihilation operators into the Nambu-like mode vector

$$\boldsymbol{\alpha} = \begin{pmatrix} \mathbf{a} \\ \mathbf{a}^\dagger \end{pmatrix}, \tag{2.66}$$

such that the quadratic Hamiltonian (2.65) can be written (up to a constant term) as

$$H_{\text{eff}} = \frac{1}{2}\boldsymbol{\alpha}^\dagger H \boldsymbol{\alpha}, \qquad\qquad H = \begin{pmatrix} \mathcal{A} & \mathcal{B} \\ \mathcal{B}^* & \mathcal{A}^* \end{pmatrix}. \tag{2.67}$$

We call H the Hamiltonian matrix.

Next, we calculate the Heisenberg equations of motion $\dot{\mathcal{O}} = \mathrm{i}/\hbar\,[H, \mathcal{O}]$ for the operators $\mathcal{O} \mapsto a_j, a_j^\dagger$. This yields the evolution $\dot{\boldsymbol{\alpha}}(t) = -\mathrm{i}\mathcal{H}\boldsymbol{\alpha}(t)$ of the mode vector, governed by the *BdG dynamical matrix*

$$\mathcal{H} = \Sigma_z H = \begin{pmatrix} \mathcal{A} & \mathcal{B} \\ -\mathcal{B}^* & -\mathcal{A}^* \end{pmatrix}. \tag{2.68}$$

Here, we have assumed that the a_j, $a_j^\dagger$ represent bosonic modes, such that their commutation relations are encoded by the matrix $\Sigma_z = \mathrm{diag}(\mathbb{1}_N, -\mathbb{1}_N) = [\boldsymbol{\alpha}, \boldsymbol{\alpha}^\dagger]$.

When squeezing interactions — which couple particle and hole operators — are absent ($\mathcal{B} = 0$), the dynamics of a_j and $a_j^\dagger$ are independent, and simply governed by the Hermitian matrices $\mathcal{A}$ and $-\mathcal{A}^*$, respectively. However, in the presence of squeezing ($\mathcal{B} \neq 0$), the bosonic dynamical matrix $\mathcal{H}$ is *non-Hermitian* and admits complex eigenvalues. It can thus generate dynamics that are not stable, where physical observables grow unbounded (or decay) in time. This is in stark contrast with the fermionic case, where the dynamical matrix $\mathcal{H}$, related to H by different commutation relations, is necessarily Hermitian [160]. We emphasize that the underlying Hamiltonian H_{eff} is still Hermitian: The non-Hermitian dynamics are induced by squeezing, not by incoherent coupling to a dissipative or pumped environment, which necessarily introduces fluctuations [163]. Studying this type of non-Hermitian dynamics is the subject of chapter 5.

The quasiparticles ψ_n, i.e. the eigenoperators that diagonalize the Hamiltonian, as well as the solution of $\mathbf{a}(t)$ can be expanded in terms of the eigenvectors $|\psi_n\rangle$ of $\mathcal{H}$ (that is, $\mathcal{H}|\psi_n\rangle = \varepsilon_n|\psi_n\rangle$ for some eigenvalue ε_n), in a similar fashion to Hermitian systems. The apparent doubling of dynamical degrees of freedom introduces symmetries in the matrix $\mathcal{H}$ that are reflected in the eigenvalues, to wit:

1. *Charge conjugation symmetry.* The mutual adjointness of creation and annihilation operators leads to a symmetry relation $\mathcal{C}\mathcal{H}\mathcal{C} = -\mathcal{H}$, where the operation $\mathcal{C} = \tau_x\mathcal{K}$ exchanges particles and holes using the matrix $\tau_x = \sigma_x \otimes \mathbb{1}_N$ (σ_x is the x Pauli matrix) and applies the complex conjugation operation $\mathcal{K}$. It implies that if $|\psi_n\rangle$ is an eigenvector of $\mathcal{H}$ with eigenvalue ε_n, then $\mathcal{C}|\psi_n\rangle$ is an eigenvector of $\mathcal{H}$ with eigenvalue $-\varepsilon_n^*$.

2. *Σ_z-pseudo-Hermiticity.* Bosonic commutation relations give rise to the symmetry relation $\Sigma_z\mathcal{H}\Sigma_z = \Sigma_z^\dagger$ known as Σ_z-pseudo-Hermiticity. It indicates that if $|\psi_n\rangle$ is an eigenvector of $\mathcal{H}$ with eigenvalue ε_n, then $\Sigma_z|\psi_n\rangle$ is an eigenvector of $\mathcal{H}$ with eigenvalue ε_n^*.

In general, the eigenvalues of $\mathcal{H}$ thus come in quartets $\{\varepsilon_n, \varepsilon_n^*, -\varepsilon_n, -\varepsilon_n^*\}$, of which some elements may be equal, for example when ε_n is purely real or imaginary. These redundancies ensure that if $\boldsymbol{\alpha}(0)$ represents a physical excitation at $t = 0$, i.e. the conjugation relations $(a_j)^\dagger = a_j^\dagger$ are satisfied between the upper half and the lower half of entries in (2.66), then the evolved state $\boldsymbol{\alpha}(t)$ will also be physical.

2.7.2. Open-system dynamics

Next, we introduce mechanical dissipation and thermal fluctuations. We use the Heisenberg-Langevin formalism to write the equation of motion

$$\dot{\boldsymbol{\alpha}}(t) = -\mathrm{i}\mathcal{M}\boldsymbol{\alpha}(t) + \boldsymbol{\alpha}_{\mathrm{in}}(t) + \mathbf{f}^{(\boldsymbol{\alpha})}, \tag{2.69}$$

governed by the open-system dynamical matrix $\mathcal{M} = \mathcal{H} - \mathrm{i}\Gamma/2$ that incorporates the dissipation matrix $\Gamma = \mathrm{diag}(\gamma_1, \ldots, \gamma_N, \gamma_1, \ldots, \gamma_N)$. The drive terms $\boldsymbol{\alpha}_{\mathrm{in}}$ describe fluctuations entering the modes and arise from the incoherent coupling to (thermal) baths with (high-temperature) Bose occupations $\bar{n}_j^{\mathrm{th}} \approx k_{\mathrm{B}}T/\hbar\Omega_i$. The drive terms $\mathbf{f}^{(\boldsymbol{\alpha})}$ encode any other forces driving the system. We note that dissipation generally means the dynamical matrix $\mathcal{M}$ does not obey Σ_z-pseudo-Hermiticity. Still, as we will see later for known Γ, the symmetries of $\mathcal{H}$ can often be revealed from the observation of spectral features related to the complex eigenvalues of $\mathcal{M}$.

We note that the resonator operators a_j in the underlying effective Hamiltonian H_{eff} in (2.65) are described in a rotating frame. Nevertheless, they fulfil the same Markovian correlations as their lab-frame counterparts, that is, $\langle\boldsymbol{\alpha}_{\mathrm{in}}(t)\boldsymbol{\alpha}_{\mathrm{in}}(t')\rangle = \mathcal{D}\delta(t-t')$ with diffusion matrix $\mathcal{D} = \mathrm{diag}(\gamma_1(\bar{n}_j^{\mathrm{th}}+1), \ldots, \gamma_1\bar{n}_j^{\mathrm{th}})$ [164]. In our analysis, we neglect quantum fluctuations by approximating $(\bar{n}_j^{\mathrm{th}}+1) \approx \bar{n}_j^{\mathrm{th}}$ in the diffusion matrix. In principle, equation (2.69) models the evolution of every experiment in this thesis, except the nonlinear experiments shown in chapter 8.

2.7.3. Quadrature evolution

In the experiments discussed in chapters 5, 6 and 7, we resolve the resonator modes into their quadratures $x_j = (a_j + a_j^\dagger)/\sqrt{2}$ and $p_j = (a_j - a_j^\dagger)/(\mathrm{i}\sqrt{2})$ to study their evolution. Following the approach in [161], we define the real matrices

$$U = \mathrm{Im}(\mathcal{B}-\mathcal{A}),\ V = \mathrm{Re}(\mathcal{A}+\mathcal{B}) \text{ and } T = \mathrm{Re}(\mathcal{A}-\mathcal{B}). \tag{2.70}$$

The quadrature vector $\mathbf{q}' = (x_1, \ldots, x_N, p_1, \ldots, p_N)^T$ then evolves as

$$\dot{\mathbf{q}}' = \mathcal{M}_{\mathbf{q}'}\mathbf{q}' - \mathbf{f}^{(\mathbf{q}')}, \tag{2.71}$$

subject to drive terms $\mathbf{f}^{(\mathbf{q}')3}$ and governed by the quadrature dynamical matrix

$$\mathcal{M}_{\mathbf{q}'} = \begin{bmatrix} U^T & T \\ -V & -U \end{bmatrix} - \Gamma/2. \tag{2.72}$$

The dynamical matrix $\mathcal{M}_{\mathbf{q}'}$ has purely real entries, reflecting the fact that quadratures can only have a real amplitude and no phase.

Finally, the vector $\mathbf{q}' = (\mathcal{S}^\dagger \otimes \mathbb{1}_N)\boldsymbol{\alpha}$ can be obtained from the mode vector $\boldsymbol{\alpha}$ using the unitary transformation

$$\mathcal{S} = \frac{1}{\sqrt{2}} \begin{bmatrix} 1 & \mathrm{i} \\ 1 & -\mathrm{i} \end{bmatrix}. \tag{2.73}$$

Note that the vector $\mathbf{q}'$ is ordered by quadrature type. For convenience, we often order the quadratures by resonator into the vector $\mathbf{q} = (x_1, p_1, \ldots, x_N, p_N)^T = \mathcal{G}\mathbf{q}'$, where $\mathcal{G}$ is the matrix that permutes the operators. The corresponding dynamical matrix then reads $\mathcal{M}_{\mathbf{q}} = \mathcal{G}\mathcal{M}_{\mathbf{q}'}\mathcal{G}^\dagger$, such that the evolution of $\mathbf{q}$ is given by

$$\dot{\mathbf{q}} = \mathcal{M}_{\mathbf{q}}\mathbf{q} - \mathbf{f}^{(\mathbf{q})}, \tag{2.74}$$

with forcing vector $\mathbf{f}^{(\mathbf{q})} = \mathcal{G}\mathbf{f}^{(\mathbf{q}')} = (f_{x_1}, f_{p_1}, \ldots, f_{x_N}, f_{p_N})^T$.

2.7.4. Susceptibility

To evaluate the response of a system to harmonic driving via the $\mathbf{f}^{(b)}$ terms at frequency ω, we Fourier transform the equations of motion (2.69) and (2.71). This results in the susceptibility matrices

$$\chi_{\boldsymbol{\alpha}}(\omega) = \mathrm{i}\left(\omega\mathbb{1} - \mathcal{M}\right)^{-1}, \tag{2.75}$$

$$\chi_{\mathbf{q}}(\omega) = \left(\mathrm{i}\omega\mathbb{1} + \mathcal{M}_{\mathbf{q}}\right)^{-1}, \tag{2.76}$$

in the mode and quadrature bases, respectively. In the absence of squeezing interactions, the system's dynamics and thus its response are fully characterized by the hopping matrix $\mathcal{A}$. In that case it suffices to consider only the reduced mode vector $\mathbf{a}$ of particle operators and its associated susceptibility matrix

$$\chi_{\mathbf{a}}(\omega) = \mathrm{i}\left(\omega\mathbb{1} - \mathcal{A} + \mathrm{i}\Gamma'/2\right)^{-1}, \tag{2.77}$$

where $\Gamma' = (\gamma_1, \ldots, \gamma_N)$ is the reduced dissipation matrix.

2.8. Experimental platform

In the remainder of this chapter, we focus on the experimental platform we use to induce nanomechanical multi-mode dynamics governed by tunable, arbitrary

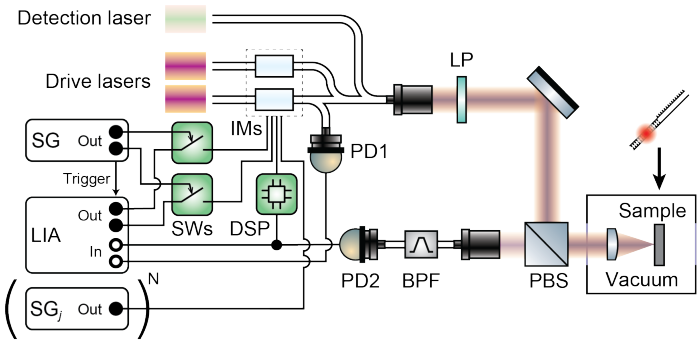

Figure 2.8: **Experimental set-up.** Schematic of the experimental set-up. Not all components are used in every experiment. IMs, intensity modulators; LP, linear polariser; PBS, polarising beamsplitter; BPF, optical bandpass filter; PD1, PD2, photodiode; DSP, digital signal processor; SWs, microwave switches; LIA, lock-in amplifier; SG, signal generator. The device, shown in Figure 2.1a, is mounted in a vacuum chamber under a $45°$ angle to facilitate cross-polarized detection. Depending on the experiment, one or two drive lasers are used in addition to a detection laser. All lasers have different wavelengths (typical spacing 1–5 nm). The BPF serves to filter out the detection laser in the read-out. The LIA ports serve to (Out) drive the IMs through an amplification stage (not shown) and to (In) analyse the intensity modulations of one drive laser (for calibration) and detection laser. If an experiment requires more modulation signals than the LIA can provide, a pool of $N = 6$ additional signal generators (labelled SG$_j$) is used. Phase coherence between additional SGs and the LIA is obtained by using the monitor detector PD1, as detailed in section 2.8.2. For time-resolved measurements, the SG is programmed to (Out) actuate the drive signal switches and trigger the LIA acquisition. The DSP optionally generates a feedback signal to modify resonator damping rates. The specific routing between signal sources and the IMs depends on the experiment.

quadratic bosonic Hamiltonians. We start by reviewing the set-up used in all experiments.

Illustrated in Figure 2.8, the set-up consists of an optical part and an electronic part. The sample is housed in vacuum chamber (pressure 2×10^{-6} mbar) to minimize the effect of air resistance on the mechanical modes, and mounted on a piezo-actuated precision stage to scan the laser focus over the sample. To assist with optical alignment, the sample is illuminated from outside the vacuum chamber using a broadband light source and imaged in transmission on a phosphor-coated NIR camera (not shown in the figure). The nanocavity is illuminated by laser light at normal incidence, focused by an objective lens (focal length 2.7 mm) co-located in the vacuum chamber. To filter light that is resonantly scattered by the cavity from light directly reflected by the substrate, we employ a cross-polarized detection scheme. In this scheme, the nanobeam device is rotated by $45°$ relative to the vertical polarization of the incoming light. Subsequently, only the converted, horizontally polarized light that has interacted with the cavity is detected.

Up to three lasers (Toptica CTL series) with individually tuned wavelengths are used to drive the optical cavity. Typical powers incident on the device are on the order of milliwatts, with an incoupling efficiency of $\eta_{\text{in}} \approx 3\%$. One laser serves as the

[3] Here we have opted for a different sign convention for the drive term than in the mode basis. This choice is not essential, as long as input-output relations are defined accordingly.

source of light used to optically detect mechanical motion (section 2.3.5), typically detuned by $\Delta_{\text{det}} = -2.5\kappa$ (6.9 nm in wavelength) from the cavity resonance. In the reflection path, detection light is filtered from the other (drive) lasers by a fiber-based tunable bandpass filter (DiCon) with a transmission window of 0.8 nm and detected on a fast, low-noise photodetector (New Focus 1811, a.c. coupled).

The two remaining lasers serve as drive lasers to induce modulated radiation pressure forces. Their intensities are modulated by individual fiber-based X-cut lithium-niobate electro-optic intensity modulators (IMs; Thorlabs LN81S-FC and Covega Mach-10 056), combined with the detection laser using fiber-based beam combiners and launched using a fiber collimator into the free-space set-up. A small portion of the modulated light of one of the drive lasers is split off in the fiber section of the set-up and fed onto a fast photodetector (New Focus 1811, d.c. coupled) to monitor and calibrate the drive modulation.

Control signals to drive the IMs are generated by a high-frequency lock-in amplifier (LIA; Zurich Instruments UHFLI). For experiments requiring more modulation signals than the LIA can provide, a pool of 6 additional signal generator ports (Siglent SDG1062X and SDG2122X) is available. One output of the lock-in amplifier carries signals to generate interactions, while the other output carries coherent excitation signals. Both outputs are routed through individual radio-frequency (RF) switches (Mini-Circuits ZYSWA-2-50DR+) to allow time-resolved driving. The connectivity between signal sources (LIA ports and external signal generators) and the IMs is tailored depending on each experiment's requirements. Signals fed into each IM are amplified by individual RF amplifiers (Mini-Circuits ZHL-32A+ with additional attenuation). For time-resolved measurements, a synchronized two-channel signal generator (Siglent SDG1062X) is used to generate pulses to actuate both RF switches and trigger the LIA acquisition.

The detected optical intensity signal is analysed by the LIA. Additionally, the detector signal is fed into a digital signal processor (DSP; RedPitaya STEMlab 125-14) that implements a configurable electronic bandpass filter with tunable gain and phase shift (using the PyRPL suite [165]). The output of the DSP is optionally combined with the control signals to control the nanobeam damping rates with measurement-based dynamical feedback.

2.8.1. Analysis of the displacement signal

The lock-in amplifier is used to isolate each resonator's displacement $x_j(t)$ by frequency filtering the electronic displacement signal. To do so, the detector voltage $V(t)$ is demodulated in parallel at each resonator's frequency Ω_j using electronic local oscillators (LOs) internal to the lock-in amplifier. For each resonator, the demodulated in-phase ($I_j(t)$) and quadrature ($Q_j(t)$) components are filtered using a third-order low-pass filter with a 3-dB bandwidth of 50 kHz, and combined into a complex amplitude $y_j(t) = I_j(t) + \mathrm{i}Q_j(t)$. This amplitude is formally equivalent to the resonator amplitude $a_j(t)$ in the rotating frame, with a scaling given by the optomechanical transduction factor and a phase rotation given by the propagation delay through the set-up. As discussed in section 2.3.6, the measured voltage variance induced by thermal displacement fluctuations of each resonator is used

to normalize $y_j(t)$. The correction procedure for the propagation phase delay is discussed in section 2.8.7.

The complex amplitudes of all resonators involved are acquired simultaneously, at a rate of 50 k to 500 k samples per second, depending on the experiment. Finally, the resulting complex time traces are either (i) analysed directly, (ii) averaged coherently over an ensemble of traces by calculating $\langle y_j(t)\rangle$, or (iii) Fourier transformed using a Hann windowing function, squared and averaged to yield spectral densities. In the last case, the low-pass filter is compensated for by dividing spectral densities by the filter frequency response.

2.8.2. Phase-coherent control signals

In our experiments, the central challenge in breaking time-reversal symmetry controllably is the generation of phase-coherent control signals. The electronic LOs oscillating at the resonator frequencies Ω_j define the rotating frame that we describe our nanomechanical system in. Even though the frequencies $\omega_\mathrm{m}^{(l)}$ of all modulation tones are distinct, the frequency relation $\omega_\mathrm{m}^{(l)} = \Omega_j \pm \Omega_k$ with the electronic LOs j and k lends each modulation tone l a well-defined phase in the rotating frame. We label the tone $l = j \pm k$ by the resonator frequency combination $j \pm k$ it addresses.

To understand this phase relation, we absorb the explicit time dependence of each tone $\cos\left(\omega_\mathrm{m}^{(l)} t + \phi_\mathrm{m}^{(l)}\right) = \cos\beta_l(t)$ into the instantaneous phase $\beta_l(t) = \omega_\mathrm{m}^{(l)} t + \phi_\mathrm{m}^{(l)}$, and similarly for each LO labelled by its resonator index j. For convenience, we denote $\phi_\mathrm{m}^{(j)}$ for the phase offset of LO j, even though it is not necessarily used as a modulation tone. Phase coherence is now attained between the interaction tone l and the *combination* of both resonator LOs j, k, since the phase difference

$$\begin{aligned}\Delta\phi_\mathrm{m}^{(j\pm k)} &= \beta_{j\pm k}(t) - (\beta_j(t) \pm \beta_k(t)) \\ &= \phi_\mathrm{m}^{(j\pm k)} - \left(\phi_\mathrm{m}^{(j)} \pm \phi_\mathrm{m}^{(k)}\right)\end{aligned} \tag{2.78}$$

is stable and does not depend on the origin of time. Physically, this phase difference may be evaluated by generating a tone with the combined instantaneous phase $\beta_j(t) \pm \beta_k(t)$ through mixing of the LOs and subsequent high-pass (low-pass) filtering, and comparing that to the interaction tone.

As we work with relatively low modulation frequencies in the MHz range, we can take a digital approach to achieve phase coherence. In fact, the lock-in amplifier we use is a digital device based on 8 numerical oscillators operating at a clock frequency of 1.8 GHz, and synthesizes its output tones on-the-fly. We can therefore access the instantaneous phase $\beta_l(t)$ directly, through the `phase` field of the demodulator sample data structure[4]. Note that the actual output signal lags the numerical oscillator by a time delay that depends on the oscillator index, equal to 16 clock cycles per oscillator index[5].

If only the LIA is used to generate control tones and no external signal generators are involved, we execute the following procedure. Before starting an experiment, at

[4] See Zürich Instruments LabOne programming manual, revision 22.08, section 2.4 for details.
[5] This is not reported in the LIA manual and took some experimentation to figure out.

time t_0, we simultaneously access the instantaneous phases $\beta_l(t_0)$ of all numerical oscillators, generating LO and interaction tones alike. We then apply a phase shift equal to $-\beta_l(t_0)$ to all oscillators, effectively defining t_0 as the origin of time. Finally, we shift the interaction tone oscillators to generate the desired Peierls phases $\varphi_{jk}, \theta_{jk}$ in the rotating frame. If the experiment requires more LOs and control signals than the 8 numerical oscillators of the LIA can provide, we follow an extended procedure that is described in section 2.9.

We note that similar functionality can be achieved using an arbitrary waveform generator (AWG), on which modulation tones can be programmed explicitly with the appropriate phase relations. However, currently we do not have access to a suitable high-frequency AWG in our lab. Moreover, while an AWG offers more flexibility in modulation patterns, its finite record length limits the maximum duration of an experiment. In contrast, our control signals can be sustained for a long time (on the order of hours), until numerical errors accrue in the digital phase registers. Finally, the integration of phase-coherent signal generation and demodulation using the same lock-in amplifier device simplifies the analysis of the mechanical displacement signals.

2.8.3. Optomechanical characterization

In Figure 2.9, we show the results of an experiment to characterize the optomechanical interaction between the cavity and the mechanical resonances coupled to it. In the thermomechanical fluctuation spectra shown in Figure 2.9a up to a maximum frequency of 20 MHz, we identify four mechanical resonances that undergo an optical spring shift as the frequency ω_{L} of a single unmodulated drive/detection laser is swept across the cavity resonance. We extract mechanical frequencies and linewidths by fitting Lorentzian functions to the individual resonator spectra shown in Figure 2.9b, and fit the extracted frequencies to the optical spring shift model (2.24) in Figure 2.9c. Across all resonators, we find agreement in the fitted cavity resonance frequency $\omega_0/(2\pi) = 195.62$ THz and linewidth $\kappa/(2\pi) = 320$ GHz (Q factor $Q \approx 600$), while the magnitude of the optical spring shift differs per resonator. We use the order-by-order approach laid out in [146] to extract the vacuum optomechanical coupling rates $g_0^{(j)}/(2\pi) = \{5.30 \pm 0.14, 5.86 \pm 0.17, 3.29 \pm 0.30, 3.12 \pm 0.89\}$ MHz from the measured intensity of nonlinear transduction.

2.8.4. Opto-thermal linewidth tuning

The small sideband resolution $\Omega_j/\kappa < 10^{-4}$ suggests negligible dynamical backaction and subsequent cavity-mediated modulation of the resonator decay rate. This is not what we observe in experiment: We measure linewidth modulations $\delta\gamma_j$ on the order of 5% of the optical spring shift $\delta\Omega_j$, with different ratios $\delta\gamma_j/\delta\Omega_j$ for each resonator. This suggests the presence of a retarded opto-thermal force [166] in addition to the instantaneous radiation-pressure force. Fine-tuning the laser intensity allows to match the two linewidths of modes 3 and 4 specifically, as they exhibit different scaling with drive laser intensity. This opportunity is used in later experiments.

The dynamical opto-thermal backaction damps or amplifies thermal fluctu-

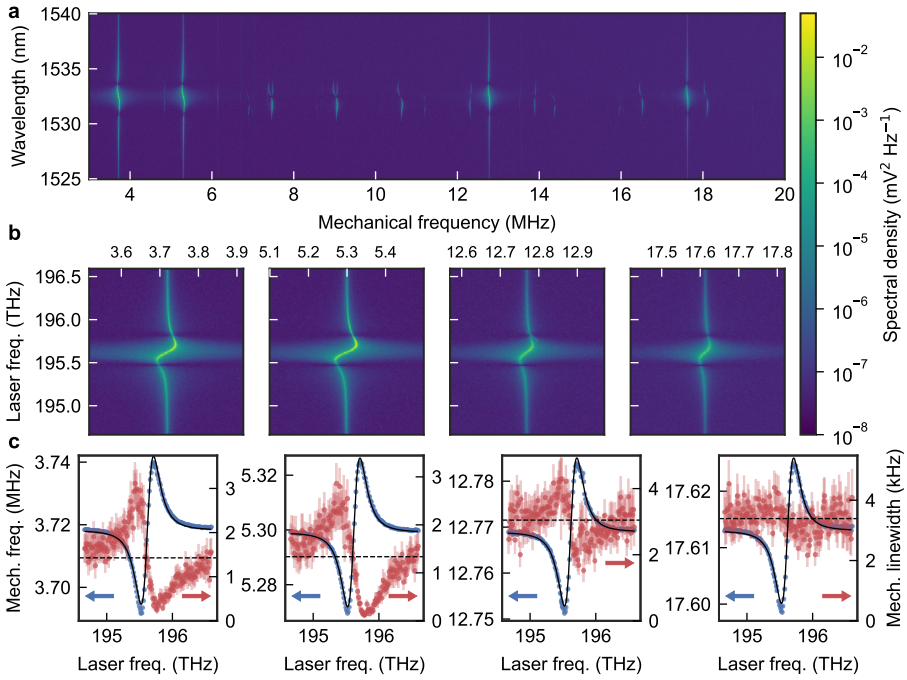

Figure 2.9: **Experimental characterization of the optical spring shift. (a)** Thermomechanical noise spectra of the first few mechanical modes imprinted on an unmodulated single drive/detection laser, as the laser's frequency ω_L is swept across the cavity resonance. The four most intense peaks around frequencies $\omega_j/(2\pi) \approx \{3.7, 5.3, 12.8, 17.6\}$ MHz correspond to flexural modes (labelled j) of the individual beam halves (Figure 2.3) and show frequency tuning characteristic to the optical spring effect (Figure 2.2), while the other modes represent nonlinearly transduced harmonics of those modes. **(b)** Zoomed-in thermomechanical noise spectra of the first four resonators. **(c)** From the spectra in (b), mechanical resonance frequencies Ω_j (blue circles) and linewidths γ_j (red circles) are extracted. The resonance frequencies are fitted using the standard optical spring model (2.24) (solid line). The small sideband resolution $\Omega_j/\kappa \approx 10^{-5}$ suggests very little change in linewidth due to dynamical cavity backaction (dashed line). The linewidth modulations we observe suggest the presence of an opto-thermal retardation effect (section 2.8.4). Displayed errors correspond to fit uncertainty, smaller than symbol size on the fitted frequencies.

ations and effectively modifies the mode temperature through $T_j = T_0\,(\tilde{\gamma}_j/\gamma_j)$ [118], where T_0 is the initial temperature and $\tilde{\gamma}_j$ is the mode's intrinsic linewidth. In the experiment shown in Figure 2.10 we confirm this behaviour, by measuring the area $A_j(\omega_L)$ of the mechanical resonance peak j imprinted on a separate, fixed frequency, far-detuned detection laser while the frequency of the drive laser is swept. The resonance peak area $A_j(\omega_L)$ is proportional to the variance $\langle x_j^2 \rangle$ of the resonator displacement x_j, which is proportional to the effective mode temperature T_j, as confirmed by a linear fit to the data. In all experiments in this thesis, we account for the optothermal modulation of effective mode temperature when normalizing.

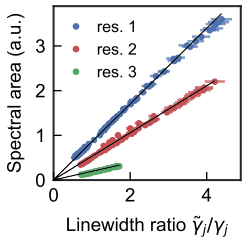

Figure 2.10: **Opto-thermal linewidth tuning.** Drive laser frequency sweep while using a separate, fixed frequency, far-detuned detection laser. The fixed transduction of mechanical motion onto this detection laser allows a comparison of resonance peak area $A_j(\omega_L)$, versus linewidth $\gamma_j(\omega_L)$ as the drive laser frequency ω_L is varied. Our data are well explained by linear fits of $A_j(\omega_L)$ versus $\tilde{\gamma}_j/\gamma_j(\omega_L)$ (dashed).

2.8.5. Calibration of control signals

To estimate the modulation depth c_m needed to induce a desired interaction rate J_{jk}, η_{jk}, we use the relation given in (2.64) and repeated here for convenience:

$$J_{jk}, \eta_{jk} = c_\mathrm{m} \frac{\sqrt{\delta\Omega_j \delta\Omega_k}}{2}.$$

Using this relation avoids the need to know the photon-phonon coupling rates $g_0^{(i)}$ and cavity incoupling rate precisely. The individual spring shifts $\delta\Omega_j$ can be measured easily by comparing and fitting thermomechanical spectra with the drive laser switched on and off. As shown in Figure 2.6a, the estimated and desired interaction rates may be off by about 10% depending on the specific circumstances. In most experiments, we estimate this discrepancy from a reference measurement and correct for it by adjusting the modulation depth.

The intensity modulators used are fiber-based interferometers with a tunable phase shift in one of the arms. The response of their transmission $I(V)$ to an (RF) voltage is therefore given by a cosine function. To find the linear operation point of the IM, a sinusoidal modulation voltage is applied while sweeping its amplitude and monitoring the modulations imprinted on the drive laser. The IM bias voltage is then varied to minimise the variation in DC transmission as a function of modulation amplitude. To compensate for frequency-dependent transmission in the RF chain and/or the electro-optic response of the IM, the relation between control signal voltage amplitude V_m and modulation depth c_m is measured individually for every tone using the DC-coupled modulation monitor detector. The measured relation is then fitted using the first-order Bessel function $J_1(x)$, derived from a Jacobi-Anger expansion of the IM cosine response.

For some experiments involving many interaction tones, the effective transduction per tone is reduced due to the stacking of their amplitudes. In this case, the actual imprinted modulation depth for each tone is monitored using the monitor detector while the experiment is running and all tones are enabled. By comparing the actual and desired modulation depth, a correction to the interaction strengths can then be determined.

2.8.6. Modulating damping by feedback

In addition to opto-thermal dynamical backaction (Figure 2.10), we control the resonator decay rates with measurement-based feedback [167, 168]. From the

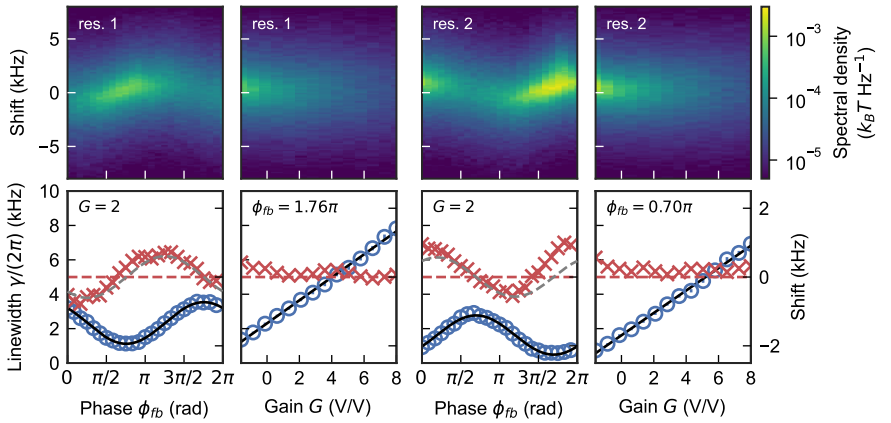

Figure 2.11: **Damping rate adjustment by feedback.** Resonator thermomechanical spectra (top row) and fitted full-width half-maximum linewidths (bottom row) adjusted by feeding back electronically filtered and phase-shifted resonator displacement signals onto the drive laser modulation (left two columns, resonator 1; right two columns, resonator 2). The resonator linewidth (circles) and frequency shift (crosses) vary sinusoidally with the feedback phase ϕ_{fb} (odd columns). By fitting the linewidth variation (solid black), the optimal phase shift to increase the damping rate is selected. The frequency variation (dashed grey) expected from the fitted linewidth modulation, relative to the resonator frequency with feedback off (dashed red), lags by $\pi/2$ radians. For the optimal feedback phase shift, an increase in linewidth is observed for increasing gain G, while the resonator frequency remains unaffected (even columns). The slope of the linear fit (solid black) can be used when setting a resonator's linewidth to a desired value.

electronic displacement signal, we obtain a feedback signal using a fast digital signal processor (DSP) that is subsequently imprinted on the drive laser intensity to actuate the resonators. The DSP filters the displacement signal around each resonator's frequency Ω_j in parallel (second-order filter half-width at half-maximum 78 kHz), applies individual gains and phase shifts, and finally combines the filtered signals digitally.

To find the optimal feedback phase shift ϕ_{fb} for each mode, we take thermomechanical spectra using a fixed feedback gain G while sweeping ϕ_{fb}, as shown in Figure 2.11. From the spectra, we extract the modulated linewidths, fit those with a sinusoidal variation and select the shift ϕ_{fb} with the most significant change in linewidth. Subsequently, for the optimal phase shift, thermomechanical spectra are taken for various settings of the feedback gain G to establish a linear relation between gain and modulated linewidth. This relation is then used to dial in the desired linewidth.

2.8.7. Coherent driving and propagation delay

The total propagation delay through the set-up, from the LIA control outputs via the sample to the LIA input, is determined by driving each of the resonators with radiation pressure modulated at frequency $\omega_{\mathrm{d}} = \Omega_j + \Delta_{\mathrm{d}}$ and measuring response $a_j(\Delta_{\mathrm{d}})$ as a function of detuning Δ_{d} (Figure 2.12). We fit the response to the me-

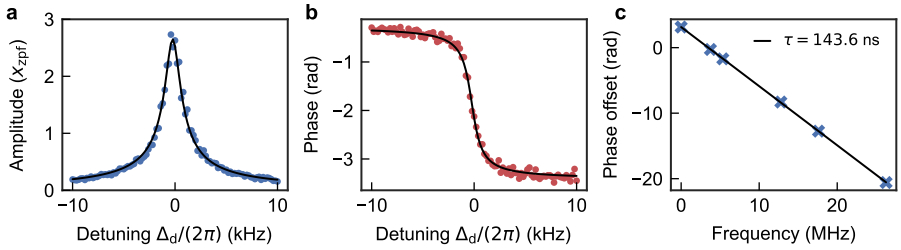

Figure 2.12: **Resonator coherent response. (a)** Amplitude $|a_1|$ and **(b)** phase ϕ_1 of the complex response $a_1(\Delta) = e^{i(\phi_1(\Delta)+\alpha_j)}|a_1(\Delta)|$ of resonator 1 to drive laser intensity modulation at a frequency ω_d close to resonance (drive detuning $\Delta_d = \omega_d - \Omega_j$). α_1 is the phase offset due to signal delay through the set-up. The mechanical response $a_1 = e^{i\alpha_1} A_1 \frac{\gamma_1/2}{i\gamma_1/2-\Delta_d}$ is fitted to the data (solid line). **(c)** Phase offsets α_j as measured when driving the first five flexural modes versus their resonance frequencies $\Omega_j/(2\pi)$. A linear fit (solid line) of $\alpha_j = -\Omega_j\tau$ indicates a propagation delay $\tau = 143.6$ ns through the set-up.

chanical susceptibility $a_j(\Delta_d) = e^{i\alpha_j} A_j \frac{\gamma_1/2}{i\gamma_1/2-\Delta_d}$ to extract the response phase offset α_j and driving strength A_j. We fit α_j versus resonator frequency Ω_j to determine the signal delay τ through the set-up, which is typically on the order of $\tau \sim 100$ ns depending on the specific signal routing required for the experiment. Importantly, we use τ to relate the quadratures of the demodulated amplitudes $y_j(t)$ to those defined by the control tones.

Finally, we note that the driving strength scales linearly with modulation depth $c_m^{(j)}$ through (2.61). However, in our analysis we use the measured ratios $A_j/c_m^{(j)}$ to relate driving strength and modulation depth, as $g_0^{(j)}$ and $\bar{n}_0$ are hard to determine accurately.

2.9. Appendix: Implementing large numbers of phase-coherent control signals

If an experiment requires more LOs and control signals than the 8 numerical oscillators of the LIA can provide, we follow an extension of the procedure outlined in section 2.8.2 that is conceptually similar but involves a more elaborate phase bookkeeping. Suppose we want to monitor the dynamics of N mechanical resonators under the influence of M modulation tones, with $N + M > 8$. As we require the LIA to analyse the mechanical signal, we implement up to $N = 7$ resonator LOs using the lowest-index numerical oscillators. The remaining free LIA oscillators are used to generate the first $8 - N$ interaction tones. The $M + N - 8$ interaction tones that remain need to be generated by external signal generators.

During the phase referencing procedure, we temporarily use the LIA oscillator with highest index $m = 8$ to 'transfer' phase coherence between the LIA and the external signal sources. First, we achieve phase coherence between the oscillators internal to the LIA as described earlier. For each externally generated modulation tone $l = j \pm k$, we execute the following steps:

1. Set the frequency of LIA oscillator $m = 8$ to match the frequency $\omega_{\mathrm{m}}^{(l)} = \Omega_j \pm \Omega_k$ of the external signal generator.
2. Access the instantaneous phases $\beta_8(t)$ of the phase transfer oscillator 8 and $\beta_j(t)$, $\beta_k(t)$ of the relevant resonator LOs.
3. Use (2.78) to evaluate the current, *arbitrary* phase $\Delta\phi_{\mathrm{m}}^{(l)}$ of oscillator 8 in the rotating frame.
4. Shift the phase of oscillator 8 by $-\Delta\phi_{\mathrm{m}}^{(l)}$ to cancel its current phase offset. We have now achieved phase coherence between the tone generated by the phase transfer oscillator and the resonator LOs.
5. Set the LIA to output a small voltage at $\omega_{\mathrm{m}}^{(l)}$ using oscillator 8. This signal imprints a weak modulation on the drive laser that we detect using the monitor detector.
6. Analyse the monitor signal using the same LIA oscillator 8 to evaluate the phase α_1 of the imprinted modulation, combined with signal delay through part of the set-up.
7. Disable the LIA output and enable a small output voltage at $\omega_{\mathrm{m}}^{(l)}$ on the external signal generator.
8. Measure the phase α_2 of the imprinted modulation using LIA oscillator 8.
9. Shift the phase of the external signal source by $-(\alpha_2 - \alpha_1)$ to achieve phase coherence between the LIA-generated tone and the externally generated tone.
10. Shift the phase of the external signal source to generate the desired Peierls phase φ_{jk} or θ_{jk} in the rotating frame. We are now done, and move on to the next external tone.

As a final step, the phase coherence of the interaction tone originally assigned to oscillator 8 is restored by following the procedure above up to step 4.

3

Synthetic magnetism in multi-plaquette phononic networks

In this chapter, we experimentally demonstrate the breaking of time-reversal symmetry in nanomechanical networks through radiation pressure control fields. We study the influence of synthetic magnetic fluxes on thermomechanical spectra, localization, and chiral dynamics. In a nano-optomechanical cavity, time-modulated laser drives couple three mechanical modes in a loop, establishing a phononic circulator. Larger networks show canonical signatures of the quantum Hall effect for phonons, including unidirectional states at the edge of the network.

Part of this chapter is based on J. del Pino, J. J. Slim & E. Verhagen. Non-Hermitian chiral phononics through optomechanically induced squeezing. *Nature* **606,** 82–87 (2022) [151]. J.d.P. and J.J.S contributed equally to this work.

3.1. Introduction

The discovery of the integer quantum Hall effect (QHE, section 1.4) in a two-dimensional electron gas subject to a perpendicular magnetic field [65] spurred the exploration of various exotic phases of matter with unique properties. It is now understood that the QHE is a basic example of a topological phase of matter; with insulating bulk and conductance at the edges of the system in states that are topologically robust against disorder and imperfections [36]. These edge states are strikingly unidirectional ('chiral'), owing to the magnetic field that effectively breaks time-reversal-($\mathcal{T}$)-symmetry for the electrons in the material.

The emergence of chiral edge states in the QHE is essentially a wave phenomenon. While thus fundamentally possible, realizing it in the optical [38] or mechanical [37] domain requires the breaking of $\mathcal{T}$-symmetry for those degrees of freedom to induce the necessary nonreciprocity. In magneto-optic materials, the Faraday effect allows to build bulk optical nonreciprocal elements like isolators and circulators. Biasing using actual magnetic fields has also allowed the realization of quantum-Hall-like topological insulators, for microwave radiation using gyrotropic materials [78] and for exciton-polaritons that exhibit Zeeman splitting [79]. Furthermore, mechanical and acoustic systems can be biased by rotation, enabling the isolation of sound [60] and the observation of unidirectional edge states in a gyroscopic metamaterial of spinning elements [9].

A different paradigm to breaking $\mathcal{T}$-symmetry is the creation of synthetic magnetic fields through suitable forms of spatiotemporal modulation [43, 44]. As we explained in section 1.3, harmonic modulation can stimulate the frequency conversion of a signal, with the modulation phase acting as a magnetic vector potential on the induced hopping between modes. Thus, combining modulations with controlled phases between multiple modes, it is possible to exploit Aharonov-Bohm interference to realize nonreciprocal transmission, for example in photonic systems [46–52], at microwave frequencies in superconducting systems [31, 35, 53–55], for cold atoms in optical lattices [56, 58, 59] and mechanics [88]. Finally, in extended lattices, combining many Aharonov-Bohm loops in all unit cells — mimicking the effect of a homogeneous magnetic field piercing the lattice — enables bosonic quantum Hall phases [73–76].

Time-varying potentials for either light or sound can be provided in multimode cavity optomechanical systems [123]. Thus, laser drives that couple photonic and mechanical modes can be used to convert the frequency of excitations and imprint nonreciprocal transfer phases. In suitable multi-mode optomechanical systems, this leads to nonreciprocal effects such as a proposed phononic circulator [122] and demonstrations of mechanically-mediated nonreciprocal transmission of photons, both in the optical and microwave domains [32, 33, 125–128]. Balancing nonreciprocal coupling and dissipation allows ideal optical isolation [129, 130]. Importantly, optomechanical interactions can also induce nonreciprocal mechanical mode coupling [63, 64]. In optomechanical lattices, topological phases for sound and light similar to the QHE were proposed [64, 134, 135].

Here we use optomechanical control and frequency conversion to bring nonreciprocity and quantum Hall physics to the domain of nanomechanical resonators.

Nanomechanical resonators have interesting potential as sensors and transducers, in information processing, and to study quantum phenomena and thermodynamic processes [16, 21]. We exploit the fact that the optical spring effect of a modulated laser can induce mechanical coupling between modes at disparate frequencies and induces a controllable synthetic gauge potential [64]. We demonstrate experimentally how a synthetic magnetic flux in a three-mode mechanical loop ('plaquette') tunes the spectra of thermomechanical fluctuations and induces chiral dynamics, establishing a laser-controlled phononic circulator. Increasing the network size to incorporate up to four plaquettes, we witness the emergence of quantum Hall behavior, including chiral states at the network edge. Our fully reconfigurable platform allows also the study of inhomogeneous magnetic fields. Specifically, we show how combinations of alternating magnetic fields in adjacent plaquettes control spectra and localization due to interference in the network. This relates our work to studies of Aharonov-Bohm caging and related localization phenomena in lattices with controlled and inhomogeneous magnetic fields [169–177].

3.2. Synthetic flux in a ring of resonators

We start with the simplest demonstration of phononic chirality, by breaking $\mathcal{T}$ symmetry in a system of three coupled nanoresonators. We employ the sliced photonic crystal nanobeam [64] shown in Figure 2.1, which supports multiple non-degenerate MHz-frequency flexural mechanical modes coupled to the optical field of a nanocavity. Figure 3.1a shows these distinct mechanical resonances in the thermomechanical noise spectrum, read out as modulations of a detuned probe laser reflected from the cavity.

As discussed in section 2.6, interactions between modes (which we will also refer to as 'resonators' in the following) with well-separated frequencies Ω_j are established by temporal modulation of the intensity of a control laser detuned from cavity resonance. Specifically, modulating at the difference frequency $\Omega_j - \Omega_k$ of resonators j and k induces a beamsplitter coupling between the resonators at a rate $J \propto c_\mathrm{m}\bar{n}_\mathrm{c}$ given in (2.64), controlled by the modulation depth c_m and average cavity population $\bar{n}_\mathrm{c}$.

Three modulation tones are applied simultaneously (Figure 3.1b) to couple the $N = 3$ lowest-frequency resonators in a ring network (Figure 3.1c). Describing the resonators by their annihilation operators a_j in frames rotating at Ω_j, the Hamiltonian for this 'beamsplitter trimer' (BST) reads

$$H_\mathrm{BST} = \sum_{j,k=1,k\neq j}^{N=3} J_{jk} e^{-\mathrm{i}\varphi_{jk}} a_j^\dagger a_k, \qquad \varphi_{kj} = -\varphi_{jk}, \tag{3.1}$$

without intrinsic dissipation. This Hamiltonian preserves phonon number and importantly, it imprints the phase offset φ_{jk} of the modulation tones in a nonreciprocal fashion on phonons transferred along the loop — precisely like the Peierls phase imprinted by a magnetic vector potential [64]. The gauge-invariant geometric phase $\Phi = \varphi_{12} + \varphi_{23} + \varphi_{31}$ around the loop then represents a synthetic flux threading the resonator plaquette.

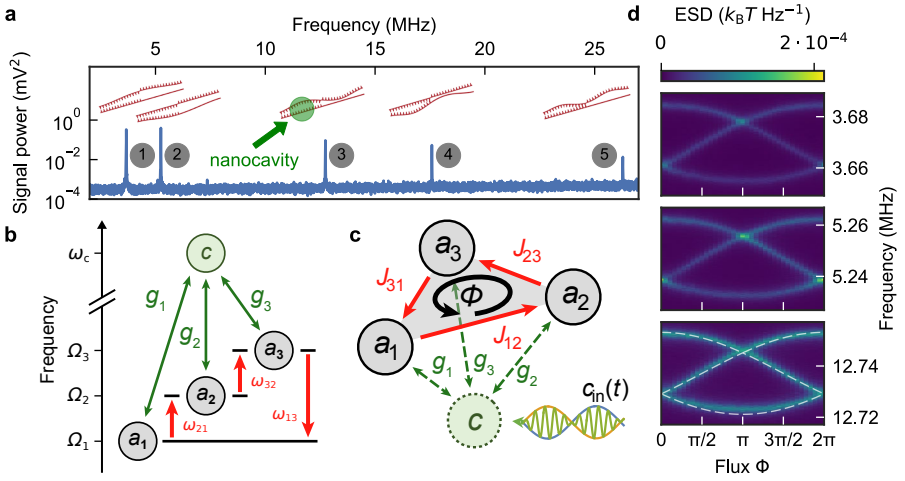

Figure 3.1: **Aharonov-Bohm interference in a nano-optomechanical network. (a)** Thermomechanical fluctuation spectrum of the sliced photonic crystal nanobeam, imprinted on a laser reflected from a nanocavity with linewidth $\kappa/(2\pi) = 320$ GHz. Resonances correspond to mechanical flexural modes at frequencies $\Omega_j/(2\pi) = \{3.7, 5.3, 12.8, 17.6, 26.2\}$ MHz with loss rates $\gamma_j/(2\pi) \approx 1 - 7$ kHz and estimated vacuum optomechanical coupling rates $g_0^{(j)}/(2\pi) = \{5.3, 5.9, 3.3, 3.1, 1.9\}$ MHz. **(b)** Mechanical modes a_j are coupled to the optical mode c (frequency $\omega_c = 195.6$ THz) with cavity-enhanced optomechanical coupling rates $g_j = g_0^{(j)}\sqrt{\bar{n}_c}$ (mean photon number $\bar{n}_c \approx 343$). Modulating the cavity field at the mechanical difference frequencies $\omega_{jk} = \Omega_j - \Omega_k$ between the three lowest-frequency resonators stimulates frequency conversions and couples the resonator pairs a_j, a_k. **(c)** In a frame rotating along with the mechanical resonators, the cavity mode is eliminated adiabatically. This leaves a loop of mechanical resonators coupled by effective time-independent beamsplitter interactions with rates $J_{jk}/(2\pi) = 8$ kHz and Peierls phases φ_{jk}. The loop is pierced by a synthetic flux $\Phi = \sum \varphi_{jk}$, where the condition $\omega_{21} + \omega_{32} + \omega_{13} = 0$ ensures that Φ is a gauge-invariant quantity. Couplings are achieved with modulation depths c_m between 0.32 and 0.42. **(d)** Measured thermomechanical noise spectra imprinted on the detection laser around each resonator's sideband versus flux. Hybridised Floquet modes tune with synthetic flux. Dashed lines represent theoretical eigenvalues given by (3.4). ESD, energy spectral density.

The hopping matrix $\mathcal{A}$ (introduced in section 2.6.3) that encodes the three beamsplitter interactions reads

$$\mathcal{A} = \begin{bmatrix} 0 & J_{12}e^{-i\varphi_{12}} & J_{31}e^{i\varphi_{31}} \\ J_{12}e^{i\varphi_{12}} & 0 & J_{23}e^{-i\varphi_{23}} \\ J_{31}e^{-i\varphi_{31}} & J_{23}e^{i\varphi_{23}} & 0 \end{bmatrix}. \tag{3.2}$$

Setting equal $J_{jk} = J$, the Hamiltonian (3.1) is translationally invariant in a gauge with equal Peierls phases $\varphi_{j,(j \bmod N)+1} = \Phi/3$, and therefore diagonal in the discrete momentum basis

$$\tilde{a}_k = \sum_{j=1}^{N} e^{-i2\pi kj/N} a_j/\sqrt{N} \quad \text{for momenta } k = \{-1, 0, 1\}. \tag{3.3}$$

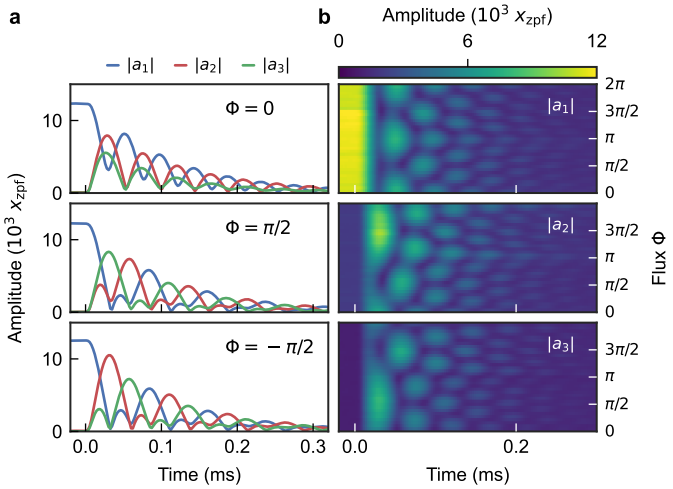

Figure 3.2: **Flux-induced circulation. (a)** Measured time evolution of resonator amplitudes $|\langle a_i \rangle| \equiv |a_i|$ for unbroken $\mathcal{T}$ symmetry ($\Phi = 0$) and broken ($\Phi = \pm\pi/2$). Resonator a_1 is coherently driven through resonantly modulated radiation pressure until $t = 0$ ms, when excitation is stopped and modulation tones implementing the couplings are established. For $\Phi = \pm\pi/2$, circulation of coherent vibrations is observed. **(b)** Measured time evolution of resonator amplitudes for varying flux, showing crossover from chiral to non-chiral transport through an intermediate regime with generally aperiodic dynamics, and reversal of chirality with flux sign ($\Phi \mapsto -\Phi$).

Equivalently, the hopping matrix (3.2) is circulant and diagonalized by Fourier modes. Through Aharonov-Bohm interference along the loop, the enclosed flux shifts the eigenfrequencies

$$\epsilon_k = 2J \cos\left(\frac{2\pi k + \Phi}{N}\right). \tag{3.4}$$

Figure 3.1d reveals these states in the thermomechanical spectrum, for each resonance splits into a (Floquet) triplet owing to strong coupling $J > \gamma_j$, with mechanical damping rates γ_j. This demonstration of nanomechanical flux-tuning is paralleled in spectra of quantum rings under magnetic fields [178].

The flux-tuning manifests Aharonov-Bohm interference over a given rotation – the mechanism ultimately responsible for chirality of quantum Hall edge states [38] and nonreciprocal dynamics [179]. Figure 3.2a shows the evolution of a mechanical excitation, initialised in resonator 1 through resonantly modulated radiation pressure. At time $t = 0$, its driving is switched off and the modulation implementing (3.1) is switched on. For $\Phi \in \{0, \pi\}$, the BST is time-reversal symmetric in an appropriate rotating frame and energy simultaneously hops to both other resonators. Any other flux breaks $\mathcal{T}$ and lifts the degeneracy between hybridized modes with opposite momentum and enables chiral energy transport. For $\Phi = \pi/2$ ($\Phi = -\pi/2$), vibrations circulate along the loop in a clockwise (counter-clockwise) fashion, with each full exchange taking time $\tau_{ex} = 2\pi/(3J\sqrt{3})$. Figure 3.2b illustrates the evolution for varying flux, where a crossover from chiral to non-chiral transport is observed

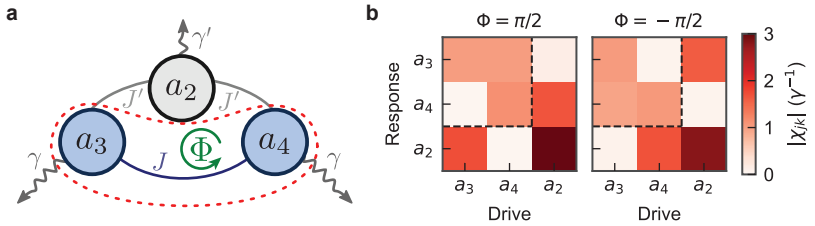

Figure 3.3: **An optomechanical phonon circulator/isolator. (a)** By setting unity cooperativity $\mathcal{C}_{jk} = 4J_{jk}/(\gamma_j\gamma_k) = 1$ along each link, the nanomechanical three-mode loop operates as a circulator for phonons. The directionality of the circulator is controlled by the flux $\Phi = \pm\pi/2$. Circulation is independent of the hierarchy of loss rates: modes a_3 and a_4 are optothermally tuned to equal linewidth $\gamma = \gamma_3 \approx \gamma_4 \approx 3.7 \times 2\pi$ kHz, while mode a_2 has lower loss rate $\gamma' = \gamma_2 = 1.3 \times 2\pi$ kHz. When disregarding the auxiliary mode a_2, the loop operates as an isolator for phonon transport between a_3 and a_4. **(b)** Susceptibility $|\chi_{jk}|$ of the measured circulator response to continuous wave driving at zero detuning. For $\Phi = \pi/2$, scattering $|\gamma\chi_{34}| \approx 1$ from a_4 to a_3 is approximately unity while the scattering $|\gamma\chi_{43}| \approx 0$ in the other direction is blocked. Isolation is reversed for $\Phi = -\pi/2$.

through an intermediate regime with generally aperiodic dynamics [180].

3.2.1. Phonon circulator/isolator

By interfacing the resonators with mechanical waveguides, the BST can be functionalized to route mechanical signals. While our device currently lacks such mechanical circuitry, in Figure 3.3a we illustrate how to operate the BST constituted by a_2, a_3 and a_4 as a proof-of-concept phonon circulator. Continuous wave driving of resonator a_k with resonantly modulated radiation pressure acts as an input, while the dissipations γ_j of each resonator to the environment constitute output channels. The trimer's amplitude response to the drive then serves as a proxy for the energy scattered through the network. Finally, by restricting our attention to the transfer between two modes (e.g. a_3 and a_4) while disregarding the energy dissipated in the last mode (e.g. a_2), the BST can be operated as a phonon isolator.

Akin to the reconfigurable superconducting microwave circuit circulator in [31], the directionality of the circulator/isolator is controlled by a $\mathcal{T}$-breaking flux $\Phi = \pm\pi/2$. The mechanical susceptibility matrix $\chi(\Delta_\mathrm{m})$ links the vector of response amplitudes $\mathbf{a} = (a_3, a_4, a_2)^T = \chi(\Delta_\mathrm{m})\mathbf{f}$ to the drive vector $\mathbf{f} = (f_3, f_4, f_2)$ (section 2.7.4) and is related to the hopping matrix $\mathcal{A}$ by

$$\chi = \mathrm{i}\left(\Delta_\mathrm{m}\mathbb{1} - \mathcal{A} + \mathrm{i}\Gamma'/2\right)^{-1}, \tag{3.5}$$

where Δ_m is the detuning of the drives and $\Gamma' = \mathrm{diag}\,(\gamma_3, \gamma_4, \gamma_2)$ the loss matrix.

Focusing first on operating the BST to isolate resonant signals ($\Delta_\mathrm{m} = 0$) between a_3 and a_4, the relevant susceptibilities for the ideal fluxes $\Phi = \pm\pi/2$ read

$$\chi_{a_3\leftarrow a_4} = (J_{23}J_{42} \pm \gamma_2 J_{34})\det(\chi), \quad \chi_{a_4\leftarrow a_3} = (J_{23}J_{42} \mp \gamma_2 J_{34})\det(\chi), \tag{3.6}$$

where $\det(\chi) = 8(\gamma_2\gamma_3\gamma_4 + 4\gamma_4 J_{23}^2 + 4\gamma_2 J_{34}^2 + 4\gamma_3 J_{42}^2)^{-1}$. Perfect isolation — with directionality controlled by the sign of Φ — is obtained when $J_{23}J_{42} = \gamma_2 J_{34}$,

which can be satisfied for any hierarchy of the loss rates γ_j. The loss rates however, in their capacity as output channel coupling rates, do control the bandwidth of the isolator [31].

Furthermore, perfect *circulation* between a_3, a_4 and the auxiliary resonator a_2 is obtained by setting $J_{jk} = \sqrt{\gamma_j \gamma_k}/2$. In this situation, the mechanical cooperativity

$$\mathcal{C}_{jk} = \frac{4J_{jk}^2}{\gamma_j \gamma_k} \tag{3.7}$$

for each link $\mathcal{C}_{jk} = 1$ is unity. The full susceptibility matrices $\chi_{\Phi=\pi/2}$ and $\chi_{\Phi=-\pi/2}$ are related by transposition and for $\mathcal{C}_{jk} = 1$ given by

$$\chi_{\Phi=\pi/2} = \chi_{\Phi=-\pi/2}^T = \begin{bmatrix} \gamma_3^{-1} & \sqrt{\gamma_3\gamma_4}^{-1} & 0 \\ 0 & \gamma_4^{-1} & \sqrt{\gamma_2\gamma_4}^{-1} \\ \sqrt{\gamma_2\gamma_3}^{-1} & 0 & \gamma_2^{-1} \end{bmatrix}. \tag{3.8}$$

Figure 3.3b demonstrates flux-tunable isolation and circulation in the experimental susceptibility matrices $\chi_{\Phi=\pi/2}$ and $\chi_{\Phi=-\pi/2}$, constructed from the responses of the BST to additional drive modulations resonant with each resonator a_j. We have chosen to fine-tune the strength of optothermal dynamical backaction (section 2.8.4) on a_3 and a_4 so that their linewidths $\gamma_3 \approx \gamma_4 = \gamma = 3.7 \times 2\pi$ kHz are matched. The backward transmission (a_4 to a_3) for $\Phi = \pi/2$ is then equal to the forward transmission (a_3 to a_4) for $\Phi = -\pi/2$.

3.3. Two interfering Aharonov-Bohm loops

While the flux tunes the eigenfrequencies (3.4) of a single Aharonov-Bohm loop with equal couplings, its eigenstates (3.3) are unaffected and evenly distributed over all resonators for any Φ. However, in networks featuring *multiple* AB loops, interference between adjacent plaquettes does affect the localization of eigenstates, ultimately leading to e.g. Aharonov-Bohm caging [169, 174, 181] and topological edge states [38] for extended lattices. We therefore explore and demonstrate multi-plaquette interference in small nanomechanical systems.

We start with the simplest multi-plaquette extension of the BST: the four-mode diamond-shaped network shown in Figure 3.4a. The diamond features two Aharonov-Bohm loops a_1 - a_3 - a_4 ('left') and a_2 - a_3 - a_4 ('right'), fused together along the central link a_3 - a_4 and pierced by independent fluxes. The relative handedness of the fluxes now crucially determines the diamond's spectrum and the localization of its eigenstates.

When the two plaquette fluxes $\Phi, -\Phi$ are handed oppositely (Figure 3.4, top), the net flux through the larger plaquette defined by the diamond's perimeter is zero. With equal couplings J along the perimeter, this guarantees the existence of an antisymmetric mode $\tilde{a}_{\text{apex}} = (a_1 - a_2)/\sqrt{2}$ localized solely on the apex resonators a_1 and a_2. Carrying no weight in the central resonators, the frequency of $\tilde{a}_{\text{apex}}$ is insensitive to the coupling J_c along the central link. Moreover, with no net flux, the Peierls phases φ_{jk} along the perimeter can always be gauged away: the fluxes are then fully sustained by the central link. This implies that the frequency of $\tilde{a}_{\text{apex}}$ is

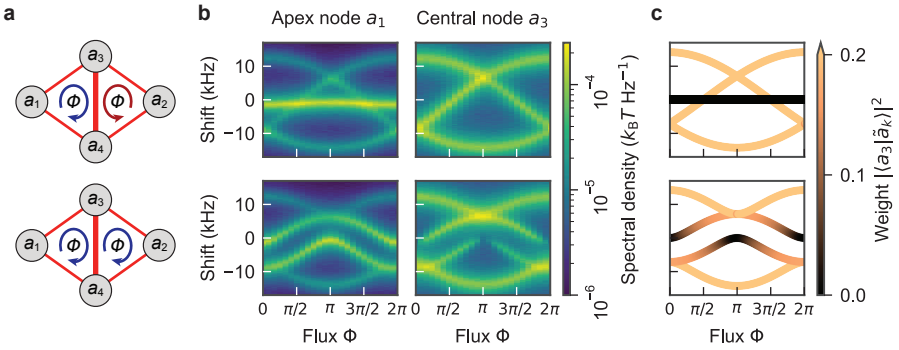

Figure 3.4: **Interference between two adjacent plaquettes in a diamond configuration. (a)** Four resonators a_j are coupled in a diamond configuration featuring two adjacent plaquettes. The plaquettes are pierced by fluxes Φ, $-\Phi$ of opposite handedness (top) or by fluxes Φ of equal handedness (bottom). The resonators are coupled along the perimeter with rate $J/(2\pi) = 5$ kHz, while the central link has rate $J_c = J\sqrt{2}$. **(b)** Thermomechanical sideband spectrum of the apex resonator a_1 (left) and the central resonator a_3 (right) for varying flux Φ. The other central and apex resonator feature similar spectra. The diamond with opposed fluxes (top) hosts flux-independent eigenmodes $\tilde{a}_k$. A single antisymmetric eigenmode $\tilde{a}_{\text{apex}}$ is localized in the apex resonators and does not tune with Φ. The other three eigenmodes are delocalized over all resonators and tune exactly like those of a single three-mode plaquette with couplings $J_c = J\sqrt{2}$ (cf. Figure 3.1d). The diamond with equal-handed fluxes (bottom) hosts eigenmodes that tune with flux both in frequency and localization. The central link induces couplings between opposite momentum eigenstates of the perimeter. As the flux 2Φ piercing the perimeter tunes opposite momentum eigenstates into resonance for $\Phi = 0, \pi$, their symmetric and antisymmetric superpositions fully localize either on the apex or the central resonators. **(c)** Weight of central resonator a_3 in each of the hybridized eigenmodes $\tilde{a}_k$ of the diamond.

insensitive to flux as well. In the thermomechanical spectra shown in Figure 3.4b, top, $\tilde{a}_{\text{apex}}$ is observed as a flat band around zero detuning that is exclusive to the sideband of the apex resonators.

The remaining three eigenmodes are sensitive to J_c and Φ, generally both in frequency and localization. However, in the special case $J_c = J\sqrt{2}$, all eigenstates are again independent of flux in the gauge where all links (including the central link) carry equal Peierls phase $\varphi_{jk} = \Phi/3$. The eigenstates are then given by $\tilde{a}_{\text{apex}}$ and

$$\tilde{a}_k = \left(a_1 + \sqrt{2}\left(e^{-\mathrm{i}2\pi k/3}a_3 + e^{\mathrm{i}2\pi k/3}a_4\right) + a_2\right)/\sqrt{6} \qquad \text{for } k = \{-1, 0, 1\}. \tag{3.9}$$

Interestingly, the $\tilde{a}_k$ retain the character of the phase-chiral momentum states of the two fused BSTs that make up the diamond. As the fluxes align along the central link, $\tilde{a}_k$ is a combination of the (non-orthogonal) left and right plaquette states with momentum k as given by (3.3). Moreover, their frequencies tune exactly as the BST eigenfrequencies (3.4) with $J \mapsto J_c = J\sqrt{2}$, as demonstrated in the thermomechanical spectra in Figure 3.4b, top.

On the other hand, when the two plaquettes are threaded by fluxes Φ of equal handedness, multi-loop interference ensures that all eigenstates have

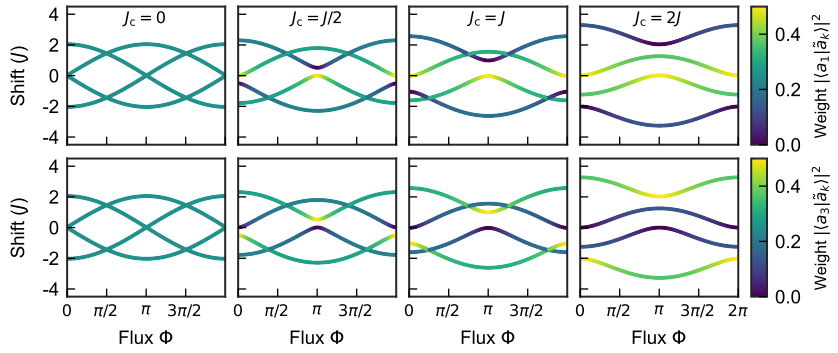

Figure 3.5: **Momentum state interactions in the equal-handed diamond.** Eigenfrequency spectra of a diamond network pierced by fluxes Φ of equal handedness (Figure 3.4a, bottom) for increasing central link strength J_c. Colours indicate the weight of the apex (top row) or central (bottom row) resonators in each eigenmode. Turning on $J_c > 0$ couples perimeter states of opposite momenta, opening a spectral gap as they are tuned on resonance for $\Phi = 0, \pi$. The resulting symmetric and antisymmetric superpositions fully localize either in the apex or central resonators.

flux-dependent weights. In this case, the perimeter is pierced by a net flux of 2Φ. We take this as a suggestion to express the diamond's Hamiltonian in the basis of momentum states b_k of the perimeter for momenta $k = \{-1, 0, 1, 2\}$. These are given by (3.3) when summing over the $N = 4$ resonators a_j in the order of their position in the loop ($a_1 \to a_3 \to a_2 \to a_4$). In the basis $\{b_0, b_2, b_1, b_{-1}\}$, the equal-handed diamond's hopping matrix is block-diagonal and reads

$$\mathcal{A}'_{\circlearrowleft\circlearrowleft} = \begin{bmatrix} \epsilon_0 + J_c/2 & -J_c/2 & 0 & 0 \\ -J_c/2 & \epsilon_2 + J_c/2 & 0 & 0 \\ 0 & 0 & \epsilon_1 - J_c/2 & J_c/2 \\ 0 & 0 & J_c/2 & \epsilon_{-1} - J_c/2 \end{bmatrix}, \tag{3.10}$$

where the ϵ_k are the eigenfrequencies of an $N = 4$ mode Aharonov-Bohm loop pierced by flux 2Φ, given in (3.4) for $\Phi \mapsto 2\Phi$.

Apart from shifting the frequencies of the b_k, the central coupling J_c is seen to couple perimeter states of opposite momentum $b_1 \leftrightarrow b_{-1}$, $b_0 \leftrightarrow b_2$ with rate $J_c/2$. As shown in Figure 3.5, this opens a spectral gap when the pair $b_1 \leftrightarrow b_{-1}$ ($b_0 \leftrightarrow b_2$) is degenerate for the non-$\mathcal{T}$-breaking flux $\Phi = 0$ ($\Phi = \pi$). Precisely at these avoided crossings, (anti)symmetric superpositions are formed in which the coupled opposite momentum states interfere to fully localize either in the apex or central resonators. Any other flux breaks the degeneracy of opposite momentum states and counters the localization. In Figure 3.4b, bottom right, flux-tunable localization is experimentally observed as a disappearance of thermomechanical sidebands. Note that for the particular ratio $J_c/J = \sqrt{2}$ used in the experiment, the expected disappearance of the upper and lower apex sideband of the apex resonator (Figure 3.4b, bottom left) for $\Phi = \pi$ and $\Phi = 0$, respectively, happens to be masked by a degeneracy.

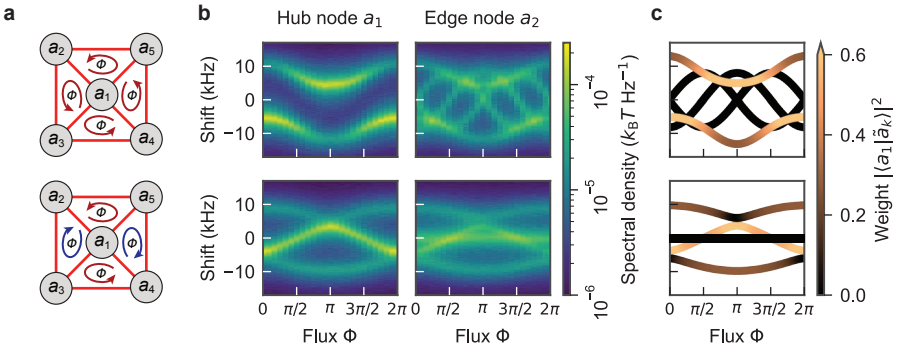

Figure 3.6: **Multi-plaquette interference in a wheel graph. (a)** Hub resonator a_1 is coupled to four edge resonators a_j in a wheel graph configuration with equal rates $J = J_s$. The wheel features four plaquettes pierced by fluxes Φ of equal handedness (top, $J/(2\pi) = 4$ kHz) or by alternating fluxes Φ, $-\Phi$ of opposite handedness (bottom, $J/(2\pi) = 3$ kHz). **(b)** Thermomechanical sideband spectrum of the hub resonator a_1 (left) and the edge resonator a_2 (right) for varying flux Φ. With equal-handed fluxes, the wheel hosts two modes that are delocalized over all resonators and three phase-chiral modes that are localized on the edge of the wheel. With opposing fluxes, the spectrum of the wheel is similar to the spectrum of the opposed-flux diamond (Figure 3.4b, top). Two degenerate, flux-insensitive eigenmodes $(a_2 - a_4)/\sqrt{2}$ and $(a_3 - a_5)/\sqrt{2}$ are formed by the antisymmetric superposition of opposite edge resonators and carry no weight in the hub. The remaining three modes delocalize over all resonators. **(c)** Weight of hub resonator a_1 in each of the hybridized eigenmodes $\tilde{a}_k$ of the wheel.

3.4. Emergence of edge states

Up until now, we have only observed localized eigenstates that are either completely insensitive to flux (in the oppositely-handed diamond), or for which the flux actually breaks the localization (in the equally-handed diamond). However, localized edge states are known to exist in extended lattices subject to magnetic gauge fields. In fact, with $\mathcal{T}$-breaking fluxes piercing the lattice, the presence of these edge states is even *topologically protected* [38]. In addition, breaking $\mathcal{T}$ lends the edge states a chiral character and allows them to contribute to topologically protected, unidirectional transport.

Motivated by this promise, we construct the small lattice shown in Figure 3.6a. Known as the five-mode wheel graph W_5, the network comprises four resonators a_j coupled in a ring (rates J), with additional spokes coupling the ring to the central hub resonator a_1 (rates J_s). We identify the network's perimeter as its 'edge', while we identify the network's hub as its 'bulk' (albeit a very small one).

First, we briefly consider the wheel network when fluxes through adjacent plaquettes are handed oppositely (Figure 3.6a, bottom). The dynamics of this system are very close to those of the oppositely-handed diamond, as once more the net flux through the perimeter is zero. In this case we find two flux-insensitive states: the antisymmetric superpositions $(a_2 - a_4)/\sqrt{2}$ and $(a_3 - a_5)/\sqrt{2}$, similar to the apex state $\tilde{a}_{\text{apex}}$ of the diamond. As shown in the thermomechanical spectra in Figure 3.6b, bottom, the three remaining states tune for the case with equal rates $J_s = J$ like those of a BST with unequal couplings $J\sqrt{2}$, $J\sqrt{2}$ and J. For the

special coupling ratio $J_s/J = \sqrt{2}$, we would find the remaining states to be flux-independent, delocalized over all resonators and tuning like those of a BST with equal couplings $J\sqrt{2}$, exactly like the diamond spectrum in Figure 3.4b, top.

However, with equally handed fluxes Φ piercing the network's four plaquettes (Figure 3.6a, top), distinct states are observed in its thermomechanical spectrum (Figure 3.6b, top) that live only on the edge. Moreover, these edge states tune with flux, revealing their chirality. Again, this motivates us to write the network's Hamiltonian using the momentum states b_k of the perimeter. In the perimeter momentum basis $\{a_1, b_0, b_1, b_2, b_{-1}\}$ supplemented by the bulk resonator state a_1, it reads

$$H_{W_5,\circlearrowleft} = J_s \left(a_1^\dagger b_0 + b_0^\dagger a_1 \right) + \sum_{k=-1}^{2} \epsilon_k b_k^\dagger b_k \tag{3.11}$$

where $\epsilon_k = J\cos(\Phi + k\pi/2)$ is the frequency given by (3.4) for the momentum-k state of a four-mode Aharonov-Bohm loop pierced by the net flux 4Φ. Here, we have chosen a gauge where the spokes carry no Peierls phase, so that the phase along each perimeter link $\varphi_{jk} = \Phi$.

The spoke coupling J_s hybridizes the zero-frequency hub state a_1 and the zero-momentum perimeter state b_0, while leaving the other perimeter states be. Increasing $J_s > 0$ opens a spectral gap and pushes away these eigenstates from zero frequency, as shown in the thermomechanical spectra in Figure 3.6b for $J_s = J$. For flux $\Phi = \pm\pi/2$, we are at zero detuning then only left with the chiral perimeter state $b_{\pm 1}$.

Next, for these $\mathcal{T}$-breaking fluxes $\Phi = \pm\pi/2$, we probe the transport of a continuous wave excitation through the wheel (Figure 3.7). When the hub resonator a_1 is driven for $\Phi = \pm\pi/2$ (Figure 3.7a, left), the edge state at zero drive detuning $\Delta_\mathrm{m} = 0$ cannot be excited. Driving the edge resonator a_2 does allow excitation of the edge state (Figure 3.7a, middle and right) and results in a peaked response around $\Delta_\mathrm{m} = 0$ for all edge resonators, while the bulk response remains flat.

Interestingly, from the relative heights of the zero-detuning peaks we see chiral transport along the edge emerge (Figure 3.7b). As the coherent transfer of energy through the network competes with dissipation, we observe the energy fed into a_2 propagating along the edge either in the clockwise or counter-clockwise direction, depending on the flux $\Phi = \pm\pi/2$. In fact, the interaction between bulk and edge is crucial for this process. Contrary to the three-mode circulator discussed before, it can be shown that the energy susceptibility matrix $|\chi_{\mathrm{AB4}}|^2$ of a four-mode Aharonov-Bohm loop is always symmetric, regardless of Φ (assuming equal couplings and decay rates). The edge alone, constituting such a loop, can therefore not sustain any chiral propagation of energy.

3.5. Conclusion and outlook

In conclusion, we studied the effects of breaking time-reversal symmetry in nanomechanical networks that are induced and controlled through time-modulated radiation pressure in a photonic crystal nanocavity. The various flexural mechanical

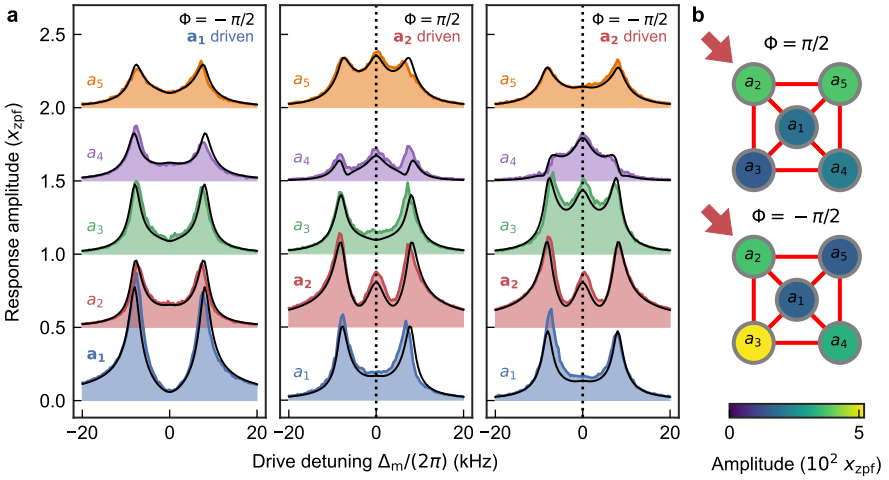

Figure 3.7: **Transport along the edge of a wheel graph. (a)** Amplitude response of the five-mode wheel network with aligned fluxes $\Phi = \pm\pi/2$ (Figure 3.6a, top) to continuous wave driving of the central resonator a_1 (left) and edge resonator a_2 (middle and right). Coupling rates $J/(2\pi) = J_s/(2\pi) = 4$ kHz. Driving the edge resonator a_2 excites the edge mode at zero detuning, while driving the hub resonator a_1 does not. Measured amplitudes are in good agreement with the response predicted by (3.5) (black lines), with all necessary parameters (coupling J, dissipation γ_j and driving strength f_j) determined independently. **(b)** Amplitude response at each site of the network when resonantly driving a_2 ($\Delta_m = 0$, indicated by dotted lines in a). Clockwise (counter-clockwise) chiral transport along the edge is observed for $\Phi = \pi/2$ ($\Phi = -\pi/2$) as vibration transfer competes with decay. Differences in clockwise and counter-clockwise transport are explained by disorder in the dissipation rates $\gamma_j/(2\pi) \approx \{1.2, 2.5, 2.7, 4.4, 6.9\}$ kHz.

modes of the system serve as a synthetic dimension, with optomechanical modulation coupling the different energy levels to form networks. The drive phases allow imprinting the Aharonov-Bohm effect for phonons traveling in a three-mode loop, leading to chiral dynamics and mechanical frequencies tuned by synthetic magnetic flux. In larger networks, we witness interference of multiple Aharov-Bohm loops and the chiral edge states that result, demonstrating the quantum Hall effect in a minimal nanomechanical network.

While the experiments were conducted in the classical domain, the observed effects should persist for arbitrarily small signals and fluctuations. Moving the demonstrated phenomena towards the quantum domain would warrant the development of these principles in sideband-resolved cavities, to avoid added fluctuations associated with quantum backaction of the control fields, and associated revised temporal driving schemes.

The high degree of active control over the system and its dynamics presents many opportunities for future studies. These include the study of localization and flat bands due to inhomogeneous fluxes and specific network topologies [169–177], the possibility to derive bulk topological properties from careful studies of unit cell spectra [182], the effects of rapidly varying magnetic fields on the long-lived mechanical excitations that these systems host, the dynamics of the systems if the

coupled resonators are self-oscillating through dynamical backaction amplification [30, 136, 183], and the effect of mechanical or optomechanical nonlinearities on the topological states of the network.

4

Chiral thermal flows in a flux-biased nano-optomechanical system

Nanomechanical systems offer a rich playground for studying nonequilibrium thermodynamics at the nanoscale, due to their low frequencies, unavoidable contact with thermal environments, and active control of system parameters. When suitably orchestrated via optomechanical interactions, multimode nanomechanical loops exhibit synthetic magnetism and host chiral phononic modes. In this chapter, we experimentally study the dynamics of thermal fluctuations in a minimal nanomechanical loop permeated by a synthetic magnetic flux, contacted by dissipative baths with inhomogeneous thermal occupancy. By correlating the thermal motion of different resonators, we directly observe circulating fluctuations and chiral eigenstates, and image the microscopic thermal currents in the loop. We find that the flow of heat is tuned by the flux, redistributing energy in the thermal steady-state. Finally, we illustrate how broken time-reversal symmetry assists the refrigeration of a hot mode in the strongly coupled regime.

4.1. Introduction

Microscopic thermodynamics — the study of fluctuations in low-dimensional, well-controlled open systems — is a vibrant field of research, both in the form of quantum thermodynamics [184, 185] and, in the classical setting, of stochastic thermodynamics [23, 24]. Recent experimental advances in the latter include autonomous heat engines [186] and fundamental tests of out-of-equilibrium fluctuations [187], while much theoretical attention goes to the conversion of heat to work at the nanoscale [188].

In this context, the ability to measure and manipulate heat flows between interacting microscopic constituents is a valuable tool. In the relatively artificial setting of a trapped ion chain, a method was proposed to image heat currents [189] to elucidate the onset of Fourier's law of heat conduction [190]. Very recently, multimode cavity nano-optomechanical systems [118] have attracted interest in this pursuit, due to their high controllability, low frequencies, and natural contact with solid-state thermal environments. Tunable, cavity-mediated transport of thermal phonons and photons has been proposed and realized in a variety of settings [63, 191–197], in addition to the imaging of heat flows from optically detected classical mechanical correlations [196]. Moreover, the optical driving allows breaking time-reversal symmetry, enabling nonreciprocal vibration transport [63] and the generation of synthetic magnetism for phonons [64, 151], analogous to e.g. magnetic fluxes induced in photonic [45] and chiral quantum fluctuations in superconducting microwave circuits [179].

In general, the combination of heat transport and (synthetic) magnetism has inspired a flurry of scientific activity. Flux-dependent temperature variations have been observed in a Josephson interferometer [198] biased by a real magnetic field. In addition, persistent directional (circulating) heat currents *in the absence of a thermal gradient*, i.e. in equilibrium, have been predicted in photonic [199] and phononic [200] lattices, as well as unidirectional heat currents along the edge of a bosonic topological insulator [201] and an optomechanical thermal diode [202]. So far, these chiral heat flows have not been observed in experiment. Meanwhile, an ongoing theoretical debate in stochastic thermodynamics questions whether breaking time-reversal symmetry can improve the efficiency of heat engines at finite power [203–206]. Conversely, it would be interesting to study the effect of breaking time-reversal symmetry on refrigeration.

Here we combine cavity-mediated phonon transport and broken time-reversal symmetry to realize chiral thermal fluctuations and flows in a nanomechanical system. We first demonstrate our ability to image microscopic cavity-mediated heat flows in a dimer of detuned resonators [196]. With both resonators coupled to bosonic baths of different occupation, we show the dimer operating as an optically driven tunable heat pump, transferring thermal energy from the low-frequency to the high-frequency resonator. We then construct a loop of three nanomechanical resonators threaded by a synthetic magnetic flux [64, 151] and observe that the flux induces circulating thermal fluctuations. Moreover, due to our unique phase-resolved driving and detection scheme, we elucidate the chiral character of the loop's thermally driven mechanical eigenstates.

Finally, we focus on heat flows and the interplay between synthetic magnetism and gradients of thermal bath occupations. We show that the directionality of heat flows can be tuned by flux, similar to the predicted tuning of persistent (heat) currents in TRS-broken phononic [200] and photonic [199] systems. Interestingly, we find that breaking TRS allows stronger refrigeration of a hot mode in the strong coupling regime, by preventing the formation of a dark (uncoupled) hybridized mode [207] — a problem commonly encountered in simultaneous sideband cooling of multiple mechanical resonators [208, 209]. Our experimental platform thus highlights a route towards improved performance of low-dimensional refrigerators and provides a unique testbed to study nonreciprocal thermodynamics and fluctuations at the nanoscale.

4.2. Correlations in thermally driven systems

We start this chapter with a brief review of the theory of thermally driven classical systems. As an example, we take a single high-Q mechanical resonator with frequency Ω, subject to viscous damping with rate $\gamma = \Omega/Q$ and force $F(t)$. We write down the Langevin equation for its complex amplitude a,

$$\dot{a} = -(\mathrm{i}\Omega + \gamma/2)\, a + \xi(t). \tag{4.1}$$

In line with section 2.3.2, we express a in units of x_{zpf} and apply the rotating wave approximation to write the evolution of the resonator as a first-order differential equation (DE) for a, rather than a second-order DE for the displacement x. The drive term $\xi(t) = -2\mathrm{i}/(m\Omega x_{\mathrm{zpf}})F(t)$ represents the force $F(t)$, with m the mass of the resonator.

The resonator experiences random interactions with the near-infinite number of degrees of freedom in the environment, commonly referred to as its *thermal bath*. These collisions generate a stochastic thermal force $F(t)$ with zero average $\langle F(t)\rangle = 0$. As the degrees of freedom in the environment continuously exchange energy, the bath quickly 'forgets' about any interaction it had with the system. Therefore, we make the common assumption that the bath is Markovian (memoryless) such that $F(t)$ shows no correlations in time [142].

A second consequence of the interaction with the thermal environment is the damping term proportional to γ. The connection between damping and thermal forces is captured in the fluctuation-dissipation theorem [142]. In the classical, high-temperature limit ($k_{\mathrm{B}}T \gg \hbar\Omega$), it states that $F(t)$ satisfies the correlator

$$\langle F(t)F(t-t')\rangle = 2\gamma m k_{\mathrm{B}} T \delta(t-t'), \tag{4.2}$$

where T is the temperature of the environment. Alternatively, following the Wiener-Khinchin theorem, the spectral density $S_{FF}(\omega) = 2\gamma m k_{\mathrm{B}}T \equiv S_{FF}$ of the thermal Langevin force is frequency-independent. The resulting flat frequency spectrum is commonly referred to as a *white noise spectrum* and $F(t)$ as a white noise process.

Because we express the complex amplitude a in units of x_{zpf}, the driving term satisfies the particularly succinct correlator

$$\langle \xi(t)\xi^*(t-t')\rangle = \bar{n}_{\mathrm{th}}\gamma\delta(t-t'), \tag{4.3}$$

where $\bar{n}_{\text{th}} = k_{\text{B}}T/(\hbar\Omega)$ denotes the occupation of the thermal (phonon) bath.

4.2.1. Onsager regression principle

Although the thermal force shows no correlations in time, the inertia of the resonator does generate correlations in the amplitude $a(t)$. For the classical nanomechanical systems under study in this chapter, those correlations are governed by the Onsager regression principle [210]: "*the average regression of fluctuations will obey the same laws as the corresponding macroscopic irreversible processes*".

Applied to the resonator in (4.1), the Onsager regression principle simply states that for positive time lag $\tau > 0$, the regression of the correlator $R_{aa}(\tau) = \langle a(\tau + t)a^*(t)\rangle$ evolves in the thermal steady-state (i.e. independent of t) as

$$\frac{\mathrm{d}R_{aa}(\tau)}{\mathrm{d}\tau} = -\left(\mathrm{i}\Omega + \gamma/2\right) R_{aa}(\tau), \tag{4.4}$$

just like $\langle a(t)\rangle$ would. To complete this description, we note that

$$R_{aa}(0) = \langle a(t)a^*(t)\rangle = \langle n(t)\rangle = \bar{n}_{\text{th}}. \tag{4.5}$$

where the occupation $n(t) = |a(t)|^2$ expresses the energy in the resonator as the number of phonons of energy $\hbar\Omega$.

4.2.2. The quantum regression theorem

For systems with linear equations of motion (i.e. those governed by a quadratic Hamiltonian), a quantum version of the Onsager regression principle is known as the *quantum regression theorem*, often used in quantum optics [211]. In the classical limit, where we replace operators by their expectation values $\hat{a} \mapsto \langle\hat{a}\rangle = a$, both approaches yield the same result. However, as we regularly adopt quantum formalism to describe the systems in this thesis, in line with conventions in the field, we invoke a quantum approach in this section as well.

In particular, we follow the approach in section 15.5 of Meystre & Sargent [212]. We group the field operators a_j, $a_j^\dagger$ describing a system of N interacting modes in the Nambu-like vector

$$\boldsymbol{\alpha} = (a_1, \ldots, a_N, a_1^\dagger, \ldots, a_N^\dagger)^T. \tag{4.6}$$

The equation of motion of $\boldsymbol{\alpha}$, derived in section 2.7.1, is extended into the Heisenberg-Langevin equation

$$\dot{\boldsymbol{\alpha}}(t) = -\mathrm{i}\mathcal{H}\boldsymbol{\alpha}(t) - \frac{\Gamma}{2}\boldsymbol{\alpha} + \boldsymbol{\xi}(t) = -\mathrm{i}\mathcal{M}\boldsymbol{\alpha}(t) + \boldsymbol{\xi}(t), \tag{4.7}$$

by adding a damping term with matrix $\Gamma = \mathrm{diag}\,(\gamma_1, \cdots, \gamma_N, \gamma_1, \cdots, \gamma_N)$ and a zero-mean stochastic vector $\boldsymbol{\xi}(t)$ that represents the noise operating on our system. Here we denote $\mathcal{M}$ for the open-system dynamical matrix given by $\mathcal{M} = \mathcal{H} - \mathrm{i}\Gamma/2$, while $\mathcal{H}$ represents the closed-system Bogoliubov-de Gennes dynamical matrix given in (2.68).

The central quantity is now the correlator matrix

$$A(t,t') \equiv \left\langle \boldsymbol{\alpha}\left(t\right)\boldsymbol{\alpha}^{T}\left(t'\right)\right\rangle . \tag{4.8}$$

The quantum regression theorem dictates the evolution of the correlator matrix in the steady state

$$\frac{\mathrm{d}A(t+\tau,t)}{\tau} = \frac{\mathrm{d}}{\mathrm{d}\tau}\left\langle \boldsymbol{\alpha}(t+\tau)\boldsymbol{\alpha}^{T}(t)\right\rangle = -\mathrm{i}\mathcal{M}\left\langle \boldsymbol{\alpha}(t+\tau)\boldsymbol{\alpha}^{T}(t)\right\rangle = -\mathrm{i}\mathcal{M}A(t+\tau,t), \tag{4.9}$$

which admits the formal solution

$$A(t+\tau,t) = \exp\left(-i\mathcal{M}t\right)A(t,t), \tag{4.10}$$

again just like the evolution of $\langle\boldsymbol{\alpha}(t)\rangle$.

For a linear system of N interacting modes, determining the one-time correlator $A(t) \equiv A(t,t)$ is slightly more complicated than for the single mode in (4.5). As detailed in [212], a generalized Einstein relation can be employed to connect the "drift" described by $\mathcal{M}$ to the "diffusion" caused by $\boldsymbol{\xi}(t)$. The evolution of the one-time correlator then reads

$$\dot{A}(t) = -\mathrm{i}\left(\mathcal{M}A(t) + A(t)\mathcal{M}^{T}\right) + \mathcal{D}, \tag{4.11}$$

with the elements of the diffusion matrix $\mathcal{D}$ encoding the white noise correlators

$$\langle\xi_j(t)\xi_k(t')\rangle = \mathcal{D}_{jk}\delta(t-t'). \tag{4.12}$$

Finally, the steady-state ($\dot{A}(t)=0$) correlator $A \equiv A(0)$ satisfies

$$\mathcal{M}A + A\mathcal{M}^{T} = -\mathrm{i}\mathcal{D}. \tag{4.13}$$

4.2.3. Hermitian closed-system dynamics

In the absence of squeezing interactions, only particular elements of the correlator matrix (4.8) are important, as we will see in this section. We start by grouping the mode annihilation operators in the vector

$$\mathbf{a} = \left(a_1, \cdots, a_N\right)^{T}. \tag{4.14}$$

Using this mode vector, we reconstruct the correlator matrix

$$A\left(t,t'\right) = \left\langle \begin{bmatrix} \mathbf{a}(t)\mathbf{a}^{T}(t') & \mathbf{a}(t)\mathbf{a}^{\dagger}(t') \\ \mathbf{a}^{*}(t)\mathbf{a}^{T}(t') & \mathbf{a}^{*}(t)\mathbf{a}^{\dagger}(t') \end{bmatrix} \right\rangle \tag{4.15}$$

where the operation $\mathbf{a}^{*}$ is understood to conjugate the operators in the vector $\mathbf{a}$ without transposing it.

In the absence of squeezing interactions, the Bogoliubov-de Gennes matrix $\mathcal{H}$ is Hermitian and has the block representation

$$\mathcal{H} = \begin{bmatrix} \mathcal{A} & 0 \\ 0 & -\mathcal{A}^{*} \end{bmatrix}, \tag{4.16}$$

with the hopping matrix $\mathcal{A}$ encoding the system's phonon-conserving beamsplitter interactions. After defining the reduced dynamical matrix $\mathcal{M}_{\mathcal{A}} = \mathcal{A} - \mathrm{i}\Gamma'/2$ with $\Gamma' = \mathrm{diag}\left(\gamma_1, \cdots, \gamma_N\right)$, the full dynamical matrix of the system reads

$$\mathcal{M} = \begin{bmatrix} \mathcal{M}_{\mathcal{A}} & 0 \\ 0 & -\mathcal{M}_{\mathcal{A}}^* \end{bmatrix}. \tag{4.17}$$

Assuming that all modes are coupled to individual, uncorrelated thermal baths, the diffusion matrix reads

$$\mathcal{D} = \begin{bmatrix} 0 & \mathcal{D}' \\ \mathcal{D}' & 0 \end{bmatrix}, \tag{4.18}$$

with $\mathcal{D}' = \mathrm{diag}\left(\gamma_1 \bar{n}_1^{\mathrm{th}}, \cdots, \gamma_N \bar{n}_N^{\mathrm{th}}\right)$ the reduced diffusion matrix. Here we assume that our system is dominated by classical noise and neglect the contribution of quantum fluctuations (i.e. $\bar{n}_j^{\mathrm{th}} \approx \bar{n}_j^{\mathrm{th}} + 1$).

Now, the block structure of the matrices (4.15), (4.17) and (4.18) proves to be helpful. Plugging them into (4.11) leads to decoupled evolution for each block of one-time correlators

$$\frac{\mathrm{d}}{\mathrm{d}t}\left\langle \mathbf{a}\mathbf{a}^T \right\rangle = -\mathrm{i}\left(\mathcal{M}_{\mathcal{A}}\left\langle \mathbf{a}\mathbf{a}^T \right\rangle + \left\langle \mathbf{a}\mathbf{a}^T \right\rangle \mathcal{M}_{\mathcal{A}}^*\right), \tag{4.19}$$

$$\frac{\mathrm{d}}{\mathrm{d}t}\left\langle \mathbf{a}\mathbf{a}^\dagger \right\rangle = -\mathrm{i}\left(\mathcal{M}_{\mathcal{A}}\left\langle \mathbf{a}\mathbf{a}^\dagger \right\rangle - \left\langle \mathbf{a}\mathbf{a}^\dagger \right\rangle \mathcal{M}_{\mathcal{A}}^\dagger\right) + \mathcal{D}', \tag{4.20}$$

where we have dropped the time argument (t) of all mode vectors for notational compactness. The steady-state solution satisfies

$$0 = \left\langle \mathbf{a}\mathbf{a}^T \right\rangle \tag{4.21}$$

$$\mathcal{D}' = \mathrm{i}\left(\mathcal{M}_{\mathcal{A}}\left\langle \mathbf{a}\mathbf{a}^\dagger \right\rangle - \left\langle \mathbf{a}\mathbf{a}^\dagger \right\rangle \mathcal{M}_{\mathcal{A}}^\dagger\right), \tag{4.22}$$

which shows that for a system with Hermitian closed-system dynamics, only the correlators $\left\langle a_j a_k^\dagger \right\rangle$ can attain finite values, while the correlators $\langle a_j a_k \rangle$ remain zero. In this chapter, we therefore restrict ourselves to studying the reduced correlator matrix

$$A'(t,t') = \left\langle \mathbf{a}(t)\mathbf{a}^\dagger(t') \right\rangle, \tag{4.23}$$

with regression evolution

$$\frac{\mathrm{d}A'(t+\tau,t')}{\mathrm{d}t} = -\mathrm{i}\mathcal{M}_{\mathcal{A}} A'(t+\tau,t'). \tag{4.24}$$

Finally, combining (4.24), (4.22) and the Wiener-Khinchin theorem allows determining the spectral density matrix

$$\mathcal{S}_{\mathbf{a}\mathbf{a}^\dagger}(\omega) = \int_{\infty}^{\infty} e^{-\mathrm{i}\omega\tau} A'(t+\tau,t)\,\mathrm{d}\tau = \chi(\omega)\mathcal{D}'\chi^\dagger(\omega) \tag{4.25}$$

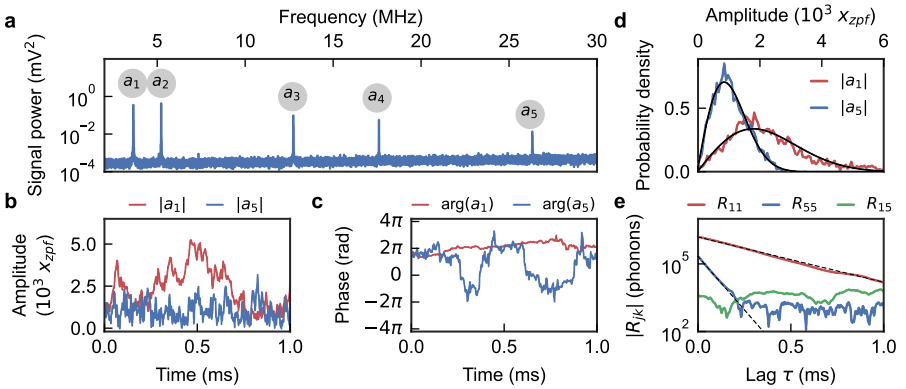

Figure 4.1: **Brownian motion of uncoupled nano-optomechanical resonators. (a)** Thermomechanical fluctuation spectrum of the sliced nanobeam, imprinted on a laser reflected from a nanocavity with linewidth $\kappa/(2\pi) = 320$ GHz. Five flexural mechanical resonances a_j are revealed, with frequencies $\omega_j/(2\pi)$ between 3.7 and 26.2 MHz. **(b)** Time trace of the thermally fluctuating amplitude $|a_j|$ of the lowest and highest frequency resonances a_1 and a_5, obtained by demodulating the optical fluctuation signal with parallel electronic local oscillators at Ω_j and subsequent low-pass filtering. **(c)** Phase fluctuations $\arg(a_j)$ corresponding to b. **(d)** Histograms of the amplitudes $|a_j|$ collected over a duration of 10 ms. Black lines represent the probability densities f_{MB} of the corresponding Maxwell-Boltzmann distribution (4.27). **(e)** Auto-correlations $R_{11}(\tau)$ and $R_{55}(\tau)$ and cross-correlations $R_{15}(\tau)$ as a function of time lag τ. Black dashed lines represent exponentially decaying amplitude correlations with rates $\gamma_j/2$ equal to half the spectral linewidth of the resonances.

from the susceptibility matrix $\chi(\omega) = -\mathrm{i}(\omega\mathbb{1} - \mathcal{M}_A)^{-1}$. For completeness, we note that in the presence of squeezing interactions ($\mathcal{B} \neq 0$), the spectral density matrix of the full correlator matrix $A(t)$ in (4.10) is given by the similar expression

$$\mathcal{S}_{\boldsymbol{\alpha}\boldsymbol{\alpha}^\dagger}(\omega) = \chi_{\boldsymbol{\alpha}}(\omega)\mathcal{D}\chi^\dagger_{\boldsymbol{\alpha}}(\omega), \tag{4.26}$$

with susceptibility matrix $\chi_{\boldsymbol{\alpha}}(\omega) = -\mathrm{i}(\omega\mathbb{1} - \mathcal{M})^{-1}$.

4.3. Brownian motion of single resonators

We move on to our experimental results, where we study the thermal motion that is naturally present in a room-temperature nanomechanical system: the sliced nanobeam presented in chapter 2. We sensitively measure thermally driven vibrations by employing the strong optomechanical interaction between its flexural mechanical modes and the photonic crystal optical nanocavity. As discussed, the displacements x_j of these optically active mechanical resonances are imprinted on the intensity of laser light reflected off the cavity. By studying the frequency content of the reflected intensity signal $z(t)$, five high-Q mechanical resonances are revealed with MHz resonance frequencies Ω_j and kHz linewidths γ_j, as shown in Figure 4.1a.

We track the thermal vibrations of these mechanical modes in time. To do so, we compare the oscillations in $z(t)$ with fixed electronic signals ('local oscillators', LOs) that oscillate at the mechanical resonance frequencies Ω_j. In particular, we demodu-

late $z(t)$ for each resonator j in parallel using a local oscillator with complex-valued representation $v_j(t) = e^{i\Omega_j t}$ and subsequent low-pass filtering. The resulting complex amplitude envelope $a_j(t)$ encodes the oscillation amplitude and phase offset of resonator j relative to its LO.

To set the stage, we first study the thermal fluctuations of individual mechanical resonators, as is routinely done in optomechanical systems. We show exemplary time traces of the Brownian motion of the lowest and highest frequency modes a_1 and a_5 in Figure 4.1b (amplitude) and 4.1c (phase). Qualitatively, we recognize two differences: the average amplitude of mode a_1 is higher (measured in units of the zero-point motion x_{zpf}), while the fluctuations of mode a_5 evolve more rapidly. The first observation is a consequence of their different frequencies: The thermal variance $a^2_{\text{rms},j} = \langle x_j^2 \rangle = 2x^2_{\text{zpf}}\bar{n}^{\text{th}}_j$ of a resonator depends on the occupation $\bar{n}^{\text{th}}_j = k_{\text{B}}T/\hbar\Omega_j$ of the thermal phonon bath (with temperature T) that it is coupled to. The second observation shows a variation in the *strength* of coupling to that environment and reflects their different dissipation rates $\gamma_1/(2\pi) = 1.5$ kHz and $\gamma_5/(2\pi) = 6.9$ kHz.

4.3.1. Statistical analysis

Next, we introduce some statistical tools to analyse the inherently stochastic thermal fluctuations quantitatively, and illustrate these tools with the time traces measured previously. One of the simplest statistical analyses we can do, beyond evaluating moments such as the mean and the variance, is to construct a histogram of the amplitude values $|a_j|$ that we find in a trace, as shown in Figure 4.1d.

Each mechanical mode (effective mass m_j) features two degrees of freedom: displacement x_j and velocity v_j. In thermal equilibrium, the total energy $E_j = m_j\Omega_j^2 x_j^2/2 + m_j v_j^2/2$ follows the exponential Boltzmann distribution $\propto \exp(-E_j/k_{\text{B}}T)$. Consequently, we expect the probability of finding a particular normalized oscillation amplitude $r_j = |a_j|/a_{j,\text{rms}}$ (with $a^2_{j,\text{rms}} = \langle |a_j|^2 \rangle$) to follow a two-dimensional Maxwell-Boltzmann distribution

$$f_{\text{MB}}(r_j) = 2r_j e^{-r_j^2}. \tag{4.27}$$

The relatively large variations of the experimental histograms in Figure 4.1d around the expected probability density functions (black lines) are due to the short time span of 10 ms over which the histograms are constructed, compared to the dissipation times $1/\gamma_j$ (on the order of 0.2 ms).

The histograms in Figure 4.1d do not reveal any of the temporal structure present in Figure 4.1b and 4.1c. To study this structure, we calculate the auto-correlations (for $j = k$) and cross-correlations (for $j \neq k$)

$$R_{jk}(\tau) = \langle a_j(t+\tau)a_k^*(t) \rangle_t \tag{4.28}$$

as a function of time lag τ. Figure 4.1e shows experimental auto- and cross-correlation functions for the fluctuations of modes a_1 and a_5. The cross-correlation $R_{15}(\tau)$ only shows instrument noise and verifies that the two resonators are fluctuating independently. On the other hand, the auto-correlations $R_{11}(\tau)$ and

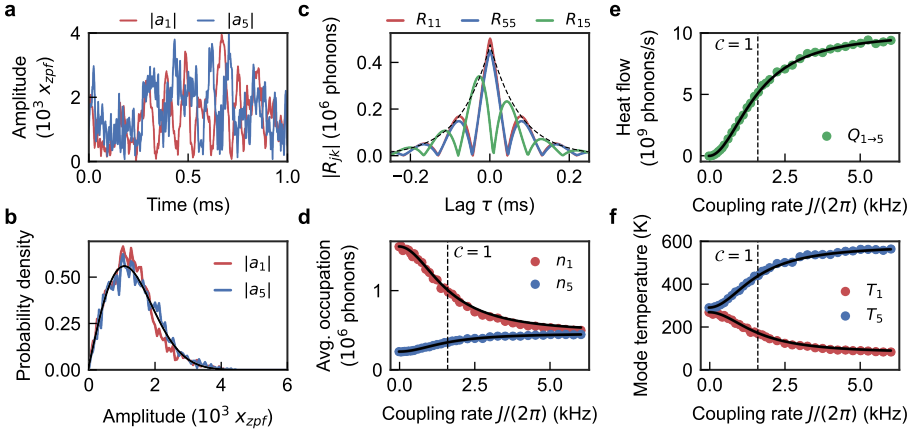

Figure 4.2: **Thermodynamics of two coupled nanomechanical resonators.** Modes a_1 and a_5 are coupled by a beamsplitter interaction of strength J. Panels a-c are shown for $J/(2\pi) = 6$ kHz. **(a)** Exemplary time traces of the amplitude fluctuations $|a_1|$ and $|a_5|$. **(b)** Histograms of the amplitudes $|a_j|$ collected over a duration of 10 ms. The black line represents the probability density $f(|a_j|)$ of the Maxwell-Boltzmann distribution (4.27)) **(c)** Auto-correlations $R_{11}(\tau)$ and $R_{55}(\tau)$ and cross-correlations $R_{15}(\tau)$ as a function of time lag τ. The dashed black line indicates an exponential decay for the average amplitude dissipation rate $\bar{\gamma}/2$. **(d)** Average thermal occupation $R_{jj}(0) = \langle |a_j(t)|^2 \rangle_t$ as a function of coupling strength J. **(e)** Heat flowing from mode 1 to mode 5 as a function of J, measured from the zero-lag cross-correlation $Q_{1\mapsto 5} = \mathrm{Im}\left[Je^{i\phi} \cdot R_{15}(0)\right]$. (f) Effective mode temperatures corresponding to the occupations in d. The black lines in panels d-f are calculated from the model laid out in section 4.4.1, while the dashed vertical lines indicate the coupling J for which the cooperativity $C = 1$.

$R_{55}(\tau)$ show amplitude correlations decaying with τ at a rate $\gamma_j/2$ (dashed lines), as predicted by the regression principle (4.4). The zero-lag correlation $R_{jj}(0) = \langle |a_j(t)|^2 \rangle_t$ is equal to the thermal variance of the modes. With the Wiener-Khinchin theorem connecting the auto-correlation function and spectral density by Fourier transform, the amplitude correlation decay rate $\gamma_j/2$ is directly related to the spectral linewidth γ_j.

4.4. Thermodynamics of a dimer

Subsequently, we study the thermodynamics of a nanomechanical dimer coupled by cavity-mediated radiation pressure forces [63, 196], employing the phonon-conserving beamsplitter interaction introduced in section 2.6. The interaction is induced parametrically by modulating the intensity of a drive laser at the difference frequency between the two mechanical modes a_1 and a_5, stimulating frequency conversion [64]. This leads to an effective interaction Hamiltonian

$$H_{\mathrm{BS}} = Je^{-i\phi} a_1^\dagger a_5 + Je^{i\phi} a_5^\dagger a_1 \tag{4.29}$$

in a frame rotating along with the two resonators. Under this Hamiltonian, phonons are exchanged in a Rabi-like oscillation between the modes a_1 and a_5 at a rate J with an interaction phase ϕ. This is illustrated in Figure 2.6b for a coherent excitation.

Similar energy exchange is observed for thermal vibrations as well. Qualitatively, the amplitude time traces in Figure 4.2a of fluctuations in the dimer indeed show thermal energy continuously being traded back and forth. Their amplitude distributions, shown in Figure 4.2b, are now very similar, while still following the two-dimensional Maxwell-Boltzmann distribution (4.27).

Yet again, the exchange of thermal energy is best revealed by looking at the correlation functions shown in Figure 4.2c. For a strongly coupled dimer, the auto-correlations $R_{11}(\tau)$ and $R_{55}(\tau)$ show an overall decay that is exponentially enveloped by the average amplitude decay with rate $\bar{\gamma}/2 = (\gamma_1 + \gamma_5)/4$. However, within this envelope, we see the disappearance and subsequent revival of correlations, with each auto-correlation dip coinciding with a high value for the cross-correlation $R_{15}(\tau)$. This indicates a Rabi-like exchange of thermal fluctuations between the modes, and has so far only been observed between resonators of equal frequency fed by artificial thermal fluctuations [196].

4.4.1. Energy, heat flow and temperature

Upon closer inspection, $R_{15}(\tau)$ proves to be asymmetric in time lag with a non-zero value at $\tau = 0$. Here, time-reversal symmetry is broken by the thermodynamic arrow of time associated with a thermal gradient, as the low-frequency mode a_1 is coupled to a phonon bath of higher occupation $\bar{n}_1^{\text{th}} > \bar{n}_5^{\text{th}}$. Moreover, by considering the continuity relation derived from the time evolution of the number operators $a_j^\dagger a_j$, we find that the microscopic *heat flow* $Q_{1\mapsto 5}$ between coupled modes is related to the zero-lag cross-correlation via [179, 201]

$$Q_{j\mapsto k} = i\left\langle Je^{\mathrm{i}\phi}a_j^\dagger a_k - Je^{-\mathrm{i}\phi}a_j a_k^\dagger \right\rangle = 2\,\mathrm{Im}\left[Je^{\mathrm{i}\phi}\cdot R_{jk}(0)\right]. \tag{4.30}$$

With our distinctive phase-resolved detection and driving scheme (section 2.8.2), we are in the unique position to evaluate (4.30) experimentally. Figure 4.2d and 4.2e show the steady-state occupations and heat flow between the resonators as the coupling J is increased.

To understand the relation between heat flow and coupling strength, we work out a model to predict the dimer's thermal steady state. First, we unpack the reduced one-time correlator matrix $A'(t,t)$ of (4.23) into a vector

$$\mathbf{v}(t) = \left\langle \left(a_1 a_1^\dagger, a_5 a_5^\dagger, a_1 a_5^\dagger, a_5 a_1^\dagger\right)^T \right\rangle. \tag{4.31}$$

Under (4.20), the evolution of $\mathbf{v}(t)$ is governed by $\dot{\mathbf{v}}(t) = -\mathcal{N}\mathbf{v}(t) + \mathbf{h}$, where $\mathbf{h} = \left(\gamma_1\bar{n}_1^{\text{th}}, \gamma_5\bar{n}_2^{\text{th}}, 0, 0\right)$ is the thermal driving vector and the thermalization matrix reads

$$\mathcal{N} = \begin{bmatrix} \gamma_1 & 0 & -\mathrm{i}\mathcal{J}^* & \mathrm{i}\mathcal{J} \\ 0 & \gamma_5 & \mathrm{i}\mathcal{J}^* & -\mathrm{i}\mathcal{J} \\ -\mathrm{i}\mathcal{J} & \mathrm{i}\mathcal{J} & \bar{\gamma} & 0 \\ \mathrm{i}\mathcal{J}^* & -\mathrm{i}\mathcal{J}^* & 0 & \bar{\gamma} \end{bmatrix}, \tag{4.32}$$

with $\jmath = Je^{i\phi}$. We can use this relation to predict the thermalization of a non-equilibrium state, as shown in the experiments in Figure 4.7.

However, at present, we are concerned with the thermal steady-state $\mathbf{v}_{\text{ss}}$, which easily follows from (4.32) as $\mathbf{v}_{\text{ss}} = \mathcal{N}^{-1}\mathbf{h}$. The steady-state heat flow (4.30) reads

$$Q_{1\mapsto 5} = \frac{4J^2\gamma_1\gamma_5}{(\gamma_1+\gamma_5)\,(4J^2+\gamma_1\gamma_5)}\Delta\bar{n}^{\text{th}} = \frac{\mathcal{C}}{1+\mathcal{C}}\frac{\gamma_1\gamma_5}{\gamma_1+\gamma_5}\Delta\bar{n}^{\text{th}}. \tag{4.33}$$

We see that the flow is driven by the bath occupation difference $\Delta\bar{n}^{\text{th}} = \bar{n}_1^{\text{th}} - \bar{n}_5^{\text{th}}$ and scales with the cooperativity $\mathcal{C} = 4J^2/(\gamma_1\gamma_5)$. The average resonator occupations are given by

$$\begin{aligned} n_{1,5} = \left\langle |a_{1,5}|^2 \right\rangle &= \frac{4J^2\left(\gamma_1\bar{n}_1^{\text{th}} + \gamma_5\bar{n}_2^{\text{th}}\right) + \gamma_1\gamma_5\,(\gamma_1+\gamma_5)\,\bar{n}_{1,5}^{\text{th}}}{(\gamma_1+\gamma_5)\,(\gamma_1\gamma_5+4J^2)} \\ &= \frac{\gamma_{1,5}\bar{n}_{1,5}^{\text{th}} \mp Q_{1\mapsto 5}}{\gamma_{1,5}} \end{aligned} \tag{4.34}$$

and express the balance between the rate $\gamma_j\bar{n}_j^{\text{th}}$ at which resonator j exchanges thermal quanta with its own bath and the heat $Q_{j\mapsto k}$ flowing out towards the other resonator k.

As shown in Figure 4.2d, the occupations predicted by this model are in excellent agreement with the experimental results. Without interaction between the modes ($J = 0$), the difference in the resonators' thermal occupation reflects the difference in their bath occupation $\bar{n}_1^{\text{th}} > \bar{n}_5^{\text{th}}$. As the interaction $J > 0$ is turned on, the occupation difference is reduced with mode a_1 cooling down while mode a_5 heats up. As a_5 is coupled to the environment more strongly ($\gamma_5 > \gamma_1$), it is able to dump the excess heat flowing in from a_1 efficiently, such that a_5 heats up less than a_1 cools down.

The changes in occupation are corroborated by the trend of the heat flow in Figure 4.2e. Here, the cooperativity $\mathcal{C}$ proves to be a central parameter, as the heat flow (4.33) scales with $\mathcal{C}/(1+\mathcal{C})$. For small $\mathcal{C}$ this prefactor scales linearly with $\mathcal{C}$ (and thus quadratically with J), while for $\mathcal{C} \to \infty$ a maximum in flow is asymptotically reached, with $\mathcal{C}/(1+\mathcal{C}) \to 1$. The occupations then equilibrate to the value $n_{1,5} = (\gamma_1\bar{n}_1^{\text{th}} + \gamma_5\bar{n}_5^{\text{th}})/(\gamma_1+\gamma_5)$. For unity cooperativity $\mathcal{C} = 1$, the heat flow is half of the maximum value.

Finally, while a description in terms of quantized phonons is convenient and standard practice even in classical nano-optomechanics, we realize that this experiment does not rely on quantum effects in any way. A more natural description is therefore found by expressing the mode energies as an effective temperature

$$T_j = \bar{n}_j^{\text{th}}\hbar\Omega_j/k_{\text{B}}. \tag{4.35}$$

Doing so reveals the nature of this experiment. As illustrated in Figure 4.2f, for $J = 0$ the effective temperatures start out very close to the temperature $T_{\text{lab}} \approx 295$ K of the laboratory environment (the small difference is explained by the opto-thermal dynamical backaction discussed in section 2.8.4). Cranking up the coupling J causes

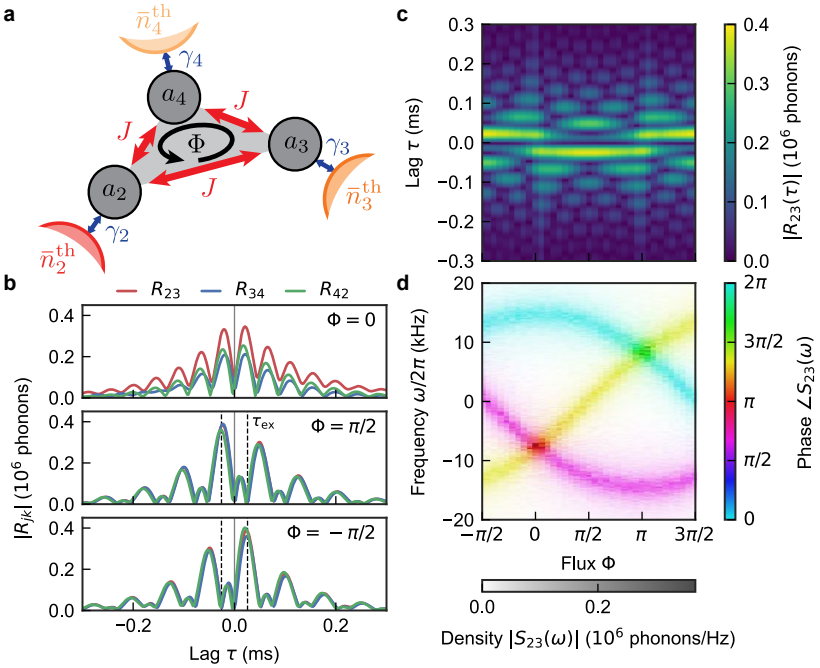

Figure 4.3: **Circulating thermal fluctuations in a flux-biased loop. (a)** A phonon circulator is formed by coupling three resonators a_j (strengths $J/(2\pi) = 7.5$ kHz) in a loop permeated by a synthetic flux Φ. Each resonator interacts with an independent phonon bath of occupation $\bar{n}_2^{\rm th} > \bar{n}_3^{\rm th} \gtrsim \bar{n}_4^{\rm th}$ through dissipation rate γ_j. **(b)** Measured cross-correlations $R_{jk}(\tau)$ as function of time lag for flux $\Phi = 0$, where the circulator is time-reversal symmetric (TRS), and for $\Phi = \pm\pi/2$, where TRS is broken. The controlled breaking of TRS induces circulating thermal fluctuations. For $\Phi = \pm\pi/2$, the intermode exchange time $\tau_{\rm ex} = \pm 2\pi/(3J\sqrt{3})$ is indicated (dashed lines). **(c)** Colour plot of the measured cross-correlation magnitude $|R_{23}(\tau, \Phi)|$. A cross-over from non-circulating to circulating fluctuations is observed when varying the flux Φ, and reversal of chirality with flux sign. **(d)** Magnitude and phase of the cross-spectral density $S_{23}(\omega, \Phi)$, obtained by Fourier transform of $R_{23}(\omega, \Phi)$. Hybridized eigenmodes of the loop, identified by their distinct phase delay between adjacent resonators, tune with synthetic flux.

the temperature T_1 to drop significantly below $T_{\rm lab}$, while T_5 is heated above $T_{\rm lab}$. This shows the dimer operating as a *heat pump*. The work required to refrigerate is supplied by the modulated drive laser field, analogous to the energy supplied by a red-detuned optical drive to convert low-energy phonons into high-energy photons in optomechanical sideband cooling schemes [118].

4.5. Fluctuations in a phonon circulator

In the remainder of this chapter, we explore the interplay between time-reversal symmetry broken by synthetic magnetism *and* by thermal gradients. A natural system to study this combination is the phonon circulator of section 3.2. Figure 4.3a depicts a circulator — formed by coupling resonators a_2, a_3 and a_4 in a loop with strengths J — embedded in its thermal environment comprising the uncorrelated

phonon baths $\bar{n}_j^{\text{th}}$. The Hamiltonian of the circulator is given in (3.1).

Disregarding the thermal environment for now, the closed-system dynamics of the circulator mode vector $\mathbf{a} = (a_2, a_3, a_4)^T$ are governed by $\dot{\mathbf{a}}(t) = -\mathrm{i}\mathcal{A}\mathbf{a}(t)$, where the (reduced) Hamiltonian matrix reads

$$\mathcal{A} = J \begin{bmatrix} 0 & e^{-\mathrm{i}\Phi/3} & e^{\mathrm{i}\Phi/3} \\ e^{\mathrm{i}\Phi/3} & 0 & e^{-\mathrm{i}\Phi/3} \\ e^{-\mathrm{i}\Phi/3} & e^{\mathrm{i}\Phi/3} & 0 \end{bmatrix}. \tag{4.36}$$

As discussed in section 3.2, a gauge-invariant synthetic magnetic flux Φ controls the time-reversal symmetry (TRS) of the closed system. In (4.36), we have chosen a gauge where the flux is distributed equally over the three links, rendering $\mathcal{A}$ *rotationally invariant*.

4.5.1. Circulating fluctuations

We first focus on the effect of a TRS-breaking flux on the temporal structure of the circulator's fluctuations. For a relatively high coupling $J/(2\pi) = 7.5$ kHz $> \gamma_j$, Figure 4.3b shows the cross-correlation magnitude $|R_{jk}(\tau)|$ of adjacent resonators as a function of time lag τ. For $\Phi = 0$ — when TRS is not broken — these are approximately symmetric in τ, with the thermal gradient $\bar{n}_2^{\text{th}} > \bar{n}_3^{\text{th}} \gtrsim \bar{n}_4^{\text{th}}$ contributing only slightly to the asymmetry. However, when TRS *is* broken by a flux $\Phi = \pm\pi/2$, the cross-correlations become markedly asymmetric in τ and evidence *circulating thermal fluctuations*, akin to the circulation of coherent vibrations witnessed in Figure 3.2a.

Indeed, following for example $R_{23}(\tau)$ when $\Phi = \pi/2$ and keeping in mind the definition (4.28), thermal energy in resonator a_2 is seen to be transferred to a_3 after the inter-mode exchange time $\tau_{\text{ex}} = 2\pi/(3J\sqrt{3})$ with high intensity. Conversely, at this time, the transfer in the other direction — noting that $R_{kj}(\tau) = R_{jk}^*(-\tau)$ — is at a minimum (see dashed lines in Figure 4.3b). The chirality (handedness) of the circulation is reversed upon reversing the flux $\Phi \mapsto -\Phi$.

In Figure 4.3c, we illustrate the cross-correlation magnitude $|R_{23}(\tau)|$ both as a function of lag τ and flux Φ. This reveals a continuous tuning of chirality with Φ, analogous to the tuning seen for coherent vibration transfer in Figure 3.2b. By taking the Fourier transform of $R_{23}(\tau)$, we obtain the power spectral density $S_{23}(\omega)$ illustrated in Figure 4.3d. Crucially, as $R_{23}(\tau)$ is a complex quantity comparing both amplitude *and* phase of adjacent resonators, the cross-spectral density $S_{23}(\omega)$ now also contains phase information, in contrast to the single-resonator spectra shown in Figure 3.1d. Especially, this allows for a phase-sensitive examination of the circulator's eigenmodes.

The three magnitude bands of S_{23} in Figure 4.3d indicate the flux-tuned frequencies of the hybridized circulator eigenmodes, while the phase of each band reveals the relative phase between resonators a_2 and a_3 in the corresponding eigenmode. With (4.36) rotationally symmetric, $S_{34}(\omega)$ and $S_{42}(\omega)$ look similar and exhibit the same relative phases. The light blue band therefore corresponds to a symmetric eigenmode where all resonators oscillate in phase for the chosen gauge (LO phases), while the other bands indicate phase-chiral eigenmodes with a $\pm 2\pi/3$

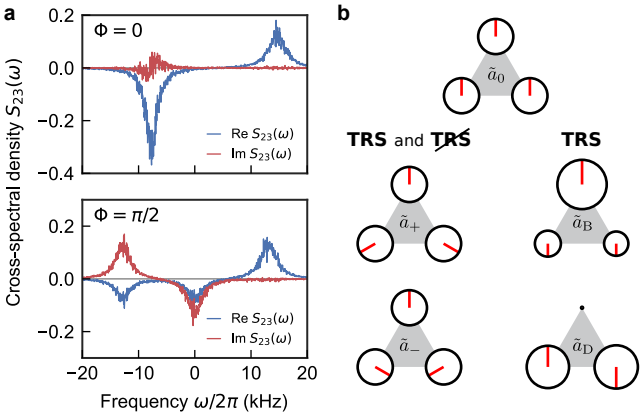

Figure 4.4: **Broken time-reversal symmetry (TRS) and chiral eigenmodes. (a)** Real and imaginary part of the cross-spectral density $S_{23}(\omega, \Phi)$ shown in Figure 4.3. For flux $\Phi = 0$, the circulator respects TRS and features a real Hamiltonian matrix $\mathcal{A}$ with real eigenvectors $\tilde{a}_j$. For flux $\Phi = \pi/2$, TRS is broken and $\mathcal{A}$ is complex with complex $\tilde{a}_j$. Each complex Lorentzian contribution to $S_{23}(\omega)$ scales with the product $\tilde{a}_j^{(2)} \cdot (\tilde{a}_j^{(3)})^*$, where $\tilde{a}_j^{(m)}$ is the weight of resonator m in the associated eigenmode $\tilde{a}_j$. This results in a real (complex) cross-spectral density for $\Phi = 0$ ($\Phi = \pi/2$). **(b)** Phasor representation of the circulator eigenmodes, with the magnitude (phase) of each resonator weight indicated by the radius (rotation) of a circle. Regardless of the breaking of TRS, eigenmodes can be described by the angular momentum eigenstates $\tilde{a}_0, \tilde{a}_-, \tilde{a}_+$ of the rotationally-invariant circulator Hamiltonian. Each resonator has equal weight, with the relative phase between adjacent resonators $0, \pm 2\pi/3$ given by the eigenstate index. When the Hamiltonian matrix $\mathcal{A}$ is real and TRS is respected, the two chiral eigenstates $\tilde{a}_\pm$ become degenerate and can be combined to form two achiral, real eigenstates $\tilde{a}_B$ and $\tilde{a}_D$ with unequal resonator weights.

inter-resonator phase lag for the same gauge (see Figure 4.4b). Finally, we note that while $\mathcal{A}_{\Phi=2\pi}$ is *gauge-equivalent* to $\mathcal{A}_{\Phi=0}$, it is not *identical*. In the present gauge, the phase of $S_{23}(\omega)$ is 6π-periodic in Φ, whereas the phase-insensitive amplitude $|S_{23}(\omega)|$ is 2π-periodic.

For the trivial flux $\Phi = 0$, the lower frequency eigenmodes become degenerate. Moreover, as TRS is preserved, they can be combined to form two different eigenmodes with real resonator weights and no TRS-breaking phase delays between resonators. This is manifested in Figure 4.3d by the trivial phase $\angle S_{23}(-J, 0) \approx \pi$ (red) at the lower crossing. To analyze the situation for the other TRS-preserving flux $\Phi = \pi$, we must be mindful of the gauge we are working in. While the phase $\angle S_{23}(J, \pi) \approx 5\pi/3$ (green) at the upper crossing appears to be non-trivial, the gauge-invariant *inter-band* phase difference $\angle S_{23}(J, \pi) - \angle S_{23}(-2J, \pi) = \pi$ *is* trivial.

Alternatively, Figure 4.4a shows the real and imaginary parts of $S_{23}(\omega, \Phi = 0, \pi/2)$. For $\Phi = \pi/2$ we distinguish three Lorentzian distributions with a complex amplitude. These complex Lorentzians fan out in evenly-distributed directions from the ω-axis in the ω- $\mathrm{Re}(S)$- $\mathrm{Im}(S)$-space. As the degeneracy of the two lower frequency modes is established for $\Phi = 0$, their cross-spectral contributions coincide to cancel out their imaginary amplitudes, resulting in a real cross-spectral density.

As discussed in section 3.2, the rotationally invariant circulator Hamiltonian (3.1) is diagonal in the discrete angular momentum basis

$$\tilde{a}_k = \sum_{j=1}^{3} e^{-i2\pi kj/3} a_j/\sqrt{3} \text{ for } k = \{-1, 0, 1\}. \tag{4.37}$$

For a thermally fully symmetric circulator (equal $\bar{n}_j^{\text{th}}$ and γ_j), it follows from (4.25) that the complex amplitude of each Lorentzian contribution in S_{23} scales with the product $\tilde{a}_j^{(2)} \cdot (\tilde{a}_j^{(3)})^*$, where $\tilde{a}_j^{(m)}$ is the weight of resonator a_m in the corresponding eigenmode $\tilde{a}_j$. This elucidates the intimate connection between (the reality of) the cross-spectral density and (the reality of) the circulator's eigenmodes.

A phasor representation of the eigenvectors of $\mathcal{A}$ is visualized in Figure 4.4b. The phase-chiral angular momentum eigenstates $\tilde{a}_0$, $\tilde{a}_+$ and $\tilde{a}_-$ have equal weights in all resonators, and are valid irrespective of the breaking of TRS. When $\tilde{a}_-$ and $\tilde{a}_+$ are tuned to be degenerate at $\Phi = 0$, they can be combined to form the two achiral eigenmodes $\tilde{a}_{\text{B}} = (\tilde{a}_+ + \tilde{a}_-)/\sqrt{2}$ and $\tilde{a}_{\text{D}} = (\tilde{a}_+ - \tilde{a}_-)/(\text{i}\sqrt{2})$ with real but unequal weights.

4.5.2. Chirality and heat flows

We now return to the interplay between flux-induced chirality and thermal gradients. We implement a circulator using the low-frequency 'hot' resonator a_1 and the high-frequency 'cold' resonators a_3 and a_4. This circulator sports a larger thermal gradient $\bar{n}_1^{\text{th}} > \bar{n}_3^{\text{th}} \gtrsim \bar{n}_4^{\text{th}}$ than the one examined in the previous section. The thermal gradient drives a heat flow from the hot resonator to the cold resonators. As shown in Figure 4.5a for a moderate coupling $J/(2\pi) = 3.6$ kHz, the average thermal occupation n_1 of the hot resonator is thus cooled from its bath occupation $\bar{n}_1^{\text{th}}$ while the cold resonators are heated up and $n_{3,4} > \bar{n}_{3,4}^{\text{th}}$.

Remarkably, we find that the flux Φ has a striking impact on the distribution of thermal energy in the circulator. For flux $\Phi = \pi/2$ ($\Phi = -\pi/2$), heat flows from the hot resonator a_1 preferentially to a_3 (a_4). This is a consequence of flux-induced chirality: hot thermal fluctuations entering a_1 circulate in a particular, Φ-dependent order as they decay, breaking the symmetry of thermal transport.

These findings are corroborated by measuring the heat flows in the circulator, illustrated in Figure 4.5b and 4.5d. The relative magnitude of the heat flows between the hot resonator and the two cold resonators is tuned by Φ, while the direction of the heat flow $Q_{3\mapsto 4}$ is reversed by reversing the flux.

Interestingly, at trivial fluxes $\Phi = 0, \pi$ we find an increase in n_1 or conversely, a decrease in the cooling of a_1. Here, the presence of time-reversal symmetry allows the formation of an eigenmode $\tilde{a}_{\text{B}}$ that is 'bright' to the hot resonator a_1 (i.e. a_1 has weight in $\tilde{a}_{\text{B}}$) and an eigenmode $\tilde{a}_{\text{D}}$ that is 'dark' (see Figure 4.4b). The dark, but cold eigenmode $\tilde{a}_{\text{D}}$ is decoupled from the hot resonator and can therefore not contribute to cooling it [207]. In Figure 4.5c, this reduction in cooling is seen to persist as J is increased.

We take a closer look at this mechanism. Figure 4.6a shows the resonator occupations in the circulator for $\Phi = 0$. As J is increased, a plateau is reached where the

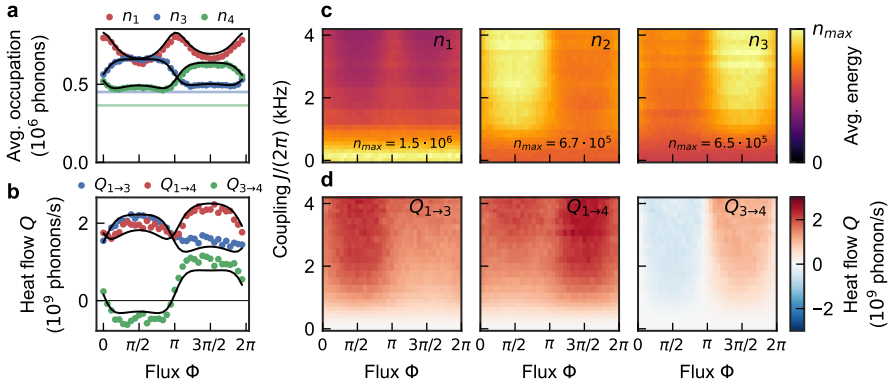

Figure 4.5: **Heat and refrigeration in a chiral system. (a)** Thermal average resonator occupation n_j in the circulator formed by coupling the modes a_1, a_3 and a_4 with strength $J/(2\pi) = 3.6$ kHz. Mode a_1 is cooled down from its bath occupation $\bar{n}_1^{\rm th} = 1.5 \cdot 10^6$, while a_3 and a_4 heat up from relative to their baths $\bar{n}_{3,4}^{\rm th} = \{0.45, 0.36\} \cdot 10^6$ (indicated by light blue and green lines). Dissipation rates $\gamma_3/(2\pi) \approx \gamma_4/(2/pi) = 3.8$ kHz are optothermally tuned to be equal, while $\gamma_1/(2\pi) = 1.5$ kHz. The chirality induced by the flux Φ redistributes thermal energy in the circulator, with heat from the hot resonator a_1 flowing preferentially to a_3 (a_4) for $\Phi = \pi/2$ ($\Phi = -\pi/2$). At trivial fluxes $\Phi = 0, \pi$, the hot resonator a_1 has no weight in the cold, 'dark' eigenmode $\tilde{a}_{\rm D}$ (cf. Figure 4.4b) and the level of cooling is reduced. **(b)** Heat flows $Q_{j\mapsto k}$ in the circulator. The direction of heat flow between the cold modes $Q_{3\mapsto4}$ is controlled by the chiral flux Φ, as is the relative flow between the hot mode and each of the cold modes. (c,d) Thermal average resonator occupations n_j and heat flows $Q_{j\mapsto k}$ as a function of both flux Φ and coupling rate J. The reduction in cooling for $\Phi = 0, \pi$ is seen to persist as J is increased. Black lines in a,b are calculated from (4.22).

hot resonator occupation n_1 remains larger than the cold resonator occupations $n_{3,4}$. In Figure 4.6b, we compare this to the related Λ-shaped resonator network, where the direct coupling between both cold resonators is absent. The Λ-system is flux-free and thus achiral. Importantly, it also hosts the dark, cold eigenmode $\tilde{a}_{\rm D}$ and shows a similar distribution of thermal energy in the strong coupling regime $J \gg \gamma_j$. In line with the realization that $\tilde{a}_{\rm D}$ does not contribute to cooling, the occupation n_1 in the Λ-network is exactly equal to that in a dimer formed by coupling a_1 with rate $J\sqrt{2}$ to an equivalent cold mode $a_{\rm eq}$ with dissipation $\gamma_{\rm eq} = \gamma_3 \approx \gamma_4$ and $\bar{n}_{\rm eq}^{\rm th} = (\bar{n}_3^{\rm th} + \bar{n}_4^{\rm th})/2$.

By breaking TRS in the circulator, we lift the degeneracy of the phase-chiral eigenstates $\tilde{a}_\pm$ and remove the dark mode $\tilde{a}_{\rm D}$. As shown in Figure 4.6c for flux $\Phi = \pi/2$, this allows to reach a lower hot resonator occupation n_1. Eventually, for $J \to \infty$, all resonators approach the same occupation $n_1 = n_3 = n_4$. Effectively, the breaking of TRS assists in the refrigeration of the hot resonator by adding an extra cooling channel [207]. We note that this effect is only important in the case of strong coupling — in the weak coupling regime with cooperativity $\mathcal{C} < 1$ smaller than unity, the average occupation and thus the cooling rate of the hot resonator is essentially the same in all three configurations shown in Figure 4.6. This indicates that dissipation dominates over correlations in weakly-coupled systems.

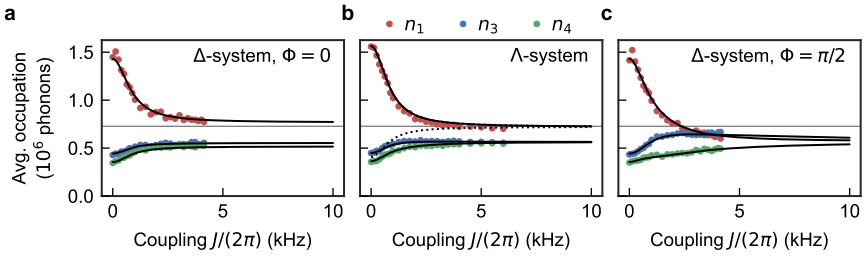

Figure 4.6: **Refrigeration assisted by broken TRS. (a)** Thermal average resonator occupation n_j of the (Δ-shaped) circulator in Figure 4.5 for flux $\Phi = 0$ as a function of coupling J. A theory extrapolation for high J (black lines) shows that a plateau is reached where the hot resonator occupation remains higher than that of the cold resonators — a consequence of the dark mode $\tilde{a}_\mathrm{D}$ being inaccessible to cool a_1. **(b)** The achiral Λ-configuration, where the coupling between the cold resonators is absent, also hosts the dark eigenmode $\tilde{a}_\mathrm{D}$ and shows a similar cooling plateau. The occupation n_1 in this configuration is exactly equal to that of a dimer formed by coupling a_1 with strength $J\sqrt{2}$ to a cold resonator with the average occupation $(\bar{n}_3^\mathrm{th} + \bar{n}_4^\mathrm{th})/2$ (dotted line). **(c)** Breaking time-reversal symmetry with a non-trivial flux $\Phi = \pi/2$ removes the dark eigenmode. The presence of three equal-weight eigenmodes improves the performance of cooling a_1 and allows equal resonator occupations to be reached for $J \to \infty$.

4.6. Competing energy transfer and thermalization

Finally, we study another manifestation of the competition between thermal relaxation and energy transfer via beamsplitter interactions. In particular, we track the thermalization of occupations and flows over time [213], in the ensemble-averaged time-resolved experiments shown in Figure 4.7. At times $t < 0$, the resonators are in only contact with their individual baths and maintain an uncoupled steady state. At time $t = 0$, interactions are instated and the resonators thermalize to the new steady-state of the coupled system. The evolution of this process is modeled in (4.20).

In the case of the dimer a_1-a_5, immediately after $t = 0$, the initial occupation difference drives a large energy transfer that greatly overshoots the eventual steady-state flow. In this process, the cold resonator n_5 is even temporarily seen to be more occupied than the hot resonator n_1. Indeed, for an arbitrarily large J, a short pulsed interaction of length π/J would allow a full swap of the resonator states [120, 214]. Here however, we see thermal relaxation kicking on a time scale $1/\gamma_j$, guiding the system to a steady-state where heat constantly flows from a_1 to a_5. Similar behaviour is seen for the circulator a_1-a_3-a_4 with TRS-breaking flux $\Phi = \pi/2$, where thermal energy is seen to slosh back and forth between the cold resonators a_3 and a_4 until a steady-state flow is reached.

4.7. Conclusions and outlook

To summarize, we have employed tunable, light-mediated mechanical interactions in a multi-mode cavity optomechanical system to manipulate and image *in situ* the transport of heat, with emphasis on the effect of controlled breaking of time-reversal symmetry by the optical drive. In a three-mode chiral phononic system, we

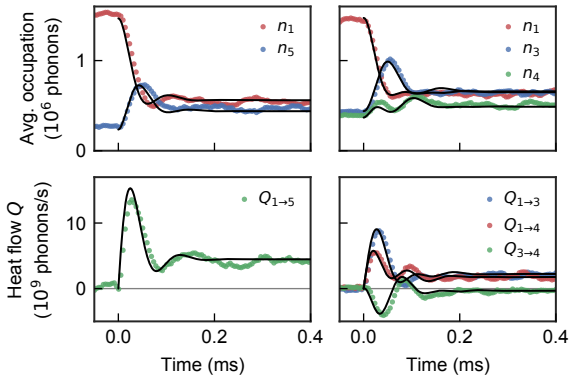

Figure 4.7: **Chirality in time-resolved thermalization.** Time-resolved ensemble averages (1000 runs) of the resonator occupations (upper row) and heat flows (lower row) in the dimer a_1-a_5 (left column, $J/(2\pi) = 5$ kHz) and circulator a_1-a_3-a_4 (right column, $J/(2\pi) = 3.6$ kHz, $\Phi = \pi/2$). The resonators are in thermal equilibrium with their baths $\bar{n}_j^{\text{th}}$ until at $t = 0$ the interactions are switched on and the correlators thermalize following (4.20) to a new steady-state. The evolution of the occupations and flows reflects the competition between energy transfer with time-scale $1/J$ and thermal relaxation with time-scales $1/\gamma_j$. In the circulator, the heat flow $Q_{3\mapsto4}$ between the cold resonators is seen to slosh back and forth until steady-state is reached.

have demonstrated circulating thermal fluctuations, chiral eigenstates, and flux-controlled directionality of heat flows. Moreover, we have found that the breaking of time-reversal symmetry assists in refrigeration: In a strongly-coupled chiral configuration, a lower phonon population could be attained for the lowest-frequency mode than is possible in an achiral configuration.

These findings put forth our experimental platform as a promising model system to investigate symmetry-broken thermodynamics at the nanoscale, and point to a direction to improve cooling in multi-mode systems. Looking forward, it may be applied to study non-equilibrium fluctuations [215], heating and cooling in anti-parity-time symmetric systems [216], and heat transport in topological insulators [201], connecting to the previous chapter of this thesis. Moreover, as we will exploit in the following chapters, dynamical modulation of the optical spring also allows inducing squeezing interactions, opening yet another direction to study nonstandard thermodynamics. The nonreciprocal routing and efficient cooling we study may also provide useful insights into the development of nonreciprocal photonic or microwave components, where the suppression of thermal noise in specific output channels is important [127, 128].

Finally, noting that the non-degenerate circulator acts as a heat pump driven by modulated light, an interesting follow-up would be to quantify the work supplied by the driving field, the efficiency of refrigeration, and the production of entropy. This angle has been overlooked in previous work on light-mediated nonreciprocal phonon transport as well [63, 196, 202], and relates to an ongoing debate on the bounds of finite power efficiency of heat engines subject to broken time-reversal symmetry [203–206].

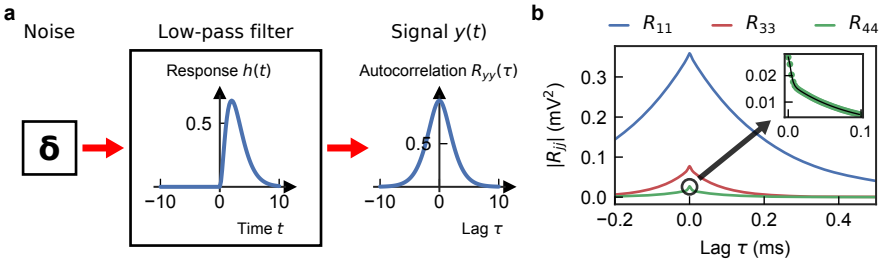

Figure 4.8: **Instrument noise in auto-correlations. (a)** In the lock-in amplifier used to analyze thermomechanical signals, δ-correlated instrument noise is filtered by a third-order low-pass filter (response $h(t)$ shown for unity time constant) in the demodulation process. This introduces time-correlations in the demodulated signal $y(t)$ and results in a peaked auto-correlation $R_{yy}(\tau) \propto h(\tau) \star h(-\tau)$ given by the convolution of $h(t)$ with itself. **(b)** Measured auto-correlation voltages $|R_{jj}(\tau)|$ for three uncoupled resonators. On top of the long-time exponential thermal decay of amplitude correlations, there is a short-time contribution of filtered noise correlations. The inset zooms in on $|R_{44}(\tau)|$ at the short time scale and shows that it is described well by the (uncorrelated) sum of the filtered noise auto-correlation and the exponential thermal decay (black line). The effect of the low-pass filter on the thermal correlations is negligible due to their different time constants $\tau_{\text{filter}} = 1.62\,\mu\text{s}$ and $\tau_{\text{th}} = 2/\gamma_4 = 81\,\mu\text{s}$. Cross-correlations between resonator signals at different frequencies do not suffer from the frequency-uncorrelated instrument noise.

4.8. Appendix: Instrument noise in auto-correlations

In the measurement of the resonators' thermal displacement, the dominant noise source is electronic noise in our instruments: a detector and a lock-in amplifier. The lock-in amplifier is used to demodulate the thermomechanical signals, and in doing so passes the voltage signal it has measured (including the instrument noise) through a digital low-pass filter. Assuming that the instrument noise is δ-correlated with spectral density S_{nn} (at least around the MHz frequencies of our resonators), this introduces time-correlations in the demodulated noise signal $y(t)$. Depicted in Figure 4.8a, this leads to a noise auto-correlation $R_{yy}(\tau) = S_{nn}(h(\tau) \star h(-\tau))$ that scales with the convolution of the low-pass filter response $h(t)$ with itself. The instrument noise gets added to the thermal auto-correlations R_{jj} that we are interested in, as demonstrated in Figure 4.8b. In all auto-correlations shown in this chapter, we correct for this noise contribution.

5

Non-Hermitian chiral phononics through optomechanically induced squeezing

Imposing chirality on a physical system engenders unconventional energy flow and responses, such as the Aharonov-Bohm effect [40] and the topological quantum Hall phase for electrons in a symmetry-breaking magnetic field. Recently, great interest has arisen in combining that principle with broken Hermiticity to explore novel topological phases and applications [106, 217–230]. In this chapter, we report unique phononic states formed when combining the controlled breaking of time-reversal symmetry with non-Hermitian dynamics, both induced through time-modulated radiation pressure forces in small nano-optomechanical networks. For phonons in a synthetic dimension, we supplement synthetic magnetism with particle-non-conserving squeezing interactions, and discover a non-Hermitian Aharonov-Bohm effect in ring-shaped networks in which mechanical quasiparticles experience parametric gain. The resulting complex mode spectra indicate flux-tuning of squeezing, exceptional points, instabilities and unidirectional phononic amplification. This rich phenomenology points the way to exploring new non-Hermitian topological bosonic phases and applications in sensing and transport that exploit spatiotemporal symmetry breaking.

This chapter is based on J. del Pino, J. J. Slim & E. Verhagen. Non-Hermitian chiral phononics through optomechanically induced squeezing. *Nature* **606,** 82–87 (2022) [151]. J.d.P. and J.J.S, contributed equally to this work.

5.1. Introduction

From the Zeeman to the quantum Hall effect, magnetic fields biasing electronic systems alter their spectrum and imprint chirality on their eigenstates. Nonreciprocal interference underlies these phenomena, as electrons travelling along a closed path gain a phase proportional to the enclosed magnetic flux that depends on direction — evidencing broken time-reversal ($\mathcal{T}$) symmetry. Such geometrical phases [40] and the resulting synthetic magnetism were recently brought to bosonic systems in photonics, acoustics, and cold atoms to explore nonreciprocal functionality [31–34] and various topological insulators [37, 38].

In a parallel, largely unconnected development, researchers turned to non-Hermitian systems including parity-time-($\mathcal{PT}$-)symmetric systems, which feature dynamical phase transitions linked to spectral singularities such as exceptional points (EPs) [98, 231]. Here, controlled gain and loss lead to unique eigenmode symmetries and tuning of *complex* eigenfrequencies ϵ. Bosonic systems form the natural realm for these phenomena, with lasing and self-oscillation ubiquitous in photonics and mechanics. In particular, bosonic *squeezing* is described by Hamiltonians that do not conserve excitation number, and engenders distinct phases showing stable or unboundedly growing dynamics [162, 163].

Very recently, the combination of topology and non-Hermiticity attracted strong interest [106, 217]. Tailoring gain and loss in topological insulators showed lasing into protected states [220, 221, 226] and topological phase transitions [222]. In principle, states with symmetries, dynamics, and spectra that are altogether different from Hermitian chiral systems are expected [218, 219]. Indeed, various non-Hermitian topological phases were predicted, with associated chirally-amplified and unstable edge modes [223–225], quadrature-dependent chiral transport [232, 233] and anomalous bulk-boundary correspondence with extreme sensitivity to boundary conditions [106, 227–230]. However, the rich combination of squeezing interactions and geometrical phases remained experimentally unexplored so far.

Here we demonstrate Aharonov-Bohm (AB) interference and chirality of nanomechanical states in multi-resonator networks where both $\mathcal{T}$-symmetry-breaking geometrical phases and non-Hermiticity are induced through radiation pressure. As exploited in the preceding chapters, suitable laser drives that stimulate frequency-converting transitions give rise to synthetic magnetism for phonons [63, 64]. At the same time, optomechanical [118] or electromechanical control can also enable parametric amplification [157–159]. In this chapter we combine both, using squeezing interactions in addition to particle-conserving interactions to create non-Hermitian dynamics without dissipation [163, 234] and uncover new geometrical phases. Using light to sensitively actuate and detect nanomechanical motion, we reveal the unique effects of this merger on chiral transport, dynamical phases, and squeezing — and actively control them in space and time.

5.2. Experimental platform

We realize combined non-Hermitian dynamics and phononic gauge fields using the experimental platform introduced in chapter 2. For clarity, we recapitulate the

essential ingredients here.

The sliced photonic-crystal nanobeam [64, 145] shown in Figure 2.1 supports multiple non-degenerate MHz-frequency flexural mechanical modes coupled to the optical field of a nanocavity. Each mode j, identified as an individual resonator, changes the cavity frequency by $g_0^{(j)} x_j$ through displacement x_j (normalized to the zero-point amplitude x_{zpf}) and experiences a force proportional to $g_0^{(j)} n_{\mathrm{c}}$, with $g_0^{(j)}$ the vacuum optomechanical coupling rate and n_{c} the intracavity photon number. Mechanical motion is read out from the intensity modulations of a detuned probe laser reflected off the cavity. The detected thermomechanical noise spectrum of the device is shown in Figure 2.3, and reveals several distinct mechanical resonances.

While the (uncoupled) mechanical resonators have well-separated eigenfrequencies Ω_j, interactions are established by temporal modulation of the intensity of a control laser detuned from cavity resonance. For optimal laser detuning $\Delta = -\kappa/(2\sqrt{3})$, with cavity decay rate $\kappa \approx 320$ GHz, mechanical displacement modulates the intracavity intensity instantaneously at phononic timescales ($\kappa \gg \Omega_j$). Mixing of a control laser intensity modulation at the difference frequency $\Omega_k - \Omega_j$ of resonators j and k with the radiation pressure force sideband of resonator j creates a sideband at Ω_k. The resulting 'cross-mode optical spring effect' [64] induces particle-conserving beamsplitter coupling between the resonators at rate $J_{jk} = c_{\mathrm{m}} g_j g_k \Delta/(\Delta^2 + \kappa^2/4)$, scaling with modulation depth c_{m} and optomechanical coupling $g_j = g_0^{(j)}\sqrt{\bar{n}_c}$ enhanced by the average cavity population $\bar{n}_c$(section 2.6).

We describe the resonators by their annihilation operators a_j in frames rotating at Ω_j. The phonon-preserving Hamiltonian that describes the nanomechanical beamsplitter interactions induced by simultaneously applying appropriate modulation tones then reads

$$H^{\mathrm{bs}} = \sum_{j \neq k} J_{jk} e^{-\mathrm{i}\varphi_{jk}} a_j^\dagger a_k, \quad \varphi_{kj} = -\varphi_{jk} \tag{5.1}$$

(5.2)

where the phase offset φ_{jk} of each modulation tone is imprinted nonreciprocally on phonons transferred between the resonators j and k [64]. Indeed, as discussed in the previous chapters, φ_{jk} represents the Peierls phase imprinted by a synthetic magnetic vector potential.

5.3. Non-Hermitian Aharonov-Bohm effect

Using these light-induced nonreciprocal beamsplitter interactions, we demonstrated a three-mode chiral phononic circulator [122] in chapter 3, dubbed the beamsplitter trimer (BST). Still, vastly richer phenomenology is uncovered by introducing squeezing interactions in the nodes and links of the network. We implement single-mode ($j = k$) or two-mode ($j \neq k$) mechanical squeezing by optical modulation at the sum frequencies $\Omega_j + \Omega_k$. As discussed in section 2.6, the resulting

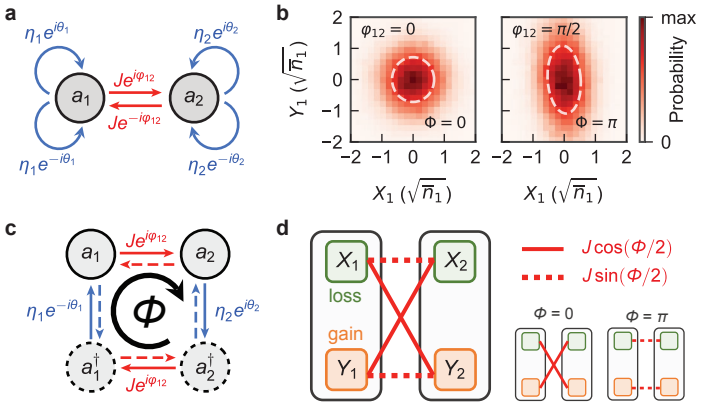

Figure 5.1: **Aharonov-Bohm interference along non-Hermitian squeezing loops (a)** The squeezing dimer encompasses two resonators driven at $2\Omega_j$ and $\Omega_2 - \Omega_1$. These introduce single-mode nanomechanical squeezing (blue self-loops) and beamsplitter coupling (red). We employ the modes labelled (3) and (4) in Fig. 2.3 as resonator 1 and 2, respectively, and tune their linewidths $\gamma_1/(2\pi) \approx \gamma_2/(2\pi) \approx \gamma/(2\pi) = 3.7$ kHz to coincide through opto-thermal backaction (section 2.8.4). **(b)** Histograms of the steady-state phase space distribution of resonator 1 for varying beamsplitter Peierls phase φ_{12}, showing its effect on thermomechanical squeezing. Dashed ellipses depict the standard deviation of the principal components of the quadrature covariance matrix. Here $\theta_1 = \theta_2 = \pi/2$. **(c)** Graph associated to the Hamiltonian matrix, unwrapping self-loops in (a) over particles (annihilated by a_j) and holes (annihilated by $a_j^\dagger$). The clockwise loop is threaded by synthetic flux Φ, the counter-clockwise loop by $-\Phi$. **(d)** Coupling diagram for the resonator quadratures X_j and Y_j, where Φ controls the coupling between squeezed (green) and anti-squeezed (orange) quadratures of the two resonators.

5

effective Hamiltonian reads

$$H^{\mathrm{sq}} = \sum_{j,k} \frac{\eta_{jk}}{2} (e^{\mathrm{i}\theta_{jk}} a_j a_k + e^{-\mathrm{i}\theta_{jk}} a_j^\dagger a_k^\dagger), \tag{5.3}$$

with interaction strength $\eta_{jk} = c_{\mathrm{m}} g_j g_k \Delta/(\Delta^2 + \kappa^2/4)$ and modulation phase θ_{jk} now imprinted on the creation or annihilation of phonon pairs. The squeezing angles θ_{jk} form a powerful control resource, complementing the Peierls phases φ_{jk} exploited in the previous chapters. Indeed, spatially patterned squeezing yields anomalous pairing terms, enabling topological bosonic states unparalleled by their fermionic (e.g. topological superconductor) counterparts and is essential for proposed topological amplifiers [225].

We first consider a 'squeezing dimer' (SD, Figure 5.1a) consisting of two resonators, each single-mode squeezed through $2\Omega_{1,2}$ modulation, and coupled through driving at $\Omega_2 - \Omega_1$. Its Hamiltonian reads

$$H_{\mathrm{SD}} = \frac{\eta_1}{2} e^{i\theta_1} a_1^2 + \frac{\eta_2}{2} e^{i\theta_2} a_2^2 + J e^{i\varphi_{12}} a_2^\dagger a_1 + \mathrm{H.c.}. \tag{5.4}$$

Remarkably, we find that the *level* of squeezing of thermal fluctuations is not only determined by the interactions' magnitudes $\eta_{1,2}$, J, but also by their phases $\theta_{1,2}$, φ_{12}. Figure 5.1b shows single-mode squeezing is maximal when $\varphi_{12} = \pi/2$ and disappears when $\varphi_{12} \in \{0, \pi\}$ if $\theta_1 = \theta_2 = \pi/2$ and $\eta_1 = \eta_2 = \eta$.

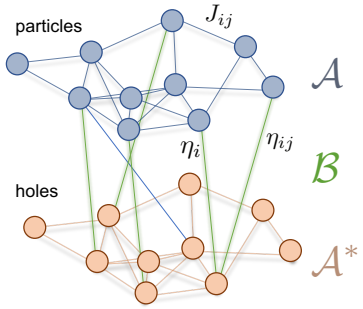

Figure 5.2: **Network graph representation of general quadratic Hamiltonians.** Schematic of an arbitrary N-mode Hamiltonian matrix H, acting on a Nambu-like vector $\boldsymbol{\alpha} = (a_1, \cdots, a_N, a_1^\dagger, \cdots, a_N^\dagger)$ (section 2.7.1). Particle annihilation (hole creation) operators, a_j, are represented by blue nodes, whereas hole annihilation (particle creation) operators are represented by orange nodes. H includes excitation-conserving interactions (matrix $\mathcal{A}$), which link particle operators (e.g. terms $\mathcal{A}_{jk} a_j^\dagger a_k$) and hole operators (e.g. terms $\mathcal{A}_{kj}^* a_k a_j^\dagger$). Squeezing interactions (with complex amplitude matrix $\mathcal{B}$) contain pairs $\mathcal{B}_{jk} a_j^\dagger a_k^\dagger$ which can be visualized to either annihilate two particles j, k or to annihilate a particle in j and create a hole in k, hence the connection between particle and hole networks (green). Mutatis mutandis, terms $\mathcal{B}_{jk}^* a_j a_k$ can be similarly visualized.

We now show that this observation is associated with a *non-Hermitian* version of AB interference. Even though the coupled-mode picture Figure 5.1a shows no plaquette, we can recognise a loop along which excitations experience a geometric phase when combining graph representation with the Bogoliubov-de Gennes (BdG) formalism [162] introduced in section 2.7. In this formalism, a_j and $a_k^\dagger$ are treated as separate degrees of freedom – 'particles' and 'holes' – and squeezing (Equation 5.3) as a *conversion* between particles and holes. An equivalent viewpoint, illustrated in Figure 2.5, is that squeezing couples positive- and negative-frequency components of the mechanical displacement.

As illustrated in Figure 5.2, we represent the mode operators a_j, $a_k^\dagger$ as the nodes of a graph, separated into two layers $\mathcal{G}_a$ and $\mathcal{G}_{a^\dagger}$ for the particle and hole annihilation operators, respectively. The Hamiltonian matrix (Eq. (2.67)) of a general quadratic bosonic system is then visualized by using the hopping matrix $\mathcal{A}$ ($\mathcal{A}^*$) as an adjacency matrix *within* the layer $\mathcal{G}_a$ ($\mathcal{G}_{a^\dagger}$) and the squeezing matrix $\mathcal{B}$, $\mathcal{B}^*$ as an adjacency matrix *between* the layers. Importantly, this representation avoids self-loops to describe on-site parametric amplification [235].

Applied to the squeezing dimer, we find that the graph representing its Hamiltonian matrix in particle-hole space (Figure 5.1c) reveals a conjugate pair of superimposed loops, threaded by gauge-invariant fluxes $\Phi = 2\varphi_{12} - \theta_1 + \theta_2$ and $-\Phi$. As these fluxes govern interference in the loop, they control the connection between the resonators' quadratures (defined such that $X_i = (a_i + a_i^\dagger)/\sqrt{2}$ ($Y_i = i(a_i^\dagger - a_i)/\sqrt{2}$) are squeezed (anti-squeezed) for $J = 0$): While $\Phi = \pi$ connects the squeezed quadratures, maximizing squeezing, $\Phi = 0$ connects squeezed quadrature X_1 to anti-squeezed quadrature Y_2 and vice versa, cancelling the overall squeezing (Figure 5.1d).

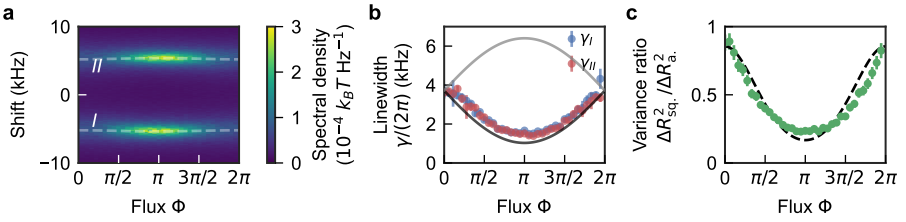

Figure 5.3: **Flux-controlled linewidth modulation and squeezing. (a)** Thermomechanical spectra for the squeezing dimer around Ω_1. **(b)** Sweeping flux continuously tunes the fitted apparent resonance linewidths $\gamma_{I,II}$ (blue and red circles), compared to the theoretical loss rate of the lowest-loss eigenfrequency of $\mathcal{H}_{\mathrm{SD}}$ (solid black). **(c)** Flux-dependent level of squeezing, measured as the ratio of the variances $\Delta R^2_{\mathrm{sq.}}$ and $\Delta R^2_{\mathrm{a.}}$ of the quadratures squeezed and anti-squeezed along the principal axes of the covariance matrix, respectively, in experiment (green) and theory (dashed, section 5.7.5). Here, $J/(2\pi) = 5.37$ kHz, $\eta_1/(2\pi) = \eta_2/(2\pi) = 1.34$ kHz, and loss rates $\gamma_1/(2\pi) \approx \gamma_2/(2\pi) = 3.7$ kHz. ESD, energy spectral density. Error bars in **b** (**c**) are dominated by fitting (statistical) uncertainties, with a small contribution from control parameter fluctuations (section 5.7.1).

5.3.1. Quadrature couplings

To understand how the flux-dependent coupling between gainy and lossy quadratures comes about, we consider the dynamics of the squeezing dimer. Following section 2.7.1, the closed system evolution of the Nambu-like mode vector $\boldsymbol{\alpha} = (a_1, a_2, a_1^\dagger, a_2^\dagger)^T$ is given by $\mathrm{i}\dot{\boldsymbol{\alpha}} = \mathcal{H}_{\mathrm{SD}}\boldsymbol{\alpha}$, and governed by the BdG dynamical matrix $\mathcal{H}_{\mathrm{SD}}$. Even without dissipation ($\gamma_i = 0$), squeezing makes $\mathcal{H}_{\mathrm{SD}}$ necessarily non-Hermitian, preserving only Σ_z-pseudo-Hermiticity ($\Sigma_z = \mathrm{diag}(\mathbb{1}, -\mathbb{1})$, $\mathcal{H}_{\mathrm{SD}}^\dagger = \Sigma_z \mathcal{H}_{\mathrm{SD}} \Sigma_z$) to satisfy bosonic commutation relations [162]. The graph representation discussed above carries over to the BdG dynamical matrix, after replacing $\mathcal{A}^* \mapsto -\mathcal{A}^*$ and $\mathcal{B}^* \mapsto -\mathcal{B}^*$[1].

Inspired by the structure in Figure 5.1c, we reorder the mode vector as $\boldsymbol{\alpha}^L = (a_1, a_2, a_2^\dagger, a_1^\dagger)$ to follow the loop. The corresponding BdG dynamical matrix $\mathcal{H}_{\mathrm{SD}}^L$ can be decomposed as $\mathcal{H}_{\mathrm{SD}}^L = \mathcal{H}_{\mathrm{SD}}^{\circlearrowleft} + \mathcal{H}_{\mathrm{SD}}^{\circlearrowright}$ using the clockwise and counterclockwise contributions

$$\mathcal{H}_{\mathrm{SD}}^{\circlearrowleft} = \begin{pmatrix} 0 & \mathcal{J} & 0 & 0 \\ 0 & 0 & -\mathrm{i}\eta & 0 \\ 0 & 0 & 0 & -\mathcal{J} \\ -\mathrm{i}\eta & 0 & 0 & 0 \end{pmatrix} \quad \text{and} \quad \mathcal{H}_{\mathrm{SD}}^{\circlearrowright} = \left(\Sigma_z \mathcal{H}_{\mathrm{SD}}^{\circlearrowleft} \Sigma_z\right)^\dagger . \tag{5.5}$$

We continue to adopt the gauge $\theta_1 = \theta_2 = \pi/2$, such that $\mathcal{J} = Je^{-\mathrm{i}\Phi/2}$.

Next, we introduce the quadrature vector[2] $\mathbf{q}_{\mathrm{SD}} = (X_1, Y_2, X_2, Y_1) = \mathcal{Q}\boldsymbol{\alpha}^L$ (section 2.7.3) and the corresponding unitary transformation $\mathcal{Q}$. In this basis, the

[1] The geometric phases recognized in the BdG graph are then trivially offset by a multiple of π relative to the Hamiltonian graph.

[2] Note the non-standard ordering of $\mathbf{q}_{\mathrm{SD}}$.

dynamical matrix $\mathcal{H}_{\mathrm{SD}}^{XY} = \mathcal{Q}\mathcal{H}_{\mathrm{SD}}^{\circlearrowleft}\mathcal{Q}^\dagger + \mathcal{Q}\mathcal{H}_{\mathrm{SD}}^{\circlearrowright}\mathcal{Q}^\dagger$ is given by

$$\mathcal{H}_{\mathrm{SD}}^{XY} = \begin{pmatrix} -\mathrm{i}\eta & \mathrm{i}J_\perp & -\mathrm{i}J_\parallel & 0 \\ -\mathrm{i}J_\perp & \mathrm{i}\eta & 0 & \mathrm{i}J_\parallel \\ \mathrm{i}J_\parallel & 0 & -\mathrm{i}\eta & \mathrm{i}J_\perp \\ 0 & -\mathrm{i}J_\parallel & -\mathrm{i}J_\perp & \mathrm{i}\eta \end{pmatrix}, \tag{5.6}$$

where the flux-dependent couplings $J_\parallel = J\sin(\Phi/2)$ (dashed lines in Figure 5.1d) and $J_\perp = J\cos(\Phi/2)$ (solid lines in Figure 5.1d) between gainy and lossy quadratures express the interference between clockwise and counterclockwise processes with nontrivial interaction phases.

5.4. Flux-controlled $\mathcal{PT}$ symmetry

Interestingly, like the synthetic flux in the beamsplitter trimer, the geometric phase Φ impacts the normal mode frequencies of the squeezing dimer. These are now generally complex — being given by the eigenvalues of the non-Hermitian BdG dynamical matrix $\mathcal{H}_{\mathrm{SD}}$. The non-Hermitian character of $\mathcal{H}_{\mathrm{SD}}$ thus carries over to the Aharonov-Bohm-like interference in the BdG loop, where now both frequency *and* linewidth evolve with flux. In the strongly coupled, dynamically stable regime ($J > \eta$, $2\eta < \gamma_j$, Figure 5.3a,b), Φ strongly tunes linewidth and thermal amplitude of the hybridised eigenmodes, in unison with squeezing (Figure 5.3c). The squeezed and anti-squeezed partners recognised for $\Phi = \pi$ in Figure 5.1d correspond to broad and narrow resonances, respectively [236], with the latter dominating the spectrum (section 5.7.2).

The complex eigenvalues define surfaces in $J/\eta - \Phi$ space (Figure 5.4a) with varying degeneracy, indicating distinct dynamical phases. Their physical properties are appreciated by studying the dynamical matrix in the quadrature basis $\mathcal{H}_{\mathrm{SD}}^{XY}$ (Eq. 5.6). For $\Phi = 0$, the matrix $\mathcal{H}_{\mathrm{SD}}^{XY} = \mathrm{diag}(\mathcal{H}_{\mathrm{SD}}^{X_1Y_2}, \mathcal{H}_{\mathrm{SD}}^{X_2Y_1})$ is block-diagonal, with the blocks

$$\mathcal{H}^{X_1Y_2} = i\begin{pmatrix} -\eta & J \\ -J & \eta \end{pmatrix} = \mathcal{H}^{X_2Y_1} \tag{5.7}$$

governing the dynamics of two degenerate, independent 'quadrature dimers' X_1Y_2 and X_2Y_1. Each of the blocks in (5.7) is $\mathcal{P}_{X_jY_j}\mathcal{T}$-symmetric, where the parity operation $\mathcal{P}_{X_jY_k}$ exchanges $X_j \leftrightarrow Y_k$ and the time reversal operation $\mathcal{T}$ is equivalent to complex conjugation $\mathrm{i} \mapsto -\mathrm{i}$.

We thus demonstrate $\mathcal{PT}$-symmetric physics by means of squeezing dynamics, instead of coupling to dissipative baths [163, 234]. The squeezing dimer features a pair of complex eigensurfaces, two-fold degenerate in real and imaginary parts. The only effect of non-zero but equal dissipation is a uniform displacement of the dynamical matrix $\mathcal{H}_{\mathrm{SD}}^{XY} \to \mathcal{H}_{\mathrm{SD}}^{XY} - i\gamma\mathbb{1}/2$ (section 5.7.3), manifesting $\mathcal{PT}$ symmetry in the basis $a_i' = a_i e^{\gamma t/2}$, i.e. 'passive' $\mathcal{PT}$ symmetry in the open system subject to additional local dissipation [98].

The thermomechanical spectra in Figure 5.4b evidence the distinct dynamic phases. Along $\Phi = 0$, we recognise behaviour of the conventional $\mathcal{PT}$-symmetric

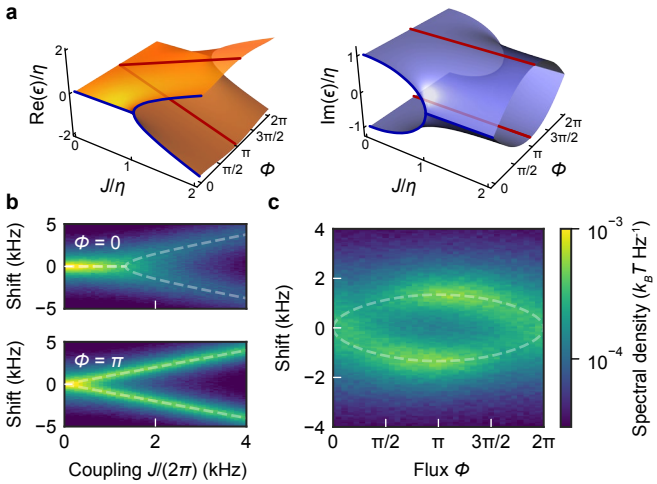

Figure 5.4: **Flux-control of non-Hermitian dynamical phases. (a)** Complex eigenfrequency surfaces of the squeezing dimer in $J-\Phi$ space for $\gamma_i = 0$, tuned by the non-Hermitian AB effect acting on its beamsplitter and squeezing links. For $\Phi \in \{0, 2\pi\}$ and $\eta = J$, $\mathcal{PT}$ symmetry breaks spontaneously and the eigenspectrum coalesces into two second-order EPs. **(b)** Fingerprints of complex degeneracies in the thermomechanical spectra for resonator 1 at $\eta/(2\pi) = 1.34$ kHz and varying J. Nonzero flux breaks $\mathcal{P}_{X_iY_j}\mathcal{T}$ symmetry explicitly, precluding EPs. **(c)** Flux-tuned spectra for resonator 1 when $J/(2\pi) \approx \eta/(2\pi) = 1.34$ kHz, showing mode coalescence at the EP at $\Phi \in \{0, 2\pi\}$. For **b** and **c**, theory eigenvalues $\mathrm{Re}(\epsilon)$ are shown as dashed lines. In this experiment, resonances 3 and 4 have been used, employing dynamical backaction to equilibrate damping rates to $\gamma_i/(2\pi) = 3.7$ kHz (section 2.8.4). Fits of frequencies and linewidths are shown in Figure 5.5.

5

dimer [98]: Eigenmodes (hosted by quadrature dimers) respect $\mathcal{PT}$ symmetry for $J > \eta$, with equal linewidths and splitting increasing with J. For $J < \eta$, $\mathcal{PT}$ symmetry is spontaneously broken, with degenerate frequencies independent of J, while linewidths split (Figure 5.5). $\mathcal{H}_{\mathrm{SD}}$ becomes defective at a degenerate pair of second-order exceptional points (one per quadrature dimer), when $J = \eta$. Accordingly, for $\Phi = 0$, the complex eigenfrequencies for each block in (5.7) are given by $\epsilon = \pm\sqrt{J^2 - \eta^2}$.

Finite fluxes break the $\mathcal{P}_{X_jY_k}\mathcal{T}$ symmetry of $\mathcal{H}_{\mathrm{SD}}^{XY}$ explicitly, eliminating exceptional points for any J or η (Figure 5.4b, bottom). The effect of flux is striking for $J \approx \eta$ (Figure 5.4c), where we find strong tuning of both frequency and linewidth, with eigenmodes coalescing at the degenerate exceptional points $\Phi \in \{0, 2\pi\}$.

Finally, we return to the role of squeezing. As shown in Figure 5.6a for $\Phi = 0$, the squeezing of the intra-mode quadratures X_1Y_1 and X_2Y_2 is gradually cancelled as J is increased. However, advised by the formation of quadrature dimers for that flux, we look for, and observe, effective two-mode squeezing between the inter-mode quadratures X_1Y_2 and X_2Y_1 instead (Figure 5.6b). The strength of the effective two-mode squeezing, expressed by the measured covariances $\sigma(X_j, Y_k) = \langle X_jY_k\rangle$ in Figure 5.6c, attains an optimum for beamsplitter strength $J_{\mathrm{opt}}^2 = (\gamma^2 - 4\eta^2)/4$ in the case of equal dissipation rates $\gamma_j = \gamma$ and bath occupations. This optimum reflects

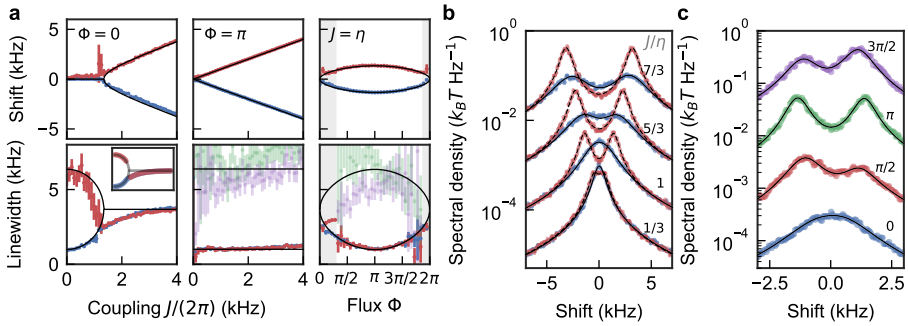

Figure 5.5: **Frequency and linewidth modulation in the squeezing dimer. (a)** Experimental resonance frequencies (top) and linewidths (bottom) obtained by fitting a superposition of Lorentzian lineshapes to the thermomechanical spectra in Figure 5.4b,c. Grey curves indicate theoretical values of $\mathrm{Re}\,(\epsilon)$ (top) and $\mathrm{Im}\,(\epsilon)$ (bottom). Two peaks were fitted to the spectra for $\Phi = 0$ (left), as for that flux both eigenvalues are expected to be doubly degenerate for all J. The observed branching of frequencies and linewidths is characteristic of an exceptional point. Four peaks were instead fitted for $\Phi = \pi$ (middle), where the exceptional point behaviour completely vanishes, and spectra are fitted well with a combination of broad and narrow peaks at two frequencies. When varying flux in the rightmost panel, the grey shaded areas depict the regions near $\Phi = 0, \pi$ where a fit of two peaks provided better results than a fit of four. Note that near the exceptional point, the non-Lorentzian nature of the spectrum causes the fitted values of the Lorentzian linewidths to deviate from the theoretical $\mathrm{Im}(\epsilon)$. This origin of the deviation is confirmed by applying the same fit procedure to theoretically predicted spectra (inset, bottom left), which shows the same deviation. Error estimation is described in section 5.7.1. **(b)** Thermomechanical spectra for several values of J/η, for $\Phi = 0$ (blue) and $\Phi = \pi$ (red). Solid lines show Lorentzian fits. **(c)** Similar, for different values of Φ at $J = \eta$.

a trade-off, as J is increased, between the rotation of the effective squeezing axes in the four-dimensional $X_{1,2}Y_{1,2}$-space from single-mode squeezing to two-mode squeezing, and an overall reduction in squeezing (section 5.7.5).

5.5. Higher-order EPs and chiral amplification

The squeezing dimer's behaviour is intrinsically quadrature-dependent, as the paths in quasiparticle space link conjugated elements a_j and $a_j^\dagger$ directly or indirectly. The response to any real excitation (a superposition of a_j's and $a_j^\dagger$'s) then depends on the particle-hole phase difference, i.e. the excited quadrature. Another example is phase-dependent amplification in the bosonic Kitaev chain (without synthetic flux) [162, 232], which we will explore in the subsequent chapters. One can, however, conceive loops without such links, expecting quadrature-independent nonreciprocity and chirality. The squeezing-free ($\mathcal{B} = 0$), Hermitian BST represents a trivial example, comprising two *disjoint* loops connecting all particles and holes, respectively (Figure 5.7a).

5.5.1. Disjoint particle-hole loops

As we will now see, a quasiparticle network with disjoint loops results in a quadrature-independent response. In general, owing to the charge conjugation

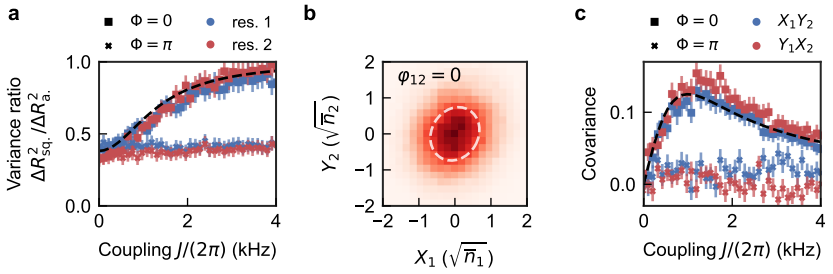

Figure 5.6: **Tunable single-mode and effective two-mode squeezing in the squeezing dimer. (a)** Intra-resonator squeezing as a function of the beamsplitter coupling J for $\eta_1/(2\pi) = \eta_2/(2\pi) = 0.5$ kHz, measured as the ratio of the variances $\Delta R^2_{\mathrm{sq.}}$ and $\Delta R^2_{\mathrm{a.}}$ of the quadratures squeezed and anti-squeezed along the principal axes of the covariance matrix, respectively. For this experiment, resonances labelled (1) and (2) in Fig. 2.3 were used. For $\Phi = \pi$, the squeezing persists as J is increased. In contrast, for $\Phi = 0$, when squeezed–anti-squeezed quadrature dimers are formed, cancellation of single-mode squeezing is observed as the variance ratios tend to 1 for increasing J. Theory squeezing ratios (dashed line) are calculated using the average $\gamma/(2\pi) = 2.2$ kHz of the experimental dissipation rates $\gamma_{1,2} = \{2.6, 1.9\}$ kHz and equal bath occupations $\bar{n}^{\mathrm{th}}_j$ for simplicity. Optothermal backaction tunes the effective $\bar{n}^{\mathrm{th}}_1 \approx \bar{n}^{\mathrm{th}}_2$ to within a few per cent. **(b)** Two-mode squeezing observed in the phase-space distribution of cross-resonator quadratures X_1 and Y_2 for $\Phi = 0$, $J = 3.5$ kHz. The dashed ellipse depicts the standard deviation of the principal components of the quadrature covariance matrix. **(c)** Covariance of the coupled quadrature pairs X_1Y_2 and Y_1X_2 as a function of J, showing no correlations for $\Phi = \pi$. For $\Phi = 0$, positive correlations $\sigma(X_1, Y_2), \sigma(Y_1, X_2) > 0$ are found when J is increased, as predicted in theory (dashed line). Error bars in **a** and **c** reflect statistical uncertainty and control parameter stability (section 5.7.1).

symmetry $\mathcal{C}$ discussed in section 2.7.1, each particle-hole loop L involving the nodes $\boldsymbol{\alpha}_L = (a_j^{(\dagger)}, \ldots, a_k^{(\dagger)})^T$ comes with a partner L^* involving the conjugated nodes $\boldsymbol{\alpha}_L^\dagger$. In the case that all M loop pairs are disjoint, the operation Π that permutes the mode vector $\boldsymbol{\alpha}$ by loop, i.e. $\boldsymbol{\alpha} \mapsto \Pi\boldsymbol{\alpha} = (\boldsymbol{\alpha}_{L_1}, \boldsymbol{\alpha}^\dagger_{L_1}, \ldots, \boldsymbol{\alpha}_{L_M}, \boldsymbol{\alpha}^\dagger_{L_M})$, *block-diagonalizes* $\mathcal{H}$:

$$\mathcal{H} \mapsto \mathcal{H}' = \Pi\mathcal{H}\Pi^\dagger = \mathrm{diag}(\mathcal{L}_1, -\mathcal{L}_1^*, \ldots, \mathcal{L}_M, -\mathcal{L}_M^*). \tag{5.8}$$

The symmetries of the BdG matrix relate the dynamical matrices $\mathcal{L}_m, -\mathcal{L}_m^*$ of partnered loops. Moreover, as the loops are disjoint, $\mathcal{L}_m, -\mathcal{L}_m^*$ will never mix particles and their corresponding hole excitations as they propagate through the graph.

Dropping the index m, the decoupled evolution of a single loop pair is thus given by $\mathrm{i}\dot{\boldsymbol{\alpha}}_L = \mathcal{L}\boldsymbol{\alpha}_L$ and $\mathrm{i}\dot{\boldsymbol{\alpha}}^\dagger_L = -\mathcal{L}^*\boldsymbol{\alpha}^\dagger_L$. Furthermore, the evolution of the energy vector $\mathbf{n}(t) = (a_j^\dagger a_j, \ldots, a_k^\dagger a_k)$ is given by

$$\mathbf{n}(t) = e^{\mathrm{i}\mathcal{L}^* t}\mathbf{n}(0)e^{-\mathrm{i}\mathcal{L}t}. \tag{5.9}$$

Importantly, when a single resonator j is initially excited, the evolution (5.9) is insensitive to the relative phase between $a_j(0)$ and $a_j^\dagger(0)$ that indicates the excited quadrature in j.

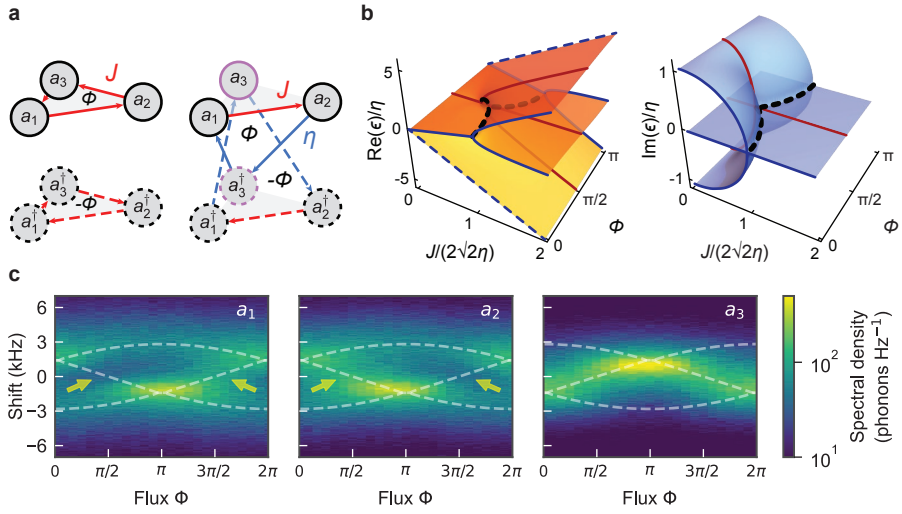

Figure 5.7: **Chirality in a non-Hermitian network. (a)** Sketch of the networks in particle-hole space corresponding to the beamsplitter trimer realized in chapter 3 (left) and the singly conjugated trimer (right), manifesting their topological resemblance. **(b)** Complex eigensurfaces for the singly conjugated trimer ($\gamma_i = \gamma$) depicted from $\Phi = 0$ to $\Phi = \pi$ for clarity. Imaginary parts are referenced to γ. A black dotted line highlights an exceptional contour separating stable and unstable dynamical phases. **(c)** Thermomechanical spectra of the three resonators (label denoted in the plot) for $\eta/(2\pi) = 1$ kHz, $J = 2\sqrt{2}\eta$. Measurement-based feedback (section 2.8.6) is employed to equalise mechanical loss rates $\gamma_j/(2\pi) = \gamma/(2\pi) = 4$ kHz. The sideband of the 'conjugated' resonator 3 is reflected in frequency compared to the other two. Localisation of eigenstates is observed, including 1-2 asymmetry indicated by arrows. Theoretical eigenfrequencies are shown as dashed lines.

5

5.5.2. The singly conjugated trimer

We find a non-Hermitian system encompassing disjoint loops by 'conjugating' one resonator in the beamsplitter trimer, i.e. swapping $a_3 \leftrightarrow a_3^\dagger$. We implement this 'singly conjugated trimer' (SCT) by modulating at $\Omega_2 - \Omega_1, \Omega_1 + \Omega_3$ and $\Omega_2 + \Omega_3$. The latter induce two-mode squeezing, resulting in the Hamiltonian

$$H_{\mathrm{SCT}} = Je^{i\varphi_{12}} a_2^\dagger a_1 + \eta_{23} e^{i\theta_{23}} a_3 a_2 + \eta_{13} e^{-i\theta_{13}} a_1^\dagger a_3^\dagger + \mathrm{H.c.} \tag{5.10}$$

and loops threaded by fluxes $\Phi = \varphi_{12} + \theta_{23} - \theta_{13}$ and $-\Phi$ (Figure 5.7a). The dynamics of each loop vector $\boldsymbol{\alpha}_L = (a_1, a_2, a_3^\dagger)$, $\boldsymbol{\alpha}_L^\dagger$ are decoupled and governed by the non-Hermitian blocks

$$\mathcal{L} = \begin{pmatrix} 0 & Je^{-\mathrm{i}\Phi} & \eta \\ Je^{\mathrm{i}\Phi} & 0 & \eta \\ -\eta & -\eta & 0 \end{pmatrix} \quad \text{and} \quad -\mathcal{L}^*, \tag{5.11}$$

respectively. Here, we adopt the gauge where $\theta_{23} = \theta_{13} = 0$ such that $\Phi = \varphi_{12}$.

The interplay of Aharonov-Bohm interference and non-Hermiticity in the singly conjugated trimer induces dynamical stability transitions, unmatched by BST. Figure 5.7a shows these as surfaces in $J/\eta - \Phi$ space for $\eta_{13} = \eta_{32} = \eta$ and equal

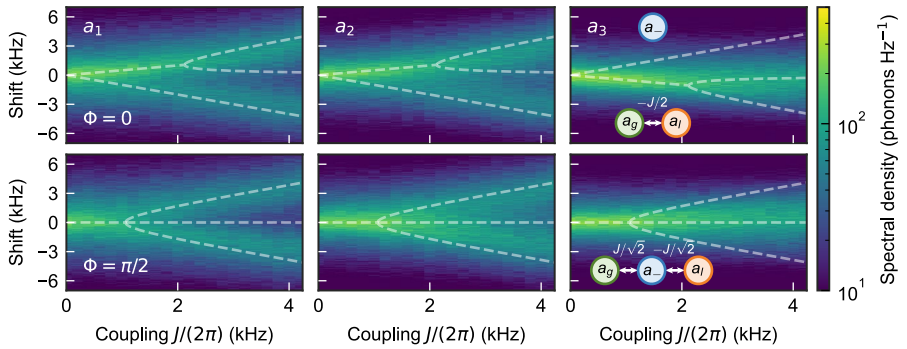

Figure 5.8: **Flux-controlled higher-order exceptional points.** Thermomechanical spectra for resonators 1, 2 and 3 for $\eta/(2\pi) = 0.75$ kHz for a trivial flux $\Phi = 0$ (top), and in the maximally chiral case $\Phi = \pi/2$ (bottom). Theoretical eigenfrequencies are shown as dashed lines. The flux-dependent coupling topology for the effective resonators a_g and a_l morphs a second-order exceptional point into a third-order one (see text). Insets show the effective $\mathcal{P}_{gl}\mathcal{T}$-symmetric dimer/trimer structure for both flux values.

dissipation $\gamma_j = 0$. We identify a stable phase with real eigenfrequencies and an unstable phase with three distinct imaginary parts.

Interestingly, for $J = 2\sqrt{2}\eta$ the (real) eigenvalues of a single loop of $\mathcal{H}_{\text{SCT}}$ coincide with those of a homogeneous BST ($J_{jk} = J$) for all Φ. The thermal spectra in Figure 5.7c show, however, that the response around Ω_3 associated with the 'conjugated' resonator (3) appears frequency-reflected, since particles (holes) evolve with positive (negative) frequencies in the non-rotating frame. Moreover, we observe asymmetries between resonators 1 and 2 in the middle band's thermal amplitude at $\Phi \in \{\pi/2, 3\pi/2\}$. This asymmetric, flux-controlled localisation of fluctuations — unattainable in the BST if $J_{31} = J_{23}$ — arises from the combination of chirality and squeezing and persists even for vacuum fluctuations (section 5.7.6). These asymmetries, akin to chiral, incoherently pumped dynamics in $\mathcal{PT}$-symmetric trimers [237], suggest the singly conjugated trimer functions like a phononic nonreciprocal amplifier [31, 32, 34, 225].

We see the singly conjugated trimer features an exceptional *contour* in the $J/\eta - \Phi$ parameter space (Figure 5.7b). As for the squeezing dimer, this relates to the spontaneous breaking of a parity-time ($\mathcal{P}_{gl}\mathcal{T}$) symmetry. The appropriate parity operation $\mathcal{P}_{gl}$ now exchanges the effective quasiparticle operators $a_{g,l} = (a_+ \mp i a_3^\dagger)/\sqrt{2}$, where $a_+ = (a_1 + a_2)/\sqrt{2}$ is the symmetric superposition of the beamsplitter-coupled resonators. Notably, a_g and a_l are the 'gainy' and 'lossy' eigenmodes for the SCT with $J = 0$, when they have complex eigenfrequencies $\epsilon_{g,l} = \pm\sqrt{2}i\eta$.

Complemented by the anti-symmetric mode $a_- = (a_1 - a_2)/\sqrt{2}$, the modes $\{a_l, a_g, a_-\}$ form a complete basis. The unitary transformation U_{gl} to this effective

basis (i.e. $\boldsymbol{\alpha}_{gl} = (a_l, a_g, a_-) = U_{gl}\boldsymbol{\alpha}_L$) reads

$$U_{gl} = \frac{1}{\sqrt{2}} \begin{pmatrix} \frac{\mathrm{i}}{\sqrt{2}} & \frac{-\mathrm{i}}{\sqrt{2}} & -1 \\ \frac{\mathrm{i}}{\sqrt{2}} & \frac{-\mathrm{i}}{\sqrt{2}} & 1 \\ 1 & 1 & 0 \end{pmatrix}. \tag{5.12}$$

In this basis, the loop matrix $\mathcal{L}_{gl} = U_{gl}\mathcal{L}U_{gl}^{\dagger} = \Xi + \Theta$ splits into a gain/loss contribution

$$\Xi = \mathrm{diag}\left(-\mathrm{i}\sqrt{2}\eta, \mathrm{i}\sqrt{2}\eta, 0\right) = U_{gl}\left(\mathcal{L}|_{J=0}\right)U_{gl}^{\dagger} \tag{5.13}$$

that reflects the complex eigenvalues of $\mathcal{L}$ when $J = 0$, and the interaction/frequency shift contribution

$$\Theta = \begin{pmatrix} \frac{1}{2}J\cos(\Phi) & -\frac{1}{2}J\cos(\Phi) & \frac{J\sin(\Phi)}{\sqrt{2}} \\ -\frac{1}{2}J\cos(\Phi) & \frac{1}{2}J\cos(\Phi) & \frac{J\sin(\Phi)}{\sqrt{2}} \\ -\frac{J\sin(\Phi)}{\sqrt{2}} & \frac{J\sin(\Phi)}{\sqrt{2}} & -J\cos(\Phi) \end{pmatrix}. \tag{5.14}$$

In contrast to the squeezing dimer, the dynamical matrix $\mathcal{L}_{gl}$ respects $\mathcal{P}_{gl}\mathcal{T}$-symmetry for arbitrary flux, where the time-reversal operator $\mathcal{T}$ applies conjugation $\mathrm{i} \mapsto -\mathrm{i}$ and reverses the flux $\Phi \mapsto -\Phi$. The coupling topology, however, is flux-dependent. We find that when $\Phi \in \{0, \pi\}$, a beamsplitter interaction $J > 0$ couples $a_g \leftrightarrow a_l$, constructing a $\mathcal{P}_{gl}\mathcal{T}$-symmetric dimer with a second-order EP at $J = 2\sqrt{2}\eta$ (Figure 5.8, top). On the other hand, for $\Phi \in \{\pi/2, 3\pi/2\}$, the third, gain-neutral mode a_- — uncoupled when $\Phi \in \{0, \pi\}$ — couples to $a_{l,g}$ in a loss-neutral-gain chain configuration. Interestingly, this trimer features spontaneous $\mathcal{P}_{gl}\mathcal{T}$ symmetry breaking at a *third-order* EP at $J = \sqrt{2}\eta$ (Figure 5.8, bottom). Indeed, the presence of a higher-order EP sitting at the nexus of two second-order exceptional contours [238] is mandated by eigensurface topology (Figure 5.7b).

Nevertheless, a non-trivial flux still breaks the mirror symmetry $\mathcal{P}_{12}$ that exchanges $a_1 \leftrightarrow a_2$. In the dynamically stable regime, we predict chiral dynamics for $\Phi = \pm\pi/2$ (Figure 5.9a) analogous to those of the beamsplitter trimer (Figure 3.2). However, due to the particle-non-conserving nature of squeezing, this periodic *pseudo-Hermitian evolution* (for $\gamma_j = 0$) now features subsequent amplification steps – where populations grow above the initial amplitude – and attenuation steps. The flux-induced chirality is reflected in the order in which these steps take place.

The flux-induced breaking of $\mathcal{P}_{12}$ also impacts the $\mathcal{P}_{gl}\mathcal{T}$-symmetry-broken phase. In a three-site, gainy-neutral-lossy chain, $\mathcal{PT}$-symmetry-broken states delocalise non-uniformly over central and boundary sites (here the pairs $a_g - a_-$ and $a_- - a_l$) [103]. Crossing the third-order EP at $\Phi = \pm\pi/2$ thus biases gain towards the bare oscillator a_1 ($\Phi = \pi/2$) or a_2 ($\Phi = -\pi/2$). This flux-tunable chiral gain becomes striking in the transient, unstable dynamics of the singly conjugated trimer, as shown in Figure 5.9b for gain exceeding dissipation. There, an initial excitation in resonator 1 (2) is amplified coherently – above initial amplitudes – towards 2 (1) for flux $\Phi = \pi/2$ ($\Phi = -\pi/2$), and attenuated quickly in the opposite

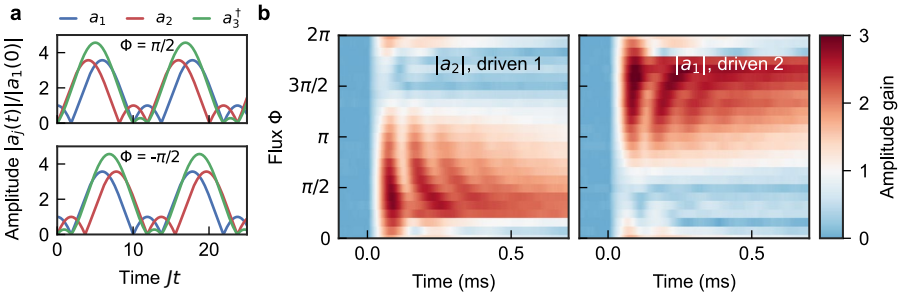

Figure 5.9: **Chiral non-Hermitian evolution. (a)** Theoretical dissipation-less ($\gamma_j = 0$) evolution of a coherent excitation initialized in resonator 1 of the SCT (amplitude $a_1(0)$) for fluxes $\Phi = \pm\pi/2$. Here, $\eta/J = 0.6$ such that the system is dynamically stable. The flux then determines the order in which subsequent amplification and attenuation steps take place as the excitation is transferred back and forth between the beamsplitter-coupled resonators 1 and 2. **(b)** Measured ratio between instantaneous and initial coherent amplitudes (normalized to phonon number), in the unstable and nonlinear regime $\eta/(2\pi) = J/(2\pi) = 5$ kHz, without feedback (mechanical loss rates $\gamma_j/(2\pi) = \{2.5, 1.6, 4.1\}$ kHz). Resonator 1 (left) or 2 (right) is driven for $t < 0$, and couplings are established when $t > 0$. This induces chirally amplified transport to the other resonator and self-oscillation bounded by nonlinear dynamics.

direction. Conversely, for $\Phi = 0$, gain distributes evenly over resonators 1 and 2 showing reciprocal dynamics. Linear analysis breaks down as the system crosses the instability threshold ($\mathrm{Im}(\epsilon) = 0$), where we see optomechanically-induced Duffing nonlinearities cause amplitude saturation and self-oscillations, even at only a few times the thermal amplitude. Indeed, this points the way to investigating strongly nonlinear systems with broken Hermiticity and time-reversal symmetry.

5.6. Conclusion and outlook

In conclusion, we observed chiral, non-Hermitian phonon dynamics in nano-optomechanical networks with fully controlled beamsplitter and squeezing interactions. Through a powerful diagrammatic framework, we uncovered new geometrical phases acting on excitations in particle-hole space that control $\mathcal{PT}$ symmetry through a non-Hermitian Aharonov-Bohm effect. The resulting phenomena of tunable squeezing, (higher-order) exceptional points and nonreciprocal amplification point to applications in nanomechanical sensing [239], signal processing [225], and Ising machines [240]. These mechanisms could be equally powerful in other bosonic domains, from photonics to cold atoms. Although the effects were probed with thermal and coherent excitations, they persist down to the quantum domain for suitable system parameters and controls, forming essential ingredients to explore new linear and nonlinear non-Hermitian topological phases.

5.7. Appendices

The following sections contain further details supporting this chapter.

5.7.1. Error estimation

The error on fitted values like frequencies and linewidths originates from multiple sources. Error bars in plots indicate $\pm 2\sigma$, i.e. a 95% confidence interval for a normal distribution.

The stability of the interaction strength over typical measurement timescales (~ 100 s) is controlled by the stability of the drive laser power (relative standard deviation $\sigma_{P_{\text{drive}}}/P_{\text{drive}} \approx 2 \cdot 10^{-3}$) entering Equation 2.64 through $\delta\Omega_i$ and the stability of the modulation tone amplitude (relative standard deviation $\sigma_{c_{\text{m}}}/c_{\text{m}} \approx 10^{-3}$).

In addition, jitter of the spring shift $\delta\Omega_i$ due to variations in drive laser power and incoupling efficiency controls the detuning of the control signals. For resonators with comparable $g_0^{(j)}$ (i.e. resonators 1 & 2 and resonators 3 & 4), the effect of detuning jitter on beamsplitter interactions – which depend only on their frequency difference – is reduced. To estimate the effect of detuning jitter on the effective linewidth change induced by squeezing interactions, a Monte Carlo method is employed.

Finally, the fit uncertainty is estimated using a numerical approximation of the Jacobian matrix.

The standard error of the experimental (co)variances $\sigma(A,B)$ of quadratures A and B is estimated using the statistical relationship $\text{Std}(\sigma(A,B)^2) \approx \sqrt{\frac{1}{n-1}\left(\sigma(A,B)^4 + \sigma(A,A)^2\sigma(B,B)^2\right)}$ where Std denotes the standard deviation. Here, n is the number of thermally independent measurement points, given by $n = T\gamma_j/2$, where $T = 0.3$ s is the duration of the measurement record and γ_j is the dissipation rate of the resonator involved.

5.7.2. Subdominant and non-Lorentzian spectral features in the squeezing dimer

In the thermomechanical noise spectra of the squeezing dimer shown in Figure 5.4, we expect narrow and broad, frequency-degenerate, resonances. We show this in the ideal SD ($\gamma_j = \gamma$), whose spectrum is obtained in closed form using the relation (4.26) obtained from the quantum regression theorem (section 4.2.2).

The noise spectrum of resonator $j \in (1,2)$ is given by the diagonal element $\mathcal{S}_{jj}(\omega)$. An explicit calculation for the SD shows that even in the simplified limit of equal resonator bath occupations $\bar{n}_j^{\text{th}} = \bar{n}^{\text{th}}$, the spectrum consists of 4 superimposed Lorentzian responses located at the real parts of the eigenfrequencies of $\mathcal{H}_{\text{SD}}$ for $\Phi = \pi$, where two pairs of resonances split by $2J$ and

$$\mathcal{S}_{jj}(\omega) \propto \gamma \sum_{\pm} \left(\frac{\bar{n}^{\text{th}} + 1}{(\gamma + 2\eta)^2 + 4(\omega \pm J)^2} + \frac{\bar{n}^{\text{th}}}{(\gamma - 2\eta)^2 + 4(\omega \pm J)^2} \right). \quad (5.15)$$

From Equation 5.15, it is apparent that the spectral weight in the rotating frame at $\pm J$ in the stable regime ($\gamma > 2\eta$) is concentrated in a dominant, narrow resonance with linewidth $\gamma - 2\eta$, on top of an additional, heavily damped contribution with linewidth $\gamma + 2\eta$.

In contrast, the branch-cut topology mandated by the EP at $\Phi = 0$ results in a non-Lorentzian thermal response. If $\Phi = 0$, the spectrum contains non-Lorentzian contributions

$$\begin{aligned} \mathcal{S}_{jj}(\omega) &\propto \frac{2\gamma\left[(2\bar{n}^{\mathrm{th}}+1)\left(\gamma^2+4\left(\eta^2+J^2+\omega^2\right)\right)-4\gamma\eta\right]}{d(\omega)}, \\ d(\omega) &= 8\omega^2\left(\gamma^2+4\left(\eta^2-J^2\right)\right)+\left(\gamma^2-4\left(\eta^2-J^2\right)\right)^2+16\omega^4. \end{aligned} \tag{5.16}$$

Equation 5.16 reduces at the EP ($J = \eta$) to an expression which shows directly a double-Lorentzian response [241]:

$$\mathcal{S}_{jj}(\omega) \propto \frac{\gamma}{2}\frac{(2\bar{n}^{\mathrm{th}}+1)\left(2J^2+\gamma^2/4+\omega^2\right)-\gamma J}{\left(\gamma^2/4+\omega^2\right)^2}. \tag{5.17}$$

This functional form implies deviations in the experimental linewidths in the vicinity of an EP obtained from Lorentzian spectral fitting (Figure 5.3).

5.7.3. Passive $\mathcal{PT}$ symmetries

We discuss the role of $\mathcal{PT}$-symmetry in systems with dissipation. When squeezing interactions – which inter-convert particles and holes – are absent ($\mathcal{B} = 0$), the dynamics of a_i and $a_i^\dagger$ are independent, and simply governed by the Hermitian matrices $\mathcal{A}$ and $-\mathcal{A}^*$, respectively (section 2.7.1), in the case of no dissipation. On top of this, if the matrix $\Gamma = \gamma\mathbb{1}$ expresses equal dissipation rates, the dynamics can be simply mapped to the closed system via a rigid displacement of the imaginary parts of eigenvalues by $\gamma/2$. This displacement is equivalent to a dynamically-offset basis transformation $\boldsymbol{\alpha}'(t) = e^{\frac{\gamma}{2}t}\boldsymbol{\alpha}(t)$ that relates the solutions of ideal and dissipative harmonic oscillators [242]. However, if squeezing is present ($\mathcal{B} \neq 0$), $\mathcal{M}$ and $\mathcal{H}$ are non-Hermitian even for $\Gamma = 0$. The mechanical modes then exhibit *non-Hermitian dynamics* in the dynamically-offset basis as well.

The time evolution of the mechanical amplitudes $\boldsymbol{\alpha}'(t)$ can be expressed in terms of the spectral decomposition of $\mathcal{H}$. A non-Hermitian $\mathcal{H}$ can host eigenvectors with complex eigenfrequencies ϵ. The different character of eigenfrequencies or *dynamical phases* in parameter space links to generalised parity-time ($G\mathcal{PT}$) symmetries of $\mathcal{H}$ and the associated eigenvectors fulfilling or spontaneously breaking the symmetry [162]. For example, purely oscillatory eigenmodes (real eigenfrequencies) indicate a stable phase (eigenvectors fulfil $G\mathcal{PT}$ symmetry), while positive imaginary eigenfrequencies indicate an unstable phase (eigenvectors break $G\mathcal{PT}$ symmetry). We note that $G\mathcal{PT}$ symmetry coexists with the other built-in symmetries of $\mathcal{H}$ (section 2.7.1) that reflect a_i-$a_i^\dagger$ splitting redundancies and must be always fulfilled by the eigenvectors.

For homogeneous dissipation ($\gamma_i = \gamma$), the symmetries of the open-system dynamical matrix $\mathcal{M}$ (section 2.7.2) are trivially related to those of $\mathcal{H}$, since $\mathcal{M} \mapsto \mathcal{H}$ in the dynamically offset basis $\boldsymbol{\alpha}'(t)$. The symmetry classification of $\mathcal{H}$ thus offers insight into dynamical phases, eigensurface topology and symmetry breaking in the open system. As an example, $\mathcal{PT}$ symmetry in $\mathcal{H}$ [95, 243] corresponds to 'quasi' or 'passive' $\mathcal{PT}$ symmetry in $\mathcal{M}$ [98, 99, 244]. In our systems, a dynamical phase

transition (i.e. spontaneous symmetry breaking) is often accompanied by an EP [103, 245] where eigenvalues and eigenvectors simultaneously coalesce and $\mathcal{H}$ is non-diagonalisable. Alternatively, eigenvalues can split off the real axis without diagonalisability loss [162].

5.7.4. Hermitian vs. non-Hermitian Aharonov-Bohm effect

Here we provide further mathematical background for the comparison between the Hermitian and the non-Hermitian Ahoronov-Bohm effect discussed in section 5.3. We use as an example a single loop with N nodes, which can be particle-like or include both particles and hole nodes. In a Hermitian ring ($\mathcal{B} = 0$), with coupling amplitudes J and periodic boundary conditions, the Hamiltonian matrix H (Equation 2.67) is diagonal in the Fourier basis $a_k = \sum_{j=1}^{N} a_j e^{-2\pi i j k/N}/\sqrt{N}$ with discrete wavenumbers k.[3] Noting $\sum_{j=1}^{N} e^{2\pi i j(k-k')/N} = N\delta_{k,k'}$ and choosing a gauge where all Peierls phases are equally distributed, $\varphi_{ij} = \Phi/N$, the ring Hamiltonian reads

$$H_{\text{ring}} = J\sum_{j=1}^{N} a_j^\dagger a_{j+1} e^{i\Phi/N} + \text{H.c.}.$$

This is transformed to the Fourier basis as

$$\begin{aligned} H_{\text{ring}} =& \frac{J}{N}\sum_{k,k'} a_k^\dagger a_{k'} e^{2\pi i j(k-k')/N} e^{2\pi i((k+\Phi/(2\pi))/N)} + \text{H.c.} \\ =& 2J\sum_{k} \cos\left((2\pi k + \Phi)/N\right) a_k^\dagger a_k. \end{aligned} \tag{5.18}$$

Aharonov-Bohm interference is manifest in the second line of Equation 5.18, where the phases φ_{ij} displace the wavenumber k, after being combined via $\sum_{k'}$.

We seek a generalisation of this idea to loops that involve particles and holes. In the BdG formalism, a Hermitian loop decomposes into a pair of particle-hole-related disjoint loops. The BdG matrix $\mathcal{H}$ in (2.68) is thus Peierls-phase dependent – from now on explicitly stated with a curly bracket notation – through the gauge-dependent Hamiltonian matrix $H(\{\varphi_{ij}\}) = \text{diag}(\mathcal{A}(\{\varphi_{ij}\}), \mathcal{A}^*(\{\varphi_{ij}\}))$. Fourier decomposition is equivalent to the block diagonal unitary transformation $\boldsymbol{\alpha}' = \mathcal{U}_H\boldsymbol{\alpha}$ with $\mathcal{U}_H = \text{diag}(U, U^*)$, where $U_{kj} = e^{-2\pi i j k/N}/\sqrt{N}$ preserves bosonic commutators ($[\mathcal{U}_\text{H}, \Sigma_z] = 0$). The BdG matrix transforms as

$$\mathcal{H}(k) = \Sigma_z \text{diag}(U^\dagger \mathcal{A}(\{\varphi_{ij}\})U, U^\dagger \mathcal{A}^*(\{\varphi_{ij}\})U), \tag{5.19}$$

with a diagonal matrix at the r.h.s., given $\mathcal{A}$ is circulant [246]. Interference including nontrivial Peierls phases now occurs within each block of $\mathcal{H}(k)$.

For loops involving particles and holes, we define Fourier modes $\mathcal{U}_\text{NH}$, with $\boldsymbol{\alpha}' = \mathcal{U}_\text{NH}\boldsymbol{\alpha}$ and $(\mathcal{U}_\text{NH})_{kj} = e^{-2\pi i j k/N}/\sqrt{N}$ that diagonalise the (Hermitian)

[3] $k \in \{-[N/2], \cdots, [N/2]\}$ for N odd, or $k \in \{-[N/2], \cdots, [N/2]-1\}$ for N even, where [] denotes the integer part function.

Hamiltonian matrix H:

$$H(\{\varphi_{ij}\},\{\theta_{ij}\}) \mapsto \mathcal{U}_{\mathrm{NH}}^{\dagger} H(\{\varphi_{ij}\},\{\theta_{ij}\})\mathcal{U}_{\mathrm{NH}}. \tag{5.20}$$

Importantly, $\mathcal{U}_{\mathrm{NH}}$ no longer respects bosonic commutation relations ($[\mathcal{U}_{\mathrm{NH}},\Sigma_z]\neq 0$), and thus does not diagonalise $\mathcal{H}$. Instead, $\mathcal{H}\mapsto\mathcal{H}'=\mathcal{U}_{\mathrm{NH}}^{\dagger}\mathcal{H}\mathcal{U}_{\mathrm{NH}}$ with

$$\mathcal{H}'(\{\varphi_{ij}\},\{\theta_{ij}\}) = \mathcal{V}\Lambda(\{\varphi_{ij}\},\{\theta_{ij}\}), \tag{5.21}$$

where $\Lambda(\{\varphi_{ij}\},\{\theta_{ij}\}) = \mathcal{U}_{\mathrm{NH}}^{\dagger} H \mathcal{U}_{\mathrm{NH}}$ is a real diagonal matrix by construction, which contains the eigenvalues of the analogous Hermitian loop, see Equation 5.18. This matrix contains the outcome of interference of Fourier waves with nontrivial Peierls phases. But on top of this effect, the Peierls-phase-independent term $\mathcal{V}=\mathcal{U}_{\mathrm{NH}}^{\dagger}\Sigma_z\mathcal{U}_{\mathrm{NH}}$ is in general a non-Hermitian matrix – being a product of non-commuting Hermitian matrices – that couples Fourier states with different k. This non-Hermitian interaction of Fourier modes with nontrivial phases, on top of their interference, embodies the non-Hermitian AB effect. Note that if all holes were replaced by particles ($\Sigma_z\to\mathbb{1}$), then a trivial coupling matrix follows $\mathcal{V}\to\mathbb{1}$, given the fact that $\mathcal{U}_{\mathrm{NH}}$ is unitary.

5.7.5. Phase-space distributions in the SD

The BdG formalism in particle-hole-space is equivalent to a description in terms of quadratures (section 2.7.3). The latter is helpful in interpreting the main features of flux-tunable quadrature squeezing in the main text. Here we discuss the representation of the nanomechanical steady states of the squeezing dimer as distributions in phase space.

We recall the quadrature vector $\mathbf{q}_{\mathrm{SD}} = (X_1,Y_2,X_2,Y_1) = \mathcal{Q}\boldsymbol{\alpha}^L$ defined in section 5.3. It follows from the quantum regression theorem (section 4.2.2) that the second moments $\mathcal{O}=\langle\mathbf{q}_{\mathrm{SD}}\mathbf{q}_{\mathrm{SD}}^T\rangle$ satisfy the evolution

$$\dot{\mathcal{O}} = \mathrm{i}\left[(\mathcal{H}_{\mathrm{SD}}^{XY} - \mathrm{i}\Gamma/2)\mathcal{O} + \mathcal{O}(\mathcal{H}_{\mathrm{SD}}^{XY} - \mathrm{i}\Gamma/2)^T\right] + 2\mathcal{D}^{XY}, \tag{5.22}$$

obtained by transforming (4.11) to the quadrature basis. The thermal steady state is then easily obtained by setting $\dot{\mathcal{O}}=0$. In addition, the first moments evolve according to $\langle\dot{\mathbf{q}}_{\mathrm{SD}}\rangle = -\mathrm{i}\mathcal{H}_{\mathrm{SD}}^{XY}\langle\mathbf{q}_{\mathrm{SD}}\rangle + \langle(\mathbf{q}_{\mathrm{SD}})_{\mathrm{in}}\rangle$. The diffusion matrix $\mathcal{D}^{XY}$ encodes the Markovian correlations $\langle(\mathbf{q}_{\mathrm{SD}})_{\mathrm{in}}^{(i)}(t),(\mathbf{q}_{\mathrm{SD}})_{\mathrm{in}}^{(j)}(t')\rangle = \mathcal{D}_{ij}^{XY}\delta(t-t')$ for the scaled input noise operators, where

$$\begin{aligned}
\langle X_{\mathrm{in}}^{(i)}(t),X_{\mathrm{in}}^{(j)}(t')\rangle &= \langle Y_{\mathrm{in}}^{(i)}(t),Y_{\mathrm{in}}^{(i)}(t')\rangle = \left(\bar{n}_i^{\mathrm{th}}+\frac{1}{2}\right)\delta(t-t'),\\
\langle X_{\mathrm{in}}^{(i)}(t),Y_{\mathrm{in}}^{(j)}(t')\rangle &= -\langle Y_{\mathrm{in}}^{(i)}(t),X_{\mathrm{in}}^{(i)}(t')\rangle = \frac{i}{2}\delta(t-t').
\end{aligned} \tag{5.23}$$

The thermal steady-state then follows a Gaussian Wigner function [247] in the quadrature amplitudes $\mathbf{r}=(x_1,y_2,x_2,y_1)^T$, namely

$$W(\mathbf{r}) = \frac{1}{(2\pi)^N\sqrt{\det\sigma}}\exp\left(-\frac{1}{2}\mathbf{r}^T\sigma^{-1}\mathbf{r}\right), \tag{5.24}$$

with a symmetric covariance matrix

$$\sigma_{ij} = \frac{1}{2}(\frac{1}{2}(\mathcal{O}_{ij} + \mathcal{O}_{ji}) - \langle q_{\mathrm{SD}}^{(i)}\rangle\langle q_{\mathrm{SD}}^{(j)}\rangle), \tag{5.25}$$

whose eigenvectors indicate axes along which (anti)squeezing occurs with magnitude given by the corresponding eigenvalues. In the absence of coherent driving, $\langle q_{\mathrm{SD}}^{(i)}\rangle = 0$. The marginal distributions for resonator k

$$W_k(x_k, y_k) = \int \prod_{i\neq k} \mathrm{d}x_i \mathrm{d}y_i W(x_1, y_1, \cdots, x_N, y_N) \tag{5.26}$$

are Gaussian distributions that show thermomechanical squeezing. These distributions can be visualised using the standard deviation ellipse defined by its (measured) covariance matrix, as shown for example shown in Figure 5.1b.

The theory curve in Figure 5.3c is calculated in the limit of equal bath occupations and dissipations $\gamma_j = \gamma$, and given by

$$\frac{\Delta R^2_{\mathrm{sq.}}}{\Delta R^2_{\mathrm{a.}}}(\Phi) = \frac{\gamma^3 - 2\eta\sqrt{(\gamma^2+4J^2)\,(\gamma^2 - 2J^2\cos(\Phi) + 2J^2)} + 4\gamma J^2}{\gamma^3 + 2\eta\sqrt{(\gamma^2+4J^2)\,(\gamma^2 - 2J^2\cos(\Phi) + 2J^2)} + 4\gamma J^2}. \tag{5.27}$$

The variance ratio (5.27) is maximal (closest to 1) at $\Phi = 0$ and minimal (i.e. largest difference in variance) at $\Phi = \pi$. In the limit $J \gg \eta$ and $\Phi = 0$, the value for this ratio reads $\frac{\Delta R^2_{\mathrm{sq.}}}{\Delta R^2_{\mathrm{a.}}}(0) \approx 1 - \frac{2\eta}{J}$ and can be made arbitrarily close to 1 by increasing the ratio J/η, while the value at $\Phi = \pi$ is J-independent: $\frac{\Delta R^2_{\mathrm{sq.}}}{\Delta R^2_{\mathrm{a.}}}(\pi) = (\gamma - 2\eta)/(\gamma + 2\eta)$.

Effective two-mode squeezing

We discuss the emergence of effective two-mode squeezing in the squeezing dimer when $\Phi = 0$. Assuming equal dissipations $\gamma_j = \gamma$ and bath occupations $\bar{n}_j^{\mathrm{th}} = \bar{n}^{\mathrm{th}}$, the covariance matrix reads

$$\begin{aligned}\sigma(\Phi = 0) = &\frac{\bar{n}^{\mathrm{th}} + \frac{1}{2}}{\gamma^2 + 4(J^2 - \eta^2)} \\ &\times \begin{pmatrix} \gamma(\gamma-2\eta)+4J^2 & 0 & 0 & J\eta \\ 0 & \gamma(\gamma-2\eta)+4J^2 & J\eta & 0 \\ 0 & J\eta & \gamma(\gamma+2\eta)+4J^2 & 0 \\ J\eta & 0 & 0 & \gamma(\gamma+2\eta)+4J^2 \end{pmatrix}.\end{aligned} \tag{5.28}$$

As indicated by the diagonal elements of (5.28) and observed in Figure 5.6a, single-mode squeezing is cancelled as the ratio J/η is increased. However, the cross-correlations indicated by the off-diagonal elements in (5.28) still suggest the existence of a basis of hybrid quadratures where squeezing can be found. This result can be referenced to the covariance matrix in the standard two-mode squeezing dimer with Hamiltonian $H_{\mathrm{TMS}} = i\eta a_1^\dagger a_2^\dagger + \mathrm{H.c.}$. This Hamiltonian produces anti-squeezing in the variables $X_1 + X_2$ and $Y_1 - Y_2$ and squeezing in $X_1 - X_2$ and $Y_1 + Y_2$, with no (single mode) squeezing on X_i or Y_i [113].

To establish a link with the standard two-mode squeezing case, we diagonalise $\sigma(\Phi = 0)$ to reveal the *rotation* of the principal (squeezing) axes of the covariance matrix. We find that the hybrid quadratures $(R^{(1)}_{\mathrm{sq.}}, R^{(2)}_{\mathrm{sq.}}, R^{(1)}_{\mathrm{a.}}, R^{(2)}_{\mathrm{a.}})^T = U(X_1, X_2, Y_1, Y_2)^T$ corresponding to the eigenvectors of $\sigma(\Phi = 0)$ are related to the resonator quadratures by the transformation

$$U = \begin{pmatrix} -\frac{\sqrt{\frac{1}{\sqrt{\xi^2+1}}+1}}{\sqrt{2}} & 0 & 0 & \frac{\xi}{\sqrt{2}\sqrt{\xi^2+\sqrt{\xi^2+1}+1}} \\ 0 & -\frac{\sqrt{\frac{1}{\sqrt{\xi^2+1}}+1}}{\sqrt{2}} & \frac{\xi}{\sqrt{2}\sqrt{\xi^2+\sqrt{\xi^2+1}+1}} & 0 \\ \frac{\xi}{\sqrt{2}\sqrt{\xi^2+\sqrt{\xi^2+1}+1}} & 0 & 0 & \frac{\xi}{\sqrt{2}\sqrt{\xi^2-\sqrt{\xi^2+1}+1}} \\ 0 & \frac{\xi}{\sqrt{2}\sqrt{\xi^2+\sqrt{\xi^2+1}+1}} & \frac{\xi}{\sqrt{2}\sqrt{\xi^2-\sqrt{\xi^2+1}+1}} & 0 \end{pmatrix}, \tag{5.29}$$

where we denote $\xi = 2J/\gamma$. From the corresponding eigenvalues, we find that $R^{(i)}_{\mathrm{sq.}}$ are squeezed whereas $R^{(i)}_{\mathrm{a.}}$ are anti-squeezed. Their variances, equal for the two squeezed (anti-squeezed) hybrid quadratures, read

$$\Delta R^2_{\mathrm{sq.}} = \frac{\gamma(2\bar{n}^{\mathrm{th}}+1)\sqrt{\xi^2+1}}{2\gamma\sqrt{\xi^2+1}+4\eta}, \qquad \Delta R^2_{\mathrm{a.}} = \frac{\gamma(2\bar{n}^{\mathrm{th}}+1)\sqrt{\xi^2+1}}{2\gamma\sqrt{\xi^2+1}-4\eta}. \tag{5.30}$$

In the strong coupling limit $\xi \gg 1$, the principal axes defined by U rotate to the antisymmetric quadratures $(X_1 - Y_2)/\sqrt{2}$ and $(X_2 - Y_1)/\sqrt{2}$ (squeezed) and the symmetric superpositions $(X_1 + Y_2)/\sqrt{2}$ and $(X_2 + Y_2)/\sqrt{2}$ (anti-squeezed). This rotation can be mapped into the standard case of two mode squeezing by H_{TMS} after considering the quadrature rotation $Y_2 \to X_2$, $X_2 \to -Y_2$. Note, however, that (5.30) indicates that the level of squeezing vanishes in this limit, since $\Delta R^2_{\mathrm{sq.}} \approx \Delta R^2_{\mathrm{a.}}$. We thus find that an inevitable trade-off between the principal axes rotating towards two-mode squeezing and a reduction in the level of effective squeezing as J is increased, as observed in Figure 5.6c.

5.7.6. Flux-asymmetries in thermomechanical spectra of the SCT

Here we demonstrate how the thermomechanical spectrum of the singly conjugated trimer is asymmetric under flipping the sign of synthetic flux $\Phi \mapsto -\Phi$, even if resonators are coupled to equal thermal occupations $\bar{n}^{\mathrm{th}}_j$ or in the limit of zero temperature. From now on we assume $\bar{n}^{\mathrm{th}}_j = \bar{n}^{\mathrm{th}}$ to simplify our analysis.

Within the stable regime $\mathrm{Im}(\epsilon) < \gamma$, where the steady state within the linear theory exists, the spectrum is readily obtained from (4.26), applied to a single block $\mathcal{L}$ (5.11). For arbitrary frequency and flux, the noise spectrum $\mathcal{S}_{ii}(\omega, \Phi)$ can be given in a closed form in terms of lengthy rational, trigonometric expressions.

As the flux-asymmetry is presented in the middle band in Figure 5.7c, it is

sufficient to consider the response at zero frequency (in the rotating frame):

$$\mathcal{S}_{11}(0,\Phi) = \frac{4\gamma}{d(\Phi)}\Big(-4\eta^2\left(\gamma^2(\bar{n}^{\text{th}}+2) - 4J^2\bar{n}^{\text{th}}\right) + \gamma^2(\bar{n}^{\text{th}}+1)\left(\gamma^2+4J^2\right) + 16\gamma\eta^2 J(2\bar{n}^{\text{th}}+1)\sin(\Phi) + 32\eta^4(\bar{n}^{\text{th}}+1)\Big), \tag{5.31a}$$

$$\mathcal{S}_{11}(0,\Phi) = \frac{4\gamma}{d(\Phi)}\Big(-4\eta^2\left(\gamma^2(\bar{n}^{\text{th}}+2) - 4J^2\bar{n}^{\text{th}}\right) + \gamma^2(\bar{n}^{\text{th}}+1)\left(\gamma^2+4J^2\right) - 16\gamma\eta^2 J(2\bar{n}^{\text{th}}+1)\sin(\Phi) + 32\eta^4(\bar{n}^{\text{th}}+1)\Big), \tag{5.31b}$$

$$\mathcal{S}_{33}(0,\Phi) = \frac{4\gamma\left(\gamma^2+4J^2\right)\left(4J^2\bar{n}^{\text{th}} + \gamma^2\bar{n}^{\text{th}} + 8\eta^2(\bar{n}^{\text{th}}+1)\right)}{d(\Phi)}, \tag{5.31c}$$

$$d(\Phi) = \left(\gamma^3 - 8\gamma\eta^2\right)^2 + 16\gamma^2J^4 + 8J^2\left(\gamma^2-4\eta^2\right)^2 + 128\eta^4J^2\cos(2\Phi).$$

While $\mathcal{S}_{33}(0,\Phi) = \mathcal{S}_{33}(0,-\Phi)$ (in fact, for all ω), the noise spectra for resonators 1 and 2 display asymmetries in flux. These asymmetries emerge as a combination of squeezing interactions ($\eta > 0$) and chirality ($\Phi \neq \{0,\pi\}$), which is maximal at $\Phi = \pm\pi/2$. Remarkably, the asymmetries persist at zero temperature ($\bar{n}^{\text{th}} \ll 1$), where only contributions from two-mode squeezed vacuum fluctuations exist:

$$\begin{aligned}\frac{\mathcal{S}_{11}(0,\Phi)}{\mathcal{S}_{11}(0,-\Phi)} &= \frac{1}{\frac{1}{2} - \frac{8\gamma\eta^2J\sin(\Phi)}{\gamma^4-8\gamma^2\eta^2+32\eta^4+4\gamma^2J^2}} - 1,\\ \frac{\mathcal{S}_{22}(0,\Phi)}{\mathcal{S}_{22}(0,-\Phi)} &= \frac{1}{\frac{1}{2} + \frac{8\gamma\eta^2J\sin(\Phi)}{\gamma^4-8\gamma^2\eta^2+32\eta^4+4\gamma^2J^2}} - 1,\end{aligned} \tag{5.32}$$

with maximum asymmetry when the condition $J = (\sqrt{\gamma^4 - 8\gamma^2\eta^2 + 32\eta^4})/(2\gamma)$ is matched.

6

Quadrature nonreciprocity: unidirectional bosonic transmission without breaking time-reversal symmetry

Nonreciprocity means that the transmission of a signal depends on its direction of propagation. Despite vastly different platforms and underlying working principles, the realisations of nonreciprocal transport in linear, time-independent systems rely on Aharonov-Bohm interference among several pathways and require breaking time-reversal symmetry. Here we extend the notion of nonreciprocity to unidirectional bosonic transport in systems with a time-reversal symmetric Hamiltonian by exploiting interference between beamsplitter (excitation preserving) and two-mode-squeezing (excitation non-preserving) interactions. In contrast to standard nonreciprocity, this unidirectional transport manifests when the mode quadratures are resolved with respect to an external reference phase. Hence we dub this phenomenon quadrature nonreciprocity. *First, we experimentally demonstrate it in the minimal system of two coupled nanomechanical modes orchestrated by optomechanical interactions. Next, we develop a theoretical framework to characterise the class of networks exhibiting quadrature nonreciprocity based on features of their particle-hole graphs. In addition to unidirectionality, these networks can exhibit an even-odd pairing between collective quadratures, which we confirm experimentally in a four-mode system, and an exponential end-to-end gain in the case of arrays of cavities. Our work opens up new avenues for signal routing and quantum-limited amplification in bosonic systems.*

This chapter is based on C. C. Wanjura, J. J. Slim, J. del Pino, M. Brunelli, E. Verhagen & A. Nunnenkamp. *Quadrature nonreciprocity: unidirectional bosonic transmission without breaking time-reversal symmetry* arXiv: 2207.08523 (2022). C.C.W. and J.J.S. contributed equally to this work.

6.1. Introduction

In a nonreciprocal system, such as an isolator, the transmission varies when interchanging input and output, in an ideal case from unity to zero [123, 249–251]. Nonreciprocity is a resource for many applications, such as sensing [239], the construction of bosonic networks with general routing capabilities [235], and the realisation of topological phases [38]. Complemented with gain, nonreciprocity amplifies weak signals while protecting the source against noise, which is beneficial for quantum information processing applications [252]. Magnetic-free isolators and directional amplifiers have been proposed based on parametric modulation [46, 49, 251], interfering parametric processes [55, 253], and reservoir engineering [130] and have been experimentally demonstrated in different platforms, e.g. superconducting circuits [31, 254, 255] and optomechanical systems [32, 33, 125–128, 131, 256].

In linear systems, achieving a nonreciprocal response relies on breaking time-reversal symmetry (TRS) in the Hamiltonian by employing real or synthetic magnetic fields and dissipation. The directionality in this standard kind of nonreciprocity (sNR) does not depend on the phase of the input signal. In this work we extend the notion of nonreciprocity in linear bosonic systems by identifying a class of systems that show a kind of unidirectional signal transmission, positioned between reciprocal and standard nonreciprocal transmission, whose (uni)directionality depends on the phase of the input signal. We dub this phenomenon quadrature nonreciprocity (qNR), as it can be revealed when resolving the signal into its quadrature components. In contrast to sNR, a qNR Hamiltonian does not break TRS, but achieves unidirectional transport by interfering beamsplitter (excitation-preserving) and two-mode squeezing (excitation non-preserving) interactions. It does not require strong Kerr nonlinearity [251, 257, 258] or spin-polarized emitters [259, 260]. We report its experimental realisations using an optomechanical network and construct a comprehensive theoretical framework exposing an entire class of qNR systems with exciting properties, including an even-odd pairing between collective quadratures and exponential end-to-end gain in resonator chains. Our work introduces a systematic tool to treat unidirectional phase-sensitive transport in bosonic lattice systems, which have recently sparked interest in connection with bosonic analogues of the Kitaev chain [162, 232, 261]. It further opens the door to studying exotic phenomena in these models, such as multi-mode entanglement [232] and non-Hermitian topology [233]. From the point of view of applications, our work opens up new avenues for signal routing and amplification.

6.2. Defining quadrature nonreciprocity (qNR)

We consider a network of N driven-dissipative bosonic modes. Their steady-state response to a coherent probe follows from the Heisenberg-Langevin equations of motion $\dot{\mathbf{q}} = \mathcal{M}_{\mathbf{q}}\mathbf{q} - \sqrt{\gamma}\mathbf{q}_{\text{in}}$ for the field quadratures $x_j \equiv (a_j + a_j^\dagger)/\sqrt{2}$ and $p_j \equiv -\mathrm{i}(a_j - a_j^\dagger)/\sqrt{2}$, where a_j denotes the annihilation operator for the bosonic mode $j \in (1, \cdots, N)$, γ the damping rate and $\mathcal{M}_{\mathbf{q}}$ the open-system dynamical matrix (section 2.7.3). We use the vector notation $\mathbf{q} \equiv (x_1, p_1, \cdots, x_N, p_N)^{\mathrm{T}}$ for the system's quadratures and similarly $\mathbf{q}_{\text{in}}$ for the quadrature inputs. We assume

that each mode dissipates only via coupling to the input-output port, although our analysis extends to general temporal coupled-mode theory [32, 262]. The scattering matrix $S(\omega)$ connects input $\mathbf{q}_{\rm in}$ and output quadratures $\mathbf{q}_{\rm out}$, oscillating with frequency ω, which satisfy the input-output boundary conditions $\mathbf{q}_{\rm out} = \mathbf{q}_{\rm in} + \sqrt{\gamma}\mathbf{q}$ [147, 263]. It reads,

$$S(\omega) \equiv \mathbb{1} + \gamma(\mathrm{i}\omega\mathbb{1} + \mathcal{M}_{\mathbf{q}})^{-1} \equiv \mathbb{1} + \gamma\chi(\omega), \tag{6.1}$$

with the susceptibility matrix $\chi(\omega) \equiv (\mathrm{i}\omega\mathbb{1} + \mathcal{M}_{\mathbf{q}})^{-1}$. We will from now on consider driving at resonance ($\omega = 0$ in a frame rotating at the mode frequencies) and write $\chi \equiv \chi(0)$, $S \equiv S(0)$ for brevity.

Let us consider a rotation of each pair of quadratures $\{x_j, p_j\}$, with respect to some external phase reference (Figure 6.1, top left), namely

$$\begin{pmatrix} x_j(\phi_j) \\ p_j(\phi_j) \end{pmatrix} = \begin{pmatrix} \cos\phi_j & \sin\phi_j \\ -\sin\phi_j & \cos\phi_j \end{pmatrix} \begin{pmatrix} x_j(0) \\ p_j(0) \end{pmatrix} \equiv R(\phi_j) \begin{pmatrix} x_j(0) \\ p_j(0) \end{pmatrix}. \tag{6.2}$$

Equation (6.2) can be understood as a $U(1)$ gauge transformation in the mode basis $\{a_j, a_j^\dagger\}$ [31, 33] (see section 6.8.1 for details). The susceptibility matrix χ transforms as

$$\chi_\phi \equiv U(\phi_j)\chi U^{\mathrm{T}}(\phi_j), \tag{6.3}$$

where we introduced $U(\phi_j) \equiv \oplus_{j=1}^{N} R(\phi_j)$.

Nonreciprocity is typically defined by asymmetry in the transmission amplitudes [249, 251]. We adopt this notion in a generalised sense, with signals split into their x, p quadratures, meaning $|S|^{\mathrm{T}} \neq |S|$ for Eq. (6.1) or, equivalently, $|\chi|^{\mathrm{T}} \neq |\chi|$. Here $|\cdots|$ denotes taking the element-wise modulus. We will say that a system exhibits quadrature nonreciprocity (qNR) if there exist at least *two* different sets of local gauges $\phi_j^{(1,2)}$ corresponding to a nonreciprocal and reciprocal susceptibility matrix, respectively. Mathematically, this implies a pair of rotations $U_{1,2} \equiv \oplus_{j=1}^{N} R(\phi_j^{(1,2)})$ such that

$$|U_1\chi U_1^{\mathrm{T}}|^{\mathrm{T}} \neq |U_1\chi U_1^{\mathrm{T}}| \qquad \text{and} \qquad |U_2\chi U_2^{\mathrm{T}}|^{\mathrm{T}} = |U_2\chi U_2^{\mathrm{T}}|. \tag{6.4}$$

6.3. qNR dimer: the simplest qNR system

We now introduce the minimal system displaying qNR: the parametrically-driven dimer shown in Figure 6.1a. It consists of two modes $a_{1,2}$ coupled via beamsplitter (BS) coupling of strength J and two-mode-squeezing (TMS) coupling of strength λ. In a frame rotating at the mode frequencies, the Hamiltonian reads

$$H_{\rm qd} = Ja_1^\dagger a_2 + \lambda a_1^\dagger a_2^\dagger + \mathrm{H.c.}, \tag{6.5}$$

which corresponds to the most general bi-linear coupling. For $J = \lambda$, we recover the well-known position-position coupling, which has been extensively studied, e.g. for implementing quantum non-demolition measurements [264, 265] or generating squeezing and entanglement [266]. This system has been introduced in

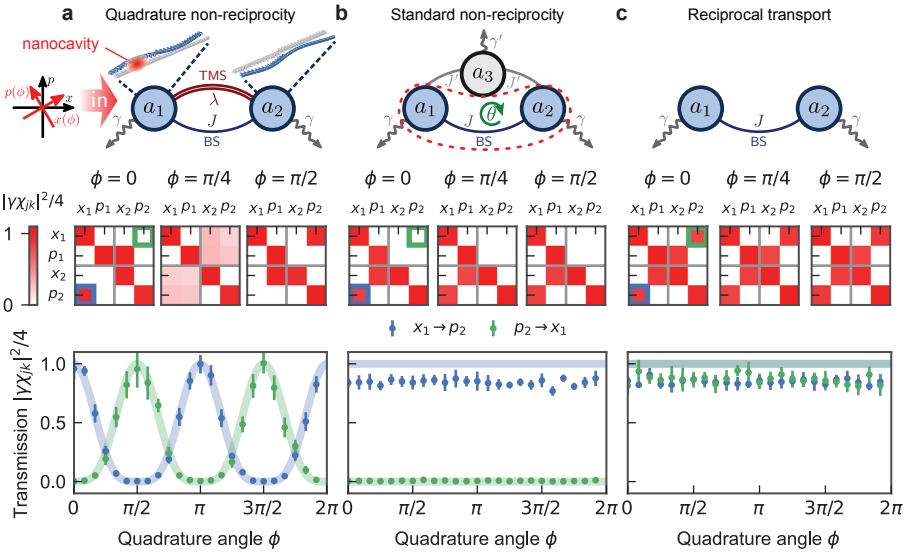

Figure 6.1: **Quadrature nonreciprocity (qNR) vs. standard nonreciprocity (sNR) vs. reciprocal transport.** Coupled-mode diagrams for three systems with distinct forms of transport (top row), realized in experiment with mechanical modes $a_{1,2}$ (resonances 3 and 4 in Figure 2.3, opto-thermally equalized decay rates $\gamma/(2\pi) = 3.7$ kHz, see section 2.8.4) subject to cavity-mediated beamsplitter (BS, strength J) and two-mode squeezing (TMS, strength λ) interactions. Coherent excitation along quadratures (red) rotated by ϕ from the reference gauge (black) is sketched (top left). Corresponding measured susceptibility matrix amplitudes $|\chi_{jk}|$ evolve differently with ϕ (middle row). Nonreciprocity manifests in χ as an asymmetric element-wise modulus $|\chi| \neq |\chi|^{\mathrm{T}}$. The elements within the green and blue boxes are plotted for a range of experimental ϕ settings (bottom row). **(a)** Two modes interact through BS and TMS of equal strength ($J = \lambda = \gamma/4$), showing qNR. Nonreciprocity vanishes for $\phi = \pi/4$, while setting $\phi = \pi/2$ inverts the transmission direction. **(b)** Auxiliary mechanical mode a_3 (resonance 2 in Figure 2.3, decay rate $\gamma'/(2\pi) = 1.3$ kHz) is coupled to $a_{1,2}$ through BS interactions of strength $J' = \sqrt{\gamma\gamma'}/2$, providing a coupling between a_1 and a_2 via a_3 that interferes with the direct coupling $J = \gamma/2$. SNR requires the breaking of TRS—realized by picking a non-trivial synthetic flux $\theta = \pi/2$—so that the susceptibility matrix is nonreciprocal for all ϕ. The same experiment is discussed in section 3.2.1 and shown in Figure 3.3b without quadrature resolution. **(c)** Reciprocal transport between two modes coupled only through BS ($J = \gamma/2$) is characterised by a symmetric χ for any phase ϕ. Error bars are obtained by repeating the measurement sweep 10 times and represent the statistical $\pm 2\sigma$ spread around the average value.

[130] as a source of (standard) nonreciprocity by combining it with dissipation, and implemented in a superconducting circuit [267] as a (bi-directional) phase-sensitive amplifier and used for qubit readout.

As we now show, it is also one of the minimal manifestations of qNR. Eq. (6.5) gives the following equations of motion for the quadratures

$$\begin{aligned}
\dot{x}_1 &= -\frac{\gamma}{2}x_1 + (J-\lambda)p_2 - \sqrt{\gamma}x_{1,\mathrm{in}},\\
\dot{p}_1 &= -\frac{\gamma}{2}p_1 - (J+\lambda)x_2 - \sqrt{\gamma}p_{1,\mathrm{in}},\\
\dot{x}_2 &= -\frac{\gamma}{2}x_2 + (J-\lambda)p_1 - \sqrt{\gamma}x_{2,\mathrm{in}},\\
\dot{p}_2 &= -\frac{\gamma}{2}p_2 - (J+\lambda)x_1 - \sqrt{\gamma}p_{2,\mathrm{in}},
\end{aligned} \tag{6.6}$$

from which it is apparent that the quadratures can decouple, due to the fact that BS and TMS couplings enter with the opposite sign. In particular, setting $J = \lambda$ in Eq. (6.6) leads to perfect decoupling between $\dot{x}_1$ ($\dot{x}_2$) and p_2 (p_1), while $\dot{p}_2$ ($\dot{p}_1$) still couples to x_1 (x_2), in a way which is formally equivalent to a cascaded quantum system [268, 269]. This is also reflected in the asymmetric susceptibility matrix

$$\chi = \begin{pmatrix} -\frac{2}{\gamma} & 0 & 0 & 0 \\ 0 & -\frac{2}{\gamma} & \frac{8J}{\gamma^2} & 0 \\ 0 & 0 & -\frac{2}{\gamma} & 0 \\ \frac{8J}{\gamma^2} & 0 & 0 & -\frac{2}{\gamma} \end{pmatrix}. \tag{6.7}$$

We interpret this property by saying that a signal encoded in quadrature x_1 can propagate from mode 1 to 2, emerging as p_2, while the reverse transduction, i.e., $p_2 \to x_1$ does not take place. When $J = \lambda > \gamma/4$, we further have $S_{x_2\to p_1} = \gamma\chi_{x_2\to p_1} > 1$, which signifies phase-sensitive amplification.

To demonstrate this unidirectional transport between quadratures, we implement Hamiltonian (6.5) in the optomechanical sliced photonic crystal nanobeam platform introduced in chapter 2. Its non-degenerate, MHz-frequency flexural mechanical modes serve as resonators a_j with distinct frequencies Ω_j, while their decay rates γ_j are adjustable through optothermal backaction (section 2.8.4) and measurement-based feedback (section 2.8.6). Effective quadratic interactions with tunable strength *and* phase are enabled by temporally modulated radiation pressure of a detuned laser [64, 151]: Specifically, intensity modulations of the laser drive at difference (sum) frequencies $\Omega_j \mp \Omega_k$ induce effective nanomechanical beamsplitter (squeezing) interactions (section 2.6).

In our measurements, we define (electronic) local oscillators (LOs) at the resonator frequencies Ω_j that demodulate – in parallel – the optically-detected displacement signal, to obtain the amplitude envelope $|a_j(t)|$ and relative phase $\varphi_j(t)$ of each resonator's harmonic motion $z_j(t) = |a_j(t)|\cos(\Omega_j t + \varphi_j(t))$. In effect, the LOs *define* a rotating frame of reference in which the resonator dynamics can be tracked by a complex amplitude $\langle a_j\rangle = |a_j|e^{i\varphi_j}$, or equivalently by the quadrature amplitudes $\langle x_j\rangle = \sqrt{2}\,\mathrm{Re}(\langle a_j\rangle)$ and $\langle p_j\rangle = \sqrt{2}\,\mathrm{Im}(\langle a_j\rangle)$. Moreover, signals to

drive the resonator quadratures coherently through radiation pressure are derived from the same LOs, turning our experiment into a lock-in measurement. The full procedure for driving and analysis is detailed in section 6.8.2.

To connect the unidirectional response of Eq. (6.7) to the definition of qNR (6.4), we need to study how the dimer transforms under a change of gauge. We measure the dimer's quadrature-resolved response, when performing the gauge transformation in Eq. (6.3) (Figure 6.1, top left). This is experimentally achieved by referring both the interaction tones and LOs to a common time origin and subsequently adding a phase offset ϕ to the LOs—rotating the quadratures they define. Note that even though the frequencies of LOs ($\Omega_{1,2}$) and interaction tones ($\Omega_1 \pm \Omega_2$) are all distinct, the fact that the latter signals can be derived from the former through mixing leads to a well-defined relation between the LO and interaction phases (section 2.8.2).

For different phases ϕ, we independently reconstruct the susceptibility matrix (6.3) for $J = \lambda$ in Figure 6.1a. The full susceptibility matrix of the qNR dimer rotated by a phase ϕ is given by

$$\chi_\phi = \begin{pmatrix} -\frac{2}{\gamma} & 0 & -\frac{4J\sin(2\phi)}{\gamma^2} & -\frac{8J\sin^2(\phi)}{\gamma^2} \\ 0 & -\frac{2}{\gamma} & \frac{8J\cos^2(\phi)}{\gamma^2} & \frac{4J\sin(2\phi)}{\gamma^2} \\ -\frac{4J\sin(2\phi)}{\gamma^2} & -\frac{8J\sin^2(\phi)}{\gamma^2} & -\frac{2}{\gamma} & 0 \\ \frac{8J\cos^2(\phi)}{\gamma^2} & \frac{4J\sin(2\phi)}{\gamma^2} & 0 & -\frac{2}{\gamma} \end{pmatrix}. \tag{6.8}$$

Here we focus on the matrix elements shown in the bottom row of Figure 6.1, namely

$$\chi_{x_1\to p_2} = \frac{8J\cos^2(\phi)}{\gamma^2}, \tag{6.9}$$

$$\chi_{p_2\to x_1} = -\frac{8J\sin^2(\phi)}{\gamma^2}. \tag{6.10}$$

It is clear that nonreciprocity only reveals itself in particular rotated quadratures. While maximal nonreciprocity is obtained for $\phi = 0$, as in Eq. (6.7), a gauge transformation reduces the 'contrast' of the nonreciprocity until, at $\phi = \pi/4$, the transport is completely reciprocal, i.e., $\chi_{x_1\to p_2} = \chi_{p_2\to x_1} = 4J/\gamma^2$, and in fact $|\chi|^{\mathrm{T}} = |\chi|$. This confirms that the dimer is indeed a qNR system, as per our definition (6.4). Further increasing ϕ swaps the direction of nonreciprocity, $a_1 \leftrightarrow a_2$, with complete reversal at $\phi = \frac{\pi}{2}$, when $\chi_{x_1\to p_2} = 0$, $\chi_{p_2\to x_1} = 8J/\gamma^2$.

In the qNR dimer, the cancellation at $\phi = \pi/4$ and the reversal of directionality fundamentally stems from TRS. We identify a system's TRS from its Hamiltonian, i.e. its dynamics in absence of local dissipation or gain. This is motivated by the fact that dissipation or gain by themselves, while breaking temporal symmetry in a 'trivial' way, cannot induce nonreciprocal behaviour: In such systems, attenuation or amplification is always equal in two directions. In section 6.8.3 we demonstrate that TRS implies the constraints $|\chi_{x_j\to x_\ell}| = |\chi_{p_\ell\to p_j}|$, $|\chi_{x_j\to p_\ell}| = |\chi_{x_\ell\to p_j}|$ for any gauges ϕ_j and reciprocity for at least one set of gauges. This is strikingly different from a system that breaks TRS, such as the isolator of Ref. [130]. In Figure 6.1b we

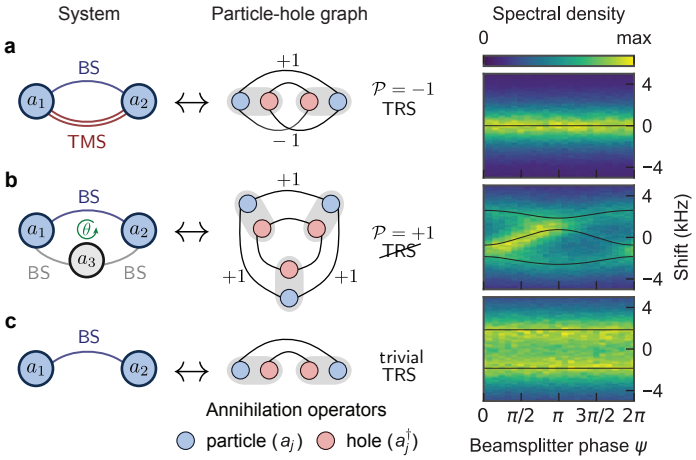

Figure 6.2: **Time-reversal symmetry and qNR.** The coupled-mode diagrams (left column) of the systems studied in Figure 6.1 are expanded using a general graph representation of quadratic Hamiltonians (middle column). Operators a_j, a_ℓ, $a_j^\dagger$, $a_\ell^\dagger$, annihilating 'particles' and 'holes' respectively, that are coupled in the equations of motions are connected through a line. **(a)** If the graph forms a double loop as is the case for the qNR dimer, TRS is always preserved. **(b)** If the resulting graph decomposes into two loops as for the sNR isolator, TRS can be broken by a gauge invariant phase, enabling sNR. **(c)** When the graph displays no loops as is the case for the trivial BS dimer, TRS is always preserved. **(right)** The spectral density of the thermal fluctuations in mode a_1 serves as an experimental signature of TRS. In a gauge where all other interactions are real, we vary the phase ψ of the BS coupling between a_1 and a_2. For (a) and (c), this does not affect the system's eigenfrequencies, given by the real part of the dynamical matrix' eigenvalues (white lines), while for (b) it signals TRS breaking. Experimental parameters are identical to those used in Figure 6.1.

show the measured susceptibility matrix for the 'sNR isolator' discussed before in section 3.2.1. It is implemented in our optomechanical system using two equal-linewidth mechanical modes a_1 and a_2, coupled directly via a BS interaction of strength J while an auxiliary lower-order mechanical mode a_3 is introduced and coupled to both a_1 and a_2 with BS strength J'. Contrary to the qNR dimer, here isolation is enabled by a $U(1)$ gauge-invariant flux θ, the relative phase between the couplings J, J' as shown in Figure 6.1b. Since nonreciprocity is controlled by the TRS-breaking flux, it is independent of local rotations in phase space by ϕ, as reflected by the phase-independent susceptibility matrices in Figure 6.1b ($|\chi_{x_1\to x_2}|^2 = |\chi_{p_1\to p_2}|^2 = 1, |\chi_{x_2\to x_1}|^2 = |\chi_{p_2\to p_1}|^2 = 0$).

For reference, we also contrast both notions of nonreciprocity against a reciprocal system. We display in Figure 6.1c the susceptibility matrix measured for two beamsplitter-coupled modes, which is completely reciprocal ($|\chi|^{\mathrm{T}} = |\chi|$) and gauge-invariant ($\chi_\phi = \chi$).

6.4. Time-reversal symmetry and qNR

The results above point to the fact that preserving TRS in the Hamiltonian is a key element, which sets qNR apart from sNR. A time-reversal symmetric Hamiltonian

imposes certain symmetries on the dynamical matrix that underlie the unique transformation properties of a qNR susceptibility matrix. This motivates us to provide a general characterisation of TRS Hamiltonians in bosonic networks. TRS means that there exists a $U(1)$ transformation

$$a_j \to e^{\mathrm{i}\phi_j} a_j, \tag{6.11}$$

that renders the coefficients in the Hamiltonian real [73]. TRS is often associated with reciprocity [251], but in fact TRS only requires $|\chi|$ to be symmetric for one set of phases $\phi_j^{(0)}$ in Eq. (6.11). This will be elaborated in section 6.8.3. Indeed, in qNR systems, reciprocity *only* occurs when $\phi_j = \phi_j^{(0)}$ (in the qNR dimer, $\phi_j^{(0)} = \phi^{(0)} = \pi/4, 3\pi/4$) and nonreciprocity occurs for all $\phi_j \neq \phi^{(0)}$. This feature, which to the best of our knowledge has not been recognised before, positions qNR precisely between reciprocity and gauge-independent sNR.

We develop a criterion to identify TRS for arbitrary quadratic bosonic Hamiltonians, based on the graph representation of the Hamiltonian matrix in the field basis, inspired by Bogoliubov-de-Gennes theory [151] and laid out before in section 5.3. We associate the Hamiltonian matrix with a graph in which the ladder operators a_j — annihilating 'particle' excitations — and $a_j^\dagger$ — annihilating 'hole' excitations — are represented as vertices and the interactions as edges, i.e., connecting a_j to a_ℓ (and $a_j^\dagger$ to $a_\ell^\dagger$) for BS between sites j, ℓ and a_j to $a_\ell^\dagger$ (and $a_j^\dagger$ to a_ℓ) for TMS. The graph representations of the three systems of Figure 6.1 display manifestly different structures (Figure 6.2), leading to a general criterion for TRS (section 6.8.4). The graph of the qNR dimer, Figure 6.2a, connects all vertices in a *double* loop visiting each site twice. Such double loops guarantee TRS for arbitrary, complex, coupling constants. In contrast, the graph of the sNR isolator, Figure 6.2b, decomposes into two disjoint loops. This structure allows to break TRS through a non-vanishing relative phase between the coupling constants. The BS dimer, Figure 6.2c, displays no loops and trivially preserves TRS.

The different graph structures, which embody the behaviour under time reversal, are catalogued in general by a $\mathbb{Z}_2$ invariant, which we call *loop product* $\mathcal{P}$. To define such a quantity, we consider the particle-hole graph for a general loop with BS and TMS interactions. Then by multiplying by (-1) for a line crossing (TMS coupling) and $(+1)$ for an uncrossed pair of lines (BS couplings) $(+1)$, the loop product $\mathcal{P}$ distinguishes between an even (disjoint loops) and odd number (double loop) of line crossings

$$\mathcal{P} \equiv (-1)^{n_{\mathrm{TMS}}}(+1)^{n_{\mathrm{BS}}} = \begin{cases} -1: & \text{double loop (TRS)} \\ +1: & \text{disjoint loops} \end{cases}, \tag{6.12}$$

with n_{BS} the number of BS couplings and n_{TMS} the number of TMS couplings. Eq. (6.12) indicates that the only requirement for TRS in a general loop is an odd number of TMS couplings, i.e. their position in the loop is irrelevant.

Complementing our graph-based theoretical criterion above, the experimental response of a system to incoherent excitation serves as a signature of a TRS Hamiltonian [151], as nontrivial fluxes manifest in the eigenfrequencies (Figure 6.2, right).

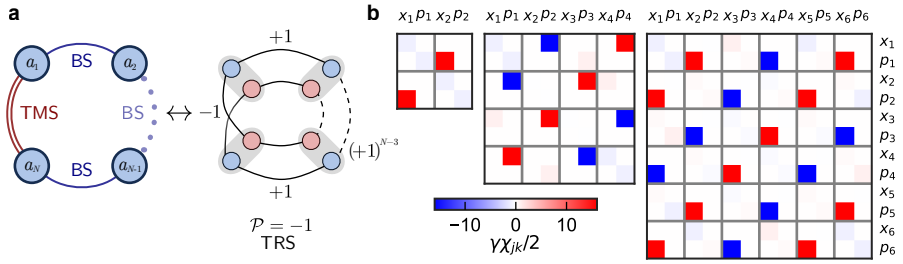

Figure 6.3: **QNR transmission in ring networks. (a)** Graph representation of a ring with N modes, featuring a single TMS interaction. The ring is closed by $N-1$ BS interactions between the remaining modes. For arbitrary N the loop product $\mathcal{P}=-1$, indicating preservation of TRS. To obtain qNR transmission, N must be even. **(b)** A feature of qNR that only becomes apparent for $N>2$ is the pairing between collective quadratures of even and odd sites in the susceptibility matrix χ, shown here in theory for $J=\lambda=2N\cdot\gamma$ and $\phi=0$.

We choose a gauge in which all interactions are real, except for the BS coupling between modes a_1 and a_2 present in all three systems studied so far, whose phase ψ we vary. Thermal fluctuations drive stochastically all mechanical quadratures homogeneously and lead to a power spectrum insensitive to ψ if there is a gauge transformation (6.11) that removes this BS phase. In our experiment, this indicates the TRS of the qNR (Figure 6.2a) and BS Hamiltonians (Figure 6.2c). Conversely, if the eigenfrequencies tune with ψ, such a gauge transformation cannot exist, marking the broken TRS of the sNR isolator (Figure 6.2b).

Finally, we stress another consequence of TRS, already visible in the dimer (see Eq. (6.10)), i.e., that quadratures travel in pairs in opposite directions. In fact, the transduction $x_j \to p_\ell$ is accompanied by $x_\ell \to p_j$ with equal transmission in the opposite direction, e.g., in Eq. (6.7), $|\chi_{x_j\to p_\ell}|^2 = |\chi_{x_\ell\to p_j}|^2$, see section 6.8.3 for details. This requirement of counter-propagating pairs of quadratures is reminiscent of other TRS systems, such as quantum spin Hall systems [36, 38].

6.5. Constructing qNR ring networks

We take now inspiration from the particle-hole graphs and look for qNR in N-mode ring networks among TRS systems ($\mathcal{P}=-1$), dubbed 'N-rings' from now on. To obtain a ring with qNR transmission, a TRS Hamiltonian is only necessary, not sufficient. We also have to guarantee that the BS and TMS couplings can interfere. The particle-hole representation allows a reinterpretation of the quadrature decoupling condition discussed along with Eq. (6.6) as constructive and destructive interference between particle-conserving and particle-non-conserving processes. This condition brings us to the necessary and sufficient criterion for qNR. Besides the odd number of TMS couplings (Eq. (6.12)), achieving qNR requires that the ring consists of an *even* number of modes. To understand why, we take a closer look at the 4-mode ring with a single TMS interaction (Figure 6.3a). The corresponding

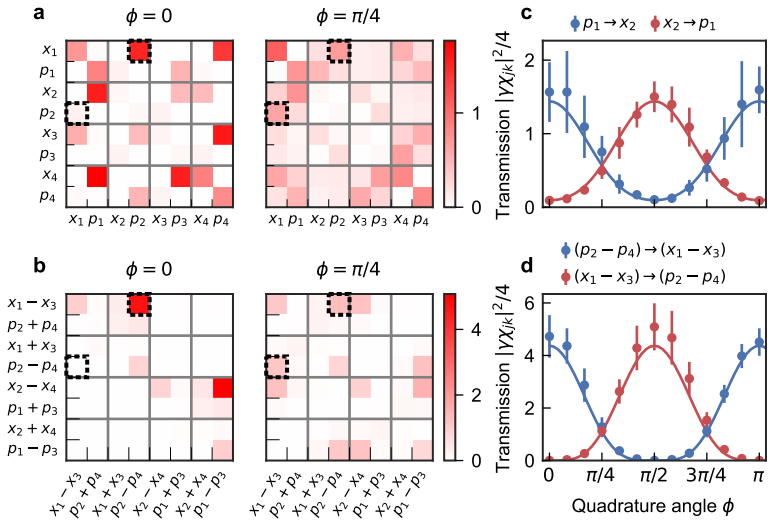

Figure 6.4: **Experimental realization of the qNR 4-ring. (a)** Susceptibility matrices $|\chi|$ for the $N = 4$ ring realized in experiment. All resonator damping rates $\gamma/(2\pi) = 10$ kHz are equalized using measurement-based feedback (section 2.8.6). Interaction rates are set to $J = \lambda = 2\pi \times 5$ kHz, the largest λ that permits a linear response to the amplified thermal noise in the experiment. For $\phi = 0$, we obtain a nonreciprocal χ that shows collective pairing, albeit with reduced contrast compared to Figure 6.3b. For $\phi = \pi/4$, χ is reciprocal, showing the qNR of transmission of the ring. **(b)** Susceptibility matrices in the basis of even and odd collective quadratures show their pairing for $\phi = 0$, when χ is block-diagonal. Similarly, reciprocal susceptibility is obtained for $\phi = \pi/4$. **(c,d)** The values of selected susceptibility matrix elements (**c**: resonator basis; dashed boxes in (a), **d**: collective basis; dashed boxes in (b)) show continuous tuning as function of quadrature angle ϕ, in theory (solid line) and experiment (circles). Even in theory, the isolation for $\phi = 0, \pi/2, \pi$ in the resonator basis (c) is not perfect, whereas in the collective basis (d) it is. Error bars are obtained by repeating the measurement sweep 10 times and represent the statistical $\pm 2\sigma$ spread around the average value.

equations of motion for equal couplings ($J = \lambda$) read

$$\begin{aligned} \dot{x}_1 &= -J(p_2 - p_4) - \frac{\gamma}{2} x_1 - \sqrt{\gamma} x_{1,\mathrm{in}} \\ \dot{p}_2 - \dot{p}_4 &= -\frac{\gamma}{2}(p_2 - p_4) - \sqrt{\gamma}(p_{2,\mathrm{in}} - p_{4,\mathrm{in}}). \end{aligned} \tag{6.13}$$

The coupling to x_1 vanishes in the second equation for the collective quadrature $(p_2 - p_4)$ due to the interference of BS and TMS couplings. Equations (6.13) have a similar structure as those for the qNR dimer (6.6), the main difference being that x_1 couples nonreciprocally to the *collective* quadrature $(p_2 - p_4)$ instead of to a local quadrature. Analogously, x_2 couples to $(p_1 - p_3)$ nonreciprocally. As a consequence, the dominant elements of the susceptibility matrix are coupling $(p_1 - p_3)$ to $-x_2$ and x_4, as well as $(p_2 - p_4)$ to $-x_1$ and x_3. This peculiar non-local pairing between even and odd quadratures is shown in Figure 6.3b for a 4-ring and carries over to larger N-rings with even N, independent of system size. The pairing is only observed if N is even, since it requires an equal number of quadratures on even and odd sites, respectively. Indeed, this condition can be proven rigorously by using

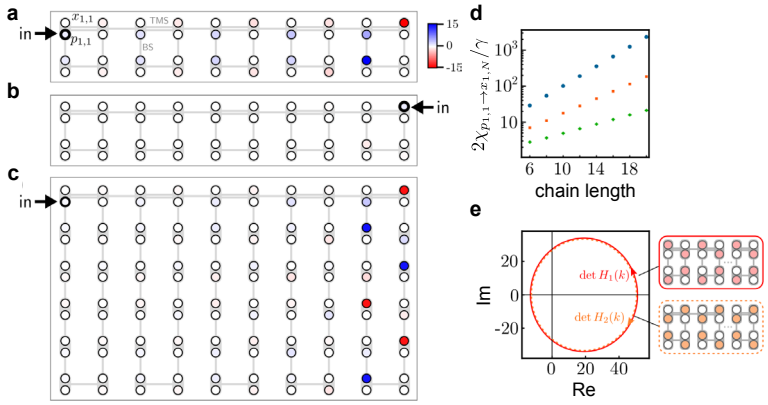

Figure 6.5: **Steady-state response of a qNR chain. (a-c)** Staggering qNR rings with BS links to form a chain, we obtain a qNR system for which the largest steady-state response is at the opposite end. We show the numerically calculated steady-state field quadratures $\langle x_{j,l}\rangle/(2\sqrt{\gamma}\langle x_{\mathrm{ss};j,l}\rangle)$, $\langle p_{j,l}\rangle/(2\sqrt{\gamma}\langle p_{\mathrm{ss};j,l}\rangle)$ (of the site in row j, column ℓ) for a 4-ring qNR chain driven at the **a** first and **b** last site; and **c** a 12-ring qNR chain. The pairing is clearly visible in the steady state response. **(d)** End-to-end gain for 4-ring (blue), 8-ring (red) and 12-ring (green) chains and $J = \lambda = 4\gamma$. The gain grows exponentially across the system and with system size. **(e)** Suggested non-Hermitian topological invariant exploiting the block-diagonal form of the Fourier-transformed dynamical matrix with blocks $\mathcal{M}_{\mathbf{q}}^{(1,2)}(k)$ (section 6.8.6).

a reduction technique on the particle-hole graphs [248].

We implement the 4-ring shown in Figure 6.3a experimentally. The measured susceptibility matrix in the resonator quadrature basis, (Figure 6.4a) illustrates its nonreciprocal response for $\phi = 0$, while the nonreciprocity vanishes completely for $\phi = \pi/4$, establishing qNR in this system. For maximum nonreciprocity ($\phi = 0$), the largest magnitude entries of the susceptibility matrix manifest the non-local coupling structure between quadratures of even and odd sites. This susceptibility matrix structure is transparent in the basis of collective quadratures (Figure 6.4b), where χ is, in fact, block-diagonal for $\phi = 0$. We note that in this basis the nonreciprocal isolation is perfect in theory (Figure 6.4d), whereas in the local basis it is not (Figure 6.4c).

6.6. Towards qNR lattices

We now take qNR one step further and use qNR rings as building blocks for constructing qNR lattices. It can be proven that if a lattice overall preserves TRS and contains at least one qNR ring, it is itself qNR [248].

Of particular interest are translationally invariant chains of qNR N-rings, which can combine qNR transmission with non-Hermitian topology [233]. One such example is given by the bosonic Kitaev chain of Ref. [232], which corresponds to a 2-ring chain with a specific choice of inter-ring coupling phases and is indeed a qNR system. Thanks to our particle-hole graph framework, we can now consider more complex scenarios. As an example, we take a chain made by qNR 4-rings connected through BS interactions. In Figure 6.5a and b, we show the simulated steady-state

field quadratures for this qNR lattice for $\phi = 0$, given a quadrature-resolved input at different sites. Nonreciprocal transmission is clearly visible, while changing the gauge to $\phi = \pi/4$ (not shown), leads to complete reciprocity, i.e., we recover the characteristic feature of qNR, Eq. (6.4). The pairing we characterised in the previous sections also manifests: an input at the $p_{1,1}$ quadrature (in which the indices stand for row and column in the array), Figure 6.5a, procures the largest steady-state response at two sites at the opposite end of the chain. The pairing is evidenced in larger qNR ring sizes, in which the steady-state response of a 12-ring chain is most prominent in every second site of the last plaquette, shaping a zig-zag line (Figure 6.5c).

In this system, qNR is accompanied by amplification with the end-to-end gain growing exponentially with the chain length (Figure 6.5d). This generalises the phase-dependent directional amplification predicted in a bosonic Kitaev chain [232]. Directional amplification with exponential end-to-end gain has been identified as a proxy of non-trivial topology [233, 270]. Based on previous results from 2-ring chains, we conjecture a connection with a non-trivial non-Hermitian winding number calculated from the determinant of a matrix [219], in our case the dynamical matrix (section 6.8.6). In Figure 6.5e, we plot the theoretical determinant of each of the diagonal blocks of the Bloch-matrix (each of the blocks accounts for a set of collective quadratures as shown in the inset) for the 4-ring qNR chain of Figure 6.5a under periodic boundary conditions. We find that the determinant of each of these blocks can be assigned a non-trivial winding number that equals in magnitude and differs in sign corresponding to the two directions of directional end-to-end gain. The opposite winding sense of these two matrix blocks is an expression of the TRS of the underlying Hamiltonian.

6.7. Conclusion and outlook

In conclusion, we introduced the novel phenomenon of quadrature nonreciprocity (qNR). In contrast to standard nonreciprocity, qNR does not break time-reversal symmetry in the Hamiltonian and presents a characteristic gauge dependence. We identified the set of bosonic networks that display qNR and reported the first experimental realisations.

Our results point to a close connection of qNR with the existence of quantum non-demolition (QND) variables and with back-action evading (BAE) measurements [264, 265]. Indeed, our characterisation of qNR simultaneously provides a powerful recipe to design systems with collective QND variables. In this context, exploring the noise properties of qNR networks we introduced will also be interesting. As they rely on interference between coherent interactions, without the necessity of dissipation, we can expect quantum-limited performance [163]. This paves the way towards quantum applications, such as efficient, noiseless sensors, quantum information routers and the generation and measurement of non-classical states, including entangled states [147, 232, 269]. Indeed, while we demonstrated the concept in the domain of nanomechanics, it could find application in e.g. classical electrical circuits [76], acoustics [271], superconducting circuits [31, 254, 255], and spin ensembles [272].

Going forward, we envision the construction of lattices from qNR rings that inherit the qNR properties similar to those of Figure 6.5. Our research opens new avenues for exploring qNR lattices and networks in which new topological phenomena may emerge similar to the quantum spin Hall effect [36, 38].

6.8. Appendices

The following sections contain further details supporting this chapter.

6.8.1. Quadrature qauge transformations

For a dynamical matrix $\mathcal{M}_a$ expressed in the basis of the fields $\{a_1, a_1^\dagger, \ldots, a_N, a_N^\dagger\}$, a gauge transformation performed on a multi-mode system with N sites can be expressed via the unitary $V \equiv \bigoplus_{j=1}^N V_j$, with $V_j = \mathrm{diag}\,(e^{\mathrm{i}\phi_j}, e^{-\mathrm{i}\phi_j})$ acting on an individual site. The dynamical matrix transforms according to $\mathcal{M}'_a(\{\phi_j\}) = V\mathcal{M}_a V^\dagger$. Moving into the quadrature basis, $x_j = (a_j + a_j^\dagger)/\sqrt{2}$, $p_j = -\mathrm{i}(a_j - a_j^\dagger)/\sqrt{2}$, we transform $\mathcal{M}'_a$ via the unitary

$$W \equiv \bigoplus_{j=1}^N \frac{1}{\sqrt{2}} \begin{pmatrix} 1 & 1 \\ -\mathrm{i} & \mathrm{i} \end{pmatrix}, \tag{6.14}$$

such that the transformed dynamical matrix in the quadrature basis $\mathcal{M}_{\mathbf{q}}(\{\phi_j\})$ is given by

$$\begin{aligned} \mathcal{M}_{\mathbf{q}}(\{\phi_j\}) &= WV\mathcal{M}_a V^\dagger W^\dagger = WVW^\dagger (W\mathcal{M}_a W^\dagger) WV^\dagger W^\dagger \\ &= WVW^\dagger \mathcal{M}_{\mathbf{q}}(0) WV^\dagger W^\dagger \equiv U\mathcal{M}_{\mathbf{q}}(0)U^\dagger. \end{aligned} \tag{6.15}$$

Therefore, in the quadrature basis, the dynamical matrix transforms under a gauge transformation according to

$$\begin{aligned} U \equiv WVW^\dagger &= \frac{1}{2}\bigoplus_{j=1}^N \begin{pmatrix} 1 & 1 \\ -\mathrm{i} & \mathrm{i} \end{pmatrix} \begin{pmatrix} e^{\mathrm{i}\phi_j} & 0 \\ 0 & e^{-\mathrm{i}\phi_j} \end{pmatrix} \begin{pmatrix} 1 & \mathrm{i} \\ \mathrm{i} & -\mathrm{i} \end{pmatrix} \\ &= \bigoplus_{j=1}^N \begin{pmatrix} \cos(\phi_j) & -\sin(\phi_j) \\ \sin(\phi_j) & \cos(\phi_j) \end{pmatrix} = \bigoplus_{j=1}^N R(\phi_j). \end{aligned} \tag{6.16}$$

This is a rotation in phase space by ϕ_j for each mode j. Setting $\phi = \phi_j$ we obtain the transformation $U(\phi) = \oplus_{j=1}^N R(\phi)$ used in (6.3).

6.8.2. Resonant driving and analysis

The central relation used to analyse the results of our experiments is the steady-state response $\mathbf{q}_{\mathrm{ss}}$ of a system of N resonators described by Hamiltonian (6.64) to resonant forces driving its quadratures with amplitudes $\mathbf{f}^{(\mathbf{q})} = (f_{x_1}, f_{p_1}, \ldots, f_{x_N}, f_{p_N})^T$, as discussed in section 2.7.4. Measured in units of the zero-point fluctuations $x_{\mathrm{zpf},j}$ the response is given by

$$\mathbf{q}_{\mathrm{ss}} = \chi_\phi(0)\mathbf{f}^{(\mathbf{q})}. \tag{6.17}$$

In our experiments, the forcing vector $\mathbf{f}^{(\mathbf{q})}$ assumes the role of the quadrature input ports $\mathbf{q}_{\text{in}} = \mathbf{f}^{(\mathbf{q})}/\sqrt{\gamma}$ defined in section 6.2.

As detailed in section 2.6.1, harmonic driving forces are generated by modulation of the drive laser intensity with frequency ω_{d}, depth c_{d} and modulation phase ϕ_{d}. The large frequency separation between modes ($|\Omega_j - \Omega_\ell| \ll \gamma_j, \gamma_\ell$) ensures that only a single mechanical resonator is driven by the modulated cavity field, and results in drive terms f_j (2.61) acting on the field operators a_j. There, we have applied the rotating wave approximation to select the positive frequency sideband of the drive modulation. Conversely, the negative frequency sideband drives the adjoint $a_j^\dagger$, with its drive term f_j^* related by conjugation. By transforming the vector $\mathbf{f}^{(a)} = (f_1, f_1^*, \ldots, f_N, f_N^*)$ to the quadrature basis using the transformation matrix W (6.14), we obtain $\mathbf{f}^{(\mathbf{q})} = W\mathbf{f}^{(a)}$.

Before each experiment, we perform a driven reference measurement for each resonator j to quantify how the modulation depth c_d is transduced into the driving term f_j (section 2.8.7). To reconstruct the on-resonance susceptibility matrix $\chi_\phi(0)$ for a given quadrature angle ϕ, we first refer all (electronic) interaction and LO tones to a common time origin at which their phases are zero (section 2.8.2). Then, we shift the LO tone phases by ϕ to rotate the quadratures they define. We turn on the modulations that generate the desired interactions, and perform a series of $2N$ experiments where we drive the quadratures one by one, with $\arg(f_j) = 0$ to drive x_j and $\arg(f_j) = \pi/2$ to drive p_j for each resonator j while the terms driving the other resonators are zero. For each of these driving conditions $\mathbf{f}_k^{(a)}$, we record the steady state response amplitudes $\{a_1, a_1^\dagger, \ldots, a_N, a_N^\dagger\}$ in the vector $\mathbf{a}_{\text{ss},k}$ after averaging with a low-pass filter (third-order filter, 3 dB bandwidth $2\pi \times 10$ Hz).

We collect the driving vectors in the matrix $\mathcal{F}^{(a)} = \left[\mathbf{f}_1^{(a)} \cdots \mathbf{f}_{2N}^{(a)}\right]$ and the steady-state responses in $A^{(a)} = [\mathbf{a}_{\text{ss},1} \cdots \mathbf{a}_{\text{ss},2N}]$. Next, we obtain the real driving matrix $\mathcal{F}^{(q)} = W\mathcal{F}^{(a)} = \left[\mathbf{f}_1^{(q)} \cdots \mathbf{f}_{2N}^{(q)}\right]$ that contains the quadrature driving amplitudes for each setting. Similarly, the real matrix $A^{(q)} = WA^{(a)} = \left[\mathbf{q}_{\text{ss},1} \cdots \mathbf{q}_{\text{ss},2N}\right]$ contains the steady-state responses in the quadrature basis. Noting that the columns of $\mathcal{F}^{(q)}$ span the entire driving space (and are in fact diagonal), equation (6.17) can be used to obtain the susceptibility matrix $\chi_\phi(0) = A^{(q)}(\mathcal{F}^{(q)})^{-1}$.

To estimate experimental errors, the full ϕ sweep from 0 to 2π is repeated 10 times. The matrix colour plots in Figure 6.1 and 6.4 show average values over all sweeps, whereas the plots of single matrix elements feature error bars that represent the statistical $\pm 2\sigma$ (i.e. a 95% confidence interval) spread around the average value.

6.8.3. Time-reversal symmetry and transport

Here we derive the implications that a TRS-preserving Hamiltonian has on the dynamical matrix of a system with added local decay. While (local) gain and loss explicitly break TRS, they only modify the diagonal of the dynamical matrix such that the underlying TRS-preserving Hamiltonian still imposes certain symmetries on the dynamical matrix and susceptibility matrix. This results in the unique transformation properties of qNR. The formalism in this and the following appendices

was developed primarily by collaborator Clara Wanjura. We include it here for completeness.

The scattering matrix of a time-reversal symmetric system

Here we show that a time-reversal symmetric Hamiltonian imposes certain properties on the scattering matrix of the system with added local gain and loss, namely that there exists at least one set of gauges for which the system's transport is reciprocal on resonance.

If the system preserves TRS, there exists a set of phases $\{\phi_j\}$ that make the Hamiltonian real [73]. Formally, we can express this in terms of the Hamiltonian matrix H (section 2.7.1),

$$\hat{H} = \sum_j \sum_\ell \left(a_j^\dagger H_{a_j^\dagger, a_\ell} a_\ell + a_j^\dagger H_{a_j^\dagger, a_\ell^\dagger} a_\ell^\dagger + \text{H.c.} \right), \tag{6.18}$$

where we explicitly distinguish the Hamiltonian operator $\hat{H}$ from the matrix H. TRS is preserved if we can find a gauge transformation V that maps H to its conjugate, i.e. that makes H real

$$(VHV^\dagger)^* \stackrel{!}{=} VHV^\dagger. \tag{6.19}$$

Note that since V is diagonal, we have $V = V^{\mathrm{T}}$ and $V^\dagger = V^*$. For the systems we are interested in here (coherent couplings with only local decay), the dynamical matrix is closely related to the Hamiltonian matrix through

$$\mathcal{M}_a = -\mathrm{i} \left(\oplus_{j=1}^N \sigma_z \right) H - \frac{\Gamma}{2}, \tag{6.20}$$

with dissipation term $\Gamma = \mathrm{diag}\left(\gamma_1, \gamma_1, \ldots, \gamma_N, \gamma_N\right)$ and Pauli matrix $\sigma_z \equiv \left(\begin{smallmatrix} 1 & 0 \\ 0 & -1 \end{smallmatrix}\right)$. Analogously,

$$H = \mathrm{i} \left(\oplus_{j=1}^N \sigma_z \right) \left[\mathcal{M}_a + \frac{\Gamma}{2} \right]. \tag{6.21}$$

Applying the TRS condition (6.19), we find an analogous relation for the dynamical matrix

$$\left(V \left[\mathcal{M}_a + \frac{\Gamma}{2} \right] V^* \right)^* = -V \left[\mathcal{M}_a + \frac{\Gamma}{2} \right] V^*. \tag{6.22}$$

We convert this to an expression for the dynamical matrix in the quadrature basis

$$\begin{aligned} V \left[\mathcal{M}_a + \frac{\Gamma}{2} \right] V^* &= V W^\dagger W \left[\mathcal{M}_a + \frac{\Gamma}{2} \right] W^\dagger W V^* \\ &= W^\dagger U \left[\mathcal{M}_{\mathbf{q}} + \frac{\Gamma}{2} \right] U^{\mathrm{T}} W \stackrel{!}{=} -\left(V \left[\mathcal{M}_a + \frac{\Gamma}{2} \right] V^* \right)^* \\ &= -(W^\dagger \underbrace{U \left[\mathcal{M}_{\mathbf{q}} + \frac{\Gamma}{2} \right] U^{\mathrm{T}}}_{\in \mathbb{R}^{N \times N}} W)^* = -W^{\mathrm{T}} U \left[\mathcal{M}_{\mathbf{q}} + \frac{\Gamma}{2} \right] U^{\mathrm{T}} W^*. \end{aligned} \tag{6.23}$$

Note that we used that U is real, such that $U^\dagger = U^{\mathrm{T}}$. Using the identities

$$WW^{\mathrm{T}} = \bigoplus_{j=1}^{N} \frac{1}{2} \begin{pmatrix} 1 & 1 \\ -\mathrm{i} & \mathrm{i} \end{pmatrix} \begin{pmatrix} 1 & -\mathrm{i} \\ 1 & \mathrm{i} \end{pmatrix} = \bigoplus_{j=1}^{N} \sigma_z = Z = W^* W^\dagger \tag{6.24}$$

we obtain a TRS condition for the dynamical matrix

$$\boxed{ZU \left[\mathcal{M}_{\mathbf{q}} + \frac{\Gamma}{2} \right] U^{\mathrm{T}} Z = -U \left[\mathcal{M}_{\mathbf{q}} + \frac{\Gamma}{2} \right] U^{\mathrm{T}}}, \tag{6.25}$$

where $Z \equiv \oplus_{j=1}^{N} \sigma_z$.

In addition to TRS, we have a second requirement on $\mathcal{M}_{\mathbf{q}}$ which follows since H is Hermitian, $H = H^\dagger$. With Eq. (6.21), we find

$$\left[\mathcal{M}_a + \frac{\Gamma}{2} \right]^\dagger Z = -Z \left[\mathcal{M}_a + \frac{\Gamma}{2} \right] \Leftrightarrow Z \left[\mathcal{M}_a + \frac{\Gamma}{2} \right] Z = - \left[\mathcal{M}_a + \frac{\Gamma}{2} \right]^\dagger . \tag{6.26}$$

It follows for the dynamical matrix of the field quadratures that

$$\left[\mathcal{M}_{\mathbf{q}} + \frac{\Gamma}{2} \right] = -WZW^\dagger \left[\mathcal{M}_{\mathbf{q}} + \frac{\Gamma}{2} \right]^{\mathrm{T}} WZW^\dagger. \tag{6.27}$$

With the definition of W and Z, we obtain

$$\begin{aligned} WZW^\dagger &= \bigoplus_{j=1}^{N} \frac{1}{2} \begin{pmatrix} 1 & 1 \\ -\mathrm{i} & \mathrm{i} \end{pmatrix} \begin{pmatrix} 1 & 0 \\ 0 & -1 \end{pmatrix} \begin{pmatrix} 1 & \mathrm{i} \\ 1 & -\mathrm{i} \end{pmatrix} \\ &= \bigoplus_{j=1}^{N} \begin{pmatrix} 0 & \mathrm{i} \\ -\mathrm{i} & 0 \end{pmatrix} \equiv \bigoplus_{j=1}^{N} \sigma_y^* \equiv Y^*, \end{aligned} \tag{6.28}$$

where the Pauli matrix $\sigma_y = \left(\begin{smallmatrix} 0 & -\mathrm{i} \\ \mathrm{i} & 0 \end{smallmatrix} \right)$. Therefore, as a consequence of only coherent couplings and local dissipation, the dynamical matrix satisfies in the quadrature basis

$$\boxed{\left[\mathcal{M}_{\mathbf{q}} + \frac{\Gamma}{2} \right] = -Y^* \left[\mathcal{M}_{\mathbf{q}} + \frac{\Gamma}{2} \right]^{\mathrm{T}} Y^*}. \tag{6.29}$$

Combining this result (6.29) with condition (6.25), which we found as a consequence of TRS, the term $\Gamma/2$ drops out and we obtain

$$ZU\mathcal{M}_{\mathbf{q}} U^{\mathrm{T}} Z = UY^* \mathcal{M}_{\mathbf{q}}^{\mathrm{T}} Y^* U^{\mathrm{T}}. \tag{6.30}$$

Note that any diagonal matrix that we add to $\mathcal{M}_{\mathbf{q}}$ drops out in this step, so diagonal modifications, such as local decay, do not change the transformation properties of

the dynamical matrix and hence of the susceptibility matrix. Now, examining UY^* and Y^*U^{T}, we find

$$\begin{aligned} UY^* &= \bigoplus_{j=1}^{N} \begin{pmatrix} \cos\phi_j & -\sin\phi_j \\ \sin\phi_j & \cos\phi_j \end{pmatrix} \begin{pmatrix} 0 & \mathrm{i} \\ -\mathrm{i} & 0 \end{pmatrix} \\ &= \mathrm{i} \bigoplus_{j=1}^{N} R(\phi_j - \pi/2) \equiv \mathrm{i}\, U(\{\phi_j - \pi/2\}), \end{aligned} \tag{6.31}$$

$$\begin{aligned} Y^*U^{\mathrm{T}} &= \bigoplus_{j=1}^{N} \mathrm{i} \begin{pmatrix} \cos(-[\phi_j-\pi/2]) & -\sin(-[\phi_j-\pi/2]) \\ \sin(-[\phi_j-\pi/2]) & \cos(-[\phi_j-\pi/2]) \end{pmatrix} \\ &= -\mathrm{i} \bigoplus_{j=1}^{N} R(-[\phi_j - \pi/2]) \equiv -\mathrm{i}\, U(\{-[\phi_j - \pi/2]\}). \end{aligned} \tag{6.32}$$

The transformation $U(\{\phi_j - \pi/2\})$ is a direct sum of rotation matrices that change the local phase of each mode j by $\phi_j - \pi/2$. With this, condition (6.30) becomes

$$ZU(\{\phi_j\})\mathcal{M}_{\mathbf{q}}U(\{-\phi_j\})Z = U(\{\phi_j - \pi/2\})\mathcal{M}_{\mathbf{q}}^{\mathrm{T}}U(\{-[\phi_j - \pi/2]\}). \tag{6.33}$$

Splitting the rotation matrices $U(\{\phi_j - \pi/2\}) = U(\{-\pi/4\})U(\{\phi_j - \pi/4\})$ and $U(\{-[\phi_j - \pi/2]\}) = U(\{-[\phi_j - \pi/4]\})U(\{\pi/4\})$, and further realising that

$$ZU(\{-\pi/4\}) = \bigoplus_{j=1}^{N} \begin{pmatrix} 1 & 0 \\ 0 & -1 \end{pmatrix} \begin{pmatrix} \cos(\pi/4) & \sin(\pi/4) \\ -\sin(\pi/4) & \cos(\pi/4) \end{pmatrix} = U(\{\pi/4\})Z, \tag{6.34}$$

$$U(\{\pi/4\})Z = \bigoplus_{j=1}^{N} \begin{pmatrix} \cos(\pi/4) & -\sin(\pi/4) \\ \sin(\pi/4) & \cos(\pi/4) \end{pmatrix} \begin{pmatrix} 1 & 0 \\ 0 & -1 \end{pmatrix} = ZU(\{-\pi/4\}), \tag{6.35}$$

we find

$$\begin{aligned} &ZU(\{\phi_j - \pi/4\})\mathcal{M}_{\mathbf{q}}U(\{-[\phi_j - \pi/4]\})Z \\ &\quad = U(\{\phi_j - \pi/4\})\mathcal{M}_{\mathbf{q}}^{\mathrm{T}}U(\{-[\phi_j - \pi/4]\}). \end{aligned} \tag{6.36}$$

We redefine the rotation matrices $\tilde{U} \equiv U(\{\phi_j - \pi/4\})$ and $\tilde{U}^{-1} = U^{\mathrm{T}} \equiv U(\{-[\phi_j - \pi/4]\})$ where each phase ϕ_j has been shifted by $-\pi/4$. This leads to a condition for the dynamical matrix of a TRS-preserving system which only consists of coherent couplings and local dissipation

$$\boxed{Z\tilde{U}\mathcal{M}_{\mathbf{q}}\tilde{U}^{\mathrm{T}}Z = (\tilde{U}\mathcal{M}_{\mathbf{q}}^{\mathrm{T}}\tilde{U}^{\mathrm{T}})^{\mathrm{T}}.} \tag{6.37}$$

In the final step, we consider how the susceptibility matrix transforms under a gauge transformation

$$\begin{aligned} \tilde{U}\chi(\omega)\tilde{U}^{\mathrm{T}} &= (\mathrm{i}\omega\mathbb{1} + \mathcal{M}_{\mathbf{q}})^{-1} = (\tilde{U}\mathrm{i}\omega\mathbb{1}\tilde{U}^{\mathrm{T}} + \tilde{U}\mathcal{M}_{\mathbf{q}}\tilde{U}^{\mathrm{T}})^{-1} \\ &= (\mathrm{i}\omega\mathbb{1} + Z\tilde{U}\mathcal{M}_{\mathbf{q}}^{\mathrm{T}}\tilde{U}^{\mathrm{T}}Z)^{-1} = Z\tilde{U}(\mathrm{i}\omega\mathbb{1} + \mathcal{M}_{\mathbf{q}}^{\mathrm{T}})^{-1}\tilde{U}^{\mathrm{T}}Z. \end{aligned} \tag{6.38}$$

This yields the condition

$$\boxed{\tilde{U}\chi(\omega)\tilde{U}^{\mathrm{T}} = Z(\tilde{U}\chi(-\omega)\tilde{U}^{\mathrm{T}})^{\mathrm{T}}Z.} \tag{6.39}$$

Taking the absolute value for each element in the site basis and noting that Z can only change the sign of each element but neither swaps entries nor changes their modulus, we obtain a condition for the susceptibility matrix of TRS-preserving system

$$\boxed{\left|\tilde{U}\chi(\omega)\tilde{U}^{\mathrm{T}}\right| = \left|\tilde{U}\chi(-\omega)\tilde{U}^{\mathrm{T}}\right|^{\mathrm{T}}.} \tag{6.40}$$

On resonance, we find $|\tilde{U}\chi(0)\tilde{U}^{\mathrm{T}}| = |\tilde{U}\chi(0)\tilde{U}^{\mathrm{T}}|^{\mathrm{T}}$. This implies that for a TRS-preserving system there exists at least one gauge in which, on resonance, the system's transport is reciprocal.

TRS results in equal transmission for pairs of quadratures

A general susceptibility matrix χ in the quadrature basis is of the form

$$\chi = \begin{pmatrix} \chi_{1,1} & \cdots & \chi_{1,j} & \cdots & \chi_{1,N} \\ \vdots & & & & \vdots \\ & & \ddots & & \\ \vdots & & & & \vdots \\ \chi_{N,1} & \cdots & \chi_{N,j} & \cdots & \chi_{N,N} \end{pmatrix}, \tag{6.41}$$

where each $\chi_{j,\ell}$ represents a block

$$\chi_{j,\ell} \equiv \begin{pmatrix} \chi_{x_j,x_\ell} & \chi_{x_j,p_\ell} \\ \chi_{p_j,x_\ell} & \chi_{p_j,p_\ell} \end{pmatrix}. \tag{6.42}$$

The element χ_{q_j,q_ℓ} with $q \in \{x,p\}$ relates an input quadrature of q_ℓ to the steady state of q_j.

Using the TRS conditions on the dynamical matrix $\mathcal{M}_{\mathbf{q}}$ that follow from combining only coherent couplings, Eqs. (6.29), we obtain a condition on the susceptibility matrix

$$\chi(\omega) = -Y^*\chi^{\mathrm{T}}(-\omega)Y^*, \tag{6.43}$$

or, specifically, for each block $\chi_{j,\ell}$, $\chi_{\ell,j} = -\sigma_y^*\chi_{j,\ell}^{\mathrm{T}}\sigma_y^*$. It follows for the elements of each block that

$$\chi_{\ell,j} = \begin{pmatrix} \chi_{x_\ell,x_j} & \chi_{x_\ell,p_j} \\ \chi_{p_\ell,x_j} & \chi_{p_\ell,p_j} \end{pmatrix} = \begin{pmatrix} 0 & 1 \\ -1 & 0 \end{pmatrix} \begin{pmatrix} \chi_{x_j,x_\ell} & \chi_{p_j,x_\ell} \\ \chi_{x_j,p_\ell} & \chi_{p_j,p_\ell} \end{pmatrix} \begin{pmatrix} 0 & 1 \\ -1 & 0 \end{pmatrix} = \begin{pmatrix} -\chi_{p_j,p_\ell} & \chi_{x_j,p_\ell} \\ \chi_{p_j,x_\ell} & -\chi_{x_j,x_\ell} \end{pmatrix}. \tag{6.44}$$

On the other hand, assuming that TRS is preserved imposes another condition on χ, namely, there exists a gauge in which χ satisfies condition (6.39) such that the individual blocks $\chi_{j,\ell}$ are constrained by

$$\chi_{\ell,j}^{\mathrm{r}} = \sigma_z(\chi_{j,\ell}^{\mathrm{r}})^{\mathrm{T}}\sigma_z = \begin{pmatrix} \chi_{x_j,x_\ell}^{\mathrm{r}} & -\chi_{p_j,x_\ell}^{\mathrm{r}} \\ -\chi_{x_j,p_\ell}^{\mathrm{r}} & \chi_{p_j,p_\ell}^{\mathrm{r}} \end{pmatrix}. \tag{6.45}$$

Here, the superscript r refers to the set of local gauges $\{\phi_1,\dots,\phi_N\}$ in which χ is reciprocal, see Eq. (6.40).

Equating these two constraints for the elements of $\chi_{j,\ell}$ (in the gauge in which χ is reciprocal), we obtain the following conditions

$$\chi^{\mathrm{r}}_{x_j,x_\ell}=-\chi^{\mathrm{r}}_{p_j,p_\ell}=t^{\mathrm{r}}_1 \qquad \text{and} \qquad \chi^{\mathrm{r}}_{x_j,p_\ell}=-\chi^{\mathrm{r}}_{p_j,x_\ell}=t^{\mathrm{r}}_2, \tag{6.46}$$

with $t^{\mathrm{r}}_{1,2}$ the susceptibility matrix element at the reciprocal gauge. Similarly,

$$\chi_{j,\ell}=\begin{pmatrix} t^{\mathrm{r}}_1 & t^{\mathrm{r}}_2 \\ -t^{\mathrm{r}}_2 & -t^{\mathrm{r}}_1 \end{pmatrix}, \qquad \text{and} \qquad \chi_{\ell,j}=\begin{pmatrix} t^{\mathrm{r}}_1 & t^{\mathrm{r}}_2 \\ -t^{\mathrm{r}}_2 & -t^{\mathrm{r}}_1 \end{pmatrix}. \tag{6.47}$$

with $t^{\mathrm{r}}_{1,2}$ the susceptibility matrix element in the reciprocal gauge. We now consider how the matrix block $\chi_{j,\ell}$ changes under a gauge transformation $U=\oplus_{j=1}^{N}R(\phi_j)$ which acts on each individual block according to

$$\chi_{j,\ell}(\phi_j,\phi_\ell)=R(\phi_j)\chi^{\mathrm{r}}_{j,\ell}R(-\phi_\ell),\chi_{\ell,j}(\phi_j,\phi_\ell)=R(\phi_\ell)\chi^{\mathrm{r}}_{\ell,j}R(-\phi_j). \tag{6.48}$$

Applying these rotations to the blocks of the susceptibility matrix (6.47) and the resulting matrix entries, we obtain constraints on the susceptibility matrix in any gauge $\chi(\phi_1,\dots,\phi_N)\equiv\chi(\{\phi_j\})$

$$\begin{aligned} \chi_{x_j,x_\ell}(\{\phi_j\})&=-\chi_{p_\ell,p_j}(\{\phi_j\}), & \chi_{p_j,p_\ell}(\{\phi_j\})&=-\chi_{x_\ell,x_j}(\{\phi_j\}),\\ \chi_{x_j,p_\ell}(\{\phi_j\})&=\chi_{x_\ell,p_j}(\{\phi_j\}), & \chi_{p_j,x_\ell}(\{\phi_j\})&=\chi_{p_\ell,x_j}(\{\phi_j\}). \end{aligned} \tag{6.49}$$

This does not automatically imply reciprocity, $|\chi|=|\chi|^{\mathrm{T}}$, and gives room for qNR. The only constraint is that the transmission between certain pairs of quadratures is the same in opposite directions.

Equal transmission for pairs of quadratures implies TRS

We now prove that the previous statement actually applies in both directions, i.e. there exists an equivalence between TRS and the equal transmission of certain pairs of quadratures in opposite directions. We start from a system whose susceptibility matrix satisfies for any set of gauges $\{\phi_j\}$

$$\begin{aligned} |\chi_{x_j,x_\ell}(\{\phi_j\})|&=|\chi_{p_\ell,p_j}(\{\phi_j\})|, & |\chi_{p_j,p_\ell}(\{\phi_j\})|&=|\chi_{x_\ell,x_j}(\{\phi_j\})|,\\ |\chi_{x_j,p_\ell}(\{\phi_j\})|&=|\chi_{x_\ell,p_j}(\{\phi_j\})|, & |\chi_{p_j,x_\ell}(\{\phi_j\})|&=|\chi_{p_\ell,x_j}(\{\phi_j\})|, \end{aligned} \tag{6.50}$$

and we ask if this always implies TRS. Indeed, we can answer this question in the affirmative provided that all the couplings in the system are coherent, i.e. Eq. (6.43) is valid[1]. Conditions (6.50) only fix the modulus of the elements of matrix blocks $\chi_{j,\ell}$ and $\chi_{\ell,j}$ such that they can, in full generality, be written as

$$\chi_{j,\ell}=\begin{pmatrix} \chi_{x_j,x_\ell} & \chi_{p_j,x_\ell} \\ \chi_{x_j,p_\ell} & \chi_{p_j,p_\ell} \end{pmatrix}, \qquad \chi_{\ell,j}=\begin{pmatrix} \chi_{p_j,p_\ell}e^{\mathrm{i}\xi^{(1)}_{j,\ell}} & \chi_{x_j,p_\ell}e^{\mathrm{i}\xi^{(2)}_{j,\ell}} \\ \chi_{p_j,x_\ell}e^{\mathrm{i}\xi^{(3)}_{j,\ell}} & \chi_{x_j,x_\ell}e^{\mathrm{i}\xi^{(4)}_{j,\ell}} \end{pmatrix} \tag{6.51}$$

[1] If we examine a system with dissipative couplings, our arguments can still be applied if we expand the dissipative coupling into coherent coupling via an auxiliary lossy bath mode which, if eliminated, would yield the desired non-local dissipator.

with some phases $\xi^{(1)}_{j,\ell} = -\xi^{(4)}_{\ell,j}$, $\xi^{(2)}_{j,\ell} = -\xi^{(3)}_{\ell,j}$. Since conditions (6.50) should hold for any gauges $\{\phi_j\}$, we check how these matrices transform and under which conditions for $\xi^{(1,2)}_{j,\ell}$ the susceptibility matrix satisfies conditions (6.50) in any gauge. We find that we need to require

$$\xi^{(1)}_{j,\ell} = \delta_{j,\ell}, \quad \xi^{(2)}_{j,\ell} = \pi + \delta_{j,\ell}, \quad \xi^{(3)}_{j,\ell} = \pi + \delta_{j,\ell}, \quad \xi^{(4)}_{j,\ell} = \delta_{j,\ell} \tag{6.52}$$

with $\delta_{j,\ell} = \pi$ corresponding to the TRS-preserving case.

Furthermore, condition (6.43) has to be fulfilled, i.e. $\chi_{\ell,j} = -\sigma^*_y \chi^{\mathrm{T}}_{j,\ell} \sigma^*_y$,

$$\begin{aligned}\sigma^*_y \chi_{\ell,j} \sigma^*_y &= \sigma^*_y \begin{pmatrix} \chi_{p_j,p_\ell} e^{\mathrm{i}\delta_{j,\ell}} & -\chi_{x_j,p_\ell} e^{\mathrm{i}\delta_{j,\ell}} \\ -\chi_{p_j,x_\ell} e^{\mathrm{i}\delta_{j,\ell}} & \chi_{x_j,x_\ell} e^{\mathrm{i}\delta_{j,\ell}} \end{pmatrix} \sigma^*_y \\ &= \begin{pmatrix} -\chi_{x_j,x_\ell} e^{\mathrm{i}\delta_{j,\ell}} & -\chi_{x_j,p_\ell} e^{\mathrm{i}\delta_{j,\ell}} \\ -\chi_{p_j,x_\ell} e^{\mathrm{i}\delta_{j,\ell}} & -\chi_{p_j,p_\ell} e^{\mathrm{i}\delta_{j,\ell}} \end{pmatrix} \overset{!}{=} \begin{pmatrix} -\chi_{x_j,x_\ell} & -\chi_{x_j,p_\ell} \\ -\chi_{p_j,x_\ell} & -\chi_{p_j,p_\ell} \end{pmatrix} = -\chi_{j,\ell}.\end{aligned} \tag{6.53}$$

Here, $\delta_{j,\ell} = \pi$ is the only solution which automatically corresponds to a TRS-preserving system. Therefore, conditions (6.50) can only be satisfied if TRS is preserved.

6.8.4. TRS criterion—full loops vs. disjoint loops

Here, we prove the statement in section 6.4 that TRS can be identified from the graph representing the system's Hamiltonian matrix in the field basis H. For this analysis, we break the system down into its minimal simple rings, i.e. such that there is only one coupling per mode pair (with the exception of the two-mode ring).

The graph representing the block of the dynamical matrix of this ring then forms one full loop, or consists of disjoint loops. We now show that full loops identify systems that always preserve TRS, while graphs displaying two disjoint loops indicate systems that allow to break TRS for certain choices of phases.

As coherent couplings, we first focus on systems with only BS or TMS terms

$$\hat{H} \equiv \sum_{j,\ell} J_{j,\ell} e^{\mathrm{i}\theta_{j,\ell}} a^\dagger_j a_\ell + \sum_{m,n} \lambda_{m,n} e^{\mathrm{i}\psi_{m,n}} a_m a_n + \mathrm{H.c.} \tag{6.54}$$

In a later step, we extend the argument to systems that include local squeezing. TRS implies that there exists a gauge transformation, $a_j \to a_j e^{\mathrm{i}\phi_j}$, that makes the coefficients of the Hamiltonian real, i.e., we need to check, if we can find a set of $\{\phi_j\}$ that removes any possible phases $\theta_{j,\ell}$, $\psi_{j,\ell}$. By asking if TRS is preserved, we ask if the following system of equations has a solution for ϕ_j

$$\theta_{j,\ell} - \phi_j + \phi_\ell = 0, \tag{6.55}$$

$$\psi_{j,\ell} + \phi_j + \phi_\ell = 0. \tag{6.56}$$

For a simple ring with N modes, the number of equations above equals N. This system of equations can be expressed in terms of the adjacency matrix A of a signed, directed graph representing the graphs of Figure 6.3, in which $A_{j,\ell} = -1$ for BS and

$j < \ell$, and $A_{j,\ell} = +1$ for TMS couplings and $j < \ell$. $A_{j,\ell} = 0$ otherwise. Eqs. (6.55) and (6.56) expressed in terms of the adjacency matrix become

$$(\mathbb{1} + \boldsymbol{A})\boldsymbol{\Phi} = \boldsymbol{\Theta} \tag{6.57}$$

with $\boldsymbol{\Phi} \equiv (\phi_1, \ldots, \phi_N)^{\mathrm{T}}$ and $\boldsymbol{\Theta}$ a vector containing the phases $\theta_{j,\ell}$, $\psi_{j,\ell}$. If TRS is preserved, the system of Eqs. (6.55) and (6.56) has at least one solution, i.e., $(\mathbb{1} + \boldsymbol{A})$ has full rank. Conversely, if TRS can be broken via a non-vanishing flux, these equations do not have a solution.

By recursively applying Gaussian elimination we prove next that full loops signal that TRS is preserved for any $\theta_{j,\ell}$, $\psi_{j,\ell}$, while two disjoint loops allow to break TRS through non-vanishing phases $\theta_{j,\ell}$, $\psi_{j,\ell}$.

Disjoint loops allow breaking TRS

First, we show here that if the graph breaks up into two disjoint loops, the system can break TRS. Recursively applying Gaussian elimination to $(\mathbb{1} + \boldsymbol{A})$, we show that the matrix rank is smaller than the number of modes N when the graph decomposes into two loops. If all sites are either coupled via beamsplitter of parametric interactions, we can, without loss of generality, reorder the matrix $(\mathbb{1} + \boldsymbol{A})$, so that it takes the following form

$$(\mathbb{1} + \boldsymbol{A}) = \begin{pmatrix} 1 & \pm 1 & 0 & 0 & \ldots & 0 & 0 \\ 0 & 1 & \pm 1 & 0 & \ldots & 0 & 0 \\ 0 & 0 & 1 & \pm 1 & \ldots & 0 & 0 \\ & & & & \ddots & & \\ 0 & 0 & 0 & 0 & \ldots & 1 & \pm 1 \\ 1 & 0 & 0 & 0 & \ldots & 0 & \pm 1 \end{pmatrix}. \tag{6.58}$$

We start by examining systems whose graphs decompose into two disjoint graphs. We note that this requires an even number of parametric couplings (pairs of $+1$, $+1$ in $\boldsymbol{\Phi}$) and any number of beamsplitter couplings.

Beamsplitter coupling followed by beamsplitter coupling

We consider the case that both mode pairs j and $(j-1)$ as well as j and $(j+1)$ are coupled via BS links. In this case, we can eliminate the jth row in $(\mathbb{1} + \boldsymbol{A})$ such that the resulting matrix looks like a direct connection between $(j-1)$ and $(j+1)$

$$(\mathbb{1} + \boldsymbol{A}) = \begin{pmatrix} \ddots & & & & \\ \ldots & 1 & -1 & 0 & \ldots \\ \ldots & 0 & 1 & -1 & \ldots \\ & & & \ddots & \end{pmatrix} \rightarrow \begin{pmatrix} \ddots & & & & \\ \ldots & 1 & -1 & 0 & \ldots \\ \ldots & 1 & 0 & -1 & \ldots \\ & & & \ddots & \end{pmatrix}. \tag{6.59}$$

If the loop *only* consists of beamsplitter interactions, then we can repeat this elimination step throughout the matrix until the last row equals the second to last row. Subsequently, the last row can be eliminated, the system does not have full rank, therefore no solution and we can, through a non-vanishing phase $\theta_{j,\ell}$, $\psi_{j,\ell}$ break TRS. This is a well know result [73].

Beamsplitter coupling followed by parametric coupling (or vice versa)

Here we can show that beamsplitter coupling between $(j-1)$ and j followed by parametric coupling between j and $(j+1)$ can, in $(\mathbb{1} + \boldsymbol{A})$, be reduced to a row

that has the same form as parametric coupling between $(j-1)$ and $(j+1)$

$$(\mathbb{1}+\boldsymbol{A}) = \begin{pmatrix} \ddots & & & & \\ \cdots & 1 & -1 & 0 & \cdots \\ \cdots & 0 & 1 & 1 & \cdots \\ & & & \ddots & \end{pmatrix} \to \begin{pmatrix} \ddots & & & & \\ \cdots & 1 & -1 & 0 & \cdots \\ \cdots & 1 & 0 & 1 & \cdots \\ & & & \ddots & \end{pmatrix}. \tag{6.60}$$

An even number of parametric couplings
An even number of parametric couplings looks like beamsplitter couplings. If they follow right after each other, the following argument holds:

$$(\mathbb{1}+\boldsymbol{A}) = \begin{pmatrix} \ddots & & & & \\ \cdots & 1 & 1 & 0 & \cdots \\ \cdots & 0 & 1 & 1 & \cdots \\ & & & \ddots & \end{pmatrix} \to \begin{pmatrix} \ddots & & & & \\ \cdots & 1 & 1 & 0 & \cdots \\ \cdots & 1 & 0 & -1 & \cdots \\ & & & \ddots & \end{pmatrix}. \tag{6.61}$$

If there are beamsplitter couplings in between, these can be reduced firstly, for instance,

$$\begin{aligned}(\mathbb{1}+\boldsymbol{A}) = &\begin{pmatrix} \ddots & & & & & & & & & \\ \cdots & 1 & 1 & 0 & \cdots & 0 & 0 & 0 & \cdots \\ \cdots & 0 & 1 & -1 & \cdots & 0 & 0 & 0 & \cdots \\ & & & & \ddots & & & & \\ \cdots & 0 & 0 & 0 & \cdots & 1 & -1 & 0 & \cdots \\ \cdots & 0 & 0 & 0 & \cdots & 0 & 1 & 1 & \cdots \\ & & & & & & & & \ddots \end{pmatrix} \to \begin{pmatrix} \ddots & & & & & & & & & \\ \cdots & 1 & 1 & 0 & \cdots & 0 & 0 & 0 & \cdots \\ \cdots & 1 & 0 & 1 & \cdots & 0 & 0 & 0 & \cdots \\ & & & & \ddots & & & & \\ \cdots & 0 & 0 & 0 & \cdots & 1 & -1 & 0 & \cdots \\ \cdots & 0 & 0 & 0 & \cdots & 0 & 1 & 1 & \cdots \\ & & & & & & & & \ddots \end{pmatrix} \\ \to \cdots \to &\begin{pmatrix} \ddots & & & & & & & & & \\ \cdots & 1 & 1 & 0 & \cdots & 0 & 0 & 0 & \cdots \\ \cdots & 1 & 0 & 1 & \cdots & 0 & 0 & 0 & \cdots \\ & & & & \ddots & & & & \\ \cdots & 1 & 0 & 0 & \cdots & 0 & 1 & 0 & \cdots \\ \cdots & 0 & 0 & 0 & \cdots & 0 & 1 & 1 & \cdots \\ & & & & & & & & \ddots \end{pmatrix} \to \begin{pmatrix} \ddots & & & & & & & & & \\ \cdots & 1 & 1 & 0 & \cdots & 0 & 0 & 0 & \cdots \\ \cdots & 1 & 0 & 1 & \cdots & 0 & 0 & 0 & \cdots \\ & & & & \ddots & & & & \\ \cdots & 1 & 0 & 0 & \cdots & 0 & 1 & 0 & \cdots \\ \cdots & 1 & 0 & 0 & \cdots & 0 & 0 & -1 & \cdots \\ & & & & & & & & \ddots \end{pmatrix}. \end{aligned} \tag{6.62}$$

Therefore, for an even number of parametric couplings, the matrix $(\mathbb{1}+\boldsymbol{A})$ can be reduced such that the last and second to last row are the same (both look like beamsplitter couplings between mode 1 and N) and one row can be eliminated. Thus, the matrix does not have full rank.

Single-mode squeezing terms / local parametric terms
Examining the graph of a system containing single-mode squeezing $\propto \eta_j e^{\psi_j} a_j^2 +$ H.c., we note that as soon as the single-mode squeezing is part of a simple ring, it decomposes the graph into two disjoint loops. This is because single-mode squeezing closes the loop on the same site[2]. In this case, TRS can again be broken through non-vanishing phases, since single-mode squeezing acts locally and fixes one phase ϕ_j of one of the operators a_j in Eq. (6.54) (e.g. if the Hamiltonian contains a term $\eta_j e^{\psi_j} a_j^2 +$ H.c. then this fixes the phase $\phi_j = \psi_j/2$ of a_j).

Multiple couplings per link in a single ring
The only simple ring with multiple (distinct) couplings per link, is the qNR dimer (main text), combining BS and TMS couplings which does not break TRS, since

$$(\mathbb{1}+\boldsymbol{A}) = \begin{pmatrix} 1 & -1 \\ 1 & 1 \end{pmatrix} \to \begin{pmatrix} 1 & 0 \\ 0 & 1 \end{pmatrix}, \tag{6.63}$$

has full rank. This is the only possibility for multiple links in a simple ring.

[2] In this case, the number of rows of $(\mathbb{1}+\boldsymbol{A})$ exceeds the number of modes in the ring.

Full loops and their conglomeration preserve TRS

We noted that disjoint loops require an even number of TMS, while a full loop occurs for an odd number of parametric couplings. In the previous calculations we showed that TRS can be broken when the number of TMS couplings is even, by bringing $(\mathbb{1} + \boldsymbol{A})$ to a form in which the second-to-last and last row were equal so that we could eliminate one to show that the matrix does not have full rank. With an odd number of couplings the second-to-last and last row are not equal, so that we cannot eliminate the last row and the matrix has full rank. This implies that TRS is always preserved when the graph of the ring displays one full loop.

In a system consisting of multiple rings, we can show using the same elimination technique that as soon as one ring with a graph displaying two disjoint loops is contained, TRS can be broken. Otherwise, TRS is automatically preserved.

6.8.5. Linear response and interference of beamsplitter and squeezing interactions

We recall from section 2.6.3 that a general quadratic, bosonic Hamiltonian can be written in the field basis of creation and annihilation modes, $\{a_i, a_i^\dagger\}$, as

$$\hat{H} = \sum_{i,j} \left\{ a_i^\dagger \mathcal{A}_{ij} a_j + \frac{1}{2}(a_i^\dagger \mathcal{B}_{ij} a_j^\dagger + a_i \mathcal{B}_{ij}^* a_j) \right\}, \tag{6.64}$$

where overall constant shifts have been removed. Here, the matrix elements $\mathcal{A}_{ij} = J_{ij} e^{-i\varphi_{ij}}$, $\mathcal{A}_{ji} = \mathcal{A}_{ij}^*$ of the Hermitian *hopping matrix* $\mathcal{A}$ encode beamsplitter interactions that conserve the total number of excitations. Similarly, we define the symmetric *squeezing matrix* $\mathcal{B}$ that encodes the particle-non-conserving squeezing interactions in its elements $\mathcal{B}_{ij} = \lambda_{ij} e^{i\theta_{ij}}$, $\mathcal{B}_{ji} = \mathcal{B}_{ij}$.

In the quadrature basis $x_j = (a_j + a_j^\dagger)/\sqrt{2}$ and $p_j = \mathrm{i}(a_j^\dagger - a_j)/\sqrt{2}$, Eq. (6.64) reads

$$\hat{H} = \sum_{i,j} \left\{ T_{ij} p_i p_j + V_{ij} x_i x_j + U_{ij} x_i p_j + U_{ij}^T p_i x_j \right\}, \tag{6.65}$$

where we define the effective potential matrices $U = \mathrm{Im}(\mathcal{B} - \mathcal{A}), V = \mathrm{Re}(\mathcal{A} + \mathcal{B})$ and kinetic energy $T = \mathrm{Re}(\mathcal{A} - \mathcal{B})$ as in section 2.7.3 [161]. The corresponding Heisenberg equations of motion read

$$\begin{pmatrix} \dot{x}_j \\ \dot{p}_j \end{pmatrix} = \sum_{k=1}^{N} \begin{pmatrix} U_{kj} x_k + T_{jk} p_k \\ -V_{jk} x_k - U_{jk} p_k \end{pmatrix} - \begin{pmatrix} \gamma_j x_j \\ \gamma_j p_j \end{pmatrix}. \tag{6.66}$$

In our platform, quadratic Hamiltonians of the form Eq. (6.64) are effectively conceived in a rotating frame of reference that oscillates at the natural frequencies of the resonators. As such, free energy terms $\propto a_i^\dagger a_i$ are absent, and the matrix elements for U, V, T read

$$\begin{aligned} V_{ij}, T_{ij} =& J_{ij} \cos(\varphi_{ij}) \pm \lambda_{ij} \cos(\theta_{ij}), \\ U_{ij} =& \lambda_{ij} \sin(\theta_{ij}) + J_{ij} \sin(\varphi_{ij}). \end{aligned} \tag{6.67}$$

These expressions show that matching interaction amplitudes and complex interaction phases can lead to a cancellation of different contributions in Eq. (6.65), decoupling quadratures from different resonators in the dynamics governed by Eq. (6.66) [162, 232]. This is the case for $\lambda_{ij} = J_{ij}$ and $\theta_{ij} = \varphi_{ij} = n\pi/2$, $n \in \mathbb{Z}$, where $T = V = 0$. This can be interpreted as destructive interference in the particle-hole space [151].

6.8.6. Non-Hermitian topological invariant

To analyse the topological properties of the chain of 4-rings shown in Figure 6.5a, we write the dynamical equations for the quadratures under periodic boundary conditions, $J = \lambda$, and obtain the dynamical matrix in the plane-wave basis. We label the four resonators of each unit cell A_ℓ for the resonators in the left column, with $\ell \in \{1, 2\}$ the row index, and B_ℓ for the right column. The resulting dynamical equations decouple into two respectively closed sets of equations for the sets of quadratures $\{x_j^{A_1}, x_j^{B_2}, p_j^{B_1}, p_j^{A_2}\}$, where j denotes the index of the unit cell, namely,

$$\begin{aligned}
\dot{x}_j^{A_1} &= -\frac{\gamma}{2} x_j^{A_1} + J p_j^{A_2} - J p_j^{B_1} + J p_{j-1}^{B_1} - \sqrt{\gamma} x_{j,\mathrm{in}}^{A_1}, \\
\dot{x}_j^{B_2} &= -\frac{\gamma}{2} x_j^{B_2} + J p_j^{A_2} - J p_j^{B_1} - \sqrt{\gamma} x_{j,\mathrm{in}}^{B_2}, \\
\dot{p}_j^{B_1} &= -\frac{\gamma}{2} p_j^{B_1} - J x_j^{A_1} - J x_j^{B_2} - J x_{j+1}^{A_1} - \sqrt{\gamma} p_{j,\mathrm{in}}^{B_1}, \\
\dot{p}_j^{A_2} &= -\frac{\gamma}{2} p_j^{A_2} - J x_j^{B_2} - J x_j^{A_1} - \sqrt{\gamma} p_{j,\mathrm{in}}^{A_2},
\end{aligned} \tag{6.68}$$

and $\{x_j^{A_2}, x_j^{B_1}, x_j^{A_1}, x_j^{B_2}\}$, reading

$$\begin{aligned}
\dot{x}_j^{A_2} &= -\frac{\gamma}{2} x_j^{A_2} + J p_j^{A_1} + J p_j^{B_2} - \sqrt{\gamma} x_{j,\mathrm{in}}^{A_2}, \\
\dot{x}_j^{B_1} &= -\frac{\gamma}{2} x_j^{B_1} - J p_j^{A_1} + J p_j^{B_2} + J p_{j+1}^{A_1} - \sqrt{\gamma} x_{j,\mathrm{in}}^{B_1}, \\
\dot{p}_j^{A_1} &= -\frac{\gamma}{2} p_j^{A_1} - J x_j^{A_2} - J x_j^{B_1} - J x_{j-1}^{B_1} - \sqrt{\gamma} p_{j,\mathrm{in}}^{A_1}, \\
\dot{p}_j^{B_2} &= -\frac{\gamma}{2} p_j^{B_2} - J x_j^{A_2} - J x_j^{B_1} - \sqrt{\gamma} p_{j,\mathrm{in}}^{B_2}.
\end{aligned} \tag{6.69}$$

The fact that these two sets decouple is a consequence of the pairing we found for qNR rings. We now switch to reciprocal space, $|j\rangle \equiv \frac{1}{\sqrt{N}} \sum_k e^{-\mathrm{i}ka} |k\rangle$, in which we used Dirac notation to denote the basis vectors $\{|j\rangle\}$ and $\{|k\rangle\}$ and a mimics a lattice spacing (we set $a = 1$). We obtain two dynamical matrices for each of these

sets

$$\mathcal{M}_{\mathbf{q}}^{(1)}(k) = \begin{pmatrix} -\frac{\gamma}{2} & 0 & J(-1+e^{-\mathrm{i}k}) & J \\ 0 & -\frac{\gamma}{2} & J & J \\ -J(1+e^{\mathrm{i}k}) & -J & -\frac{\gamma}{2} & 0 \\ -J & -J & 0 & -\frac{\gamma}{2} \end{pmatrix},$$
$$\mathcal{M}_{\mathbf{q}}^{(2)}(k) = \begin{pmatrix} -\frac{\gamma}{2} & 0 & J & J \\ 0 & -\frac{\gamma}{2} & J(-1+e^{\mathrm{i}k}) & J \\ -J & -J(1+e^{-\mathrm{i}k}) & -\frac{\gamma}{2} & 0 \\ -J & -J & 0 & -\frac{\gamma}{2} \end{pmatrix}. \tag{6.70}$$

We calculate a topological invariant from each matrix, namely the winding number of their determinant

$$\nu_{1,2} = \frac{1}{2\pi\mathrm{i}} \int_0^{2\pi} \mathrm{d}k \, \det \mathcal{M}_{\mathbf{q}}^{(1,2)}(k). \tag{6.71}$$

We find

$$\begin{aligned} \det \mathcal{M}_{\mathbf{q}}^{(1,2)}(k) = &-2J^4 \cos(k) + \frac{1}{16}\left(\gamma^4 + 16J^4 + 12\gamma^2 J^2\right) \\ &\pm i\left(2J^4 + \frac{\gamma^2 J^2}{2}\right)\sin(k), \end{aligned} \tag{6.72}$$

in which we choose the $(-)$ sign for $\det \mathcal{M}_{\mathbf{q}}^{(1)}(k)$ and the $(+)$ sign for $\det \mathcal{M}_{\mathbf{q}}^{(2)}(k)$. These two curves wind in opposite directions in the complex plane, as k evolves from 0 to 2π, inducing the opposite sign for ν_1 and ν_2 (see Figure 6.5e).

Above, we used the plane-wave basis to identify the non-trivial topology of each block $\mathcal{M}_{\mathbf{q}}^{(1)}(k)$, $\mathcal{M}_{\mathbf{q}}^{(2)}(k)$. The eigenvalues of $\mathcal{M}_{\mathbf{q}}^{(1)}(k)$ are also the eigenvalues of $\mathcal{M}_{\mathbf{q}}^{(2)}(k)$, albeit for a different k. Together they form a degenerate sub-space. To obtain the physical (and real) eigenvectors, i.e. pairs of canonically conjugated, real valued quadratures, we need to superpose eigenvectors from these sub-spaces.

7

Optomechanical realization of the bosonic Kitaev chain

We report an experimental realization of the bosonic Kitaev chain, a one-dimensional non-Hermitian topological system which features unidirectional phase-dependent amplification and stability that depends strongly on boundary conditions. Analogous to the fermionic Kitaev-Majorana chain, we induce both hopping and pairing interactions between mechanical modes in a chain, through parametrically modulated radiation pressure forces of a laser control field. In a four-mode system, we investigate the characteristic exponential phase-dependent amplification, and show that the localization of mechanical energy in and dynamical stability of the chain depend crucially on its boundary conditions. These results represent the demonstration of non-Hermitian synthetic topological lattices with bosonic dynamics that do not have fermionic counterpart, and establish a model system to study non-Hermitian topology and its applications.

7.1. Introduction

In previous chapters, we studied the interplay between particle-conserving beamsplitter interactions and particle-non-conserving parametric amplification, and the resulting non-Hermitian dynamics in small systems. For extended lattices, non-Hermitian dynamics combined with suitable lattice symmetries are known to result in unique, non-Hermitian topological phases [106, 107, 217, 219, 222, 273–276]. Whereas topological invariants in Hermitian systems are always defined on the structure of their *eigenvectors* [36, 69], non-Hermitian systems may also exhibit topology in the band structure of their complex *eigenvalues* (section 1.5) [106, 218, 223, 225, 273, 274, 277–279]. The topological description of periodic non-Hermitian systems is further enriched by complementing the eigenvector topology characterizing Hermitian topological insulators by the topological nature of exceptional points [107]. A rigorous classification of non-Hermitian topological phases analogous to the Hermitian case was constructed [273, 274].

In addition to line gaps, which map to regular band gaps in Hermitian systems [219, 274], the *spectral topology* of non-Hermitian systems is characterized by point gaps: Regions in the complex plane that are enclosed by a non-Hermitian band, to which an *eigenvalue winding number* can be assigned [107, 219]. A widely studied phenomenon related to such spectral structure is the non-Hermitian skin effect (NHSE), i.e. the accumulation of a macroscopic number of states at system boundaries [112, 280–285], which was observed experimentally in various systems from photonics to acoustics and cold atoms [227–230, 286–289]. While the significance of the topological origin of the NHSE is a topic of debate [107, 217, 219, 230, 233, 282, 283, 285, 290, 291], its central feature, a strong sensitivity to boundary conditions, is clear: With periodic boundary conditions the system features a winding, typically unstable complex spectrum with delocalized states, while the spectrum of a system with open boundaries collapses to a line with localized eigenvectors and typically stable dynamics — illustrating the breakdown of the conventional relation between infinite and finite systems that underlies the Hermitian bulk-boundary correspondence [106].

In this field, recently a bosonic analogue was proposed [232] of the electronic Kitaev chain that underlies topologically protected Majorana zero modes in specific one-dimensional superconductors [292]. This bosonic Kitaev chain (BKC), formed by coupling an array of bosonic modes with beamsplitter (i.e. hopping) and two-mode squeezing (i.e. pairing) interactions, has remarkable properties, including quadrature-dependent chiral transport, crucial sensitivity to boundary conditions and phase-sensitive amplification that is not limited by a standard gain-bandwidth product [232]. It has also been predicted to offer applications in quantum sensing, allowing an exponential boost of sensitivity to a signal that perturbs the end of the chain as a function of chain length [293]. Its amplification behaviour can be linked to the topological properties of its dynamical matrix [233]. In the presence of dissipation, the ends of the chain are expected to support metastable edge states that have been considered by some as bosonic Majorana zero modes [261].

Similar to its fermionic counterpart, the bosonic Kitaev chain is best understood in terms of the Hermitian quadrature operators x_j and p_j of each bosonic site j. By

setting appropriate interaction phases, the x_j quadratures completely decouple from their p_j counterparts, with the couplings in the two subchains asymmetric in direction. This resembles the physics of the non-Hermitian Hatano-Nelson chain [110] or the chiral transport in the quantum spin Hall effect [36]. However, despite its appealing features, it is yet to be realized in experiment.

Here we use the quadrature nonreciprocal (qNR) dimer introduced in the previous chapter as a building block to realize the bosonic Kitaev chain in a nanomechanical setting. By balancing the required hopping and two-mode squeezing interactions, we observe that phase-dependent transport in the chain becomes fully nonreciprocal, with directionality controlled by the quadrature of the injected signal. Furthermore, we demonstrate that each link of the chain acts as an amplifier, such that signals may grow (or decay) exponentially along the chain. This strikingly impacts the dynamics of chains with periodic boundary conditions: As the per-link gain exceeds unity, signals are amplified indefinitely and the chain becomes dynamically unstable. We observe this transition by studying the thermomechanical spectrum of the closed chain. In contrast, we demonstrate that the open chain remains stable, marking the crucial sensitivity of the chain to its boundary conditions — a consequence of the non-Hermitian skin effect. Finally, we study the importance of the phases of the hopping and squeezing interactions in the chain, and observe that tuning them allows to transition from a global to a local response of the chain. These results demonstrate the interesting physics of bosonic topological systems with non-Hermitian dynamics.

7.2. The bosonic Kitaev chain

In Figure 7.1a we show the bosonic Kitaev chain (BKC) proposed in [232]: A one-dimensional array of modes coupled simultaneously by beamsplitter (BS) and two-mode squeezing (TMS) interactions with complex rates J and λ, respectively. The Hamiltonian that describes this system reads

$$H_{\mathrm{BKC}} = \sum_j \left(J a_{j+1}^\dagger a_j + \lambda a_{j+1}^\dagger a_j^\dagger + \mathrm{H.c.} \right), \tag{7.1}$$

where the modes are described by their annihilation operators a_j and labelled by the index j.

Hamiltonian (7.1) describes a chain of quadrature nonreciprocal (qNR) dimers as introduced in the previous chapter. It is thus most naturally described in terms of the mode quadratures

$$x_j = (a_j + a_j^\dagger)/\sqrt{2}, \qquad p_j = (a_j - a_j^\dagger)/(\mathrm{i}\sqrt{2}). \tag{7.2}$$

The coupling between the quadratures, expressed for example in their equations of motion (Figure 7.1b), depends on the phase of the BS and TMS interactions. In the previous chapter, we chose J and λ to be real. For a single qNR dimer, this choice is not essential — any interaction phase can be removed by changing the gauge that defines the quadratures x_j, p_j.

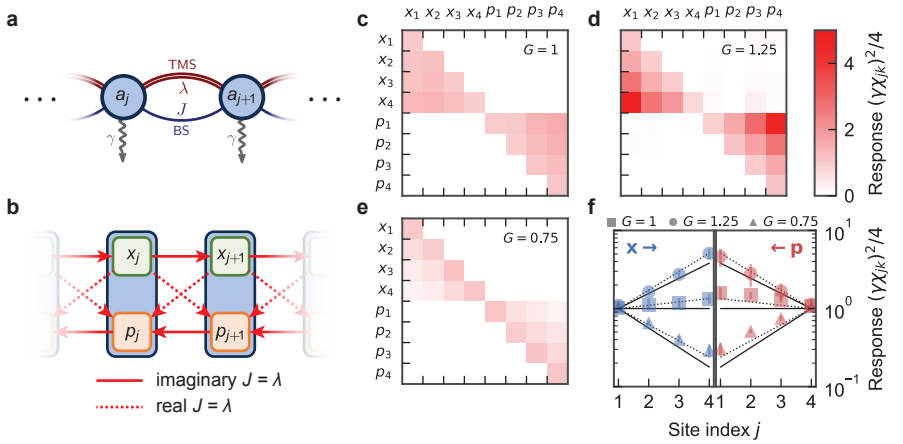

Figure 7.1: **Bosonic Kitaev chain (BKC) and quadrature-dependent chiral transport. (a)** In the BKC, modes a_j are simultaneously coupled in a chain by beamsplitter (BS) and two-mode squeezing interactions (TMS) with rates J and λ, respectively. Modes are subject to dissipation with rate γ. **(b)** Representation of the BKC equations of motion. For a chain where $J = \lambda = \mathrm{i}\mu$ only have a positive imaginary part $\mu > 0$, i.e. the BKC proper [232], x_j (p_j) quadratures exclusively drive their right (left) neighbours (solid arrows). For positive, real $J = \lambda > 0$, quadratures p_j are driven by x_j quadratures of both neighbours (dashed arrows). **(c)** Measured susceptibility matrix χ^2 (squared element-wise) for an open BKC with $N = 4$ modes and imaginary coupling rates $J = \lambda = \mathrm{i}\mu$. The chain is implemented using four nanomechanical modes (resonances 1-4 in Figure 2.3 subject to light-mediated BS and TMS interactions with strengths $\mu/(2\pi) \approx 2$ kHz. Feedback (section 2.8.6) is employed to equalize the resonator damping rates $\gamma_j/(2\pi) \approx \gamma \approx 8$ kHz. Excitations propagate chirally along the chain with a quadrature-dependent direction, and experience an amplitude gain per link given by the ratio $G = 4\mu/\gamma \approx 1$. **(d)** Similar, with $\mu \approx 2.5$ kHz such that excitations are amplified along the chain with per-link gain $G \approx 1.25 > 1$. **(e)** Here, $\mu \approx 1.5$ kHz. Excitation amplitudes decrease in transport as $G \approx 0.75 < 1$ **(f)** Susceptibility matrix elements $\chi^2_{x_j,x_1}$ ($\chi^2_{p_j,p_4}$) are shown in the left (right) panel, corresponding to the first (last) column of panels (c-e), and illustrate the propagation of energy injected in the left-most quadrature x_1 (right-most quadrature p_4) through the chain. Solid lines represent nominal per-link gains $G = \{0.75, 1, 1.25\}$. We see that the observed responses are better explained by interaction rates μ increased by 5%, which carries over to G (dashed lines). Error bars are obtained by repeating the measurement sweep 5 times and represent the statistical $\pm 2\sigma$ spread around the average value.

This is, however, not the case for a chain. Setting the rates $J = \lambda = \mu > 0$ to be purely real, positive and balanced, instantiates a chain of quadrature-converting qNR dimers: Each quadrature p_j is coupled to both of its neighbours x_{j-1} and x_{j+1}, whereas p_j itself does not drive any neighbouring quadratures (Figure 7.1b, dashed lines). In section 7.5 we will see that this chain has a purely local response.

On the contrary, the BKC proper — the system discussed in [232] — is obtained by setting the rates J and λ to be purely imaginary. This completely decouples the x_j quadratures from the p_j quadratures. Moreover, for the particular case of balanced rates $J = \lambda = \mathrm{i}\mu$ with positive imaginary part $\mu > 0$, the couplings become fully unidirectional: Quadratures x_j are only forced by their neighbour x_{j-1} on the left, whereas p_j are only forced by their neighbour p_{j+1} on the right. The BKC then decouples into two fully directional chains of coupled quadratures with

opposite orientations (Figure 7.1b, solid lines), reminiscent of counter-propagating spin-polarized edge currents in the quantum spin Hall effect [36]. Furthermore, these subchains of quadratures coupled by asymmetric hoppings resemble the Hatano-Nelson chain [110], where mode operators are coupled by beamsplitter interactions with asymmetric amplitudes. However, we emphasize that the Hatano-Nelson Hamiltonian is fundamentally non-Hermitian, while the Hamiltonian H_{BKC} in (7.1) underlying the BKC is Hermitian.

7.3. Quadrature-dependent chiral transport

We implement a BKC with $N = 4$ modes in experiment, using the flexural mechanical resonances of the sliced nanobeam introduced in chapter 2. Nanomechanical BS and TMS interactions are induced between the detuned mechanical modes (resonance frequencies Ω_j) through modulated radiation pressure forces, exerted by the field of a common nanocavity coupled to all modes. By suitable modulations of a drive laser, effective mechanical interactions are tunable both in strength and in phase. Furthermore, we build on the experimental methods laid out in the previous chapters to actuate and detect nanomechanical motion with quadrature resolution (sections 2.8.2, 6.8.2), and use measurement-based feedback to equalize the damping rates of all modes to $\gamma_j = \gamma = 8$ kHz (section 2.8.6).

First, we probe the response of the open BKC to resonant driving with modulated radiation pressure. We collect the steady-state amplitudes in the vector $\vec{q} = (x_1, p_1, \ldots, x_N, p_N)^T$, and the drive term acting on each quadrature in the vector $\mathbf{f}^{(\mathbf{q})} = (f_{x_1}, f_{p_1}, \ldots, f_{x_N}, f_{p_N})$. The real matrix χ that relates these quantities through $\vec{q} = \chi \mathbf{f}^{(\mathbf{q})}$ is called the susceptibility matrix (section 2.7.4). In signal transport, one is often concerned with the transmitted energy x_j^2, p_j^2 rather than amplitude x_j, p_j. This is characterized by the matrix χ^2, where the square $(\cdot)^2$ is applied element-wise.

In Figure 7.1c, we show the energy susceptibility matrix χ^2 for the BKC with $N = 4$ modes and $J = \lambda = \mathrm{i}\mu$, $\mu/(2\pi) \approx 2$ kHz. The measured matrix is block-diagonal, indicating the decoupling of x_j and p_j. Moreover, within each block we clearly observe chiral transport: The block describing the x_j quadratures is lower triangular, indicating that energy injected in x_j only travels to the right. Conversely, the other block, describing the p_j quadratures, is upper triangular and reveals leftward transport of energy. Notably, this isolates excitations in the quadratures x_4 and p_1 from the rest of the chain, in a fashion resembling the edge-localized Majorana zero modes in the fermionic Kitaev chain. However, as x_4 and p_1 commute, their 'quasiparticle' superposition can never form a delocalized canonical bosonic mode like their fermionic Majorana counterparts [232]. Still, these states have been theoretically analyzed for their specific stability, localization, and sensitivity properties [232, 261] (and dubbed 'Majorana bosons' by some [261]).

As discussed in the previous chapter, a qNR dimer offers the opportunity to amplify signals in transport through the presence of two-mode parametric gain. Since it constitutes a chain of concatenated qNR dimers, this carries over to the BKC. The output of each dimer serves as the input for the next, in a way that is

formally equivalent to a cascaded quantum system [268, 269]. As the parametric amplification competes with incoherent dissipation, the amplitude gain per link in the balanced BKC (with $J = \lambda = \mathrm{i}\mu$) is given by the ratio $G = 4\mu/\gamma$.

For the experiment shown in Figure 7.1c, the interaction rate setting $\mu/(2\pi) = 2$ kHz induces a per-link gain $G \approx 1$ close to unity. A signal injected in any site x_j (p_j) thus emerges at all sites $x_{k>j}$ to the right ($p_{k<j}$ to the left) with equal amplitude. In Figure 7.1d,e, interaction rates $\mu/(2\pi) = \{2.5, 1.5\}$ kHz induce per-link gains $G = 1.25$ and 0.75, respectively, such that injected energy emerges with exponentially growing or decaying magnitude along the chain (Figure 7.1f). The corresponding theoretical energy susceptibility matrix for all three cases is given in the basis $\{x_1, \dots x_4, p_1, \dots, p_4\}$ by

$$\chi^2 = \frac{4}{\gamma^2} \begin{pmatrix} 1 & & & & & & & \\ G^2 & 1 & & & & & & \\ G^4 & G^2 & 1 & & & & & \\ G^6 & G^4 & G^2 & 1 & & & & \\ & & & & 1 & G^2 & G^4 & G^6 \\ & & & & & 1 & G^2 & G^4 \\ & & & & & & 1 & G^2 \\ & & & & & & & 1 \end{pmatrix}. \tag{7.3}$$

7.4. Boundary conditions and stability

In a perfectly balanced, open BKC, the linear per-link gain G can be made arbitrarily large by increasing μ, while the total signal amplification G^N along the chain remains bound by its finite length N. The open BKC thus remains dynamically stable for any value of μ. [232]

This is markedly different in the closed BKC: By connecting the last resonator a_N to the first resonator a_1, excitations can circulate along the loop. If the per-link gain $G > 1$ then exceeds unity, excitations grow indefinitely and the closed BKC becomes unstable. As pointed out in [232], the boundary conditions of a BKC thus dramatically impact its dynamics, complex eigenfrequencies and eigenmodes. This holds true for unbalanced ($J \neq \lambda$) BKCs as well, and links to the dependence of the dynamical (topological) properties of non-Hermitian asymmetric hopping models — such as the Hatano-Nelson chain [110] and the BKC itself — on their boundary conditions [107, 112, 219, 290].

In Figure 7.2, we probe the stability of a four-mode balanced BKC ($J = \lambda = \mathrm{i}\mu$) under thermal driving of all quadratures. For the open chain, the thermomechanical spectrum of resonator 1 (Figure 7.2a, left) shows an increase in spectral intensity with increasing μ, while the lineshape of the thermal resonance remains similar. In contrast, the spectrum of the closed chain (Figure 7.2a, right) shows a resonance with narrowing linewidth as μ approaches the instability threshold at $\mu = \gamma/4$, when $G = 1$. Beyond this threshold, the amplitude of the resonators is bound by nonlinearities and a sharp resonance peak remains.

By integrating the spectra in Figure 7.2a, we obtain an estimate for resonator 1's average energy in the thermal steady-state, as illustrated in Figure 7.2b. We see that

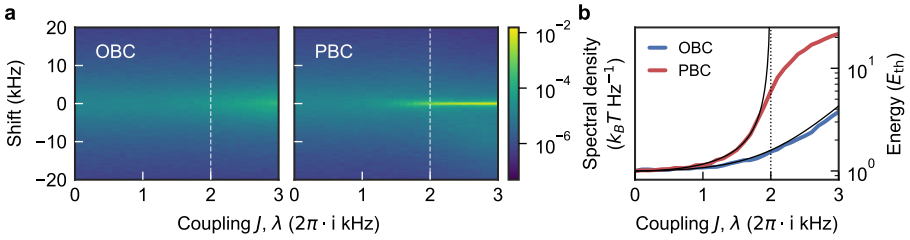

Figure 7.2: **Boundary-dependent stability. (a)** Thermomechanical spectra of the BKC proper around the resonance of lowest-frequency mode 1, for open (left) and closed (right) boundary conditions and equal dissipation rates $\gamma \approx 8$ kHz. As the coupling $\mu = J/\mathrm{i} = \lambda/\mathrm{i}$ is increased, the spectral intensity of the thermally driven open chain increases, whereas its linewidth remains similar. In contrast, the resonance linewidth of the closed chain decreases with increasing μ, until the linear system becomes unstable beyond threshold $\mu = \gamma/4$ (dashed lines). In the experiment, amplitudes are bound by nonlinearities and a narrow resonance peak remains. **(b)** Thermal steady-state energy in the lowest-frequency resonator 1 of the open and closed BKCs, obtained by integrating the spectra in (a) and expressed relative to the thermal energy E_{th} in the uncoupled resonator (when $J = \lambda = 0$). The open chain shows amplification of thermal energy injected into the chain, bound by the finite length of the chain. The linear closed chain has an infinite effective amplification length, such that the steady-state amplitude of amplified fluctuations diverges as the per-link gain $G = 4\mu/\gamma \to 1$ approaches unity (dashed line). Thermal energies predicted from (7.4) and (7.5) are shown (black lines) and correspond well with the measured values.

the amplification of thermal fluctuations is much larger in the chain with periodic boundary conditions than in the open chain.

By solving the Sylvester equation (4.13) for the correlator matrix in the thermal steady-state, derived in section 4.2.2 from the quantum regression theorem, we calculate the average thermal energies in the open and closed chains. For simplicity, we assume equal population $\bar{n}^{\mathrm{th}} = \bar{n}_j^{\mathrm{th}}$ in the baths coupled to each resonator. The average thermal populations in resonator 1 are then given by

$$n_1^{\mathrm{OBC}} = \bar{n}^{\mathrm{th}} \left(1 + G^2/4 + 3G^4/16 + 5G^6/32\right), \tag{7.4}$$

$$n_1^{\mathrm{PBC}} = \bar{n}^{\mathrm{th}} \left(1 + \frac{1}{2}\frac{G^2}{1-G^2}\right) \tag{7.5}$$

for open and periodic boundary conditions, respectively. As shown in Figure 7.2b, these expressions predict our measured energies well, since the effective occupations of the thermal baths are tuned closer by the feedback we apply. Importantly, we see from (7.5) that the amplification is expected to diverge in the closed chain as the per-link gain $G = 4\mu/\gamma \to 1$ approaches unity. This is where the correspondence with the measurements breaks down, as the experimental amplitudes are limited by nonlinearities.

Since the closed chain with equal bath occupations is translationally invariant, expression (7.5) holds in fact for all resonators. This does not apply to the open chain, where we find that the two outer sites $n_1^{\mathrm{OBC}} = n_4^{\mathrm{OBC}}$ have equal populations, whereas the inner sites have populations

$$n_2^{\mathrm{OBC}} = n_3^{\mathrm{OBC}} = \bar{n}^{\mathrm{th}} \left(1 + G^2/2 + 3G^4/16\right) \tag{7.6}$$

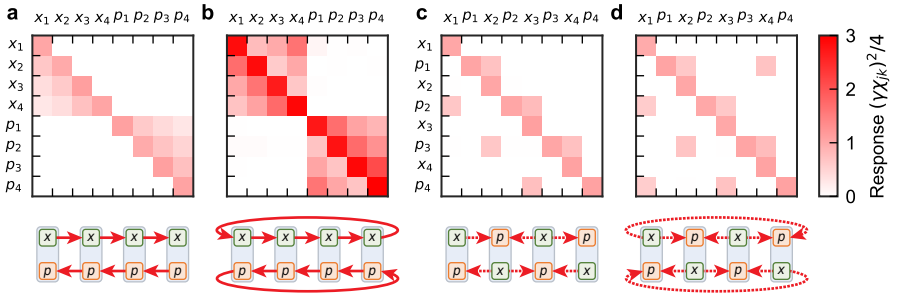

Figure 7.3: **Transition from global to local response tuned by interaction phase.** Measured susceptibility matrices χ^2 (top row, squared element-wise), for chains with $N = 4$ modes (dissipation rates $\gamma = 8$ kHz) coupled by BS and TMS interactions with rates $\mu \approx 1.5$ kHz. Chains (illustrated in the bottom row) are constructed with open or closed boundaries and either purely real or imaginary interactions, dictating the connectivity between quadratures (Figure 7.1a). **(a)** When the interaction rates $\lambda = J = i\mu$, $\mu > 0$ are purely imaginary, the chain shows a global response to excitations with quadrature-dependent directionality. In this case, open boundary conditions truncate the propagation of energy at the outermost quadratures x_4 and p_1. The same experiment is shown in Figure 7.1e and repeated for clarity. **(b)** Closing the chain allows energy to circulate along the loop. Here, the per-link gain $G < 1$ is smaller than unity, so that excitations eventually die out and the loop remains stable. Quadratures of different type x_j and p_j remain completely decoupled. **(c)** Setting the interaction phases to purely real, positive rates $J = \lambda = \mu > 0$ changes the connectivity between quadratures and leads to a local, nearest-neighbour-only response. Note that for clarity, the basis in which χ is described is reordered. **(d)** For this setting of interaction phases, the response remains local in the closed chain. The effective amplification length of just 1 site thus procures stable linear dynamics regardless of the value of μ.

that grow as a polynomial in G with lower degree than in (7.4). This reflects the shorter length of the effective amplification chains that feed the inner sites.

7.5. Transition from global to local response

Finally, we return to the effect of the phases of the BS and TMS interactions. We have seen that the BKC proper, with imaginary interaction rates, is characterized by a *global* response. Interestingly, choosing the rates J,λ to be real and balanced in magnitude ($|J| = |\lambda|$) results in a chain characterized by a *local* response instead.

We study this transition in Figure 7.3 for chains with interaction rate magnitudes $\mu \approx 1.5$ kHz and per-link gain $G = 0.75 < 1$ smaller than unity. In Figure 7.3a, b we choose imaginary interaction rates $J = \lambda = i\mu$. For clarity, the response of the open chain (Figure 7.1e) is repeated in Figure 7.3a. In addition, Figure 7.3b shows the response measured in the corresponding closed chain. While the decoupling between x_j and p_j remains, excitations now wrap around from $x_4 \to x_1$ and $p_1 \to p_4$. Overall, the continued propagation of energy around the loop leads to a higher response than in the open chain, in line with the difference in amplification observed for thermal fluctuations (Figure 7.2b).

The measured response strikingly changes when we chose real interaction rates $J = \lambda = \mu$ instead (Figure 7.3c, d). The susceptibility matrices then show that energy injected in a quadrature x_j only elicits a response in the neighbouring quadratures p_{j-1}, p_{j+1}. In turn, the quadratures p_j do not drive their neighbours at

all, truncating further propagation of energy. In this case, the only effect of closing the chain (Figure 7.3d) is to equip the outermost sites with two neighbours instead of one. Notably, the response of the chain remains local, and as a consequence, the stability of the chain is no longer affected by its boundary conditions.

After swapping the role of the quadratures x_{2j} and p_{2j} in every other site $2j$, the chain with real interactions can be viewed as a chain of qNR dimers with opposing directionalities (Figure 7.3c, d, bottom row). While real interactions guarantee that only quadratures of opposite flavours are coupled, the directionality of this coupling is controlled by the relative sign of J and λ. This inspires a way to construct a proper BKC with real interaction rates: By setting $\lambda = -J$ for every other link, the propagation directions align and two decoupled chains of alternating quadrature flavours emerge. While this has been pointed out before in [232], here we link it to the connectivity of the underlying qNR dimers.

7.6. Conclusions and outlook

In conclusion, we realized a nanomechanical implementation of the bosonic Kitaev chain through optomechanical parametric driving, and demonstrated its characteristic dynamic stability and phase-dependent unidirectional transport. Moving forward, we note that many interesting properties of the BKC are still left unexplored, including its different resilience to perturbations in dissipation and detuning. Furthermore, the BKC implemented here could serve as an experimental testbed to study the topological invariants underlying directional amplification in arrays [233], the exploration of non-Hermitian nonreciprocal and topological phenomena in more complex networks and two-dimensional lattices, and the conditions for the non-Hermitian skin effect. This model, and the general driving methods we employ to implement it, could be extended to other parametrically driven systems including optical resonators and superconducting circuits, and find potential applications in signal amplification and sensing [293].

8

Conclusions and outlook

In this thesis, we have developed an experimental platform that allows exploring the effects of breaking time-reversal symmetry and Hermiticity in the domain of nanomechanical resonators. With this platform, we demonstrated several key results on nonreciprocal responses, unidirectional amplification, tuning of non-Hermitian dynamical phases, signatures of Hermitian and non-Hermitian topological features, manipulation of thermal flows and resulting refrigeration performance, and pattern formation and localization in nanomechanical networks. In this final chapter, we discuss implications of our findings and present an outlook on opportunities for further research. In this spirit, we conclude by presenting some preliminary experiments that demonstrate light-mediated effective mechanical nonlinearities.

8.1. Control, coherence and interactions

The optomechanical methods that form the basis of the platform offer a high degree of control. This allowed us to present the general capability to realize arbitrary quadratic bosonic Hamiltonians in small resonator networks. The platform thus serves as a powerful model system to study the physics of such networks. In particular, this connects to the field that studies topological phases in bosonic matter; both Hermitian phases such as the quantum Hall effect, as well as non-Hermitian topological phases. At the same time, our results on the tuning of dynamical phases associated with parity-time ($\mathcal{PT}$) symmetry constitute the first implementation of a $\mathcal{PT}$-symmetric system where the required non-Hermiticity is induced by coherent interactions, as was put forward recently [163].

The high coherence of our nanomechanical resonators combined with sensitive optical readout, which readily resolves thermal fluctuations, allows accurate observation of dynamics. We demonstrated that high effective interaction strengths can be easily achieved, to allow operation in the mechanical strong coupling regime. In fact, we foresee that they could also approach the regime where they exceed the

mechanical frequency itself, for example by increasing the optical input efficiency [64]. This would allow studying networks in the ultrastrong coupling regime where the rotating wave approximation breaks down.

Furthermore, we note that the coherence in our systems could be enhanced straightforwardly by operating them at lower temperatures [146]. Alternatively, one could turn to ultralow-dissipation resonators such as those in softly-clamped and/or stressed silicon nitride structures [294–296], or actively control the decay through feedback, as we have already demonstrated.

Another opportunity that we did not yet explore in this work, but could be readily implemented, is to rapidly vary couplings in strength and/or phase; faster than the dissipation in the system or even its evolution (oscillation period) itself. In principle, this offers a wide range of research prospects, including the study of synthetic electric fields (i.e. varying magnetic fields) and the physics that they induce such as Bloch oscillations and dynamic localization [297–301].

Additionally, the dynamically unstable regime presents possibilities for further research. For example, if we look at the singly conjugated trimer in the self-oscillating regime (e.g. as shown in Figure 5.9b), the high-amplitude oscillations would themselves cause strong modulation of the intracavity field. Those modulations in term influence the mechanics through backaction. An interesting question is whether the broken time-reversal symmetry of the self-oscillating system then persists if would we stop the driving, which induced the symmetry-breaking time-modulation in the first place, and what the associated dynamics are. Such behaviour would be an example of a dynamical gauge field [136]. Moreover, coupled resonators that self-oscillate in mode-locked (synchronized) fashion are known to be more stable than single limit-cycle resonators [29, 30]. We do not know yet whether broken time-reversal symmetry could generally impact the stability (phase noise) of a self-oscillating network.

8.2. From small to large networks

The high degree of control over network nodes and their connectivity creates a versatile testbed to study interesting phases of matter. In particular in the areas of non-Hermitian and nonlinear topological matter, a complete overview of possibilities is currently lacking. We envision that the parametrically induced squeezing interactions that we demonstrate could serve as building blocks of a variety of non-Hermitian topological systems of different dimensions, beyond the proof-of-concept demonstrations we presented.

While Hermitian and non-Hermitian topological systems are theoretically studied usually in infinite lattices, we showed that some key associated phenomena can be observed in systems as small as 4 or 5 resonators. Still, it could be very interesting to increase the number of available nodes. We note that the current networks are in principle not limited by fabrication disorder on the frequencies: One can simply dial in the precise modulation frequency needed given the observed mechanical frequencies. However, increasing the number of resonators will 'crowd the spectrum' and increase the risk of unwanted resonances between (mixed) harmonics of the various resonator frequencies, negatively impacting the individual addressability of

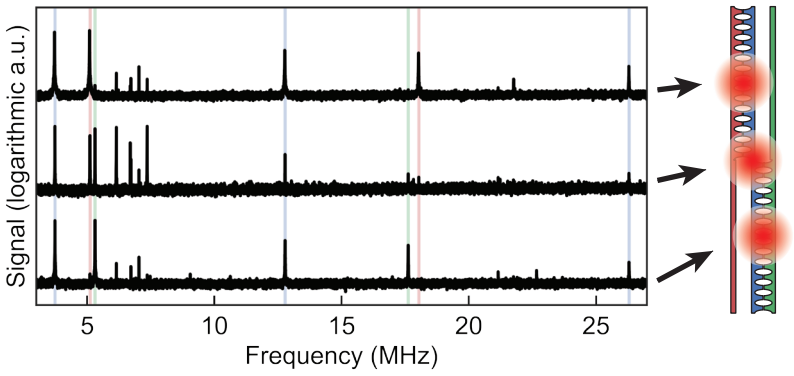

Figure 8.1: **Scaling up in real space.** Typical thermomechanical spectra of the double-cavity sliced nanobeam nanostructure, imprinted on a laser reflected from three different focus positions (indicated by arrows). The three nanobeams in the system are schematically represented on the right. Seven distinct, optomechanically-active nanomechanical resonances are observed. These are colour-matched with their corresponding oscillating nanobeam. Whereas in the top and bottom spectra the laser only interacts with a single cavity and its mechanical modes, the middle spectrum is obtained by aligning the laser in the middle, such that it interacts simultaneously with both cavities. Experiments in this thesis have employed optical excitation of a single cavity (bottom row) coupled to the 5 five flexural modes at frequencies $\Omega_j/(2\pi) = \{3.7, 5.3, 12.8, 17.6, 26.2\}$ MHz. Additional peaks are caused by nonlinear optomechanical transduction [146].

effective interactions. A possible countermeasure to this challenge lies in increased coherence of the resonators, as discussed above.

On the other hand, one could also deal with the issue of spectral crowding by embracing degeneracies instead. By realizing a structure with physically distinct but equally designed resonators on a chip, multiple transitions can be simultaneously addressed by the same modulation [64]. Although this reduces the number of individually controlled phases, that is not necessarily a problem to study large-scale phenomena such as topological phases [64, 74].

In this spirit, we can think of scaling up by addressing multiple cavities similar to our system. In fact, the device we have used in this thesis, shown in Figure 2.1 and featuring two optical cavities coupled to three vibrating elements, was already designed with this in mind. We show a proof-of-concept experiment in Figure 8.1, where we see that 7 modes can be addressed through a single laser beam that couples to two cavities from normal incidence. Mathew et al. have argued how this could be extended into a large lattice [64].

Alternatively, the cavities could be positioned along a single waveguide, such that they interact optically through the waveguide, with each cavity addressing a certain number (e.g. 6-8) of strongly coupled mechanical modes. Furthermore, other mechanical systems could be interesting, especially those that host a large number of mechanical resonances by design, for example long on-chip mechanical waveguides [302] or bulk acoustic wave resonators [303].

8.3. Stochastic thermodynamics

We have used the tunable interactions in our platform to image and manipulate thermal flows in resonator networks. In particular, broken time-reversal symmetry was seen to impact the performance of refrigeration. Some aspects of this process remain to be uncovered: For example, how do we quantify the work supplied by the optical driving field to refrigerate, or the production of entropy? Moreover, can we then quantify the efficiency of the refrigeration process? Does breaking time-reversal symmetry improve that efficiency in some regimes?

Conversely, it would be an interesting goal to construct a microscopic thermal engine [186] using our platform. Of particular interest would be the bounds on its efficiency at finite power when time-reversal symmetry is broken, which is still a topic of debate [203–206]. A candidate process to induce the nonlinearity required to create an autonomous engine will be discussed in section 8.6.

Alternatively, our system could serve as an interesting testbed in the field of stochastic thermodynamics [23, 24], to probe for example fundamental aspects of out-of-equilibrium fluctuations [187] or heating and cooling in anti-parity-time symmetric systems [216]. Another route would be to study heat transport in topological insulators [201]. Finally, it could be interesting to study the performance of thermodynamic systems when quantum fluctuations are significant, i.e. to perform fundamental experiments in 'quantum thermodynamics' [21].

8.4. Towards the quantum regime

A natural question to ask is whether the concepts and methods developed in this thesis could be extended down to the quantum regime, i.e. for mechanical signals at the few-phonon level, nonclassical mechanical quantum states, and vacuum fluctuations. Such an extension would be particularly timely, as phonons are now actively considered as media for transporting quantum information on a chip, owing to their high coherence and their ability to interface different quantum systems. As such, they can serve as a bus for quantum information, transducers from one degree of freedom to another, and as quantum memory elements [21, 304].

In that context, the symmetry breaking and parametric amplification that we study can have interesting applications. Unidirectional quantum-limited amplification is one example [134]. Circulation is highly useful in routing quantum information efficiently among nodes in a network, and isolators serve to shield quantum systems from unwanted back-propagating noise that would decohere them. More broadly, manipulating the flow of noise and general strategies to shield sensitive quantum systems is thus an important topic for further research.

However, when extending the methods we deployed down to the quantum regime, we need to be mindful of quantum backaction: The quantum fluctuations of the laser that is used to establish the couplings add incoherent mechanical fluctuations. These are significant if the quantum cooperativity $4g^2/(\kappa\gamma(\bar{n}^{\mathrm{th}}+1)) > 1$ exceeds unity, which is to be expected if one wishes to reach strong mechanical coupling in the quantum regime ($\bar{n}^{\mathrm{th}} \approx 0$). In optomechanics, approaches to mitigate the effect of quantum (radiation pressure) backaction include on the one

hand feedback, and on the other hand operation in the resolved sideband regime [118].

The latter seems especially useful to achieve strong quantum-coherent mechanical coupling, and was in fact considered in theory in different cavity optomechanical systems [134]. It likely requires rethinking the precise way the systems are driven (temporally modulated), as that would differ from the temporal drives we use now in the bad-cavity limit. We note that it is theoretically known that effective quadratic mechanical Hamiltonians can be implemented also in sideband-resolved systems [305]. The development of suitable systems is still an interesting endeavour: The aforementioned phononic waveguides and bulk acoustic resonators come to mind, as in those a large number of resonators can be coupled with high cooperativity to a single optical mode [302] or superconducting qubit [303].

8.5. Sensing

Nanomechanics is especially interesting for precise sensing of small forces, electromagnetic fields [306], and masses [17, 18]. An interesting question is whether smartly designed resonator networks, and in particular the breaking of symmetries could help sensing. In recent years, many researchers have turned to parity-time symmetric systems to potentially assist sensing [100, 104, 105, 307]. However, the actual enhancement of sensitivity in such systems is still under debate [101, 239, 308].

The precise way in which our methods can induce and control exceptional points could provide an interesting testbed in that context. Moreover, we could study both in the passive and near the unstable regime. Indeed, marked differences in fluctuation dynamics have been predicted between those [309].

Interestingly, it has been predicted that nonreciprocal networks could lead to a real performance advantage in sensing, by effectively enhancing a signal due to a perturbation that breaks a nonreciprocal state without adding noise [239]. Moreover, in the bosonic Kitaev chain we realized in chapter 7, it has been predicted that sensitivity to a perturbation of the last resonator in the chain would be exponentially enhanced as a function of the number of resonators in the chain [293]. Testing whether these and other networks with broken time-reversal symmetry and Hermiticity could give a true advantage to sensor performance would be a highly important undertaking — in which any advantageous nano-optomechanical approach could be directly applied to e.g. force or mass sensing.

8.6. Controlled nanomechanical nonlinearities

In Figure 5.9b, we observed the effects of optomechanical nonlinearity limiting the amplitude of the self-oscillating singly conjugated trimer. In fact, our systems are nonlinear already at low amplitudes [146], which arises from the fact that the mechanical displacement detunes the cavity away from resonance by such an amount that the change in intracavity field (and thus the radiation pressure backaction) is no longer linearly proportional to the displacement (Figure 8.2a). In particular, this means that the optical spring effect would be nonlinear.

Adding nonlinearity in our networks could have some fascinating possibilities. First, it could enable the engines we mentioned above, and lead to modified energy transport in microscopic power grids [310].

Second, it could be a resource for information processing. An example is reservoir computing, where nonlinear resonators are coupled to perform together a specific computing task on an input encoded on the resonator drives. In reservoir computing, one carefully trains the way in which one reads out the network in order to perform the wanted task. Instead, we could tune all parameters in the network to reconfigure it fully and attempt to achieve optimal computing performance. Moreover, we could study thermal noise, and thus thermal limits to computation [311].

Third, it could be a versatile testbed to study nonlinear topological phases of matter and resulting emergent phenomena [38, 312–318]. In a system where the hopping between resonators depends nonlinearly on their excitation amplitude, it can happen that a topologically nontrivial domain is induced through the excitation of the edge state it hosts [319–321]. This edge state is then a topological soliton that can travel dynamically through the system, changing the topological structure while it does. Various other intriguing phenomena have recently been observed. These include the observation of nonlinear soliton edge states in quantum-Hall-like waveguide arrays [315], quantized nonlinear Thouless pumping [322], and even behavior reminiscent of fractional quantization [323]. Whether this is linked to the fractional Hall effect in strongly correlated electron systems is not yet understood.

8.6.1. Cavity-mediated Duffing nonlinearity

Because of the high appeal of nonlinearity in future studies, we conclude this outlook with an experimental exploration of the nonlinearities that we can induce and control in our nano-optomechanical platform. While optically-mediated mechanical nonlinearities have been considered before [324–326], here we focus on their tunability, their effect on thermal fluctuations, and importantly, their extension to light-mediated mechanical interactions. In particular, we present a light-induced tunable mechanical Duffing nonlinearity, as well as a nonlinear beamsplitter interaction that can modify the dynamics and spectral response of a two-mode system. The latter could be a potential building block for nonlinear mechanical topological insulators [319].

In an optomechanical cavity driven by a fixed drive laser with dimensionless detuning $u_0 = 2\Delta_0/\kappa$, the displacement x of the mechanical resonator modulates the intracavity photon number $n_\mathrm{c} \propto h(u_0 + 2Gx/\kappa)$. Here, G is the optomechanical coupling strength and we assume operation in the bad cavity limit $\kappa \gg \Omega$ with Ω the mechanical frequency. Because the dimensionless cavity response function

$$h(u) = \frac{1}{1+u^2}, \tag{8.1}$$

given before in (2.18), is nonlinear, mechanical motion is nonlinearly transduced onto the intracavity intensity, and generates harmonics of the mechanical oscillation in the reflected intensity [146]. Particularly, when the displacement-induced

shift of the optical resonance is on the order of the cavity linewidth, $Gx \sim \kappa$, the nonlinearity of the cavity response function becomes important. In our device, this happens already at a few times the average thermal amplitude of the room-temperature resonators.

The modulated intracavity field also acts back on the mechanical resonator through radiation pressure, resulting in the optical spring effect. In section 2.3.4, we determined the *linear* optical spring shift $\delta\Omega$ from the linear term in the Taylor expansion (2.21) of $n_\mathrm{c}(x)$, and neglected the higher-order terms. In this section, we revisit that approximation.

In particular, as the quadratic term vanishes when the linear spring shift is maximal, we focus on the term cubic in x. Generally, the nondimensionalized displacement $z(t)$ of a resonator with a third-order nonlinearity satisfies the differential equation

$$\ddot{z}(t) = -\alpha z(t) - \gamma \dot{z}(t) - \beta z(t)^3 + f(t) \tag{8.2}$$

where α is the linear stiffness, γ the damping rate, β the nonlinear stiffness coefficient, and $f(t)$ the force acting on the resonator. This equation of motion is known as the *Duffing equation*, and corresponds to a symmetric quartic potential. Its dynamics have been widely studied, and are known to give rise to bistability, hysteresis, bifurcations, and chaos [156, 327–329].

In line with section 2.3.4, we express the displacement of the mechanical resonator using the dimensionless coordinate $z \equiv x/x_\mathrm{zpf}$. Expanding $n_\mathrm{c}(z)$ up to third order, as illustrated in Figure 8.2a, then gives the form

$$\beta = \frac{8\Omega g_0^4 n_\mathrm{max} h'''(u_0)}{3\kappa^3} = -6\Omega\delta\Omega\frac{g_0^2}{\kappa^2} \tag{8.3}$$

for the nonlinear coefficient. The last expression is valid for the two detunings $u_0 = \pm 1/\sqrt{3}$ where the linear spring shift $\delta\Omega$ is maximally positive and negative, respectively. Interestingly, as the intensity of the laser drive enters (8.3) through n_max, or equivalently through $\delta\Omega$, the interaction with the cavity induces a *tunable* effective mechanical Duffing nonlinearity.

8.6.2. Nonlinear spring shift

In the following, we explore the effects of this tunable nonlinearity in our platform. We start with an experiment where resonator 3 (frequency $\Omega_3/(2\pi) = 17.6$ MHz, estimated photon-phonon coupling rate $g_0/(2\pi) = 3.1 \pm 0.9$ MHz) is driven coherently to high amplitudes by the modulations of a weak 'force' laser (intensity $P_\mathrm{f} = 0.1$ mW) that is resonant with the cavity. In addition, a strong 'spring' laser (intensity $P_\mathrm{s} = 1.0$ mW) detuned by $u_- = -1/\sqrt{3}$ ($u_+ = 1/\sqrt{3}$) induces the optimal negative (positive) optical spring shift $\delta\Omega/(2\pi) \approx \pm 30$ kHz in the resonator. Finally, motion is read out from the modulations imprinted on a third, far-detuned ($u_\mathrm{det} = -5.0$) 'detect' laser reflected off the cavity (intensity $P_\mathrm{det} = 1.0$ mW).

As shown in Figure 8.2b, we measure the thermomechanical spectrum of the resonator as a function of the modulation depth c_d driving the resonator. The coherent high-amplitude oscillations appear as a narrow peak with increasing amplitude,

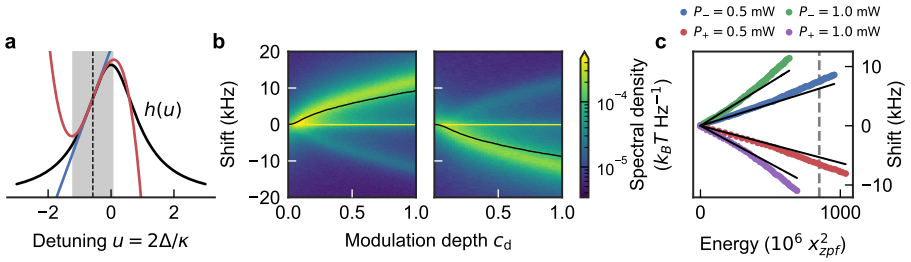

Figure 8.2: **Cavity-mediated Duffing nonlinearity. (a)** Cavity response $h(u)$ as a function of dimensionless detuning $u = 2\Delta/\kappa$. The dashed line indicates the detuning $u_- = -1/\sqrt{3}$ where the linear spring shift $\delta\Omega$, derived from the linear approximation to $h(u)$ (blue line), is maximally negative. As the second-order derivative $h''(u_-)$ vanishes, the next-higher-order approximation is cubic in u (red curve). The grey area corresponds to the largest mechanical amplitudes measured in panels (b) and (c) for $c_d = 1$. **(b)** Thermomechanical spectra of resonator 3 while coherently driven by modulations (depth c_d) of a weak 'force' laser resonant with the cavity. A strong 'spring' laser detuned by $\Delta = -\kappa/(2\sqrt{3})$ ($\Delta = \kappa/(2\sqrt{3})$) induces a negative (positive) optical spring shift in the left (right) panel, while resonator motion is read out from modulations imprinted on a third, far-detuned ($\Delta_{det} = -2.5\kappa$) 'detect' laser reflected off the cavity. The spectra show an intense, narrow contribution of driven oscillations, saturating the colour scale. In addition, two bands are observed with different intensities. The most intense band shifts up (down) in frequency for negative (positive) spring shift and corresponds to thermal fluctuations on top of the driven amplitude. The weaker band is a 'ghost' that arises from nonlinear transduction. **(c)** Fitted center frequency of the thermal contribution plotted against the square of the driven amplitude measured from linear transduction. For each detuning $u_\pm$, two different drive laser intensities $P_\pm$ are shown. The dashed line corresponds to the mechanical displacement that induces a shift of magnitude $|u_\pm|$ in the cavity resonance. Black lines in (b) and (c) show the estimated frequency shift (8.10) of the nonlinear susceptibility.

saturating the colour scale. Remarkably, the broad spectrum of thermal vibrations now shifts in frequency, with the direction of the shift depending on the spring laser detuning: For negative linear spring shift the thermal band moves up in frequency (Figure 8.2b, left), while for negative linear spring shift it moves down (Figure 8.2b, right). In addition, a weak, frequency-reflected 'ghost' band appears that moves in the other direction, presumably arising from nonlinear transduction [146] that mixes the thermal fluctuations with the strong coherent oscillations. Alternatively, the additional weaker band could also reflect actual frequency content of the motion, as observed before in nonlinear electromechanical [236] and microwave [330] systems. As these two effects arise in part from interactions with different laser fields, they could potentially be distinguished by varying the detection laser intensity or detuning.

From this measurement, we observe that the strong coherent oscillation alters the susceptibility of the resonator to thermal forces. In an attempt to model the nonlinear susceptibility to an additional small force on top of the strong coherent driving, we employ the method of harmonic balance [331, 332]. This approach, commonly used to evaluate the dynamics of Duffing oscillators [328], relies on expanding the motion $z(t)$ as a Fourier series and then truncating that expansion beyond a specified order, while balancing the amplitudes of the remaining harmon-

ics. We assume the form

$$f(t) = f_{\mathrm{d}} \cos(\omega_{\mathrm{d}} t + \phi_{\mathrm{d}}) + f_{\mathrm{p}} \cos(\omega_p t + \phi_{\mathrm{p}}) \tag{8.4}$$

for the force driving the resonator, which includes the strong drive with amplitude f_{d}, frequency ω_{d}, and phase offset ϕ_{d} and a (small) additional periodic driving force described likewise by f_{p}, ω_{p} and ϕ_{p}. We will call the small drive the 'probe' force, while referring to the strong drive as the 'pump'. For simplicity, we assume that the frequencies ω_{d} are incommensurate, such that the phase offsets are not essential and we can set $\phi_{\mathrm{d}} = \phi_{\mathrm{p}} = 0$ without affecting the dynamics.

In response to this composite force, we seek an approximate solution to the resonator evolution of the form

$$z(t) = z_1 \cos(\omega_{\mathrm{p}} t + \phi_1) + z_2 \cos(\omega_{\mathrm{p}} t + \phi_2). \tag{8.5}$$

We insert (8.5) and (8.4) into the Duffing equation (8.2) and balance the fundamental harmonics at ω_{p} and ω_{d}. First, we solve for the 'pump' amplitude z_1 while neglecting the 'probe' amplitude ($z_2 = 0$). This results in the well-known equation

$$z_1^2 \left[\left(\omega_{\mathrm{d}}^2 - \alpha - \frac{3}{4} \beta z_1^2 \right)^2 + (\gamma \omega_{\mathrm{d}})^2 \right] = f_{\mathrm{d}}^2 \tag{8.6}$$

that describes the frequency response of a Duffing oscillator to a single driving tone. Next, we solve for the probe amplitude z_2 in the presence of the pump,

$$z_2^2 \left[\left(\omega_{\mathrm{p}}^2 - \alpha - \frac{3}{4} \beta \left(2 z_1^2 + z_2^2 \right) \right)^2 + (\gamma \omega_{\mathrm{p}})^2 \right] = f_{\mathrm{p}}^2. \tag{8.7}$$

Assuming that $z_1 \gg z_2$ in the term in brackets, we arrive at the approximation

$$z_2 = \frac{f_{\mathrm{p}}^2}{(\mu^2 - \omega_{\mathrm{p}}^2)^2 + \gamma^2 \omega_{\mathrm{p}}^2} \tag{8.8}$$

for the amplitude of motion at the probe frequency. This corresponds exactly to the susceptibility of a linear harmonic oscillator with natural frequency μ. Its nonlinearly shifted frequency μ is given by the expression

$$\mu^2 = \alpha + \frac{3}{2} \beta z_1^2. \tag{8.9}$$

Finally, after plugging the expression (8.3) for the radiation-pressure-induced β into (8.9), we arrive at the expression

$$\delta \Omega_{\mathrm{nl}} = -\frac{9}{2} \delta \Omega \frac{g_0^2}{\kappa^2} z_1^2 \tag{8.10}$$

that describes this *nonlinear* contribution to the spring shift of the probe susceptibility, derived under the assumption that $\delta \Omega_{\mathrm{nl}} \ll \Omega$.

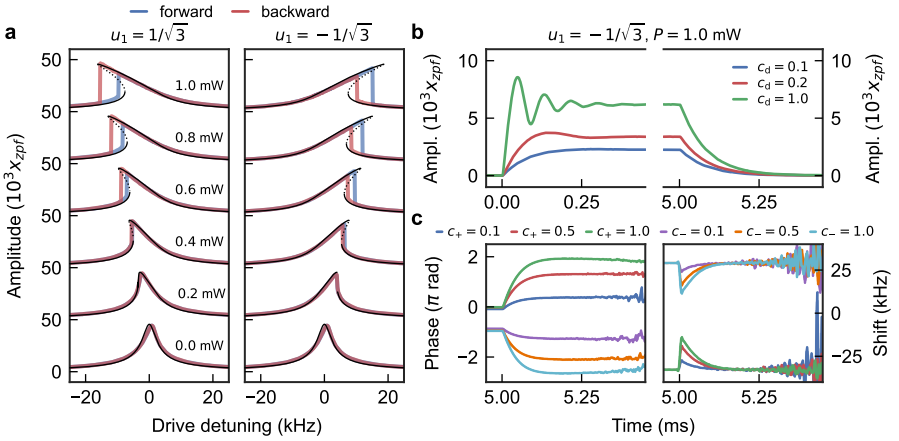

Figure 8.3: **Frequency response and ringdown of a single resonator with tunable nonlinearity. (a)** Amplitude response to coherent force laser modulations with a fixed depth $c_d \approx 0.5$ as a function of detuning $\Delta_d = \omega_d - \Omega_3$ of the driving tone, for spring laser detuning $u_1 = u_+$ (left) and $u_1 = u_-$ (right). The intensity of the spring laser is varied from $P_s = 0.0$ mW to $P_s = 1.0$ mW, with the corresponding responses offset for clarity. Forward and backward detuning sweeps are indicated by blue and red lines, respectively. Predicted response amplitudes from (8.6) are shown in black for photon-phonon coupling $g_0 = 3.4$ MHz, with dashed lines indicating the unstable branch **(b)** Time-resolved ring-up and ring-down of the nonlinear resonator obtained in a pulsed experiment, for spring laser detuning $u_1 = u_-$. Coherent modulations are applied on the force laser width depths $c_d = \{0.1, 0.2, 1.0\}$. **(c, left)** Demodulated phase $\alpha(t)$ as the nonlinear resonator rings down. Traces are shown for two different spring laser detunings $u_\pm$ and three different modulation depths $c_\pm = \{0.1, 0.5, 1.0\}$, where the index $\pm$ indicates the corresponding laser detuning. **(c, right)** Instantaneous frequencies Ω_{nl} calculated from the derivative of the phases shown in the left panel, expressed relative to the intrinsic mechanical frequency $\tilde{\Omega}_3$ of the resonator. During the ringdown, when the resonator is evolving freely, Ω_{nl} is seen to approach the intrinsic frequency regardless. Time-resolved measurements are averaged coherently over 1000 runs.

We calculate $\delta\Omega_{nl}$ for the pump amplitudes measured in Figure 8.2b (black lines). Even though (8.10) is derived for a coherent probe tone, it appears to predict the nonlinear shift of the susceptibility to incoherent thermal forces reasonably well. As shown in Figure 8.2c, the sign and magnitude of β are tuned by the detuning and intensity of the spring laser. Finally, we note that the pump squared amplitude z_2^2 is measured from its linear transduction on the detection laser, which results in an underestimate for higher amplitudes [146]. Presumably, this contributes to the underestimation of $\delta\Omega_{nl}$ observed in Figure 8.2c for higher amplitudes. More precise measurements (including an improved estimate of g_0) and a further theoretical analysis to treat incoherent driving are warranted.

8.6.3. Response to coherent driving

Next, we investigate the frequency response to strong coherent driving. In Figure 8.3a, we show the response of the resonator to modulations of the force laser with a fixed depth $c_d \approx 0.5$ and variable detuning $\Delta_d = \omega_d - \Omega_3$ relative to the

(linearly spring-shifted) resonance frequency Ω_3. When the spring laser is off, we observe a resonance that is approximately symmetric, indicative of a linear resonator response.

Turning on the spring laser with detuning $u_1 = 1/\sqrt{3}$ induces a softening Duffing nonlinearity $\beta < 0$ that increases in magnitude for increasing spring laser intensity P_s. For the given amplitude of the driving force, bistability in the response amplitude is observed for $P_\mathrm{s} \geq 0.6$ mW. The low- and high-amplitude stable branches can be probed by sweeping the detuning forward and backward, respectively. Conversely, by turning on the spring laser with detuning $u_1 = -1/\sqrt{3}$, a hardening Duffing nonlinearity $\beta > 0$ is induced. In that case, the characteristics of the response appear reflected in frequency. In both cases, the frequency response can be modelled by (8.6). We find that this agrees well with experiment upon adjusting the value of the photon-phonon coupling to $g_0 = 3.4$ MHz, which is within the error bounds of the previous, independently measured value $g_0 = 3.1 \pm 0.9$ MHz.

8.6.4. Nonlinear ringdown

We can also probe the dynamics of the nonlinear resonator in the time domain. In Figure 8.3b, we show a pulsed, time-resolved experiment where a coherent driving tone ($\omega_\mathrm{d} = \Omega_3$) is turned on at $t = 0$ and turned off at $t = 5$ ms in the presence of a strong spring laser. For a small driving force, the steady-state amplitude is reached without overshooting, as expected for a linear resonator. However, for larger driving forces, the amplitude is seen to overshoot and oscillate until steady-state is reached.

After the driving is stopped, the resonator rings down. It is then free to evolve at its natural frequency, which for a Duffing oscillator is known to depend on amplitude [328, 329]. In experiment, we can estimate the instantaneous frequency $\Omega_\mathrm{nl}(t)$ from the evolution of the demodulated phase

$$\alpha(t) = \int_{t_0}^{t} [\Omega_\mathrm{nl}(\tau) - \omega_\mathrm{d}] \, \mathrm{d}\tau \tag{8.11}$$

relative to the local oscillator at frequency ω_d used to analyse the resonator signal. In Figure 8.3c, left, we show the demodulated phase $\alpha(t)$ as the resonator rings down for two different spring laser detunings $u_\pm$ and three different modulation depths $c_\pm = \{0.1, 0.5, 1.0\}$, where the index $\pm$ indicates the corresponding laser detuning. To reach higher driven amplitudes, these modulations are now imprinted on the stronger spring laser.

From these, we calculate the corresponding instantaneous frequencies $\Omega_\mathrm{nl}(t) = \alpha'(t) + \omega_\mathrm{d}$ as shown in Figure 8.3c, right. These reveal that for higher amplitudes, the frequency of free oscillations tends towards the intrinsic, non-spring-shifted mechanical frequency. Intuitively, this makes sense: For larger and larger vibrations, the cavity resonance frequency is far-detuned from the drive laser most of the time, and radiation pressure should therefore impact the resonator dynamics less and less. The nonlinear optical spring shift thus counteracts the linear optical spring shift, as seen in (8.10) as well.

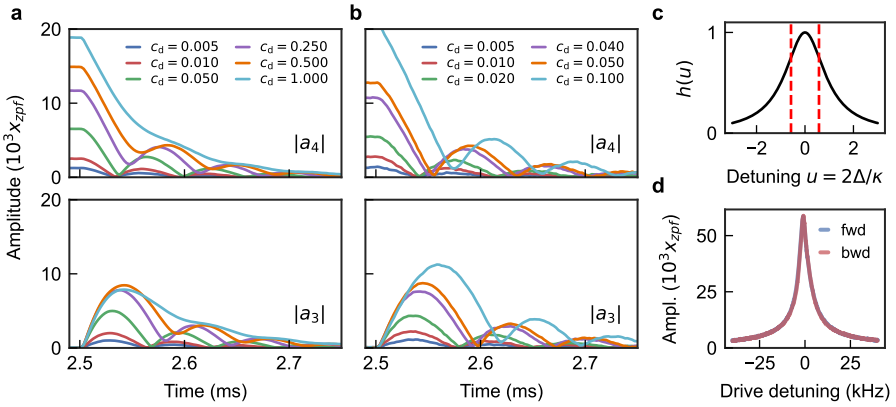

Figure 8.4: **Evolution of nonlinearly coupled resonators. (a)** Time-resolved, pulsed experiment involving one strong spring laser (detuning u_-, intensity $P = 1$ mW) and one detect laser. Resonator 4 (top) is excited to high amplitude by strong coherent modulations of the spring laser, with depths up to $c_\mathrm{d} = 1.0$. At time $t = 2.5$ ms, the drive tone is switched off and a spring laser modulation at the frequency difference $\Omega_4 - \Omega_3$ between resonators 3 (bottom) and 4 is turned on, with depth $c_\mathrm{m} = 0.5$. Through the cavity-mediated nonlinear optical spring, this modulation induces a nonlinear coupling between them with a rate J that depends on their amplitudes. In addition, the resonators experience individual nonlinear spring shifts. Traces are coherently averaged over 1000 runs. **(b)** The pulsed experiment is repeated in the presence of an additional strong spring laser tuned to induce the optimal positive spring shift (detuning u_+). The intensity of this laser is matched to that of the negative spring laser, such that the individual resonators experience no net spring shift. This allows higher driven amplitudes to be reached for the same modulation depth, and we reduce the range of modulation depths accordingly to achieve similar driven amplitudes as in panel (a). Modulations on the negative spring laser again induce a nonlinear coupling. **(c)** Cavity response $h(u)$, with red dashed lines indicating the opposite detunings $u_\pm$ of the two spring lasers. **(d)** Measured frequency response as function of the detuning of a small modulation tone driving resonator 4. The cavity is illuminated by two balanced spring lasers with intensities $P_\pm \approx 1$ mW. Drive modulations are imprinted on the positive spring laser. For similar mechanical amplitudes as attained in Figure 8.3a for a single spring laser, we observe the symmetric response characteristic of a linear resonator, and no bistability.

8.6.5. Optically-mediated nonlinear interactions

The cavity-mediated effective mechanical interactions we have used throughout this thesis rely on the linear, 'cross-resonator' optical spring. The nonlinear contribution observed here is therefore also expected to impact the effective coupling rate J when such coupling is established between resonators. Such a dependence of the coupling rate J on mechanical amplitude is of potential interest; for example, it is precisely the ingredient that is necessary to yield nonlinear topological solitons in the theory of Hadad et al. [319, 320].

In Figure 8.4a, we show experimental signatures of such nonlinear coupling. In these experiments, resonator 4 is coherently driven at various amplitudes c_d, until at $t = 2.5$ ms the drive is switched off and a difference-frequency tone that couples resonator 4 to resonator 3 is switched on. We observe Rabi oscillations similar to those in Figure 2.6b. However, for large driving, the period of the Rabi oscillations is altered, revealing a nonlinear dependence of J on the mechanical amplitude. In

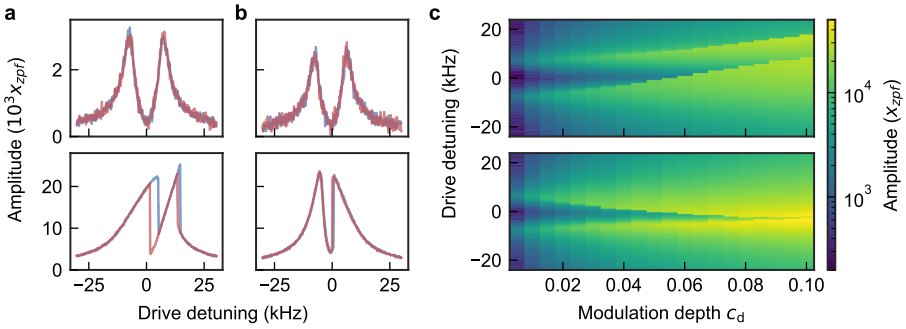

Figure 8.5: **Frequency response of nonlinearly coupled resonators. (a)** Measured response amplitude of resonator 3 in the presence of a single negative spring laser. The detuning of weak (top, $c_d = 0.01$) and strong (bottom, $c_d = 0.08$) modulations driving resonator 3 is swept forward (blue) or backward (red). A coupling tone with depth $c_m = 0.5$ is imprinted on the negative spring laser to induce nonlinear coupling between resonators 3 and 4. **(b)** Similar, with the addition of a strong positive spring laser to cancel the single-resonator spring shift. Modulation depths are adjusted (top, $c_d = 0.005$; bottom, $c_d = 0.045$) to attain similar driven amplitudes. **(c)** Colour plots of the response amplitude of resonator 3 for forward detuning sweeps in the presence of a single negative spring laser (top) or double-laser driving (bottom). The modulation depth c_d of the coherent tone driving resonator 3 is varied. For a single spring laser, both response peaks shift in the same frequency direction as c_d is increased. For the double-laser driving condition, the two response peaks are seen to approach each other.

addition, we see that the visibility of the Rabi oscillations diminishes. This is due to the nonlinear frequency shifts of the *individual* resonators, which detunes their frequency difference from the applied modulation frequency and causes the Rabi oscillations to be incomplete.

Interestingly, one can create a pure cross-resonator nonlinearity by simultaneously applying two 'spring' lasers, at detunings u_+ and u_- (see Figure 8.4c). As the spring shifts of the lasers have opposite signs, the optical spring on the individual resonators can be cancelled. Indeed, we see in Figure 8.4d that the individual-resonator Duffing nonlinearity vanishes under that condition. However, modulating one of the laser intensities around its mean still induces a cross-resonator spring effect, with associated nonlinearity. The resulting amplitude-dependent Rabi oscillations are shown in Figure 8.4b, where we observe that the fringe visibility is recovered. We now also clearly recognize that the coupling rate J in fact increases during the ringdown, as the average resonator amplitude decreases due to dissipation.

These mechanisms are also apparent in spectroscopy of the nonlinearly coupled resonators. Figure 8.5a,b show the driven response of resonator 3 in the presence of a coupling tone, for low (top) and high (bottom) drive amplitudes. In panel a, a single 'spring' laser is applied, whereas in panel b two lasers cancel the single-resonator spring shifts. In the latter case, large amplitudes cause an apparent reduction of the mode splitting. Note moreover that the bistabilities apparent in the difference between up- and down-scans of probe frequency are negligible when the individual spring shifts are cancelled. Figure 8.5c shows this behavior in more detail, plotting the response spectra as a function of drive strength for the single 'spring' laser (top) and the double-laser condition (bottom).

In conclusion, we demonstrated a highly tunable optically-induced mechanical Duffing nonlinearity that originates from the intrinsic nonlinearity of a cavity optomechanical system. The fact that the sign and magnitude of the single-resonator nonlinear coefficient, as well as the change of coupling rate J with mechanical amplitude can be individually controlled presents interesting opportunities for the creation of tailored nonlinear mechanical networks. We envision that those could be used to study information processing and computing capabilities as well as nonlinear topological phases in combination with time-reversal symmetry breaking and non-Hermiticity in optomechanical metamaterials [319, 320].

Bibliography

1. C. Kittel. *Introduction to solid state physics* 8th ed (Wiley, Hoboken, NJ, 2005).
2. J. D. Joannopoulos. *Photonic crystals: molding the flow of light* 2nd ed (Princeton University Press, Princeton, 2008).
3. S. A. Cummer, J. Christensen & A. Alù. Controlling sound with acoustic metamaterials. *Nat. Rev. Mater.* **1,** 16001 (2016).
4. R. Lakes. Foam structures with a negative Poisson's ratio. *Science* **235,** 1038–1040 (1987).
5. D. Schurig, J. J. Mock, B. J. Justice, S. A. Cummer, J. B. Pendry, A. F. Starr & D. R. Smith. Metamaterial electromagnetic cloak at microwave frequencies. *Science* **314,** 977–980 (2006).
6. T. Ergin, N. Stenger, P. Brenner, J. B. Pendry & M. Wegener. Three-dimensional invisibility cloak at optical wavelengths. *Science* **328,** 337–339 (2010).
7. D. R. Smith, J. B. Pendry & M. C. K. Wiltshire. Metamaterials and negative refractive index. *Science* **305,** 788–792 (2004).
8. V. M. Shalaev. Optical negative-index metamaterials. *Nat. Photon.* **1,** 41–48 (2007).
9. L. M. Nash, D. Kleckner, A. Read, V. Vitelli, A. M. Turner & W. T. M. Irvine. Topological mechanics of gyroscopic metamaterials. *Proc. Natl. Acad. Sci. U.S.A.* **112,** 14495–14500 (2015).
10. S. Xiao, T. Wang, T. Liu, C. Zhou, X. Jiang & J. Zhang. Active metamaterials and metadevices: a review. *J. Phys. D: Appl. Phys.* **53,** 503002 (2020).
11. H. Nassar, B. Yousefzadeh, R. Fleury, M. Ruzzene, A. Alù, C. Daraio, A. N. Norris, G. Huang & M. R. Haberman. Nonreciprocity in acoustic and elastic materials. *Nat. Rev. Mater.* **5,** 667–685 (2020).
12. S. Reich, J. Maultzsch, C. Thomsen & P. Ordejón. Tight-binding description of graphene. *Phys. Rev. B* **66,** 035412 (2002).
13. J. R. Hook & H. E. Hall. *Solid state physics* 2. ed. (Wiley, Chichester, 1991).
14. A. N. Cleland. *Foundations of nanomechanics* (Springer Berlin Heidelberg, Berlin, Heidelberg, 2003).
15. M. Poot & H. S. van der Zant. Mechanical systems in the quantum regime. *Phys. Rep.* **511,** 273–335 (2012).

16. A. Bachtold, J. Moser & M. I. Dykman. *Mesoscopic physics of nanomechanical systems* arXiv: 2202.01819 (2022).

17. T. P. Burg, M. Godin, S. M. Knudsen, W. Shen, G. Carlson, J. S. Foster, K. Babcock & S. R. Manalis. Weighing of biomolecules, single cells and single nanoparticles in fluid. *Nature* **446,** 1066–1069 (2007).

18. K. Jensen, K. Kim & A. Zettl. An atomic-resolution nanomechanical mass sensor. *Nat. Nanotechnol.* **3,** 533–537 (2008).

19. T. Bagci, A. Simonsen, S. Schmid, L. G. Villanueva, E. Zeuthen, J. Appel, J. M. Taylor, A. Sørensen, K. Usami, A. Schliesser & E. S. Polzik. Optical detection of radio waves through a nanomechanical transducer. *Nature* **507,** 81–85 (2014).

20. J. Bochmann, A. Vainsencher, D. D. Awschalom & A. N. Cleland. Nanomechanical coupling between microwave and optical photons. *Nat. Phys.* **9,** 712–716 (2013).

21. S. Barzanjeh, A. Xuereb, S. Gröblacher, M. Paternostro, C. A. Regal & E. M. Weig. Optomechanics for quantum technologies. *Nat. Phys.* **18,** 15–24 (2022).

22. K. L. Ekinci & M. L. Roukes. Nanoelectromechanical systems. *Rev. Sci. Instr.* **76,** 061101 (2005).

23. U. Seifert. Stochastic thermodynamics, fluctuation theorems and molecular machines. *Rep. Prog. Phys.* **75,** 126001 (2012).

24. S. Ciliberto. Experiments in stochastic thermodynamics: Short history and perspectives. *Phys. Rev. X* **7,** 021051 (2017).

25. E. Romero, N. P. Mauranyapin, T. M. F. Hirsch, R. Kalra, C. G. Baker, G. I. Harris & W. P. Bowen. *Scalable nanomechanical logic gate* arXiv: 2206.11661 (2022).

26. J. Chan, T. P. M. Alegre, A. H. Safavi-Naeini, J. T. Hill, A. Krause, S. Gröblacher, M. Aspelmeyer & O. Painter. Laser cooling of a nanomechanical oscillator into its quantum ground state. *Nature* **478,** 89–92 (2011).

27. R. Riedinger, A. Wallucks, I. Marinković, C. Löschnauer, M. Aspelmeyer, S. Hong & S. Gröblacher. Remote quantum entanglement between two micromechanical oscillators. *Nature* **556,** 473–477 (2018).

28. R. B. Karabalin, M. C. Cross & M. L. Roukes. Nonlinear dynamics and chaos in two coupled nanomechanical resonators. *Phys. Rev. B* **79,** 165309 (2009).

29. M. Zhang, S. Shah, J. Cardenas & M. Lipson. Synchronization and phase noise reduction in micromechanical oscillator arrays coupled through light. *Phys. Rev. Lett.* **115,** 163902 (2015).

30. L. Mercadé, K. Pelka, R. Burgwal, A. Xuereb, A. Martínez & E. Verhagen. *Floquet phonon lasing in multimode optomechanical systems* arXiv: 2101.10788 (2021).

31. K. M. Sliwa, M. Hatridge, A. Narla, S. Shankar, L. Frunzio, R. J. Schoelkopf & M. H. Devoret. Reconfigurable Josephson circulator/directional amplifier. *Phys. Rev. X* **5,** 041020 (2015).

32. F. Ruesink, M.-A. Miri, A. Alù & E. Verhagen. Nonreciprocity and magnetic-free isolation based on optomechanical interactions. *Nat. Commun.* **7,** 13662 (2016).

33. K. Fang, J. Luo, A. Metelmann, M. H. Matheny, F. Marquardt, A. A. Clerk & O. Painter. Generalized non-reciprocity in an optomechanical circuit via synthetic magnetism and reservoir engineering. *Nat. Phys.* **13,** 465–471 (2017).

34. L. Mercier de Lépinay, C. F. Ockeloen-Korppi, D. Malz & M. A. Sillanpää. Nonreciprocal transport based on cavity Floquet modes in optomechanics. *Phys. Rev. Lett.* **125,** 023603 (2020).

35. A. Nunnenkamp, J. Koch & S. M. Girvin. Synthetic gauge fields and homodyne transmission in Jaynes–Cummings lattices. *New J. Phys.* **13,** 095008 (2011).

36. M. Z. Hasan & C. L. Kane. *Colloquium* : Topological insulators. *Rev. Mod. Phys.* **82,** 3045–3067 (2010).

37. S. D. Huber. Topological mechanics. *Nat. Phys.* **12,** 621–623 (2016).

38. T. Ozawa, H. M. Price, A. Amo, N. Goldman, M. Hafezi, L. Lu, M. Rechtsman, D. Schuster, J. Simon, O. Zilberberg & I. Carusotto. Topological photonics. *Rev. Mod. Phys.* **91,** 015006 (2019).

39. Y. Aharonov & D. Bohm. Significance of electromagnetic potentials in the quantum theory. *Phys. Rev.* **115,** 485–491 (1959).

40. E. Cohen, H. Larocque, F. Bouchard, F. Nejadsattari, Y. Gefen & E. Karimi. Geometric phase from Aharonov–Bohm to Pancharatnam–Berry and beyond. *Nat. Rev. Phys.* **1,** 437–449 (2019).

41. A. Khein & D. F. Nelson. Hannay angle study of the Foucault pendulum in action-angle variables. *Am. J. Phys.* **61,** 170–174 (1993).

42. S. Pancharatnam. Generalized theory of interference, and its applications: Part I. Coherent pencils. *Proc. Indian Acad. Sci.* **44,** 247–262 (1956).

43. D. L. Sounas & A. Alù. Non-reciprocal photonics based on time modulation. *Nat. Photon.* **11,** 774–783 (2017).

44. A. Kamal. A parametric device as a nonreciprocal element. *Proc. IRE* **48,** 1424–1430 (1960).

45. K. Fang, Z. Yu & S. Fan. Photonic Aharonov-Bohm effect based on dynamic modulation. *Phys. Rev. Lett.* **108** (2012).

46. Z. Yu & S. Fan. Complete optical isolation created by indirect interband photonic transitions. *Nat. Photon.* **3,** 91–94 (2009).

47. Z. Yu & S. Fan. Optical isolation based on nonreciprocal phase shift induced by interband photonic transitions. *Appl. Phys. Lett.* **94,** 171116 (2009).

48. T. Kodera, D. L. Sounas & C. Caloz. Artificial Faraday rotation using a ring metamaterial structure without static magnetic field. *Appl. Phys. Lett.* **99,** 031114 (2011).

49. H. Lira, Z. Yu, S. Fan & M. Lipson. Electrically driven nonreciprocity induced by interband photonic transition on a silicon chip. *Phys. Rev. Lett.* **109,** 033901 (2012).

50. D. L. Sounas & A. Alù. Angular-momentum-biased nanorings to realize magnetic-free integrated optical isolation. *ACS Photon.* **1,** 198–204 (2014).

51. N. A. Estep, D. L. Sounas, J. Soric & A. Alù. Magnetic-free non-reciprocity and isolation based on parametrically modulated coupled-resonator loops. *Nat. Phys.* **10,** 923–927 (2014).

52. L. D. Tzuang, K. Fang, P. Nussenzveig, S. Fan & M. Lipson. Non-reciprocal phase shift induced by an effective magnetic flux for light. *Nat. Photon.* **8,** 701–705 (2014).

53. J. Kerckhoff, K. Lalumière, B. J. Chapman, A. Blais & K. W. Lehnert. On-chip superconducting microwave circulator from synthetic rotation. *Phys. Rev. Applied* **4,** 034002 (2015).

54. B. Abdo, K. Sliwa, L. Frunzio & M. Devoret. Directional amplification with a Josephson circuit. *Phys. Rev. X* **3,** 031001 (2013).

55. A. Kamal, J. Clarke & M. H. Devoret. Noiseless non-reciprocity in a parametric active device. *Nat. Phys.* **7,** 311–315 (2011).

56. J. Dalibard, F. Gerbier, G. Juzeliūnas & P. Öhberg. *Colloquium* : Artificial gauge potentials for neutral atoms. *Rev. Mod. Phys.* **83,** 1523–1543 (2011).

57. A. Eckardt. Colloquium: Atomic quantum gases in periodically driven optical lattices. *Rev. Mod. Phys.* **89,** 011004 (2017).

58. A. Celi, P. Massignan, J. Ruseckas, N. Goldman, I. B. Spielman, G. Juzeliūnas & M. Lewenstein. Synthetic gauge fields in synthetic dimensions. *Phys. Rev. Lett.* **112,** 043001 (2014).

59. M. Aidelsburger, S. Nascimbene & N. Goldman. Artificial gauge fields in materials and engineered systems. *C. R. Phys.* **19,** 394–432 (2018).

60. R. Fleury, D. L. Sounas, C. F. Sieck, M. R. Haberman & A. Alù. Sound isolation and giant linear nonreciprocity in a compact acoustic circulator. *Science* **343,** 516–519 (2014).

61. Y. Wang, B. Yousefzadeh, H. Chen, H. Nassar, G. Huang & C. Daraio. Observation of nonreciprocal wave propagation in a dynamic phononic lattice. *Phys. Rev. Lett.* **121,** 194301 (2018).

62. Y. Chen, X. Li, H. Nassar, A. N. Norris, C. Daraio & G. Huang. Nonreciprocal wave propagation in a continuum-based metamaterial with space-time modulated resonators. *Phys. Rev. Applied* **11,** 064052 (2019).

63. H. Xu, L. Jiang, A. A. Clerk & J. G. E. Harris. Nonreciprocal control and cooling of phonon modes in an optomechanical system. *Nature* **568,** 65–69 (2019).

64. J. P. Mathew, J. del Pino & E. Verhagen. Synthetic gauge fields for phonon transport in a nano-optomechanical system. *Nat. Nanotechnol.* **15,** 198–202 (2020).

65. K. v. Klitzing, G. Dorda & M. Pepper. New method for high-accuracy determination of the fine-structure constant based on quantized Hall resistance. *Phys. Rev. Lett.* **45,** 494–497 (1980).

66. K. von Klitzing, T. Chakraborty, P. Kim, V. Madhavan, X. Dai, J. McIver, Y. Tokura, L. Savary, D. Smirnova, A. M. Rey, C. Felser, J. Gooth & X. Qi. 40 years of the quantum Hall effect. *Nat. Rev. Phys.* **2,** 397–401 (2020).

67. R. B. Laughlin. Quantized Hall conductivity in two dimensions. *Phys. Rev. B* **23,** 5632–5633 (1981).

68. B. Jeckelmann & B. Jeanneret. The quantum Hall effect as an electrical resistance standard. *Rep. Prog. Phys.* **64,** 1603–1655 (2001).

69. M. Asorey. Space, matter and topology. *Nat. Phys.* **12,** 616–618 (2016).

70. C. L. Kane & E. J. Mele. Quantum spin Hall effect in graphene. *Phys. Rev. Lett.* **95,** 226801 (2005).

71. B. A. Bernevig, T. L. Hughes & S.-C. Zhang. Quantum spin Hall effect and topological phase transition in HgTe quantum wells. *Science* **314,** 1757–1761 (2006).

72. M. König, S. Wiedmann, C. Brüne, A. Roth, H. Buhmann, L. W. Molenkamp, X.-L. Qi & S.-C. Zhang. Quantum spin Hall insulator state in HgTe quantum wells. *Science* **318,** 766–770 (2007).

73. J. Koch, A. A. Houck, K. L. Hur & S. M. Girvin. Time-reversal-symmetry breaking in circuit-QED-based photon lattices. *Phys. Rev. A* **82,** 043811 (2010).

74. K. Fang, Z. Yu & S. Fan. Realizing effective magnetic field for photons by controlling the phase of dynamic modulation. *Nat. Photon.* **6,** 782–787 (2012).

75. N. Goldman, J. C. Budich & P. Zoller. Topological quantum matter with ultracold gases in optical lattices. *Nat. Phys.* **12,** 639–645 (2016).

76. J. Ningyuan, C. Owens, A. Sommer, D. Schuster & J. Simon. Time- and site-resolved dynamics in a topological circuit. *Phys. Rev. X* **5,** 021031 (2015).

77. F. D. M. Haldane & S. Raghu. Possible realization of directional optical waveguides in photonic crystals with broken time-reversal symmetry. *Phys. Rev. Lett.* **100,** 013904 (2008).

78. Z. Wang, Y. Chong, J. D. Joannopoulos & M. Soljačić. Observation of unidirectional backscattering-immune topological electromagnetic states. *Nature* **461,** 772–775 (2009).

79. S. Klembt, T. H. Harder, O. A. Egorov, K. Winkler, R. Ge, M. A. Bandres, M. Emmerling, L. Worschech, T. C. H. Liew, M. Segev, C. Schneider & S. Höfling. Exciton-polariton topological insulator. *Nature* **562,** 552–556 (2018).

80. S. Barik, A. Karasahin, C. Flower, T. Cai, H. Miyake, W. DeGottardi, M. Hafezi & E. Waks. A topological quantum optics interface. *Science* **359,** 666–668 (2018).

81. N. Parappurath, F. Alpeggiani, L. Kuipers & E. Verhagen. Direct observation of topological edge states in silicon photonic crystals: Spin, dispersion, and chiral routing. *Sci. Adv.* **6,** eaaw4137 (2020).

82. X.-T. He, E.-T. Liang, J.-J. Yuan, H.-Y. Qiu, X.-D. Chen, F.-L. Zhao & J.-W. Dong. A silicon-on-insulator slab for topological valley transport. *Nat. Commun.* **10,** 872 (2019).

83. S. Arora, T. Bauer, R. Barczyk, E. Verhagen & L. Kuipers. Direct quantification of topological protection in symmetry-protected photonic edge states at telecom wavelengths. *Light: Sci. Appl.* **10,** 9 (2021).

84. M. C. Rechtsman, J. M. Zeuner, Y. Plotnik, Y. Lumer, D. Podolsky, F. Dreisow, S. Nolte, M. Segev & A. Szameit. Photonic Floquet topological insulators. *Nature* **496,** 196–200 (2013).

85. L. Yuan, Q. Lin, M. Xiao & S. Fan. Synthetic dimension in photonics. *Optica* **5,** 1396 (2018).

86. E. Lustig, S. Weimann, Y. Plotnik, Y. Lumer, M. A. Bandres, A. Szameit & M. Segev. Photonic topological insulator in synthetic dimensions. *Nature* **567,** 356–360 (2019).

87. A. Dutt, Q. Lin, L. Yuan, M. Minkov, M. Xiao & S. Fan. A single photonic cavity with two independent physical synthetic dimensions. *Science* **367,** 59–64 (2020).

88. A. Darabi, X. Ni, M. Leamy & A. Alù. Reconfigurable Floquet elastodynamic topological insulator based on synthetic angular momentum bias. *Sci. Adv.* **6,** eaba8656 (2020).

89. R. Süsstrunk & S. D. Huber. Observation of phononic helical edge states in a mechanical topological insulator. *Science* **349,** 47–50 (2015).

90. J. Cha, K. W. Kim & C. Daraio. Experimental realization of on-chip topological nanoelectromechanical metamaterials. *Nature* **564,** 229–233 (2018).

91. J. Ma, X. Xi, Y. Li & X. Sun. Nanomechanical topological insulators with an auxiliary orbital degree of freedom. *Nat. Nanotechnol.* **16,** 576–583 (2021).

92. H. Ren, T. Shah, H. Pfeifer, C. Brendel, V. Peano, F. Marquardt & O. Painter. Topological phonon transport in an optomechanical system. *Nat. Commun.* **13,** 3476 (2022).

93. Y. Ashida, Z. Gong & M. Ueda. Non-Hermitian physics. *Adv. Phys.* **69,** 249–435 (2020).

94. Y. Yamamoto, K. Aihara, T. Leleu, K.-i. Kawarabayashi, S. Kako, M. Fejer, K. Inoue & H. Takesue. Coherent Ising machines—optical neural networks operating at the quantum limit. *npj Quantum Inf.* **3,** 49 (2017).

95. C. M. Bender & S. Boettcher. Real spectra in non-Hermitian Hamiltonians having PT symmetry. *Phys. Rev. Lett.* **80,** 5243–5246 (1998).

96. M. Parto, Y. G. N. Liu, B. Bahari, M. Khajavikhan & D. N. Christodoulides. Non-Hermitian and topological photonics: optics at an exceptional point. *Nanophotonics* **10,** 403–423 (2020).

97. R. El-Ganainy, K. G. Makris, M. Khajavikhan, Z. H. Musslimani, S. Rotter & D. N. Christodoulides. Non-Hermitian physics and PT symmetry. *Nat. Phys.* **14,** 11–19 (2018).

98. Ş. K. Özdemir, S. Rotter, F. Nori & L. Yang. Parity–time symmetry and exceptional points in photonics. *Nat. Mater.* **18,** 783–798 (2019).

99. H. Li, A. Mekawy, A. Krasnok & A. Alù. Virtual parity-time symmetry. *Phys. Rev. Lett.* **124,** 193901 (2020).

100. J. Wiersig. Enhancing the sensitivity of frequency and energy splitting detection by using exceptional points: Application to microcavity sensors for single-particle detection. *Phys. Rev. Lett.* **112,** 203901 (2014).

101. W. Langbein. No exceptional precision of exceptional-point sensors. *Phys. Rev. A* **98,** 023805 (2018).

102. W. Chen, Ş. Kaya Özdemir, G. Zhao, J. Wiersig & L. Yang. Exceptional points enhance sensing in an optical microcavity. *Nature* **548,** 192–196 (2017).

103. H. Hodaei, A. U. Hassan, S. Wittek, H. Garcia-Gracia, R. El-Ganainy, D. N. Christodoulides & M. Khajavikhan. Enhanced sensitivity at higher-order exceptional points. *Nature* **548,** 187–191 (2017).

104. Y.-H. Lai, Y.-K. Lu, M.-G. Suh, Z. Yuan & K. Vahala. Observation of the exceptional-point-enhanced Sagnac effect. *Nature* **576,** 65–69 (2019).

105. J. Wiersig. Review of exceptional point-based sensors. *Photon. Res.* **8,** 1457 (2020).

106. E. J. Bergholtz, J. C. Budich & F. K. Kunst. Exceptional topology of non-Hermitian systems. *Rev. Mod. Phys.* **93,** 015005 (2021).

107. K. Ding, C. Fang & G. Ma. Non-Hermitian topology and exceptional-point geometries. *Nat Rev Phys* **4,** 745–760 (2022).

108. H. Xu, D. Mason, L. Jiang & J. G. E. Harris. Topological energy transfer in an optomechanical system with exceptional points. *Nature* **537,** 80–83 (2016).

109. Y. S. S. Patil, J. Höller, P. A. Henry, C. Guria, Y. Zhang, L. Jiang, N. Kralj, N. Read & J. G. E. Harris. Measuring the knot of non-Hermitian degeneracies and non-commuting braids. *Nature* **607,** 271–275 (2022).

110. N. Hatano & D. R. Nelson. Vortex pinning and non-Hermitian quantum mechanics. *Phys. Rev. B* **56,** 8651–8673 (1997).

111. T. E. Lee. Anomalous edge state in a non-Hermitian lattice. *Phys. Rev. Lett.* **116,** 133903 (2016).

112. S. Yao & Z. Wang. Edge states and topological invariants of non-Hermitian systems. *Phys. Rev. Lett.* **121,** 086803 (2018).

113. H.-A. Bachor & T. C. Ralph. *A guide to experiments in quantum optics* 1st ed. (Wiley, 2019).

114. G. Breitenbach, S. Schiller & J. Mlynek. Measurement of the quantum states of squeezed light. *Nature* **387,** 471–475 (1997).

115. M. Tse *et al.* Quantum-enhanced advanced LIGO detectors in the era of gravitational-wave astronomy. *Phys. Rev. Lett.* **123,** 231107 (2019).

116. B. P. Abbott *et al.* Observation of gravitational waves from a binary black hole merger. *Phys. Rev. Lett.* **116,** 061102 (2016).

117. N. Brahms, T. Botter, S. Schreppler, D. W. C. Brooks & D. M. Stamper-Kurn. Optical detection of the quantization of collective atomic motion. *Phys. Rev. Lett.* **108,** 133601 (2012).

118. M. Aspelmeyer, T. J. Kippenberg & F. Marquardt. Cavity optomechanics. *Rev. Mod. Phys.* **86,** 1391–1452 (2014).

119. J. D. Teufel, T. Donner, D. Li, J. W. Harlow, M. S. Allman, K. Cicak, A. J. Sirois, J. D. Whittaker, K. W. Lehnert & R. W. Simmonds. Sideband cooling of micromechanical motion to the quantum ground state. *Nature* **475,** 359–363 (2011).

120. E. Verhagen, S. Deléglise, S. Weis, A. Schliesser & T. J. Kippenberg. Quantum-coherent coupling of a mechanical oscillator to an optical cavity mode. *Nature* **482,** 63–67 (2012).

121. T. A. Palomaki, J. D. Teufel, R. W. Simmonds & K. W. Lehnert. Entangling mechanical motion with microwave fields. *Science* **342,** 710–713 (2013).

122. S. J. M. Habraken, K. Stannigel, M. D. Lukin, P. Zoller & P. Rabl. Continuous mode cooling and phonon routers for phononic quantum networks. *New J. Phys.* **14,** 115004 (2012).

123. E. Verhagen & A. Alù. Optomechanical nonreciprocity. *Nat. Phys.* **13,** 922–924 (2017).

124. M. Hafezi & P. Rabl. Optomechanically induced non-reciprocity in microring resonators. *Opt. Express* **20,** 7672 (2012).

125. J. Kim, M. C. Kuzyk, K. Han, H. Wang & G. Bahl. Non-reciprocal Brillouin scattering induced transparency. *Nat. Phys.* **11,** 275–280 (2015).

126. Z. Shen, Y.-L. Zhang, Y. Chen, C.-L. Zou, Y.-F. Xiao, X.-B. Zou, F.-W. Sun, G.-C. Guo & C.-H. Dong. Experimental realization of optomechanically induced non-reciprocity. *Nat. Photon.* **10,** 657–661 (2016).

127. N. R. Bernier, L. D. Tóth, A. Koottandavida, M. A. Ioannou, D. Malz, A. Nunnenkamp, A. K. Feofanov & T. J. Kippenberg. Nonreciprocal reconfigurable microwave optomechanical circuit. *Nat. Commun.* **8,** 604 (2017).

128. G. A. Peterson, F. Lecocq, K. Cicak, R. W. Simmonds, J. Aumentado & J. D. Teufel. Demonstration of efficient nonreciprocity in a microwave optomechanical circuit. *Phys. Rev. X* **7,** 031001 (2017).

129. M.-A. Miri, F. Ruesink, E. Verhagen & A. Alù. Optical nonreciprocity based on optomechanical coupling. *Phys. Rev. Applied* **7,** 064014 (2017).

130. A. Metelmann & A. A. Clerk. Nonreciprocal photon transmission and amplification via reservoir engineering. *Phys. Rev. X* **5,** 021025 (2015).

131. S. Barzanjeh, M. Wulf, M. Peruzzo, M. Kalaee, P. B. Dieterle, O. Painter & J. M. Fink. Mechanical on-chip microwave circulator. *Nat. Commun.* **8,** 953 (2017).

132. F. Ruesink, J. P. Mathew, M.-A. Miri, A. Alù & E. Verhagen. Optical circulation in a multimode optomechanical resonator. *Nat. Commun.* **9,** 1798 (2018).

133. Z. Shen, Y.-L. Zhang, Y. Chen, F.-W. Sun, X.-B. Zou, G.-C. Guo, C.-L. Zou & C.-H. Dong. Reconfigurable optomechanical circulator and directional amplifier. *Nat. Commun.* **9,** 1797 (2018).

134. V. Peano, C. Brendel, M. Schmidt & F. Marquardt. Topological phases of sound and light. *Phys. Rev. X* **5,** 031011 (2015).

135. M. Schmidt, S. Kessler, V. Peano, O. Painter & F. Marquardt. Optomechanical creation of magnetic fields for photons on a lattice. *Optica* **2,** 635 (2015).

136. S. Walter & F. Marquardt. Classical dynamical gauge fields in optomechanics. *New J. Phys.* **18,** 113029 (2016).

137. P. F. Cohadon, A. Heidmann & M. Pinard. Cooling of a mirror by radiation pressure. *Phys. Rev. Lett.* **83,** 3174–3177 (1999).

138. J. Kepler. *De cometis libelli tres* (Andrae Apergeri, Sebastiani Mylii, Augsburg, 1619).

139. P. Lebedew. Untersuchungen über die Druckkräfte des Lichtes. *Ann. Phys.* **311,** 433–458 (1901).

140. E. F. Nichols & G. F. Hull. The pressure due to radiation. *Astrophys. J.* **17,** 315 (1903).

141. A. Ashkin. Acceleration and trapping of particles by radiation pressure. *Phys. Rev. Lett.* **24,** 156–159 (1970).

142. W. P. Bowen & G. J. Milburn. *Quantum optomechanics* (CRC Press, Taylor & Francis Group, 2016).

143. R. Leijssen. *Measuring mechanical motion using light confined at the nanoscale* (Technische Universiteit Eindhoven, Eindhoven, 2017).

144. D. R. Mason. *Dynamical behavior near exceptional points in an optomechanical system* (Yale University, New Haven, CT, 2018).

145. R. Leijssen & E. Verhagen. Strong optomechanical interactions in a sliced photonic crystal nanobeam. *Sci. Rep.* **5,** 15974 (2015).

146. R. Leijssen, G. R. La Gala, L. Freisem, J. T. Muhonen & E. Verhagen. Nonlinear cavity optomechanics with nanomechanical thermal fluctuations. *Nat. Commun.* **8,** 16024 (2017).

147. A. A. Clerk, M. H. Devoret, S. M. Girvin, F. Marquardt & R. J. Schoelkopf. Introduction to quantum noise, measurement, and amplification. *Rev. Mod. Phys.* **82,** 1155–1208 (2010).

148. A. B. Shkarin, N. E. Flowers-Jacobs, S. W. Hoch, A. D. Kashkanova, C. Deutsch, J. Reichel & J. G. E. Harris. Optically mediated hybridization between two mechanical modes. *Phys. Rev. Lett.* **112,** 013602 (2014).

149. M. J. Weaver, F. Buters, F. Luna, H. Eerkens, K. Heeck, S. de Man & D. Bouwmeester. Coherent optomechanical state transfer between disparate mechanical resonators. *Nat. Commun.* **8,** 824 (2017).

150. F. Reiter & A. S. Sørensen. Effective operator formalism for open quantum systems. *Phys. Rev. A* **85,** 032111 (2012).

151. J. del Pino, J. J. Slim & E. Verhagen. Non-Hermitian chiral phononics through optomechanically induced squeezing. *Nature* **606,** 82–87 (2022).

152. I. Mahboob, H. Okamoto, K. Onomitsu & H. Yamaguchi. Two-mode thermal-noise squeezing in an electromechanical resonator. *Phys. Rev. Lett.* **113,** 167203 (2014).

153. A. Leuch, L. Papariello, O. Zilberberg, C. L. Degen, R. Chitra & A. Eichler. Parametric symmetry breaking in a nonlinear resonator. *Phys. Rev. Lett.* **117,** 214101 (2016).

154. M. Calvanese Strinati, L. Bello, A. Pe'er & E. G. Dalla Torre. Theory of coupled parametric oscillators beyond coupled Ising spins. *Phys. Rev. A* **100,** 023835 (2019).

155. L. Bello, M. Calvanese Strinati, E. G. Dalla Torre & A. Pe'er. Persistent coherent beating in coupled parametric oscillators. *Phys. Rev. Lett.* **123,** 083901 (2019).

156. J. Guckenheimer & P. Holmes. *Nonlinear oscillations, dynamical systems, and bifurcations of vector fields* (Springer New York, New York, NY, 1983).

157. D. Rugar & P. Grütter. Mechanical parametric amplification and thermomechanical noise squeezing. *Phys. Rev. Lett.* **67,** 699–702 (1991).

158. D. Bothner, S. Yanai, A. Iniguez-Rabago, M. Yuan, Y. M. Blanter & G. A. Steele. Cavity electromechanics with parametric mechanical driving. *Energy spectra of quantum rings* **11,** 1589 (2020).

159. A. Pontin, M. Bonaldi, A. Borrielli, F. S. Cataliotti, F. Marino, G. A. Prodi, E. Serra & F. Marin. Squeezing a thermal mechanical oscillator by stabilized parametric effect on the optical spring. *Phys. Rev. Lett.* **112,** 023601 (2014).

160. J.-P. Blaizot & G. Ripka. *Quantum theory of finite systems* (MIT Press, Cambridge, Mass., 1986).

161. R. Rossignoli & A. M. Kowalski. Complex modes in unstable quadratic bosonic forms. *Phys. Rev. A* **72,** 032101 (2005).

162. V. P. Flynn, E. Cobanera & L. Viola. Deconstructing effective non-Hermitian dynamics in quadratic bosonic Hamiltonians. *New J. Phys.* **22,** 083004 (2020).

163. Y.-X. Wang & A. A. Clerk. Non-Hermitian dynamics without dissipation in quantum systems. *Phys. Rev. A* **99,** 063834 (2019).

164. E. B. Aranas, M. J. Akram, D. Malz & T. S. Monteiro. Quantum noise spectra for periodically driven cavity optomechanics. *Phys. Rev. A* **96,** 063836 (2017).

165. L. Neuhaus, R. Metzdorff, S. Chua, T. Jacqmin, T. Briant, A. Heidmann, P.-F. Cohadon & S. Deleglise. PyRPL (Python Red Pitaya Lockbox) — An open-source software package for FPGA-controlled quantum optics experiments. in *2017 Conference on Lasers and Electro-Optics Europe & European Quantum Electronics Conference (CLEO/Europe-EQEC)* (IEEE, Munich, Germany, 2017), 1–1.

166. B. D. Hauer, T. J. Clark, P. H. Kim, C. Doolin & J. P. Davis. Dueling dynamical backaction in a cryogenic optomechanical cavity. *Phys. Rev. A* **99,** 053803 (2019).

167. M. Poggio, C. L. Degen, H. J. Mamin & D. Rugar. Feedback cooling of a cantilever's fundamental mode below 5 mK. *Phys. Rev. Lett.* **99,** 017201 (2007).

168. M. Rossi, D. Mason, J. Chen, Y. Tsaturyan & A. Schliesser. Measurement-based quantum control of mechanical motion. *Nature* **563,** 53–58 (2018).

169. J. Vidal, R. Mosseri & B. Douçot. Aharonov-Bohm cages in two-dimensional structures. *Phys. Rev. Lett.* **81,** 5888–5891 (1998).

170. M. Aidelsburger, M. Atala, S. Nascimbène, S. Trotzky, Y.-A. Chen & I. Bloch. Experimental realization of strong effective magnetic fields in an optical lattice. *Phys. Rev. Lett.* **107,** 255301 (2011).

171. J. Struck, C. Ölschläger, M. Weinberg, P. Hauke, J. Simonet, A. Eckardt, M. Lewenstein, K. Sengstock & P. Windpassinger. Tunable gauge potential for neutral and spinless particles in driven optical lattices. *Phys. Rev. Lett.* **108,** 225304 (2012).

172. K. Fang & S. Fan. Controlling the flow of light using the inhomogeneous effective gauge field that emerges from dynamic modulation. *Phys. Rev. Lett.* **111,** 203901 (2013).

173. S. Longhi. Aharonov–Bohm photonic cages in waveguide and coupled resonator lattices by synthetic magnetic fields. *Opt. Lett.* **39,** 5892 (2014).

174. S. Mukherjee, M. Di Liberto, P. Öhberg, R. R. Thomson & N. Goldman. Experimental observation of Aharonov-Bohm cages in photonic lattices. *Phys. Rev. Lett.* **121,** 075502 (2018).

175. M. Kremer, I. Petrides, E. Meyer, M. Heinrich, O. Zilberberg & A. Szameit. A square-root topological insulator with non-quantized indices realized with photonic Aharonov-Bohm cages. *Nat. Commun.* **11,** 907 (2020).

176. V. Brosco, L. Pilozzi & C. Conti. Two-flux tunable Aharonov-Bohm effect in a photonic lattice. *Phys. Rev. B* **104,** 024306 (2021).

177. J. Cabedo, J. Claramunt, J. Mompart, V. Ahufinger & A. Celi. Effective triangular ladders with staggered flux from spin-orbit coupling in 1D optical lattices. *Eur. Phys. J. D* **74,** 123 (2020).

178. A. Fuhrer, S. Luscher, T. Ihn, T. Heinzel, K. Ensslin, W. Wegscheider & M. Bichler. Energy spectra of quantum rings. *Nature* **413,** 822–825 (2001).

179. P. Roushan *et al.* Chiral ground-state currents of interacting photons in a synthetic magnetic field. *Nat. Phys.* **13,** 146–151 (2017).

180. Y.-P. Wang, W. Wang, Z.-Y. Xue, W.-L. Yang, Y. Hu & Y. Wu. Realizing and characterizing chiral photon flow in a circuit quantum electrodynamics necklace. *Sci. Rep.* **5,** 8352 (2015).

181. D. Leykam, A. Andreanov & S. Flach. Artificial flat band systems: from lattice models to experiments. *Adv. Phys: X* **3,** 1473052 (2018).

182. C.-E. Bardyn, S. D. Huber & O. Zilberberg. Measuring topological invariants in small photonic lattices. *New J. Phys.* **16,** 123013 (2014).

183. K. Pelka, V. Peano & A. Xuereb. Chimera states in small optomechanical arrays. *Phys. Rev. Res.* **2,** 013201 (2020).

184. J. M. R. Parrondo, J. M. Horowitz & T. Sagawa. Thermodynamics of information. *Nat. Phys.* **11,** 131–139 (2015).

185. S. Vinjanampathy & J. Anders. Quantum thermodynamics. *Contemporary Physics* **57,** 545–579 (2016).

186. M. Serra-Garcia, A. Foehr, M. Molerón, J. Lydon, C. Chong & C. Daraio. Mechanical autonomous stochastic heat engine. *Phys. Rev. Lett.* **117,** 010602 (2016).

187. M. Rademacher, M. Konopik, M. Debiossac, D. Grass, E. Lutz & N. Kiesel. Nonequilibrium control of thermal and mechanical changes in a levitated system. *Phys. Rev. Lett.* **128,** 070601 (2022).

188. G. Benenti, G. Casati, K. Saito & R. S. Whitney. Fundamental aspects of steady-state conversion of heat to work at the nanoscale. *Phys. Rep.* **694,** 1–124 (2017).

189. A. Bermudez, M. Bruderer & M. B. Plenio. Controlling and measuring quantum transport of heat in trapped-ion crystals. *Phys. Rev. Lett.* **111,** 040601 (2013).

190. D. Manzano, M. Tiersch, A. Asadian & H. J. Briegel. Quantum transport efficiency and Fourier's law. *Phys. Rev. E* **86,** 061118 (2012).

191. A. Xuereb, C. Genes, G. Pupillo, M. Paternostro & A. Dantan. Reconfigurable long-range phonon dynamics in optomechanical arrays. *Phys. Rev. Lett.* **112,** 133604 (2014).

192. A. Xuereb, A. Imparato & A. Dantan. Heat transport in harmonic oscillator systems with thermal baths: application to optomechanical arrays. *New J. Phys.* **17,** 055013 (2015).

193. S. Barzanjeh, M. Aquilina & A. Xuereb. Manipulating the flow of thermal noise in quantum devices. *Phys. Rev. Lett.* **120,** 060601 (2018).

194. S. M. Ashrafi, R. Malekfar, A. R. Bahrampour & J. Feist. Optomechanical heat transfer between molecules in a nanoplasmonic cavity. *Phys. Rev. A* **100,** 013826 (2019).

195. K. Y. Fong, H.-K. Li, R. Zhao, S. Yang, Y. Wang & X. Zhang. Phonon heat transfer across a vacuum through quantum fluctuations. *Nature* **576,** 243–247 (2019).

196. C. Yang, X. Wei, J. Sheng & H. Wu. Phonon heat transport in cavity-mediated optomechanical nanoresonators. *Nat. Commun.* **11,** 4656 (2020).

197. M. H. J. de Jong, J. Li, C. Gärtner, R. A. Norte & S. Gröblacher. Coherent mechanical noise cancellation and cooperativity competition in optomechanical arrays. *Optica* **9,** 170 (2022).

198. F. Giazotto & M. J. Martínez-Pérez. The Josephson heat interferometer. *Nature* **492,** 401–405 (2012).

199. L. Zhu & S. Fan. Persistent directional current at equilibrium in nonreciprocal many-body near field electromagnetic heat transfer. *Phys. Rev. Lett.* **117,** 134303 (2016).

200. Z. Denis, A. Biella, I. Favero & C. Ciuti. Permanent directional heat currents in lattices of optomechanical resonators. *Phys. Rev. Lett.* **124,** 083601 (2020).

201. Á. Rivas & M. A. Martin-Delgado. Topological heat transport and symmetry-protected boson currents. *Sci. Rep.* **7,** 6350 (2017).

202. A. Seif, W. DeGottardi, K. Esfarjani & M. Hafezi. Thermal management and non-reciprocal control of phonon flow via optomechanics. *Nat. Commun.* **9,** 1207 (2018).

203. G. Benenti, K. Saito & G. Casati. Thermodynamic bounds on efficiency for systems with broken time-reversal symmetry. *Phys. Rev. Lett.* **106,** 230602 (2011).

204. K. Brandner, K. Saito & U. Seifert. Strong bounds on Onsager coefficients and efficiency for three-terminal thermoelectric transport in a magnetic field. *Phys. Rev. Lett.* **110,** 070603 (2013).

205. R. Luo, G. Benenti, G. Casati & J. Wang. Onsager reciprocal relations with broken time-reversal symmetry. *Phys. Rev. Res.* **2,** 022009 (2020).

206. S. Saryal, S. Mohanta & B. K. Agarwalla. Bounds on fluctuations for machines with broken time-reversal symmetry: A linear response study. *Phys. Rev. E* **105,** 024129 (2022).

207. D.-G. Lai, J.-F. Huang, X.-L. Yin, B.-P. Hou, W. Li, D. Vitali, F. Nori & J.-Q. Liao. Nonreciprocal ground-state cooling of multiple mechanical resonators. *Phys. Rev. A* **102,** 011502 (2020).

208. C. F. Ockeloen-Korppi, M. F. Gely, E. Damskägg, M. Jenkins, G. A. Steele & M. A. Sillanpää. Sideband cooling of nearly degenerate micromechanical oscillators in a multimode optomechanical system. *Phys. Rev. A* **99,** 023826 (2019).

209. J. Huang, D.-G. Lai, C. Liu, J.-F. Huang, F. Nori & J.-Q. Liao. Multimode optomechanical cooling via general dark-mode control. *Phys. Rev. A* **106,** 013526 (2022).

210. L. Onsager. Reciprocal relations in irreversible processes. II. *Phys. Rev.* **38,** 2265–2279 (1931).

211. C. W. Gardiner & P. Zoller. *Quantum noise: a handbook of Markovian and non-Markovian quantum stochastic methods with applications to quantum optics* 3rd ed (Springer, Berlin ; New York, 2004).

212. P. Meystre & M. Sargent. *Elements of quantum optics* 4th ed (Springer, Berlin ; New York, 2007).

213. G. Clos, D. Porras, U. Warring & T. Schaetz. Time-resolved observation of thermalization in an isolated quantum system. *Phys. Rev. Lett.* **117,** 170401 (2016).

214. M. Frimmer, J. Gieseler & L. Novotny. Cooling Mechanical Oscillators by Coherent Control. *Phys. Rev. Lett.* **117,** 163601 (2016).

215. J. M. Horowitz & T. R. Gingrich. Thermodynamic uncertainty relations constrain non-equilibrium fluctuations. *Nat. Phys.* **16,** 15–20 (2020).

216. C. Jiang, Y.-L. Liu & M. A. Sillanpää. *Energy-level-attraction and heating-resistant-cooling of mechanical resonators with exceptional points* arXiv: 2011.13587 (2020).

217. C. Coulais, R. Fleury & J. van Wezel. Topology and broken Hermiticity. *Nat. Phys.* **17,** 9–13 (2021).

218. S. Lieu. Topological symmetry classes for non-Hermitian models and connections to the bosonic Bogoliubov–de Gennes equation. *Phys. Rev. B* **98,** 115135 (2018).

219. Z. Gong, Y. Ashida, K. Kawabata, K. Takasan, S. Higashikawa & M. Ueda. Topological phases of non-Hermitian systems. *Phys. Rev. X* **8,** 031079 (2018).

220. P. St-Jean, V. Goblot, E. Galopin, A. Lemaître, T. Ozawa, L. Le Gratiet, I. Sagnes, J. Bloch & A. Amo. Lasing in topological edge states of a one-dimensional lattice. *Nat. Photon.* **11,** 651–656 (2017).

221. B. Hu, Z. Zhang, H. Zhang, L. Zheng, W. Xiong, Z. Yue, X. Wang, J. Xu, Y. Cheng, X. Liu & J. Christensen. Non-Hermitian topological whispering gallery. *Nature* **597,** 655–659 (2021).

222. J. M. Zeuner, M. C. Rechtsman, Y. Plotnik, Y. Lumer, S. Nolte, M. S. Rudner, M. Segev & A. Szameit. Observation of a topological transition in the bulk of a non-Hermitian system. *Phys. Rev. Lett.* **115,** 040402 (2015).

223. R. Barnett. Edge-state instabilities of bosons in a topological band. *Phys. Rev. A* **88,** 063631 (2013).

224. V. Peano, M. Houde, C. Brendel, F. Marquardt & A. A. Clerk. Topological phase transitions and chiral inelastic transport induced by the squeezing of light. *Nat. Commun.* **7,** 10779 (2016).

225. V. Peano, M. Houde, F. Marquardt & A. A. Clerk. Topological quantum fluctuations and traveling wave amplifiers. *Phys. Rev. X* **6,** 041026 (2016).

226. M. A. Bandres, S. Wittek, G. Harari, M. Parto, J. Ren, M. Segev, D. N. Christodoulides & M. Khajavikhan. Topological insulator laser: Experiments. *Science* **359,** eaar4005 (2018).

227. A. Ghatak, M. Brandenbourger, J. van Wezel & C. Coulais. Observation of non-Hermitian topology and its bulk–edge correspondence in an active mechanical metamaterial. *Proc. Natl. Acad. Sci. U.S.A.* **117,** 29561–29568 (2020).

228. T. Helbig, T. Hofmann, S. Imhof, M. Abdelghany, T. Kiessling, L. W. Molenkamp, C. H. Lee, A. Szameit, M. Greiter & R. Thomale. Generalized bulk–boundary correspondence in non-Hermitian topolectrical circuits. *Nat. Phys.* **16,** 747–750 (2020).

229. S. Weidemann, M. Kremer, T. Helbig, T. Hofmann, A. Stegmaier, M. Greiter, R. Thomale & A. Szameit. Topological funneling of light. *Science* **368,** 311–314 (2020).

230. K. Wang, A. Dutt, K. Y. Yang, C. C. Wojcik, J. Vučković & S. Fan. Generating arbitrary topological windings of a non-Hermitian band. *Science* **371,** 1240–1245 (2021).

231. M.-A. Miri & A. Alù. Exceptional points in optics and photonics. *Science* **363,** eaar7709 (2019).

232. A. McDonald, T. Pereg-Barnea & A. A. Clerk. Phase-dependent chiral transport and effective non-Hermitian dynamics in a bosonic Kitaev-Majorana chain. *Phys. Rev. X* **8,** 041031 (2018).

233. C. C. Wanjura, M. Brunelli & A. Nunnenkamp. Topological framework for directional amplification in driven-dissipative cavity arrays. *Nat. Commun.* **11,** 3149 (2020).

234. T. T. Koutserimpas & R. Fleury. Nonreciprocal gain in non-Hermitian time-Floquet systems. *Phys. Rev. Lett.* **120,** 087401 (2018).

235. L. Ranzani & J. Aumentado. Graph-based analysis of nonreciprocity in coupled-mode systems. *New J. Phys.* **17,** 023024 (2015).

236. J. S. Huber, G. Rastelli, M. J. Seitner, J. Kölbl, W. Belzig, M. I. Dykman & E. M. Weig. Spectral evidence of squeezing of a weakly damped driven nanomechanical mode. *Phys. Rev. X* **10,** 021066 (2020).

237. C. A. Downing, D. Zueco & L. Martín-Moreno. Chiral current circulation and PT symmetry in a trimer of oscillators. *ACS Photon.* **7,** 3401–3414 (2020).

238. W. Tang, X. Jiang, K. Ding, Y.-X. Xiao, Z.-Q. Zhang, C. T. Chan & G. Ma. Exceptional nexus with a hybrid topological invariant. *Science* **370,** 1077–1080 (2020).

239. H.-K. Lau & A. A. Clerk. Fundamental limits and non-reciprocal approaches in non-Hermitian quantum sensing. *Nat. Commun.* **9,** 4320 (2018).

240. I. Mahboob, H. Okamoto & H. Yamaguchi. An electromechanical Ising Hamiltonian. *Sci. Adv.* **2,** e1600236 (2016).

241. K. Takata, K. Nozaki, E. Kuramochi, S. Matsuo, K. Takeda, T. Fujii, S. Kita, A. Shinya & M. Notomi. Observing exceptional point degeneracy of radiation with electrically pumped photonic crystal coupled-nanocavity lasers. *Optica* **8,** 184 (2021).

242. J. A. Richards. *Analysis of periodically time-varying systems* (Springer Berlin Heidelberg, Berlin, Heidelberg, 1983).

243. C. E. Rüter, K. G. Makris, R. El-Ganainy, D. N. Christodoulides, M. Segev & D. Kip. Observation of parity–time symmetry in optics. *Nat. Phys.* **6,** 192–195 (2010).

244. M. Ornigotti & A. Szameit. Quasi PT-symmetry in passive photonic lattices. *J. Opt.* **16,** 065501 (2014).

245. W. D. Heiss. The physics of exceptional points. *J. Phys. A: Math. Theor.* **45,** 444016 (2012).

246. R. M. Gray. Toeplitz and circulant matrices: A review. *Found. Trends Commun. Inf. Theory* **2,** 155–239 (2005).

247. C. Weedbrook, S. Pirandola, R. García-Patrón, N. J. Cerf, T. C. Ralph, J. H. Shapiro & S. Lloyd. Gaussian quantum information. *Rev. Mod. Phys.* **84,** 621–669 (2012).

248. C. C. Wanjura, J. J. Slim, J. del Pino, M. Brunelli, E. Verhagen & A. Nunnenkamp. *Quadrature nonreciprocity: unidirectional bosonic transmission without breaking time-reversal symmetry* arXiv: 2207 . 08523 (2022).

249. L. Deák & T. Fülöp. Reciprocity in quantum, electromagnetic and other wave scattering. *Ann. Phys.* **327,** 1050–1077 (2012).

250. D. Jalas, A. Petrov, M. Eich, W. Freude, S. Fan, Z. Yu, R. Baets, M. Popović, A. Melloni, J. D. Joannopoulos, M. Vanwolleghem, C. R. Doerr & H. Renner. What is — and what is not — an optical isolator. *Nat. Photon.* **7,** 579–582 (2013).

251. C. Caloz, A. Alù, S. Tretyakov, D. Sounas, K. Achouri & Z.-L. Deck-Léger. Electromagnetic nonreciprocity. *Phys. Rev. Applied* **10,** 047001 (2018).

252. B. Abdo, F. Schackert, M. Hatridge, C. Rigetti & M. Devoret. Josephson amplifier for qubit readout. *Appl. Phys. Lett.* **99,** 162506 (2011).

253. D. Malz, L. D. Tóth, N. R. Bernier, A. K. Feofanov, T. J. Kippenberg & A. Nunnenkamp. Quantum-limited directional amplifiers with optomechanics. *Phys. Rev. Lett.* **120,** 023601 (2018).

254. B. Abdo, A. Kamal & M. Devoret. Nondegenerate three-wave mixing with the Josephson ring modulator. *Phys. Rev. B* **87,** 014508 (2013).

255. F. Lecocq, L. Ranzani, G. A. Peterson, K. Cicak, R. W. Simmonds, J. D. Teufel & J. Aumentado. Nonreciprocal microwave signal processing with a field-programmable Josephson amplifier. *Phys. Rev. Applied* **7,** 024028 (2017).

256. D. B. Sohn, O. E. Örsel & G. Bahl. Electrically driven optical isolation through phonon-mediated photonic Autler–Townes splitting. *Nat. Photon.* **15,** 822–827 (2021).

257. L. Fan, J. Wang, L. T. Varghese, H. Shen, B. Niu, Y. Xuan, A. M. Weiner & M. Qi. An all-silicon passive optical diode. *Science* **335,** 447–450 (2012).

258. Y.-X. Wang, C. Wang & A. A. Clerk. *Quantum nonreciprocal interactions via dissipative gauge symmetry* arXiv: 2203 . 09392 (2022).

259. C. Sayrin, C. Junge, R. Mitsch, B. Albrecht, D. O'Shea, P. Schneeweiss, J. Volz & A. Rauschenbeutel. Nanophotonic optical isolator controlled by the internal state of cold atoms. *Phys. Rev. X* **5,** 041036 (2015).

260. S. Buddhiraju, A. Song, G. T. Papadakis & S. Fan. Nonreciprocal metamaterial obeying time-reversal symmetry. *Phys. Rev. Lett.* **124,** 257403 (2020).

261. V. P. Flynn, E. Cobanera & L. Viola. Topology by dissipation: Majorana bosons in metastable quadratic Markovian dynamics. *Phys. Rev. Lett.* **127,** 245701 (2021).

262. S. Fan, W. Suh & J. D. Joannopoulos. Temporal coupled-mode theory for the Fano resonance in optical resonators. *J. Opt. Soc. Am. A* **20,** 569 (2003).

263. C. W. Gardiner & M. J. Collett. Input and output in damped quantum systems: Quantum stochastic differential equations and the master equation. *Phys. Rev. A* **31,** 3761–3774 (1985).

264. V. B. Braginsky, Y. I. Vorontsov & K. S. Thorne. Quantum nondemolition measurements. *Science* **209,** 547–557 (1980).

265. A. A. Clerk, F. Marquardt & K. Jacobs. Back-action evasion and squeezing of a mechanical resonator using a cavity detector. *New J. Phys.* **10,** 095010 (2008).

266. M. Brunelli, D. Malz & A. Nunnenkamp. Conditional dynamics of optomechanical two-tone backaction-evading measurements. *Phys. Rev. Lett.* **123,** 093602 (2019).

267. T.-C. Chien, O. Lanes, C. Liu, X. Cao, P. Lu, S. Motz, G. Liu, D. Pekker & M. Hatridge. Multiparametric amplification and qubit measurement with a Kerr-free Josephson ring modulator. *Phys. Rev. A* **101,** 042336 (2020).

268. H. J. Carmichael. Quantum trajectory theory for cascaded open systems. *Phys. Rev. Lett.* **70,** 2273–2276 (1993).

269. C. W. Gardiner. Driving a quantum system with the output field from another driven quantum system. *Phys. Rev. Lett.* **70,** 2269–2272 (1993).

270. D. Porras & S. Fernández-Lorenzo. Topological amplification in photonic lattices. *Phys. Rev. Lett.* **122,** 143901 (2019).

271. Z. Zhang, Q. Wei, Y. Cheng, T. Zhang, D. Wu & X. Liu. Topological creation of acoustic pseudospin multipoles in a flow-free symmetry-broken metamaterial lattice. *Phys. Rev. Lett.* **118,** 084303 (2017).

272. T. M. Karg, B. Gouraud, C. T. Ngai, G.-L. Schmid, K. Hammerer & P. Treutlein. Light-mediated strong coupling between a mechanical oscillator and atomic spins 1 meter apart. *Science* **369,** 174–179 (2020).

273. K. Kawabata, S. Higashikawa, Z. Gong, Y. Ashida & M. Ueda. Topological unification of time-reversal and particle-hole symmetries in non-Hermitian physics. *Nat. Commun.* **10,** 297 (2019).

274. K. Kawabata, K. Shiozaki, M. Ueda & M. Sato. Symmetry and topology in non-Hermitian physics. *Phys. Rev. X* **9,** 041015 (2019).

275. S. Weimann, M. Kremer, Y. Plotnik, Y. Lumer, S. Nolte, K. G. Makris, M. Segev, M. C. Rechtsman & A. Szameit. Topologically protected bound states in photonic parity–time-symmetric crystals. *Nature Mater* **16,** 433–438 (2017).

276. M. Pan, H. Zhao, P. Miao, S. Longhi & L. Feng. Photonic zero mode in a non-Hermitian photonic lattice. *Nat Commun* **9,** 1308 (2018).

277. K. Wang, A. Dutt, C. C. Wojcik & S. Fan. Topological complex-energy braiding of non-Hermitian bands. *Nature* **598,** 59–64 (2021).

278. H. Shen, B. Zhen & L. Fu. Topological Band Theory for Non-Hermitian Hamiltonians. *Phys. Rev. Lett.* **120,** 146402 (2018).

279. B. Flebus, R. A. Duine & H. M. Hurst. Non-Hermitian topology of one-dimensional spin-torque oscillator arrays. *Phys. Rev. B* **102,** 180408 (2020).

280. S. Yao, F. Song & Z. Wang. Non-Hermitian Chern Bands. *Phys. Rev. Lett.* **121,** 136802 (2018).

281. F. K. Kunst, E. Edvardsson, J. C. Budich & E. J. Bergholtz. Biorthogonal Bulk-Boundary Correspondence in Non-Hermitian Systems. *Phys. Rev. Lett.* **121,** 026808 (2018).

282. V. M. Martinez Alvarez, J. E. Barrios Vargas & L. E. F. Foa Torres. Non-Hermitian robust edge states in one dimension: Anomalous localization and eigenspace condensation at exceptional points. *Phys. Rev. B* **97,** 121401 (2018).

283. N. Okuma, K. Kawabata, K. Shiozaki & M. Sato. Topological origin of non-Hermitian skin effects. *Phys. Rev. Lett.* **124,** 086801 (2020).

284. K. Zhang, Z. Yang & C. Fang. Universal non-Hermitian skin effect in two and higher dimensions. *Nat. Commun.* **13,** 2496 (2022).

285. K. Zhang, Z. Yang & C. Fang. Correspondence between winding numbers and skin modes in non-Hermitian systems. *Phys. Rev. Lett.* **125,** 126402 (2020).

286. L. Xiao, T. Deng, K. Wang, G. Zhu, Z. Wang, W. Yi & P. Xue. Non-Hermitian bulk–boundary correspondence in quantum dynamics. *Nat. Phys.* **16,** 761–766 (2020).

287. Q. Liang, D. Xie, Z. Dong, H. Li, H. Li, B. Gadway, W. Yi & B. Yan. Dynamic Signatures of Non-Hermitian Skin Effect and Topology in Ultracold Atoms. *Phys. Rev. Lett.* **129,** 070401 (2022).

288. L. Zhang, Y. Yang, Y. Ge, Y.-J. Guan, Q. Chen, Q. Yan, F. Chen, R. Xi, Y. Li, D. Jia, S.-Q. Yuan, H.-X. Sun, H. Chen & B. Zhang. Acoustic non-Hermitian skin effect from twisted winding topology. *Nat Commun* **12,** 6297 (2021).

289. W. Wang, X. Wang & G. Ma. Non-Hermitian morphing of topological modes. *Nature* **608,** 50–55 (2022).

290. Y. Xiong. Why does bulk boundary correspondence fail in some non-hermitian topological models. *J. Phys. Commun.* **2,** 035043 (2018).

291. M. Brunelli, C. C. Wanjura & A. Nunnenkamp. *Restoration of the non-Hermitian bulk-boundary correspondence via topological amplification* arXiv: 2207.12427 (2022).

292. A. Y. Kitaev. Unpaired Majorana fermions in quantum wires. *Phys.-Usp.* **44,** 131–136 (10S 2001).

293. A. McDonald & A. A. Clerk. Exponentially-enhanced quantum sensing with non-Hermitian lattice dynamics. *Nat. Commun.* **11,** 5382 (2020).

294. S. S. Verbridge, H. G. Craighead & J. M. Parpia. A megahertz nanomechanical resonator with room temperature quality factor over a million. *Appl. Phys. Lett.* **92,** 013112 (2008).

295. Y. Tsaturyan, A. Barg, E. S. Polzik & A. Schliesser. Ultracoherent nanomechanical resonators via soft clamping and dissipation dilution. *Nat. Nanotechnol.* **12,** 776–783 (2017).

296. A. H. Ghadimi, S. A. Fedorov, N. J. Engelsen, M. J. Bereyhi, R. Schilling, D. J. Wilson & T. J. Kippenberg. Elastic strain engineering for ultralow mechanical dissipation. *Science* **360,** 764–768 (2018).

297. P. Zapletal, S. Walter & F. Marquardt. Dynamically generated synthetic electric fields for photons. *Phys. Rev. A* **100,** 023804 (2019).

298. P. Zapletal & A. Nunnenkamp. Dynamical generation of synthetic electric fields for photons in the quantum regime. *Quantum Sci. Technol.* **4,** 044001. arXiv: 1902.00765 (2019).

299. N. R. A. Lee, M. Pechal, E. A. Wollack, P. Arrangoiz-Arriola, Z. Wang & A. H. Safavi-Naeni. Propagation of microwave photons along a synthetic dimension. *Phys. Rev. A* **101,** 053807 (2020).

300. C. W. Peterson, W. A. Benalcazar, M. Lin, T. L. Hughes & G. Bahl. Strong nonreciprocity in modulated resonator chains through synthetic electric and magnetic fields. *Phys. Rev. Lett.* **123,** 063901 (2019).

301. D. H. Dunlap & V. M. Kenkre. Dynamic localization of a charged particle moving under the influence of an electric field. *Phys. Rev. B* **34,** 3625–3633 (1986).

302. R. N. Patel, Z. Wang, W. Jiang, C. J. Sarabalis, J. T. Hill & A. H. Safavi-Naeini. Single-mode phononic wire. *Phys. Rev. Lett.* **121,** 040501 (2018).

303. Y. Chu, P. Kharel, W. H. Renninger, L. D. Burkhart, L. Frunzio, P. T. Rakich & R. J. Schoelkopf. Quantum acoustics with superconducting qubits. *Science* **358,** 199–202 (2017).

304. A. Laucht *et al.* Roadmap on quantum nanotechnologies. *Nanotechnology* **32,** 162003 (2021).

305. M. Schmidt, M. Ludwig & F. Marquardt. Optomechanical circuits for nanomechanical continuous variable quantum state processing. *New J. Phys.* **14,** 125005 (2012).

306. L. M. de Lépinay, B. Pigeau, B. Besga, P. Vincent, P. Poncharal & O. Arcizet. A universal and ultrasensitive vectorial nanomechanical sensor for imaging 2D force fields. *Nat. Nanotechnol.* **12,** 156–162 (2017).

307. R. Kononchuk, J. Cai, F. Ellis, R. Thevamaran & T. Kottos. Exceptional-point-based accelerometers with enhanced signal-to-noise ratio. *Nature* **607,** 697–702 (2022).

308. R. Duggan, S. A. Mann & A. Alù. Limitations of sensing at an exceptional point. *ACS Photon.* **9,** 1554–1566 (2022).

309. K. V. Kepesidis, T. J. Milburn, J. Huber, K. G. Makris, S. Rotter & P. Rabl. PT-symmetry breaking in the steady state of microscopic gain–loss systems. *New J. Phys.* **18,** 095003 (2016).

310. J. Huber & P. Rabl. Active energy transport and the role of symmetry breaking in microscopic power grids. *Phys. Rev. A* **100,** 012129 (2019).

311. T. Conte *et al. Thermodynamic Computing* arXiv: 1911.01968 (2019).

312. S. Xia, D. Kaltsas, D. Song, I. Komis, J. Xu, A. Szameit, H. Buljan, K. G. Makris & Z. Chen. Nonlinear tuning of PT symmetry and non-Hermitian topological states. *Science* **372,** 72–76 (2021).

313. L. J. Maczewsky, M. Heinrich, M. Kremer, S. K. Ivanov, M. Ehrhardt, F. Martinez, Y. V. Kartashov, V. V. Konotop, L. Torner, D. Bauer & A. Szameit. Nonlinearity-induced photonic topological insulator. *Science* **370,** 701–704 (2020).

314. S. Mukherjee & M. C. Rechtsman. Observation of Floquet solitons in a topological bandgap. *Science* **368,** 856–859 (2020).

315. S. Mukherjee & M. C. Rechtsman. Observation of unidirectional soliton-like edge states in nonlinear Floquet topological insulators. *Phys. Rev. X* **11,** 041057 (2021).

316. S. Lin, L. Zhang, T. Tian, C.-K. Duan & J. Du. Dynamic Observation of Topological Soliton States in a Programmable Nanomechanical Lattice. *Nano Lett.* **21,** 1025–1031 (2021).

317. E. J. Meier, F. A. An & B. Gadway. Observation of the topological soliton state in the Su–Schrieffer–Heeger model. *Nat Commun* **7,** 13986 (2016).

318. M. S. Kirsch, Y. Zhang, M. Kremer, L. J. Maczewsky, S. K. Ivanov, Y. V. Kartashov, L. Torner, D. Bauer, A. Szameit & M. Heinrich. Nonlinear second-order photonic topological insulators. *Nat. Phys.* **17,** 995–1000 (2021).

319. Y. Hadad, A. B. Khanikaev & A. Alù. Self-induced topological transitions and edge states supported by nonlinear staggered potentials. *Phys. Rev. B* **93,** 155112 (2016).

320. Y. Hadad, V. Vitelli & Andrea Alu. Solitons and propagating domain walls in topological resonator arrays. *ACS Photon.* **4,** 1974–1979 (2017).

321. Y. Hadad, J. C. Soric, A. B. Khanikaev & A. Alù. Self-induced topological protection in nonlinear circuit arrays. *Nat. Electron.* **1,** 178–182 (2018).

322. M. Jürgensen, S. Mukherjee & M. C. Rechtsman. Quantized nonlinear Thouless pumping. *Nature* **596,** 63–67 (2021).

323. M. Jürgensen, S. Mukherjee, C. Jörg & M. C. Rechtsman. *Quantized Fractional Thouless Pumping of Solitons* arXiv: 2201.08258 (2022).

324. H. Li, Y. Chen, J. Noh, S. Tadesse & M. Li. Multichannel cavity optomechanics for all-optical amplification of radio frequency signals. *Nat. Commun.* **3,** 1091 (2012).

325. M. Ashour, J. N. Caspers, E. M. Weig & P. Degenfeld-Schonburg. Spontaneous parametric down-conversion induced by optomechanical gradient forces in nanophotonic waveguides. *Phys. Rev. A* **103,** 023513 (2021).

326. J. N. Westwood-Bachman, T. Firdous, A. E. Kobryn, M. Belov & W. K. Hiebert. Isolation of optomechanical nonlinearities in nanomechanical cantilevers. *Phys. Rev. A* **105,** 053517 (2022).

327. P. Holmes & D. Rand. The bifurcations of Duffing's equation: An application of catastrophe theory. *J. Sound Vibr.* **44,** 237–253 (1976).

328. D. W. Jordan & P. Smith. *Nonlinear ordinary differential equations: an introduction for scientists and engineers* 4th ed (New York : Oxford University Press, Oxford [England], 2007).

329. I. Kovacic & M. J. Brennan. *The Duffing equation: nonlinear oscillators and their phenomena* (Wiley, Chichester, West Sussex, U.K. ; Hoboken, N.J, 2011).

330. F. Fani Sani, I. C. Rodrigues, D. Bothner & G. A. Steele. Level attraction and idler resonance in a strongly driven Josephson cavity. *Phys. Rev. Research* **3,** 043111 (2021).

331. M. Krack & J. Gross. *Harmonic balance for nonlinear vibration problems* (Springer International Publishing, Cham, 2019).

332. J. Košata, J. del Pino, T. L. Heugel & O. Zilberberg. HarmonicBalance.jl: A Julia suite for nonlinear dynamics using harmonic balance. *SciPost Phys. Codebases,* 6 (2022).

Summary

Orchestrating nanomechanical motion with light

Light is a versatile tool to perceive and measure the world around us. It can also be used to actively move or even shape objects, for example in optical tweezers or laser cutting. In this thesis, we use carefully configured laser light to detect and control the motion of nanomechanical resonators. In particular, we use the light as a medium to connect multiple mechanical resonators into small, highly tunable networks. These networks can be seen as small instances of 'metamaterials', with resonators as building blocks and optically controlled couplings. The flexibility of the optical driving allows to break fundamental symmetries such as time-reversal ($\mathcal{T}$) symmetry and the conservation of energy, and endows our nanomechanical networks with unusual properties and responses.

Nanomechanical resonators are conceptually simple, yet surprisingly versatile physical systems. Their ability to interface with many different degrees of freedom puts them forward as sensors and transducers even for quantum signals, while their high coherence and tunability find application in signal filtering and processing. In addition, nanomechanical resonators are used to create computational elements and perform fundamental tests of (quantum) mechanics. Studying and controlling the physics of nanomechanical resonators is therefore a worthwhile endeavour.

We develop an experimental platform to construct networks of nanomechanical resonators connected via time-modulated radiation pressure, and explore their dynamics. Multiple nondegenerate flexural mechanical resonances of a silicon nanostructure couple simultaneously to a photonic crystal nanocavity, allowing sensitive optical readout of mechanical motion with a resolution well below the thermal fluctuation level. By suitable modulation of a detuned drive laser, light-mediated effective mechanical couplings are established. Both beam-splitter and squeezing interactions can be induced by stimulating the appropriate frequency conversions. We implement a phase-coherent driving and detection scheme that allows the construction of arbitrary multi-mode quadratic phononic Hamiltonians in (synthetic) space and time. Finally, we have control over mechanical damping rates both through feedback and dynamical optothermal backaction.

We first focus on beam-splitter interactions and construct phononic networks that are subject to $\mathcal{T}$-breaking synthetic magnetic fields. For a three-mode network with a single plaquette, we observe chiral circulation of coherent vibrations. For networks featuring multiple plaquettes, we demonstrate interference between

aligned and opposed magnetic fluxes. Finally, in a small nanomechanical metamaterial comprising a five-mode lattice pierced by a homogeneous synthetic flux, we demonstrate the emergence of chiral transport of phonons along the edge, akin to the topological quantum Hall effect observed in two-dimensional electronic materials.

Next, we turn our attention to the interplay of synthetic magnetism and thermal fluctuations in the single-plaquette three-mode loop. The chirality imposed earlier on coherent excitations is shown to carry over to thermally excited vibrations. Combined with the different Bose occupations of the thermal baths feeding the mechanical resonators, flux-dependent circulation of energy leads to a redistribution of thermal energy in the loop. We develop a procedure to directly measure the flow of heat along the network's links, revealing flux-controlled reversal of thermal flow. Interestingly, we find that the breaking of time-reversal symmetry assists in the refrigeration of a hot mode in a strongly coupled loop, thus providing insight in the performance of thermodynamic processes under broken $\mathcal{T}$-symmetry.

Exploiting the opportunity to induce non-Hermitian nanomechanical dynamics through optomechanically-induced squeezing, we reveal a non-Hermitian version of the Aharonov-Bohm effect, and demonstrate it in two different systems. The first comprises a beam-splitter coupled dimer where both modes additionally experience single-mode squeezing. We show that this 'squeezing dimer' features a geometric phase, revealed diagrammatically after applying the Bogoliubov-de Gennes formalism — treating the modes' creation and annihilation operators as separate particle-like and hole-like degrees of freedom. This geometric phase, acting as a flux through the non-Hermitian particle-hole loop, now tunes both frequency and linewidth of the dimer's normal modes. Moreover, squeezing, stability, and the occurrence of exceptional points are all tuned by the flux as well.

The second system is a three-mode loop closed by a single beam-splitter and two two-mode squeezing interactions, which features a flux-tunable third-order exceptional point and unidirectional phononic amplification. Altogether, this rich phenomenology points the way to exploring new non-Hermitian topological bosonic phases and applications in sensing and transport that exploit spatiotemporal symmetry breaking.

Non-reciprocal transport is generally associated with the breaking of $\mathcal{T}$-symmetry. However, for quadrature-resolved signal transmission, we introduce an extended notion of unidirectional transmission, dubbed 'quadrature non-reciprocity' (qNR), that does not rely on the breaking of $\mathcal{T}$-symmetry. Instead, it relies on the interference of beam-splitter and two-mode squeezing interactions. We develop a theoretical framework to characterize and identify qNR for arbitrary systems, and test it in experiment for a two-mode dimer and a four-mode ring. The topological structure of the non-Hermitian eigenspectrum of chains comprising qNR elements is studied in theory, and linked to the occurrence of directional amplification in such chains.

To study quadrature-resolved dynamics in extended systems, we implement one of the seminal models put forward earlier in this field: the bosonic Kitaev chain (BKC). We show that the transmission of excitations through the BKC is chiral, with

the direction of propagation depending on the excited quadrature. The BKC has other unusual properties as well, that have no analogue in its extensively studied fermionic counterpart. In particular, the presence of squeezing interactions allows to amplify or damp signals that propagate along the chain. By closing the chain into a ring, a dramatic change in stability is observed as signals are then allowed to amplify indefinitely. The strong dependence of the BKC's dynamics on its boundary conditions is a uniquely non-Hermitian effect that links to the non-Hermitian skin effect. By tuning the phases of the hopping and squeezing interactions, we show a transition from global to local response in the chain.

Finally, as an outlook, we move beyond the linear response of our optomechanical resonators. We present experiments demonstrating that the cavity response can induce a highly-tunable effective Duffing nonlinearity for mechanical motion. The nonlinearity is shown to carry over to light-mediated effective mechanical interactions, while it can be cancelled on the single-resonator level by a two-laser driving scheme. These tunable nonlinear interactions could provide a toolbox to study nonlinear topological phenomena.

Samenvatting

Nanomechanische beweging manipuleren met licht

Licht is een veelzijdig hulpmiddel: we gebruiken het als de primaire manier om de wereld om ons heen waar te nemen, en technieken op basis van licht zijn tot uiterst precieze metingen in staat. Ook kan licht gebruikt worden om objecten te verplaatsen of zelfs vorm te geven, bijvoorbeeld in optische pincetten of lasersnijtechnieken. In dit proefschrift gebruiken we zorgvuldig geconfigureerd laserlicht om de beweging van nanomechanische resonatoren te detecteren en te besturen. Preciezer gezegd; we gebruiken het licht als medium om meerdere mechanische resonatoren met elkaar te verbinden zodat ze kleine, uitzonderlijk goed regelbare netwerken vormen. Deze netwerken kunnen worden beschouwd als kleine stukjes 'metamateriaal', met resonatoren als bouwstenen en optisch gestuurde koppelingen. Net als in een gewoon materiaal worden de collectieve eigenschappen van een metamateriaal bepaald door door die bouwstenen en koppelingen. De flexibiliteit van de optische aandrijving maakt het echter mogelijk om fundamentele symmetrieën te breken, zoals tijdomkerings-($\mathcal{T}$-)symmetrie en behoud van energie, en geeft onze netwerken ongebruikelijke eigenschappen en responsen.

Nanomechanische resonatoren zijn conceptueel eenvoudige, doch verrassend veelzijdige fysieke systemen. Hun vermogen tot wisselwerking met een breed scala aan andere fysische vrijheidsgraden maakt ze goede sensoren en signaalomzetters, zelfs voor kwantumsignalen, terwijl hun hoge coherentie en grote mate van afstembaarheid toepassing vinden in signaalfiltering en -verwerking. Daarnaast kunnen nanomechanische resonatoren gebruikt worden om informatie te verwerken en fundamentele testen van (kwantum)mechanica uit te voeren. Dit alles maakt het bestuderen en beïnvloeden van de fysica van nanomechanische resonatoren de moeite waard.

Dit proefschrift beschrijft de ontwikkeling van een experimenteel platform waarin we netwerken van nanomechanische resonatoren kunnen construeren, die verbonden zijn via tijdgemoduleerde stralingsdruk, en verkennen hiermee de door het licht gecontroleerde mechanische dynamica. Meerdere niet-ontaarde mechanische buigingsmodi van een silicium nanostructuur koppelen tegelijk aan een optische nanotrilholte, gedefinieerd in een fotonisch kristal. Hierdoor is een gevoelige optische uitlezing van mechanische beweging mogelijk, met een resolutie die ver onder het niveau van thermische fluctuaties ligt. Door geschikte intensiteitsmodulatie van een verstemde aandrijflaser, worden door licht bemiddelde,

effectieve mechanische koppelingen tot stand gebracht. Zowel conservatieve (of '*beamsplitter*') interacties, als parametrische versterking (of '*squeezing*') kunnen worden geïnduceerd door de juiste frequentieconversies te stimuleren. We implementeren een fase-coherente meet- en aandrijfmethode, zodat willekeurige, multi-modale kwadratische fononische Hamiltonianen kunnen worden aangelegd in (synthetische) ruimte en tijd. Ten slotte hebben we controle over mechanische demping, zowel door terugkoppeling op basis van gemeten verplaatsing, als door dynamische optothermische krachten.

We richten ons eerst op conservatieve interacties en construeren fononische netwerken die onderhevig zijn aan $\mathcal{T}$-brekende synthetische magnetische velden. Voor een netwerk met drie modi en een enkele plaquette observeren we chirale circulatie van coherente trillingen. Voor netwerken met meerdere plaquettes demonstreren we interferentie tussen gelijkgerichte en tegengestelde magnetische fluxen. Ten slotte construeren we een klein nanomechanisch metamateriaal bestaande uit een rooster van vijf modi doorkruist door een homogeen magnetisch veld, en demonstreren hierin het ontstaan van chiraal fonontransport langs de rand van het materiaal — vergelijkbaar met het topologische kwantum-Hall effect in een tweedimensionaal elektrongas.

Aansluitend richten we ons op het samenspel tussen synthetisch magnetisme en thermische fluctuaties, in een lus van drie trillingsmodi met een enkele plaquette. De chiraliteit die eerder werd waargenomen voor coherente excitaties blijkt ook van toepassing op thermisch aangeslagen trillingen. In combinatie met de verschillende Bose-bezettingen van de thermische baden die de trillingsmodi opwarmen, leidt de fluxafhankelijke circulatie van energie tot een herverdeling van thermische energie in de lus. We ontwikkelen een procedure om de warmtestroom langs de verbindingen van het netwerk rechtstreeks te meten. Hiermee laten we een fluxgestuurde omkering van warmtestromen zien. Bovendien ontdekken we dat het breken van de tijdomkeringssymmetrie helpt bij het koelen van een warme trillingsmodus in een sterk gekoppelde lus. Hierdoor krijgen we inzicht in de prestaties van thermodynamische processen onder gebroken $\mathcal{T}$-symmetrie.

Vervolgens maken we gebruik van de mogelijkheid om niet-Hermitische bewegingen te induceren middels optomechanisch geïnduceerde parametrische versterking, of *squeezing*. We leggen een niet-Hermitische versie van het Aharonov-Bohm-effect bloot, en demonstreren dit in twee verschillende systemen. Het eerste omvat een conservatief gekoppeld dimeer, waarbij beide modi daarnaast ook individueel parametrisch versterkt worden. We laten zien dat dit 'squeezing dimeer' een geometrische fase heeft, die schematisch kan worden onthuld door toepassing van het Bogoliubov-de Gennes-formalisme — waarbij de creatie- en annihilatieoperatoren van de trillingsmodi worden beschreven als onafhankelijke, deeltje- en gatachtige vrijheidsgraden. Deze geometrische fase, die werkt als een flux door de niet-Hermitische lus van deeltjes en gaten, beïnvloedt nu zowel de frequentie als de lijnbreedte van de eigentrillingen van het dimeer. Bovendien worden squeezing, stabiliteit en het voorkomen van uitzonderlijke punten ('*exceptional points*') ook alle beïnvloed door de flux.

Het tweede systeem is een lus van drie trillingsmodi, die wordt gevormd door

een enkele conservatieve koppeling en twee intermodale parametrische versterkingsprocessen. Dit systeem vertoont een fluxgevoelig uitzonderlijk punt van derde orde en richtingsgevoelige versterking van vibraties. Al met al wijst deze rijke fenomenologie de weg naar de verkenning van nieuwe, niet-Hermitische topologische bosonische fasen, en toepassingen in sensoren en signaaltransmissie die gebruik maken van gebroken symmetrieën in ruimte en tijd.

Richtingsgevoelige (niet-reciproke) transmissie wordt over het algemeen in verband gebracht met het breken van $\mathcal{T}$-symmetrie. Voor kwadratuur-opgeloste signaaloverdracht introduceren we echter een uitgebreider begrip van unidirectionele transmissie, 'kwadratuur-niet-reciprociteit' (kNR) genaamd, dat niet afhankelijk is van het breken van $\mathcal{T}$-symmetrie. In plaats daarvan vindt het zijn oorsprong in de interferentie tussen conservatieve interacties en intermodale parametrische versterking. We ontwikkelen een theoretisch raamwerk om kNR voor willekeurige systemen te herkennen en te karakteriseren, en testen het experimenteel in een dimeer van twee en een ring van vier resonatoren. We bestuderen in theorie de topologische structuur van het niet-Hermitische (complexe) eigenspectrum van ketens bestaande uit kNR-elementen, en relateren dit aan het optreden van directionele versterking in zulke ketens.

Om kwadratuur-opgeloste dynamiek in uitgebreide systemen te bestuderen, implementeren we een van de elementaire modellen die eerder op dit gebied te berde zijn gebracht: de bosonische Kitaev-keten (BKK). We laten zien dat de overdracht van excitaties in de BKK een chiraal karakter heeft, waarbij de voortplantingsrichting afhangt van de aangeslagen kwadratuur. De BKK heeft ook andere ongebruikelijke eigenschappen, die geen overeenkomst hebben in zijn uitgebreid bestudeerde, fermionische tegenhanger. In het bijzonder maakt de aanwezigheid van parametrische versterking het mogelijk om signalen dit zich langs de keten voortplanten te versterken of te dempen. Door de ketting tot een ring te sluiten, vindt een ingrijpende verandering in stabiliteit plaats, aangezien signalen vervolgens eeuwig versterkt kunnen worden. De dynamiek van de BKK is dus sterk afhankelijk van haar randvoorwaarden — een uniek, niet-Hermitisch effect dat samenhangt met het niet-Hermitische skineffect. Door de fasen van de conservatieve en de parametrische processen te variëren, tonen we een overgang in de keten van globale naar lokale respons.

Tot slot kijken we, bij wijze van vooruitzicht, voorbij de lineaire respons van onze optomechanische resonatoren. We presenteren experimenten, waarin we aantonen dat de frequentierespons van de trilholte een bijzonder regelbare effectieve Duffing-niet-lineariteit voor beweging voortbrengt. In het bijzonder wordt deze niet-lineariteit ook overgedragen op door licht bemiddelde effectieve mechanische interacties, terwijl deze voor enkele resonatoren kan worden opgeheven middels een aandrijfschema met twee lasers. Deze regelbare niet-lineaire interacties zouden een essentiële bouwsteen kunnen zijn voor het bestuderen van niet-lineaire topologische verschijnselen.

Acknowledgments

Welcome! We both made it all the way to the end of my thesis — I hope you enjoyed reading it. I would like to dedicate this final section to the process of its creation, focusing in particular on the many people that have helped me along the way. While every PhD project has its ups (intriguing yet sensible results, paper accepted, presentation well-received) and downs (stumbling in the dark, failed fabrication, endless days in lab), overall I look back on these four+ years with a sense of achievement and most importantly, fond memories.

In a large part, this feeling is the result of the very fruitful collaboration with my promotor and group leader, Ewold. Over these four years, you gave me the freedom to grow while never losing me out of sight. Thank you for being both extremely enthusiastic and dependable, despite the many balls that you keep in the air. Your scientific eagerness always inspires me, and has often helped me regain motivation when I had had enough. I have learned a lot from you, especially when it comes to the art of writing down and presenting results. Your input to this thesis has been invaluable.

Javier, I am grateful to have always had you on my side, despite your moving to Zürich halfway through. You have been a great mentor and friend, and I thoroughly enjoyed our nearly daily chats about physics and life. This thesis would have been impossible without you.

Andreas, thank you for the many interesting discussions and, of course, being my copromotor. The same goes for the rest of the qNR team, Clara & Matteo: While the six of us never met together in person, I am proud of what we have achieved by collaborating digitally!

These experiments would not have been possible without the excellent support staff at AMOLF. Let me start with a shout-out to our lab technicians, Jan Bonne and Daniël, who kept the place running smoothly and safely. A big thank you also to the NanoLab staff for their endless efforts to keep the cleanroom up: Bob, Dimitry, Andries, Igor, Dylan, Arthur, Laura and Hans. From the electronics department, I'd like to honour Bob and especially Ronald for their help in extending the capabilities of my set-up. My gratitude also goes out to Niels and Petra, who have helped me on various occasions.

My closest colleagues from the Photonic Forces group have been central to my time at AMOLF, both scientifically and socially. John, thank you for showing me the ropes on the nanobeam set-up while sitting on your throne in lab. Giada, I have fond memories of the many hours we spent together in the cleanroom and I

wish you all the best on your quest to combine art and science. Roel, mijn kerel, I appreciate the many conversations we had; it was great to share this experience with you and I'm happy to have you as my paranymph. Jente, my other contemporary, your enthousiasm and ability to keep going are inspirational, as is your knowledge of beers and fries. René, I had great fun sharing an office with you and admire your dry-witted, impeccably timed humorous remarks — defying the German stereotype. Pascal, I enjoyed very much our times together in the lab and in particular our wild ride home from Erlangen. Robin, the many discussion we had over lunch and coffee about broad-ranging topics were always a delight. Thank you, Nikhil, Georgios and Johneph, who is no longer with us, for putting up with me in the office. Finally, I thank Cesare, Laura, Karel, Lars, Alejandro, Menno and Fons for their contribution to the great PhoFo atmosphere.

As a place of scientific collaboration, AMOLF is unique. I learned a great deal from discussions with other group leaders, in particular Femius, Said and Marc. Also unique is the supportive and positive social atmosphere. This is embodied by the countless friendly interactions I had over lunch, in the works council, at the coffee table, in the cleanroom, and in the hallway, with a long list of wonderful people including Alex, Andrea, Annemarie, Ariane, Deba, Eline, Evelijn, Falco, Giel, Giorgio, Hugo, Imme, Isabelle, Jan, Jenny, Jorijn, Joris, Kevin, Lucie, Lukas, Manuel, Mareike, Marnix, Matthias, Nasim, Nelson, Nick, Nika, Ramon, Ronald, Ruslan, Rutger, Sanghamitra, Simone, Susan, Tom, Vashisht, and Zhou. I hope to see you all again some time!

Outside of work, there are many people that have supported me and coloured my life. To my housemates Michiel, Bas (2x), Marie and Jordy, supplemented by Shweta, Marcella and Jan: It was always a pleasure to come home to you after a long day in the lab, or to game excessively during lockdown. A special thanks to my bicycle mate Stijn, with whom I have had the pleasure to share many micro- and macro-adventures. The same goes for my brothers-in-arms Daan, Michiel, Robbert, and Tom. I am glad for the many other friends I made in Delft and Rotterdam as well, including Jelle, David, Tom, Tom, Laurie, Dirk-Jan, Anne-Nynke, Daan, Evert, Joeri, Bauke, Lennart, Duco, Lieske, Willemijn, Terry, Marijke, Marlies, Hanna, Maartje and Rik.

You can take the Groninger out of Groningen, but you can't take Groningen out of the Groninger — at least not out of this one. Thank you, Bram, Karst Jan, Cyntha, Jan-peter, Dennie, Hans, Thomas, Luuk, Luurt, Willemijn, Sanne, Robbert, Ger, Bas, Rik, Valerie, Thibauld and Flip, for looking after the place in my absence and for always welcoming me back into your lives when I'm there. I wouldn't have been the same without you. I'm also happy to have stayed in touch with those who have fanned out: George, Steven, Thomas, Pien, Marte Sophie and Jop.

Finally, I want to express my gratitude to my wonderful family. To my parents: Thank you for always being there for me. I'm very proud of my (little) sister and paranymph Mieke, the original dr. Slim. And last but not least, I want to thank my dearest partner Juliette, who has supported and encouraged me without fail. I hope to go on many more adventures with you, both big and small. You are always in my heart.

About the author

Jesse Slim was born in 1992 in Groningen, the Netherlands. He studied Applied Physics and Applied Mathematics at Delft University of Technology, obtaining a Bachelor's degree in both in 2015. In his final research project for this double degree programme, he imaged the mode shapes of graphene microdrums using laser interferometry, in the lab of Warner Venstra and Herre van der Zant.

He went on to obtain a Master's degree in Applied Physics from the same university in 2018, after completing three research rotations. First, he joined the long-distance quantum communication group led by Rupert Ursin, at the Institute for Quantum Optics and Quantum Information (IQOQI) in Vienna, where he worked on a set-up to measure atmospheric turbulence. He then completed his thesis project in the diamond quantum network group led by Ronald Hanson, at Delft University of Technology. There, he developed and demonstrated fast feed-forward control to realign nuclear-spin memory qubits after entanglement attempts between remote NV center electron spins. For his last rotation, he worked with David DiVincenzo at RWTH Aachen in the quantum information theory group on extending the rotating wave formalism — commonly applied in qubit control — to higher orders.

After graduating, Jesse worked at Hukseflux Thermal Sensors B.V. as a research & development assistant for six months. Subsequently, he joined the Photonic Forces group at AMOLF in Amsterdam as a Ph.D. researcher. There, he worked on a project to control nanomechanical motion with light under the supervision of prof. Ewold Verhagen. The results of this project are presented in this thesis.

Jesse presented his work at several national and international conferences, receiving the Oral Presentation Award at WOMBAT 2022 in Erlangen. In addition, he was elected to the AMOLF works council for a two year term to represent the interests of AMOLF employees, assisted in teaching the AMOLF Python course, and participated in a number of outreach activities.

Jesse enjoys programming, cycling, ice skating, good food and travelling.